AN ABSTRACT OF THE THESIS OF

Edward I. Tollerud for the degree of Doctor of Philosophy in Atmospheric Sciences presented on June 1, 1983.

Title: An Observational Study of the Wind Fields Associated with GATE Cloud Clusters

Redacted for privacy

Abstract approved:

Dr. Steven K. Esbensen

The wind and thermodynamic fields associated with eastern Atlantic cloud clusters are studied using radiosonde data from the Global Atmospheric Research Program Atlantic Tropical Experiment (GATE). These data are from the gridded set of winds prepared by Dr. Katsuyuki Ooyama (AOML-NOAA) and Dr. Jan-Hwa Chu (SSEC, University of Wisconsin, Madison) using an objective analysis scheme designed by Dr. Ooyama. Similarly-analysed thermodynamic data prepared by Dr. Steven Esbensen (Oregon State University) are also used.

Case studies of the vorticity budget for the 4 September squall and the 5 September cluster show significant contributions by all budget terms including the residual, which is interpreted as the effects of cumulus convection, mesoscale cloud lines, or other small-scale circulations. The residual is particularly large in the boundary layer and upper troposphere. The fields of winds and vorticity budget terms in the upper troposphere of the two systems are similar. However, at the level of the mid-tropospheric jet, the small-scale production of vorticity is significantly different in the two systems.

A technique for compositing clusters using satellite-derived cloud-top data is applied to GATE data from Phase 3. Vertical

motions within and below the anvils are in accord with previous studies. Frictionally-induced inflow is found to be of secondary importance to the development and maintenance of cluster circulations. The composited vorticity budget residuals are again large in the boundary layer and upper troposphere.

A large-magnitude asymmetric vorticity couplet observed in the upper troposphere of individual clusters and in composite results is examined. Cluster-scale twisting and motions at meso- or smaller scales are found to produce the couplet, while cluster-scale divergence is the primary destructive agent. A deceleration of the strong easterlies at this level produces these couplets. Possible mesoscale and cumulus sources of this deceleration are discussed.

Present schemes that parameterize vorticity production by cumulus convection are found to be inconsistent with similar schemes that parameterize momentum production. Furthermore, these vorticity parameterizations cannot describe the production of the upper-tropospheric couplets discussed above. An alternate parameterization, formed by taking the curl of the parameterized momentum source, does qualitatively describe the couplets.

An Observational Study of the Wind Fields Associated with GATE Cloud Clusters

by

Edward I. Tollerud

A THESIS

submitted to

Oregon State University

in partial fulfillment of
the requirements for the
degree of

Doctor of Philosophy

Completed June 1, 1983

Commencement June 1984

APPROVED:

Redacted for privacy

Assistant Professor of Atmospheric Sciences in charge of major

Redacted for privacy

Chairman of the Department of Atmospheric Sciences

Redacted for privacy

Dean of Graduate School

Date thesis is presented June 1, 1983

Typed by Sheri Kellogg for Edward I. Tollerud

To My Parents

ACKNOWLEDGEMENTS

Among all those whose help was instrumental in the preparation of this thesis, I owe the greatest thanks to my research advisor, Dr. Steven Esbensen. To a considerable extent, my understanding of tropical meteorology is a result of his. I gratefully acknowledge his help both as a scientific colleague and as a friend.

I would also like to thank the other members of my doctoral committee (Dr. James Deardorff, Dr. Young-June Han, Dr. Victor Madsen, Dr. William Quinn, and Dr. C. R. N. Rao) for their helpful comments during the writing of this thesis and for their participation in previous phases of my graduate program. In particular, discussions with Drs. Deardorff, Han, and Rao have helped me past troublesome portions of my research.

Many of my fellow students have also helped me in various ways, and I thank them collectively here. I have particularly profitted from many discussions with Jough-Tai Wang.

I have received excellent computing support through the facilities of the Climatic Research Institute. I thank Dr. W. L. Gates for kindly making them available to me. Shiang Heh has programmed many of the plotting and data retrieval routines that were instrumental to my research. Bill McKie, Bob Mobley, and Wells Matthews have also helped me with computing problems.

The figures in this thesis were drafted by Kathryn Torvik and Carolyn Guynup. I thank Sheri Kellogg for typing the final version of this thesis. Earlier versions of Chapter 7 (which has been submitted for publication in the Monthly Weather Review) were typed by Liz Webb and Cindy Beck.

It is customary in a thesis heavily dependent upon observations to thank the people who made the observations. I take this opportunity to thank the personnel of the GATE experiment and

those who subsequently organized the observations into usable forms. I owe a special measure of appreciation to Dr. Katsuyuki Ooyama and Dr. Jan-Hwa Chu for preparing the wind data, to Dr. Steven Esbensen for preparing the thermodynamic data, and to Dr. Stephen Cox for providing the satellite radiation data.

It would be an understatement to say that this thesis would not have been completed without the help and perseverance of my wife, Barb Brown. I thank her for her professional assistance and her patience, and I presume that I shall someday have the opportunity to return the favor.

The research upon which this thesis is based was sponsored by NSF grants ATM-8019251 and ATM-8213130.

TABLE OF CONTENTS

LIST OF FIGURES

LIST OF TABLES

AN OBSERVATIONAL STUDY OF THE WIND FIELDS ASSOCIATED WITH GATE CLOUD CLUSTERS

CHAPTER 1. INTRODUCTION

The most striking features that appear on satellite pictures of the tropical oceans are undoubtedly the groups of deep clouds that develop in concert near the intertropical convergence zone. In their mature and late stages, the tops of these clouds merge to form the extensive anvils that are the most noticeable feature of these so-called "cloud clusters." Occasionally a cluster will develop into a tropical depression or a hurricane and become a self-perpetuating system of great intensity.

Because of their ubiquity, size, and relative longevity, cloud clusters have become the subject of much investigation and speculation. In particular, this speculation has often concerned the possibility that they represent a scale of motion intermediate between the synoptic waves observed in the tropics and individual cumulonimbus clouds. The research described in this thesis is intended to shed some further light on this subject by observationally determining the structure of the wind fields (and to a lesser extent the thermodynamic fields) associated with clusters. In the process, it is also possible to reach some conclusions about the relationship that clusters bear to larger circulations on the one hand and to smaller meso- and cumulus scales on the other.

Prior to GATE (the GARP Atlantic Tropical Experiment, where GARP stands for the Global Atmospheric Research Program) in 1974, observations of the evolution of individual cloud clusters were severely limited by data availability. With the completion of the gridded GATE Phase 3 wind set of Ooyama (AOML-NOAA) and Chu (SSEC, University of Wisconsin, Madison) and the similarly

gridded set of temperature and relative humidity prepared by Esbensen (Oregon State University) there is now data that can begin to resolve the space and time scales of larger GATE clusters. The wind set is used here both as the basic source of momentum, divergence, vertical velocity, and vorticity fields and as input to a vorticity budget. The thermodynamic set provides information about the temperature and moisture structure of the two clusters chosen for a detailed investigation.

Since the primary goal of this work is to describe the structure of cloud clusters, the emphasis throughout will be on observations. Chapter 2 provides a brief overview of tropical convective systems and a summary of the previous investigations that are of most relevance to the present study. In Chapter 3, the data sets that are most important to this thesis are described. Chapter 4 includes a description of the methodologies used to compute terms of a vorticity budget and to construct an "anvil index" from satellite-derived cloud top data. Fields of this latter quantity can be used to determine the location and stage in the life cycle of clusters. Case studies of three major GATE clusters, the moving squall-cluster on 4 September and the two paired slow-moving clusters on 5 September, make up Chapter 5. Next, in Chapter 6, the results of the compositing of cluster wind fields are presented. Among the most significant of the features observed in both the individual case studies and the composite are the large-amplitude vorticity couplets that are found in the upper troposphere. The structure and evolution of these couplets is the subject of Chapter 7. In Chapter 8, implications of these observations for the proposed schemes to parameterize the effect of subgrid circulations on resolved momentum and vorticity fields are discussed. Chapter 9 includes a summary and discussion of the significance of the results of the thesis and some suggestions for further research on tropical convection and cloud cluster circulations.

CHAPTER 2. BACKGROUND

Although cloud clusters are the primary subject of this thesis, clouds in the tropics are organized into other patterns as well. These systems cover a wide spectrum of scales, ranging from small cumulus clouds to the intertropical convergence zone (ITCZ) which extends (with occasional breaks) across entire ocean basins. Before describing results from the previous investigations that are most relevant to this thesis, it will be useful to first give a brief overview of the kinds of convective systems that are found over the tropical oceans.

2.1 An overview of convective systems in the tropics

Figure 2.1 lists the most prominent of the tropical convective systems (the ITCZ is not included) and shows their approximate time and space scales. On Fig. 2.2 they are compared again in a more diagrammatic fashion.

Starting with the larger scales and working down, Fig. 2.3 indicates that the ITCZ (which is located between 5°N and 10°N over both oceans) has quite long zonal dimensions but is relatively narrow (about 500 km). Climatologically, it is a region of general upward motion and convection brought about by the lower-tropospheric convergence of the southeast trade winds from the Southern Hemisphere and the northeast trades from the Northern Hemisphere. It is an important part of the Hadley circulation that exports large amounts of excess energy to higher latitudes. Although it is often tacitly assumed to extend continuously around the Earth, at a given time or longitude an ITCZ may not necessarily be evident; like the Hadley cell, its longitudinal continuity in long-term averages (cf. Fig. 2.3) is largely a statistical result. In fact, the major part of the upward mass flux in the ITCZ takes place not in generalized upward motion in the entire region but

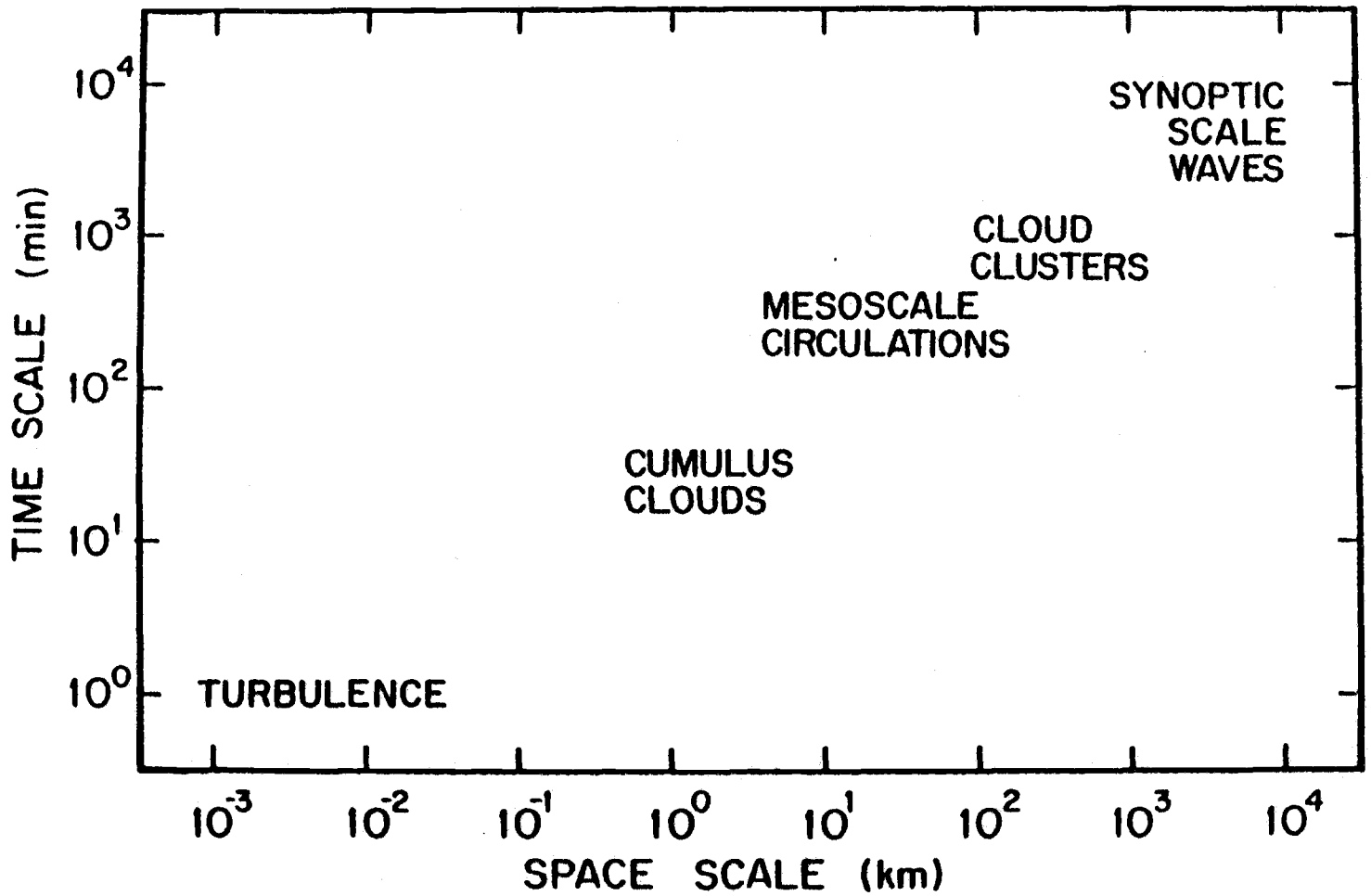

Figure 2.1. Relevant time and space scales of GATE disturbances (from Esbensen et al., 1982).

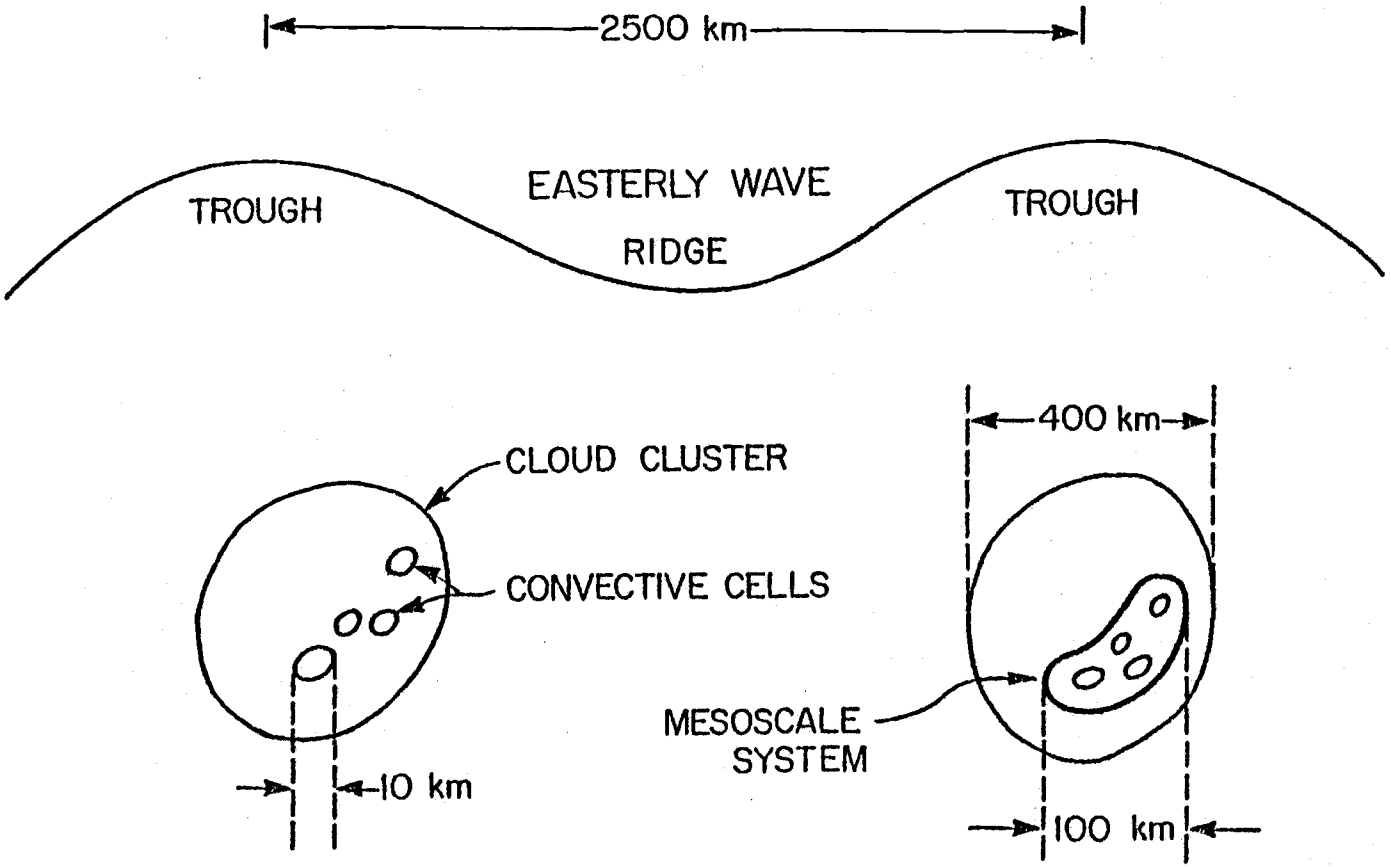

Figure 2.2. Schematic diagram of GATE convective systems (adapted from Yanai et al., 1982). The stated horizontal distances are typical dimensions and are only roughly to scale.

(a) PACIFIC OCEAN

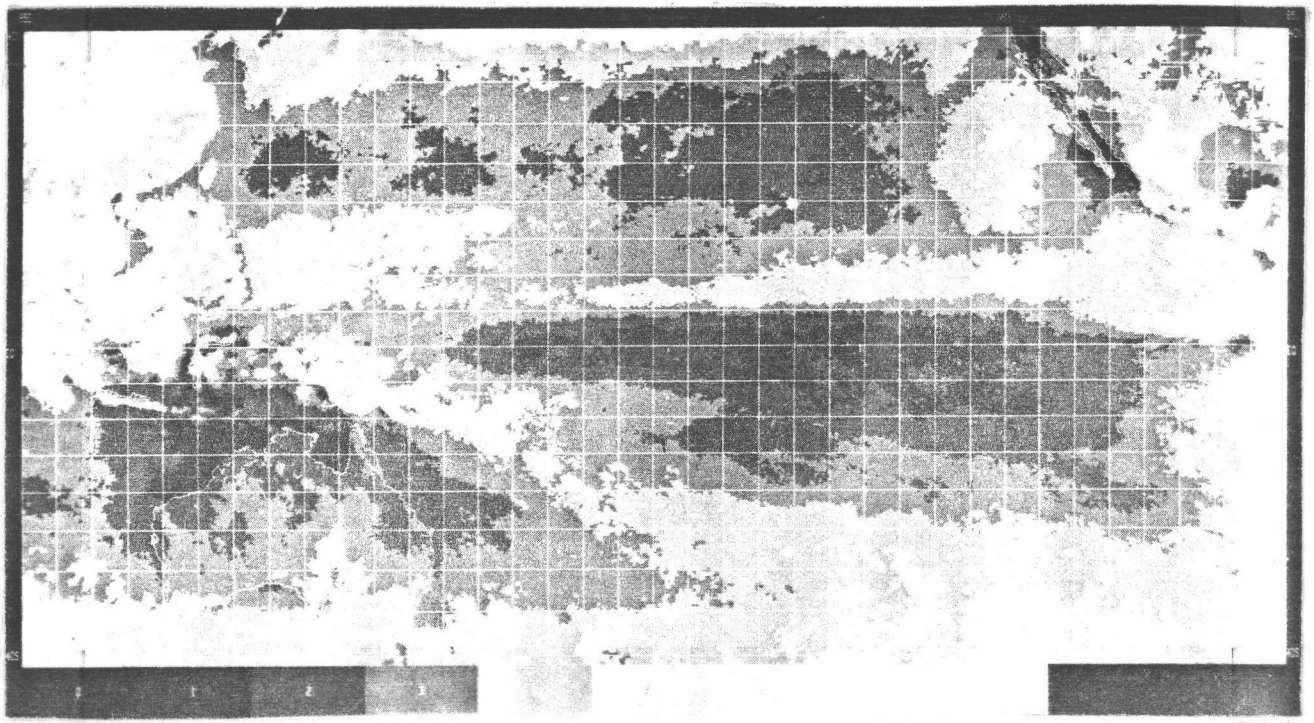

Figure 2.3. Satellite-derived relative cloud cover composited over Septembers between 1967 and 1970 over (a) the Pacific basin and (b) the Atlantic basin. Tick marks along the sides denote the equator; the Mercator grid lines are spaced at intervals of 5 degrees of latitude and longitude. The hexagon in (b) is the GATE A/B ship array.

(b) ATLANTIC AND INDIAN OCEANS

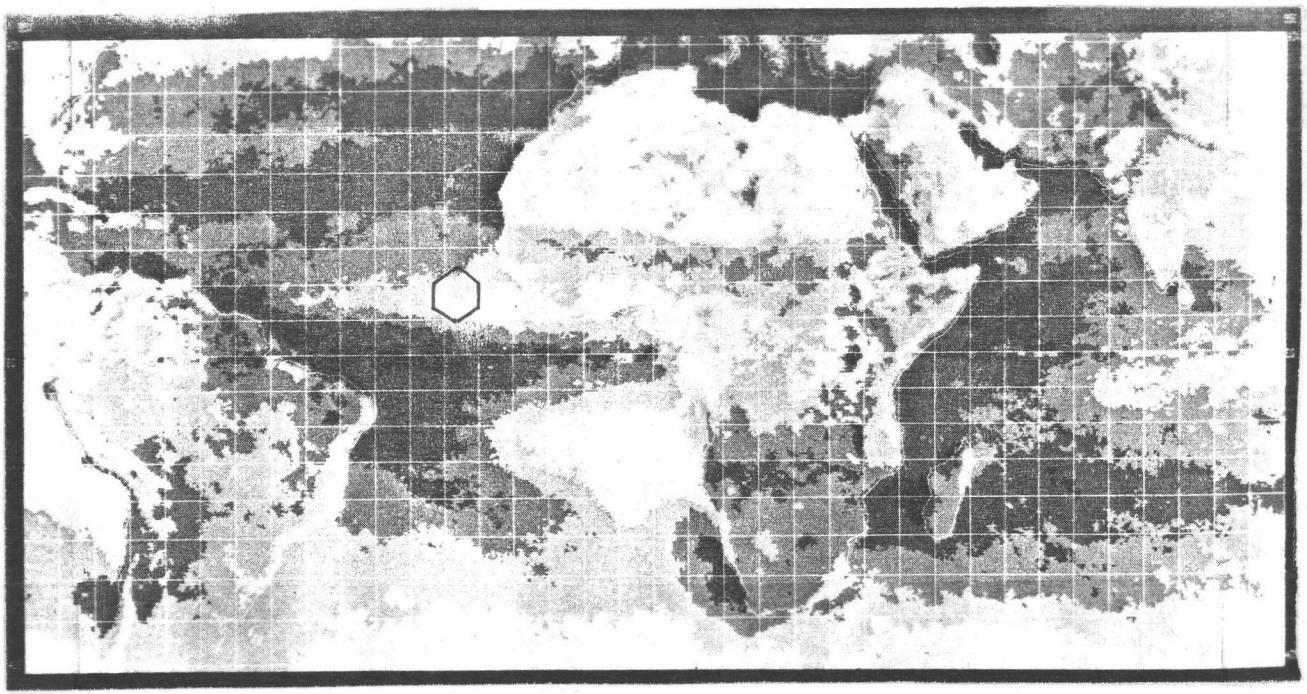

Figure 2.3 (continued)

rather in the updraft cores of individual cumulonimbus clouds. Between the clouds the vertical motion is weakly upward or subsiding.

Superimposed upon the ITCZ in the GATE area, there is a monsoon circulation in which low-level inflow eastward toward the African continent is replaced at higher levels by westward outflow from the continent. The streamlines on Fig. 2.4 show the structure of the wind fields associated with this feature. The monsoon circulation near the surface produces a cross-equatorial flow from the Southern Hemisphere which curves eastward upon crossing the equator. Thus, the low-level convergence here is more properly described as a convergence of the northeast trades with the southwest monsoon flow. As a result, the distinction in the region between a classical ITCZ and the convergent flow of the West African monsoon is hazy at best.

Perhaps the predominant motions in the mid-troposphere during GATE were those due to the synoptic-scale easterly waves that moved across the GATE array in very nearly a continuous succession (Figs. 2.2 and 2.5). Although discernible in each of the three phases of GATE, these waves had their largest amplitudes during Phase 3. The level of maximum amplitude was approximately 635 mb; however, their effects can be seen in observations at all tropospheric levels. 635 mb was also the height of a strong easterly wind maximum, with which the waves were undoubtedly associated. Details emerging from GATE studies of easterly waves suggest that the waves originate over the eastern or central Sahel region due to instabilities of the easterly jet much like those modeled for the case of an internal atmospheric jet by Charney and Stern (1962). These instabilities can be brought about by meridional temperature gradients and/or by meridional shear of the wind (Burpee, 1972; Albignat and Reed, 1980). The most active region of the waves is just north of the GATE A/B ship array. Observational studies have shown that these waves strongly modulate the

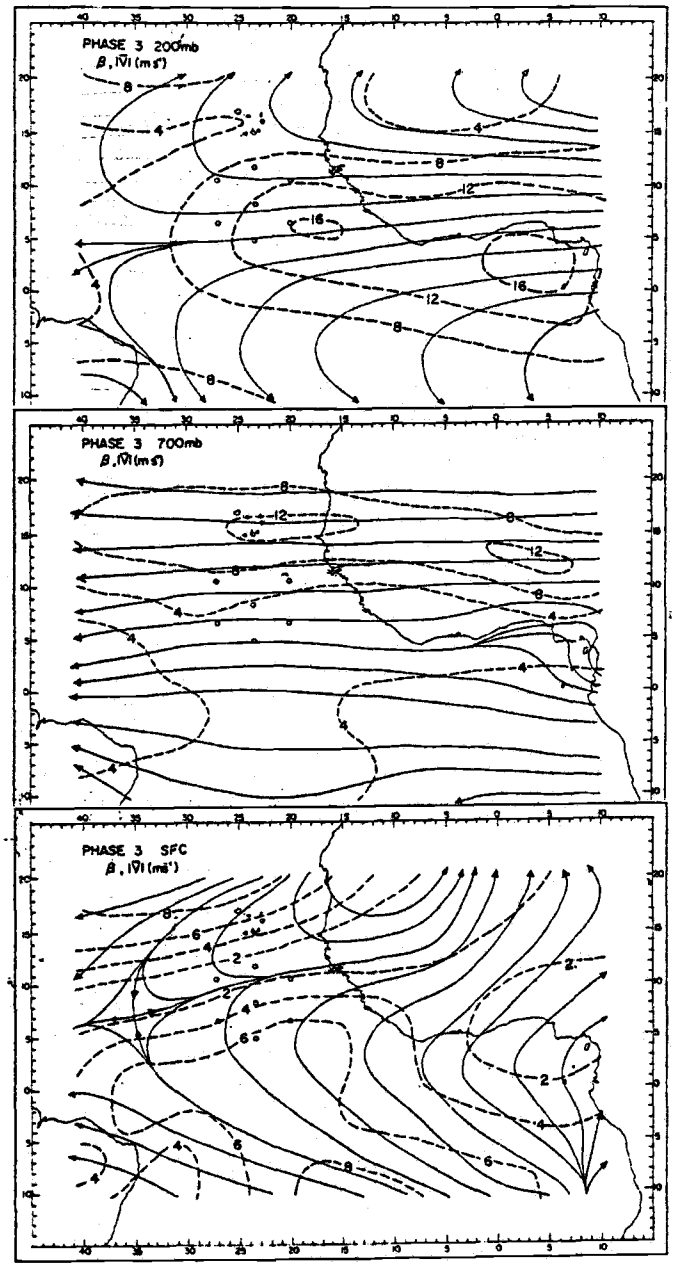

Figure 2.4. Streamlines and isotachs at the surface, 700 mb, and 200 mb for the average flow during Phase 3 of GATE. Units of the isotachs are ms^{-1}. From Vincent (1981).

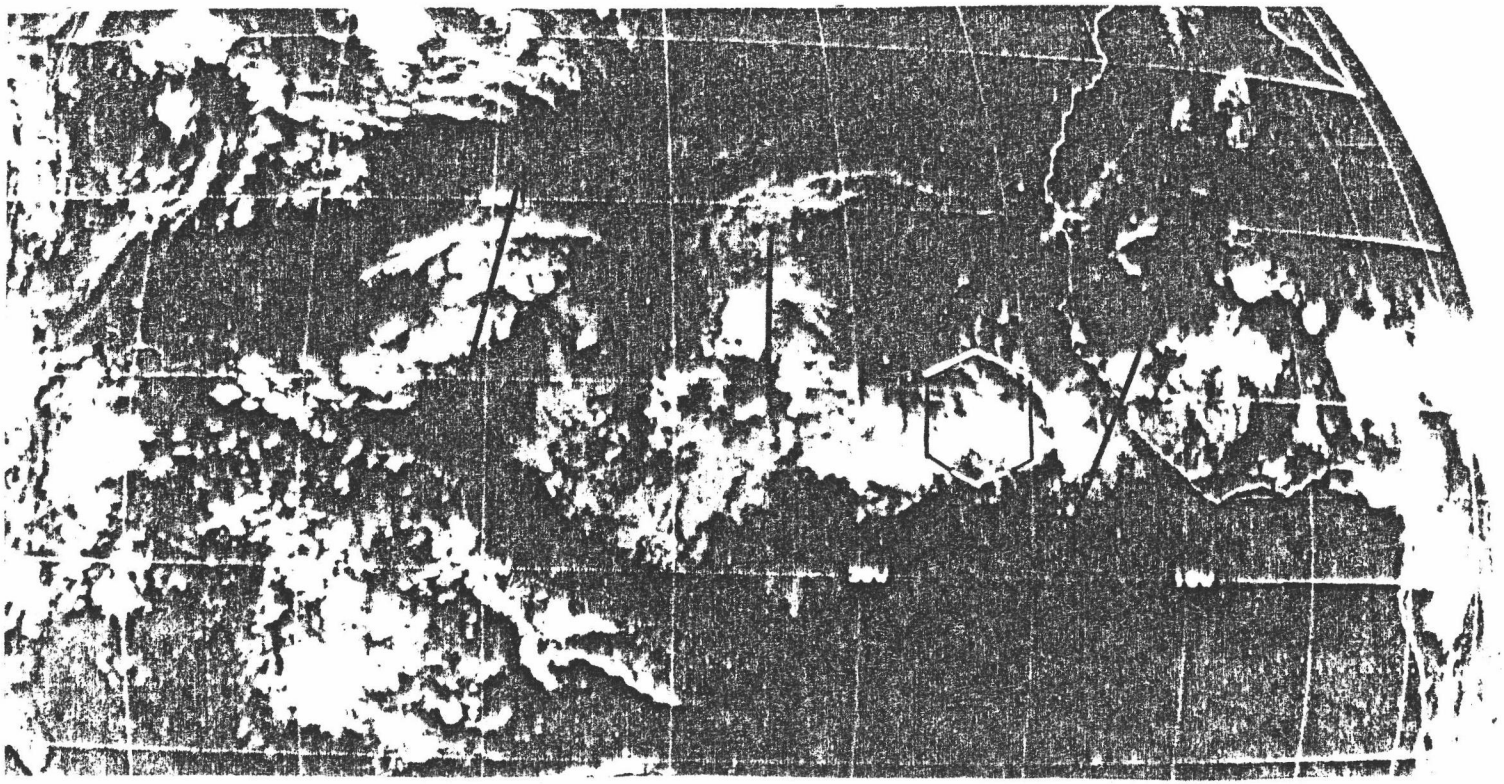

Figure 2.5. Infrared satellite picture of the tropical Atlantic made at 1800 GMT on 4 September 1974. The hexagon is the GATE A/B ship array. Troughs of easterly waves are denoted by solid dark lines. The positions of the troughs near 11°W and 35°W were determined from the 700 mb streamline analysis of Krishnamurti et al. (1979); the location of the trough at 50°W was estimated from the cloud observations themselves.

occurrence of convective clouds and cloud clusters (Payne and McGarry, 1977); it is this modulation of convection that makes the waves distinguishable on Fig. 2.5.

The next largest recognizable convective entities in the GATE region were the clusters of clouds whose tops eventually coalesced to form deep, horizontally extensive anvils. Satellite pictures made during GATE (Fig. 2.6) and in many other tropical locations have shown that these "cloud clusters" are an ubiquitous feature of the tropical atmosphere. Since they are the primary concern of this thesis, they will be described in detail in the next section and in subsequent chapters. In this overview it is simply noted that clusters tend to occur near the ITCZ and, as indicated by Fig. 2.2, in the trough region of easterly waves, though these are certainly not the only regions in which they are found.

As Fig. 2.2 suggests, cloud clusters in the tropics are made up of one or more smaller mesoscale systems, which often take the form of propagating lines of clouds. The mesoscale line marked by arrows on Fig. 2.7 is one of many that could have been picked out from the 5 September clusters. Within these cloud lines are embedded individual cumulonimbus clouds like the one photographed on Fig. 2.8. The complex cloud structure evident in the photograph was typical of GATE.

The observations employed in this thesis can resolve systems as large as or larger than cloud clusters. Thus, the evidence presented about these scales will be direct in the sense that the observations upon which they are based are adequate to describe the systems directly. For the smaller scales, conclusions must be inferred from diagnostic analyses or physical reasoning based on the results of the larger-scale observations. Chapter 3 contains further discussion of the ways in which the observations affect the interpretation of these convective systems.

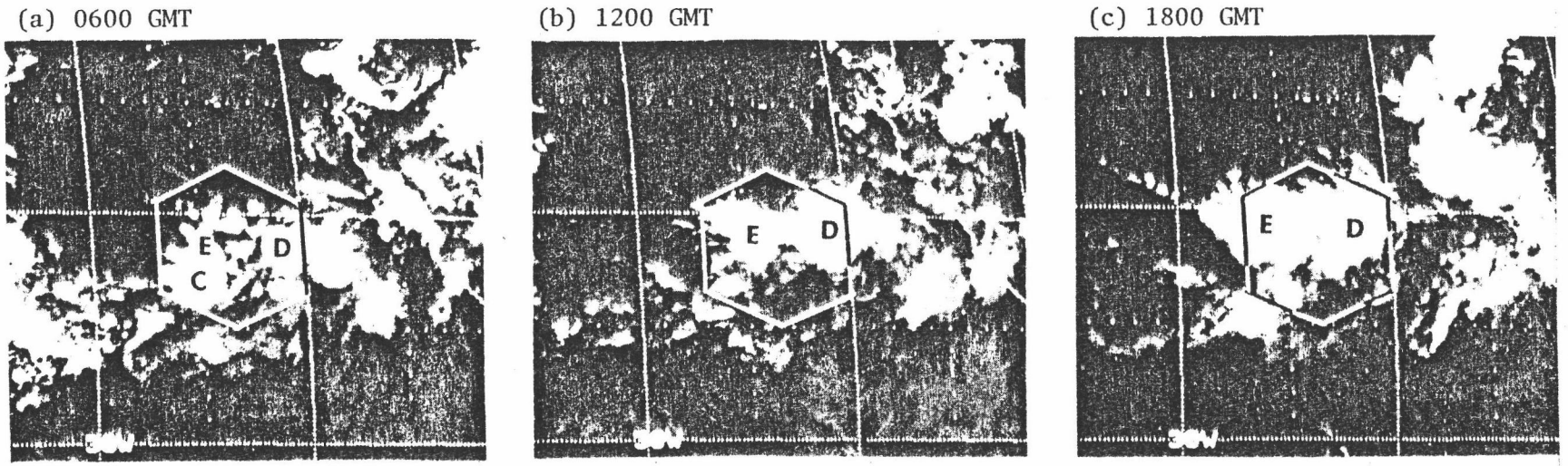

Figure 2.6. Infrared satellite picture of GATE area on 5 September at (a) 0600 GMT, (b) 1200 GMT, and (c) 1800 GMT. "E" denotes the western of the two clusters that formed on this day, and "D" denotes the eastern. The clouds labeled by "C" are remnants of the squall-cluster which moved across the GATE area on 4 September. The photographs were taken from Ogura et al. (1979).

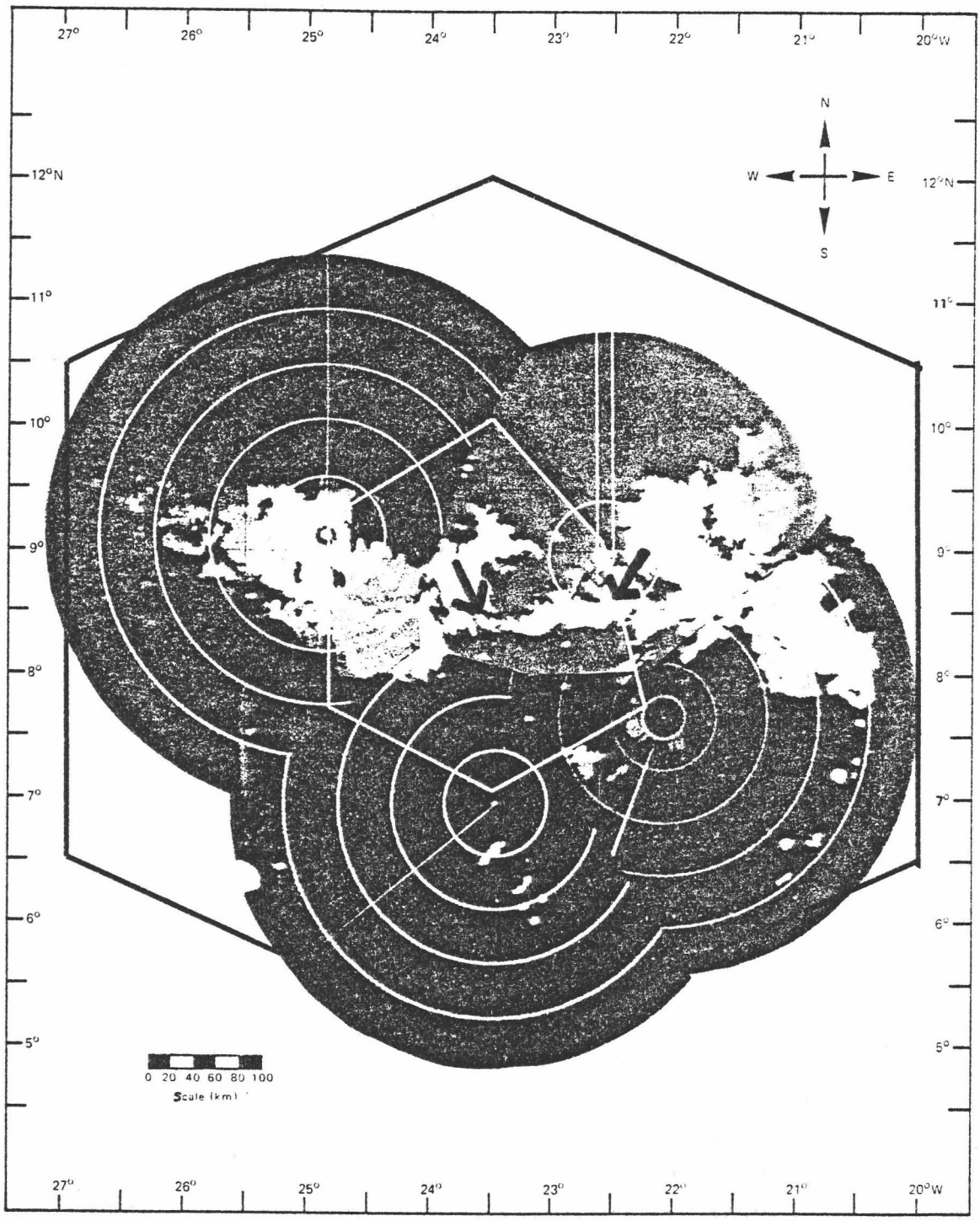

September 5, 1974 (Julian day 248), 1200 GMT.

Figure 2.7. Shipboard radar observations of the 5 September clusters at 1200 GMT (from Arkell and Hudlow, 1977). The outer and inner ship arrays are shown by the two nested hexagons. The two dark arrows mark the ends of a mesoscale convective line approximately 100 km long and 25-50 km wide.

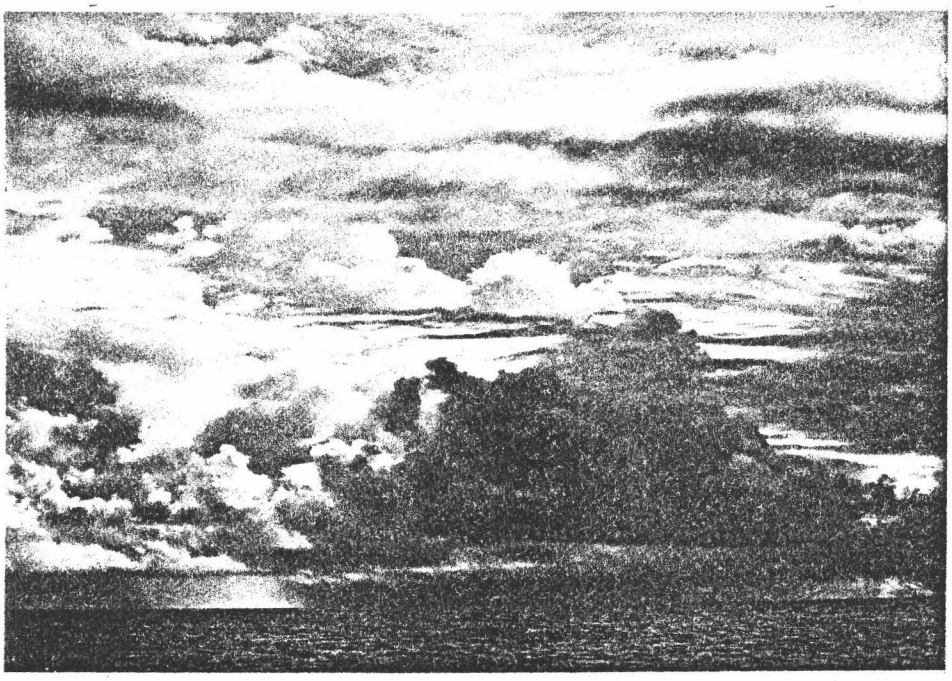

Figure 2.8. Cumulonimbus cloud photographed from the B ship array (the inner hexagon of ships).

2.2 Previous research on the interactions between cumulus convection and larger scale circulations

The pictures in the preceding section leave the unmistakable impression that cumulus clouds, owing to their ubiquity and apparent organization, might play an important role in the tropics. Indeed, even before daily satellite photographs demonstrated the extent and frequency of cluster and ITCZ convection, observationalists and theorists were reaching this conclusion. By computing a heat budget for the tropics, Riehl and Malkus (1958) were able to determine that the required heat transport out of the tropics could only be accomplished if sensible and latent heat were first transported upwards by protected cumulus cores ("hot towers") within the ITCZ. A finite number of cumulonimbus towers could, in fact, meet the transport requirements if they were sufficiently shielded from entrainment in the mid-troposphere, where the thermodynamic energy in the tropics is statistically a minimum. In this way, deep cumulus clouds could have a profound effect on larger-scale circulations even though they cover a small percentage of the actual area of the tropics. This idea replaced the notion that the slow general rising motion of a large-scale Hadley cell could accomplish the required upward transport.

Building upon this pioneering work, later investigators were able to quantitatively estimate the contribution of cumulus clouds to large-scale heat and moisture balances by using simple cloud models (Yanai et al., 1973; Gray, 1973; Ogura and Cho, 1973; Nitta, 1975). For instance, Yanai et al. (1973) computed the bulk properties of cloud clusters in the Pacific Ocean. They determined that a cumulus ensemble heats its environment primarily by inducing (by virtue of the upward mass flux within the clouds of the ensemble) a compensating mass subsidence in the environment. This subsidence also dries the environment, a drying which is counteracted at lower and middle levels by the detrainment of large amounts of water vapor and liquid water by shallow cumuli. Due to

this mid-level moistening and the consequent evaporative cooling, shallow cumuli help support deep convection by providing an environment conducive to the development of deep updraft cores.

Since these diagnostic studies of the early 70's, the importance of cumulus transports of heat and moisture, and the physical mechanisms that are involved in these transports, have both become widely recognized. Researchers at that time also began to suggest mechanisms by which clouds might significantly affect large-scale fields of momentum (Ooyama, 1971; Schneider and Lindzen, 1976; Stevens et al., 1977) and vorticity (Holton and Colton, 1972; Reed and johnson, 1974). Because geopotential gradients in the tropics are small and hence difficult to measure, most studies aimed at this question have concentrated on the vorticity equation in pressure coordinates, where these gradients do not appear. Diagnosing vorticity budgets at different scales and in different parts of the tropics, researchers have consistently found large residuals, which they interpret to be the result of cumulus convection (Holton and Colton, 1972; Williams and Gray, 1973; Ruprecht and Gray, 1976; Hodur and Fein, 1977; Fein, 1977; Chu et al., 1981). A survey of the results from these studies is provided in Chu et al. (1981).

Most of the vorticity budget studies from GATE have been at easterly wave (synoptic) scale (Shapiro, 1978; Stevens, 1979; Cho and Cheng, 1979; Cheng et al., 1980; Esbensen et al., 1982). Results from two of these studies are shown on Figs. 2.9 and 2.10. On Fig. 2.9, taken from Esbensen et al. (1982) (hereafter referred to as ETC), the vertical profiles of the vorticity budget residual (Z) are large-scale averages, the dotted curve corresponding to residuals resulting from budget terms computing from Phase 3 averages and the solid curve corresponding to residuals resulting from budget terms which were first composited within easterly wave categories and then averaged across categories. The relatively

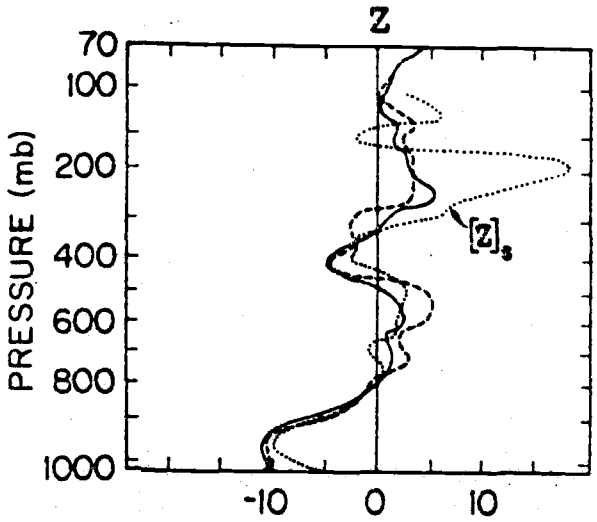

Figure 2.9. Vertical profiles of Z at center of the A/B ship array. See text for explanation of the individual profiles. Units are 10^{-11} s^{-2}. From Esbensen et al. (1982).

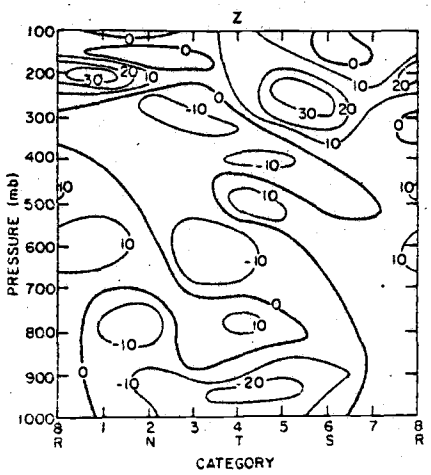

Figure 2.10. Vertical crossection of Z across easterly wave categories at center of the A/B ship array. The ridge and trough of the wave are indicated by "R" and "T," respectively. The location in the wave of the maximum 700 mb northerly and southerly winds are indicated, respectively, by "N" and "S." Units are 10^{-11} s^{-2}. From Stevens (1979).

small difference between these two curves demonstrates that the waves are essentially linear. This result is consistent with the studies of Shapiro and Stevens mentioned previously. The third profile on the figure, labeled as $[Z]_s$, from Stevens' study, was also computed from large-scale averages of the vorticity budget terms. On all the curves, the most prominent low-level feature is a large sink of positive vorticity at and just above the surface. As Stevens suggests, this feature may be due at least in part to frictional dissipation.

Comparison of the profile of $[Z]_s$ with the two from ETC demonstrates that there is still some uncertainty about the magnitude of the residual at upper-tropospheric levels in the GATE area. The large vorticity source found by Stevens is also reflected to some degree by other budget studies. The upper-tropospheric residual diagnosed by ETC, however, is significantly smaller. In the studies that do find large upper-tropospheric sources, the tendency has been to interpret the production of vorticity by Z as a mixing process, with cumulus clouds extracting positive vorticity from the ambient flow at low levels and returning it again to the ambient flow higher in the troposphere (Williams and Gray, 1973; Reed and Johnson, 1974). As ETC point out, however, the upper-tropospheric values of Z in the GATE area must be interpreted cautiously because of the large horizontal variations of Z there. This subject will be thoroughly discussed in Chapter 7. At the very least, this discrepancy shows that the different analysis procedures used by Stevens and by ETC, and also perhaps the difference in vertical resolution between the analyses in the upper atmosphere (that of ETC being finer), apparently makes a significant difference even for large-scale time-averaged fields.

The vertical section across the wave shown in Fig. 2.10 is from Stevens (1979). To some extent, the tendency for larger values to occur in categories 2-5, where convective activity also tended to

be a maximum, strengthens the assumed association of Z with convective activity. However, the extreme values of Z at upper levels are in categories where convective activity is small. Since the large-scale profile of $[Z]_s$ in the previous figure can be considered as an average across the wave of the values on Fig. 2.10, an association between the large vorticity source of the vertical profile and convection is tenuous.

Several attempts have been made to parameterize the apparent vorticity source diagnosed in budget studies. Some of these parameterizations will be discussed in Chapter 8.

2.3 Cluster-related studies

2.3.1 Research previous to GATE

Photographs from the then-new meteorological satellites in the 1960's revealed that tropical convection is very typically organized into clusters. Along with this realization came speculation that circulations on the scale of clusters might be significant enough to require a change in the way that scientists viewed the tropics. For instance, the commonly-applied conceptual model of a large-scale tropical circulation that interacts only with an ensemble of randomly-occurring cumulus clouds would not be adequate if there existed middle-scale circulations of the size of clusters which could interact both up- and down-scale. A great deal of interest in, and investigations of, cluster-related phenomena was thus engendered.

Due to extreme data sparsity over the tropical oceans, observational studies of clusters previous to GATE consisted mainly of satellite studies of characteristics of the cluster cloud and radiation fields (e.g., Martin and Suomi, 1972). Notable exceptions to this were the compositing studies of Gray and his colleagues (Gray, 1973; Ruprecht and Gray, 1976), which will be discussed later, and

the observational study of an intense Pacific mesoscale event by Zipser (1969). Zipser found an extensive area of unusually dry air behind a squall line that moved across a set of island observing stations. Using the observed fields of equivalent potential temperature, which he assumed to be approximately conserved in the wake region of the squall, he concluded that the dry air must have originated at higher levels and descended to its present height in meso- to cluster-scale downdrafts. Since this study, numerous similar mesoscale regions have been observed, and many attempts have been made to establish directly that these downdrafts exist (Zipser's study and many to follow could only infer their existence from thermodynamic profiles) and to determine their origin.

2.3.2 GATE case studies

GATE provided an excellent opportunity to acquire first-hand observations of clusters and other mesoscale convective systems. The experiment was intentionally located in a region of high cluster frequency, and the telescoping arrangement of observing ships allowed simultaneous observation of clusters and their environment. In addition, aircraft penetrations of some of the systems, nearly continuous radar and satellite coverage, and other specialized observations resulted in a wealth of data about convective systems of all scales. Consequently, a substantial volume of literature about all aspects of convection in GATE has evolved. Houze and Betts (1981) give a thorough review of this literature. The discussion to follow concentrates on cluster-related studies.

One of the most valuable aspects of the GATE data is the chance it gives for in-depth case studies of individual clusters. Two of the most widely investigated of the clusters during Phase 3 are the squall-cluster on 4 September and the double cluster on the following day. The 4 September cluster belongs to one of the two subcategories of GATE clusters, the so-called "squall clusters,"

which propagated faster than the larger-scale flow at all levels, moving from east to west in this case. The other subcategory, the "non-squall clusters," remained essentially stationary during their life cycles or moved very slowly. The clusters on 5 September belonged to this subcategory.

Houze (1977) studied the 4 September squall in detail by assembling all available ship observations and correlating them with radar data from several of the ships. The resulting picture of the squall structure resembles that of Zipser (1969) in many respects, including the relative inflow into a "front" at its leading edge, and the inferred mesoscale downdrafts at its rear. Houze determined that fully half of the precipitation from this system fell from its large trailing anvil, the rest falling from isolated cumulonimbus towers that formed along the squall front. This result strongly suggests that there is mesoscale ascent within the anvil, since the remnants of old cumulonimbus towers that formed along the squall front and were then absorbed into the trailing anvil presumably would be unable to produce this amount of precipitation or to maintain the anvil precipitation as long after the frontal passage as is observed.

Zipser (1977) also discussed this possibility. On the basis of his observations of squalls in GATE and elsewhere, he suggested the conceptual model of a tropical squall shown on Fig. 2.11. Two distinct kinds of downdrafts are postulated: the mesoscale downdrafts behind the front described previously, and convective downdrafts which originate in the squall-front convection due to precipitation loading and evaporative cooling. The convective downdrafts spread out when they reach the surface, producing new cell growth at the squall's leading edge and severely modifying the subcloud air in the wake of the squall (see, for instance, Seguin and Garstang, 1976, and Barnes and Garstang, 1982). The hypothesized anvil processes of Fig. 2.11 are the same as those suggested by Houze (1977), with mesoscale motions providing the uplift required for the anvil precipitation to form.

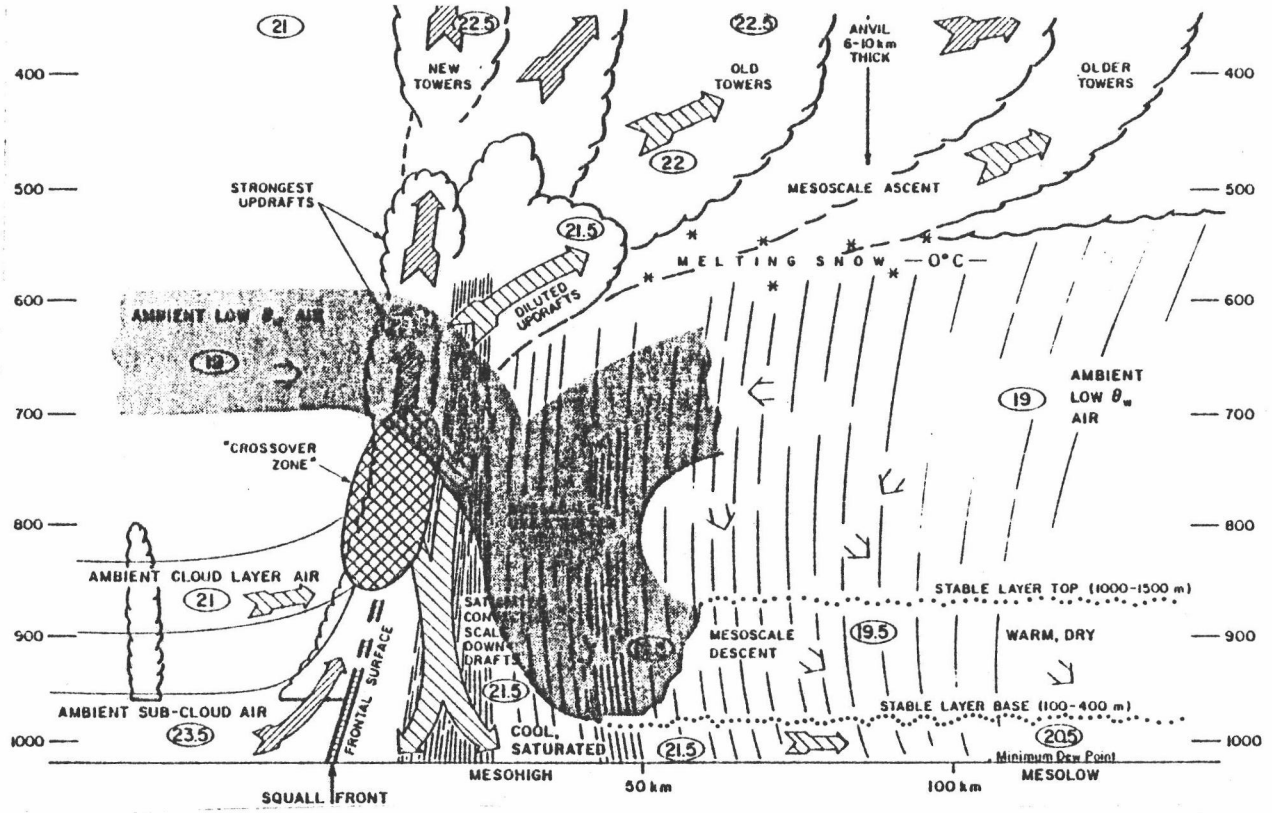

Figure 2.11. Schematic cross section through a class of squall systems. All flow is relative to the squall line, which is moving from right to left. Circled numbers are typical values of wet-bulb potential temperature in degrees Celsius. From Zipser (1977).

In order to more firmly establish the existence of the inferred anvil updraft, Gamache and Houze (1982) composited several separate observations relative to the front of another GATE squall (on 12 September). The resulting fields of divergence demonstrate in a more direct manner that the updraft and the lower-tropospheric downdraft do in fact exist. What physical mechanisms actually drive these vertical motions has still not been conclusively determined, although the numerical simulations of Brown (1979) suggest that condensational warming within the anvil is capable of producing the observed magnitude of upward motion, and that evaporation of precipitation falling out of the anvil can produce a mesoscale downdraft beneath the anvil.

Although they do not have a distinct leading edge of convection like the squall clusters, the slow-moving non-squall clusters observed in GATE apparently share many of the same anvil characteristics. The two such clusters that formed on 5 September were among the most intense in the entire experiment. The two developed in relatively close proximity in space and time and in response to approximately the same synoptic conditions, but appeared to be distinct systems in other respects. Leary (1979) and Ogura et al. (1979) described the general synoptic setting. They noted that the clusters occur just prior to passage of an easterly wave trough and in conjunction with a surface confluence zone related to the West African monsoon and possibly also to the ITCZ.

Using shipboard radar data, Leary and Houze (1979) (hereafter, LH) examined the evolution of the individual "mesoscale precipitation features" (MPF's; their terminology) that make up the clusters. These MPF's about 5 of which are delineated by LH at any given time in the clusters' evolution, moved about in relation to each other and interacted in such a manner as to enhance the development of further convection. Indications of the presence of these truly "mesoscale" features are present on the radar picture of Fig. 2.7

and on the satellite picture of the clusters made at an early stage of their development (Fig. 2.6a). In the upper atmosphere during the later stages of the clusters the anvils of the MPF's merge, so that the individual MPF's are indistinguishable in satellite observations made at these times (cf. Fig. 2.6b-c). The structure of the large cluster anvils is apparently similar to that deduced for the 4 September squall cluster and other GATE clusters. In these essentially stationary clusters, however, anvil cloud is found in all directions from the convective cells. As Fig. 2.11 suggests, the anvil cloud in squall clusters is generally found in the wake of the cumulonimbus cells that form along the squall front.

Nitta (1977), Ogura et al. (1979), and Sikdar and Hentz (1980) used radiosonde data to calculate vertical velocities, cumulus mass flux, and other derived quantities for the 5 September clusters.

To the author's knowledge, there are no studies previous to this thesis which describe the horizontal structure of the vorticity field or the evolution of vorticity budget terms during the life cycle of individual clusters.

2.3.3 Composite studies

Like the individual cumulus clouds that inhabit them, convective systems in general vary greatly from case to case. For this reason, many GATE investigators have attempted to isolate the essential characteristics of these systems from the individual variations by compositing. The unprecedented quantity and resolution of GATE data has, on the one hand, encouraged these composite studies. On the other hand, the relatively short period of fully-analyzed observations during the third phase of GATE means that some features (easterly waves, for instance) will be relatively

lightly sampled. Nevertheless, much knowledge has been gained from composites of the easterly waves that occurred in GATE (e.g., Norquist et al., 1977; Thompson et al, 1979; the vorticity budget studies cited earlier).

The number of clusters sampled during GATE is also fairly small (about 10 large clusters in Phase 3), but the data abundance for each helps to make up for this deficiency. Frank (1978) composited wind and thermodynamic data at one point (the center of the A/B array) into life cycle composites of squall and non-squall clusters. His composites are similar in overall structure to the easterly wave composites of Thompson et al. (1979), demonstrating again the inherent difficulty in separating cluster motions from easterly wave motions. Since his composites are made at a single location, they do not provide information about the horizontal fields associated with clusters.

Various other compositing techniques have been applied to study cluster-scale and other mesoscale circulations. Using easterly wave composites of the radiosonde winds of Ooyama and Chu (described in the following chapter), ETC separated out the contribution to the vorticity budget residual Z (as defined in Chapter 4) due to cluster-scale motions (their Z_B). They found that in the middle to upper troposphere Z_B is a significant fraction (about 1/2) of the total residual and equally as consistent across the wave as the total residual. In the previously-cited work of Gamache and Houze (1982), the authors composited wind observations relative to the gust front of the 12 September squall cluster, using the propagation direction of the squall to determine the orientation of their horizontal grid. In order to interpret their composite fields, they assumed that the squall is in an approximately steady state during the 12 hour period from which observations are taken. At slightly smaller mesoscales, Zipser et al. (1981) and LeMone (1983) composited aircraft flights transverse to

a line of cumulonimbus clouds. By assuming an approximately steady-state and two-dimensional flow, they were able to compute a composite transverse structure of the cloud line. A few of their more interesting conclusions are: (1) pressure effects across the line significantly accelerate the flow transverse to the line, while cumulus-scale mixing processes seem to have a more significant effect on the flow parallel to the line; (2) twisting effects significantly effect the low-level vorticity fields near the line; and (3) this cloud line is similar in many respects to the larger and more intense squall clusters of GATE.

In a long succession of papers, Gray and his colleagues at Colorado State University (CSU) have composited cluster data from all regions of the tropics, including the GATE region (see, for instance, Gray, 1973; Williams and Gray, 1973; Ruprecht and Gray, 1976; McBride and Gray, 1980a and 1980b). Their composites have been produced from radiosonde data amassed from all available stations in a particular region (for instance, the west Atlantic) over a long period. Using satellite cloud observations to determine the location of clusters, they have then "binned" the radiosonde observations into 4° by 4° geographical boxes based on their location relative to the cluster center and on their time of occurrence with respect to the stage of development of the cluster. By locating bins at locations surrounding the cluster center, they are able to produce horizontal composite fields. Typically, each box has included many hundreds of observations and the resulting averaged fields thus represent several hundreds of individual clusters. Using these composites, they have addressed a diverse set of questions about cluster structure and development.

Conceptually, these composites are similar to the composites that will be discussed in Chapter 6. For instance, both composite schemes describe the horizontal variations across a cluster as well as the vertical variations; both give at least a rough idea

of the evolution of these fields during the life cycle of a cluster; and the observations in both were binned in relation to the center of a satellite-observed mass of cloud determined to be a cluster. However, the resolution of the CSU composites is significantly coarser than that of the data sets employed in this thesis. Since all observations within each 4° by 4° (450 km by 450 km) box are averaged, the CSU compositing scheme can effectively resolve wavelengths that are 900 km or longer. This distance is twice the minimum resolvable wavelength of the data sets used here, which is about 450 km. A 900 km resolution may be adequate to describe the environment in which the cluster circulation develops, but it is inadequate to describe the internal structure of the clusters investigated in this thesis, which were ∿450 km in horizontal dimension.

The CSU composites include a substantially larger number of clusters than do the composites described here. However, this advantage may be lost if in the process they also include a less homogeneous set of "events" and thereby lose some of their sharpness. Comparing results from the CSU composites with GATE observations of various scales shows that the CSU composite fields are closer in magnitude to larger-scale GATE fields than to cluster fields composited as in this thesis. The vorticity budget fields of Williams and Gray (1973), for instance, are roughly the same size as the Phase 3 averages in Fig. 2.9, which are in turn 5-10 times smaller than the composite vorticity budget terms that will be presented in Chapter 6. These differences could be real, as the clusters composited are in different regions, but it is likely that much of the difference is due to the different compositing techniques.

CHAPTER 3. DATA

Three data sets play vital roles in this thesis: the set of gridded winds of Ooyama and Chu mentioned previously, the set of similarly-analyzed thermodynamic data of Esbensen also mentioned previously, and a set of gridded cloudtop data prepared from satellite radiation observations by Cox and Griffith (1979; hereafter, CG). All three sets are from Phase 3 of GATE. In this chapter the analysis scheme applied to the first two sets is summarized and the method used by CG to calculate cloudtop values is described.

3.1 Radiosonde wind and thermodynamic data

This section gives a partial quantitative description of the scheme that Ooyama and Esbensen employed to interpolate observations to a regular grid. A thorough mathematical description is, however, beyond its scope. A good qualitative description of the entire analysis procedure is given in ETC. In lieu of restating that description in the text, it has been included as Appendix A. Since the general structure of the analysis is somewhat complex, reference to it at this point will help to illuminate the more specific discussion which follows.

The analysis techniques used to calculate gridded winds are essentially the same as those used to calculate temperature and relative humidity. In essence, the problem was to produce a regular grid of values with as fine a resolution as feasible from the radiosonde observations made at each ship in the GATE ship array.

Fig. 3.1 shows the GATE array and the grid chosen by Ooyama and Esbensen on which to output their interpolated values. For the archived data sets, horizontal grid intervals of 1/2° of

longitude and 1/2° of latitude were chosen. These intervals were selected for convenience and do not signify that the sets can resolve horizontal features of 1/2° (55 km) horizontal extent. The domain of the analysis extended from 4°N to 13°N and from 19°W to 28°W.

Ultimately, of course, the scales resolved are limited by the average distance between the fifteen ships in the GATE array and by the average time between radiosonde ascents. As Fig. 3.1 shows, the average distance between ships was approximately 150 km; the nominal time between ascents was 3 hours. At these space and time scales large clusters can be resolved but smaller mesoscale motions do not appear in the analyzed fields.

Fig. 3.2 illustrates the vertical grid chosen for the archived sets. In all, there are 41 analyzed pressure levels (twice the number shown in the figure), with the grid intervals varying in depth to give good resolution in both the upper and lower troposphere. The top of the analyzed volume is set at 70 mb. Values were computed every three hours during the 20 days of Phase 3 at each point in the grid volume, thus giving 161 analysis times containing blocks of data that have 19 grid points along both horizontal axes and 41 grid points along the vertical.

The wind set includes the zonal and meridional components of velocity, relative vorticity, divergence, and vertical velocity ($\omega = dp/dt$) computed in two ways. Both ω estimates were computed via the kinematic method, whereby the continuity equation is integrated with height. The ω values used in this thesis, the "balanced" vertical velocities, were corrected so that they vanish at the surface and again at 100 mb near the tropopause. This correction was accomplished by adding a small constant amount of horizontal divergence at each level.

Gridded fields of temperature and relative humidity were produced in the same format as the wind data.

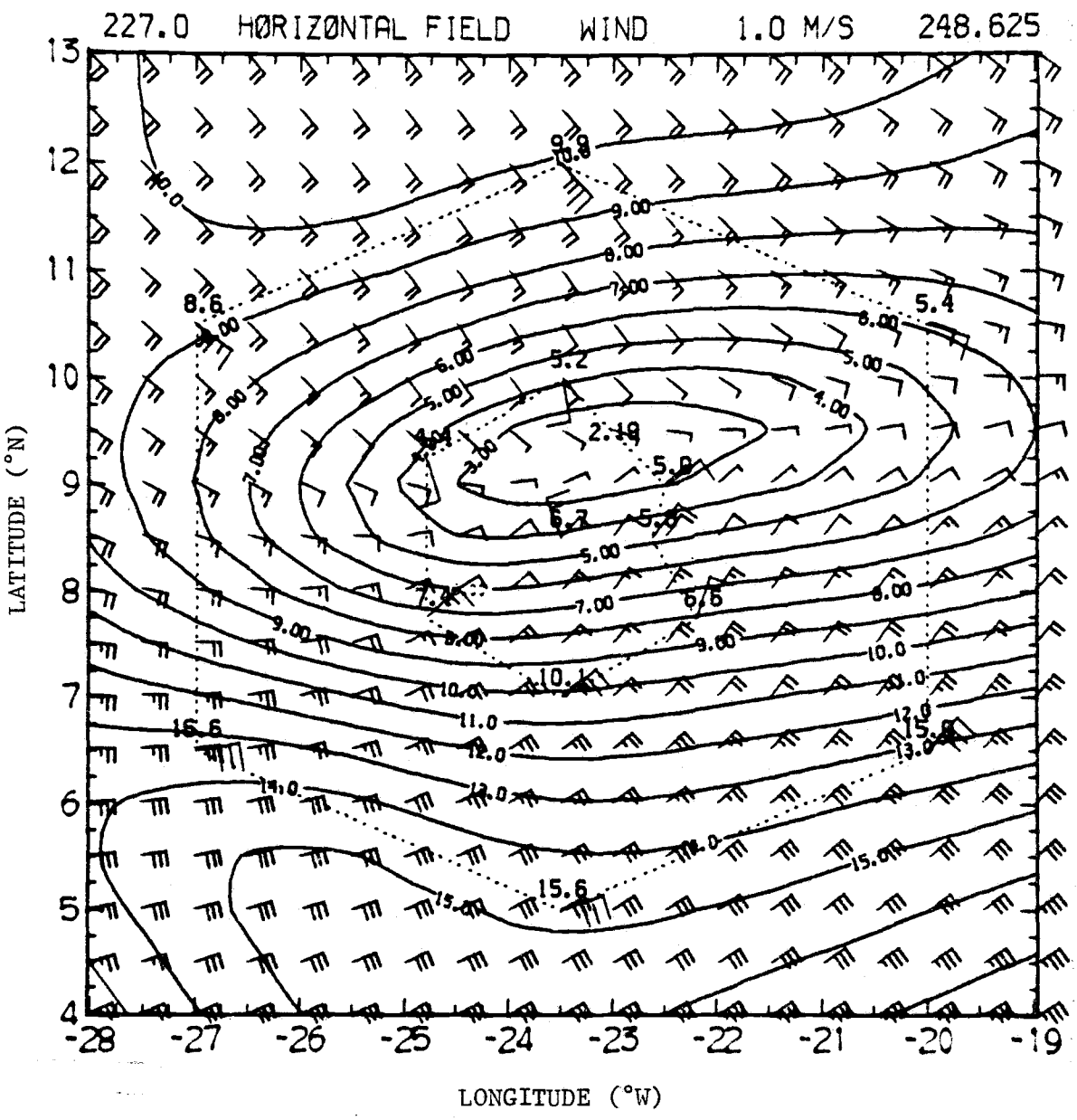

Figure 3.1. Horizontal contour plot of windspeed at 227 mb at 1500 GMT on 5 September 1974. Units are ms^{-1}; contour interval is 1 ms^{-1}. Vertices of the dotted hexagons are locations of observing ships. The tips of the wind barbs of the horizontal wind mark locations of grid points.

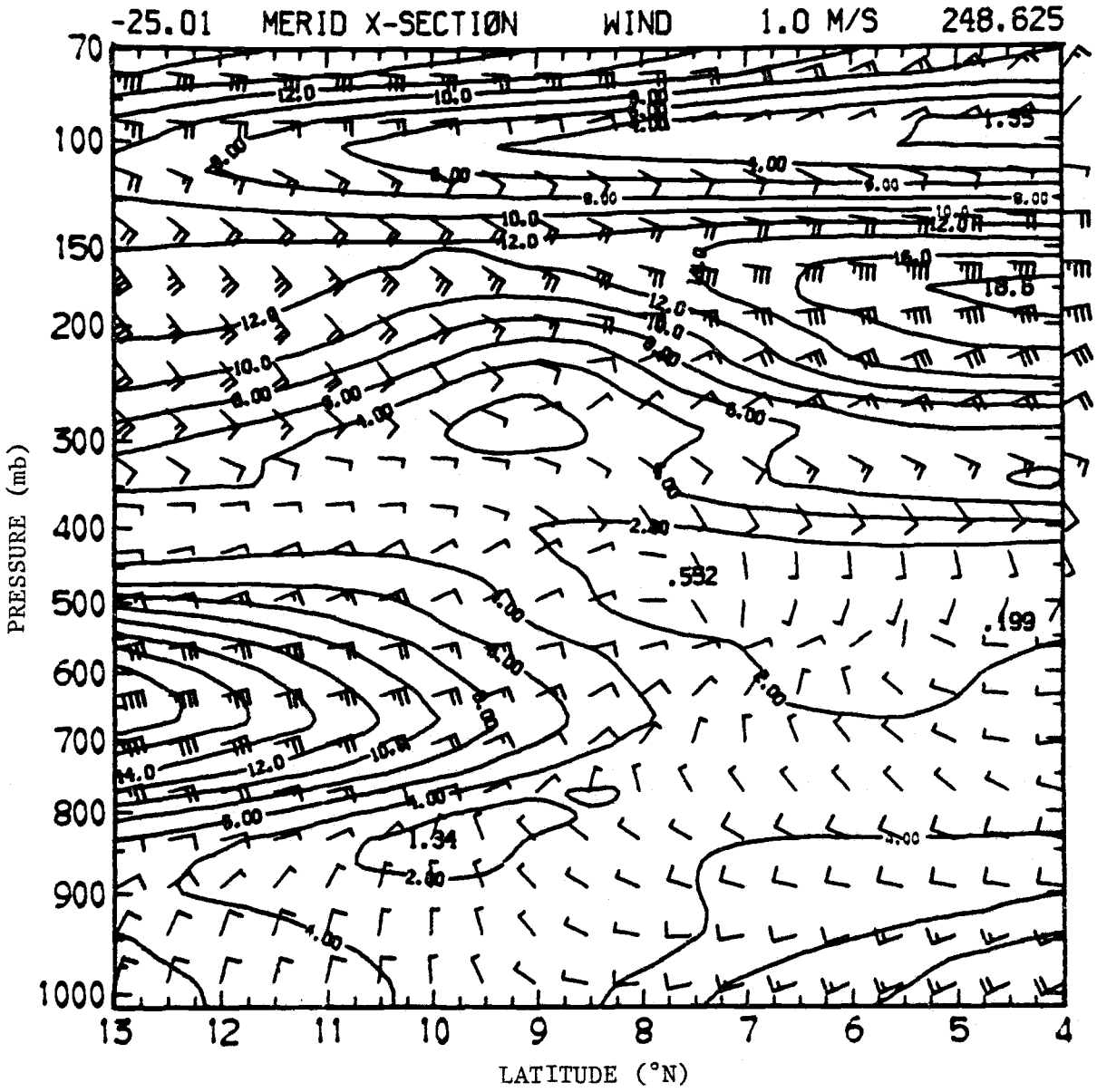

Figure 3.2. Meridional cross section of windspeed at 25°W at 1500 GMT on 5 September 1974. Units are ms^{-1}. The tips of the wind barbs of the horizontal wind mark locations of grid points; only even-numbered levels have barbs.

The analysis was performed in three spectral bands which were based on the breakdown of the physical scales known to exist in the GATE area. Fig. 3.3 shows the wavelengths in each of the bands. Motions at periods greater than 8 days (8 days being the half-power cutoff of this band) made up the "8DLP" (long-period) band or "norm field." The "E" band extended from 2 days to 8 days, thus encompassing the easterly wave motions whose period averaged about 4 days during Phase 3 of GATE. The periods that the "D" band could resolve extended downward from 2 days to a cutoff value determined by parameters in the analysis scheme. Although some freedom was possible in choosing this cutoff, the range of possible values was limited by the time interval between soundings. Both Ooyama and Esbensen chose parameters that resulted in a half-power response at a 12-hour period (cf. Fig. 3.3).

By providing a means of separating motions of different scale and of different physical origin, the breakdown of the data into spectral bands is a very useful tool for the examination of GATE radiosonde data. In addition, the breakdown into spectral bands allows the statistics necessary for the analysis scheme to be calculated separately in the D and E bands, an important feature given the very different nature of the variations in these bands.

It is not possible, however, to categorically interpret motions in any one of the three bands as being purely of one type. As Appendix A notes, some difficulties of interpretation are presented by the complicated mix of scales of motion in the GATE area. It might be hoped, for instance, that the ITCZ would be well described by the norm field. However, the relatively small meridional extent of the ITCZ meant that its spatial variations could not be resolved by the norm field (as Appendix A explains, the norm field has limits on its spatial resolution as well as on its time resolution). Furthermore, if the position or intensity of

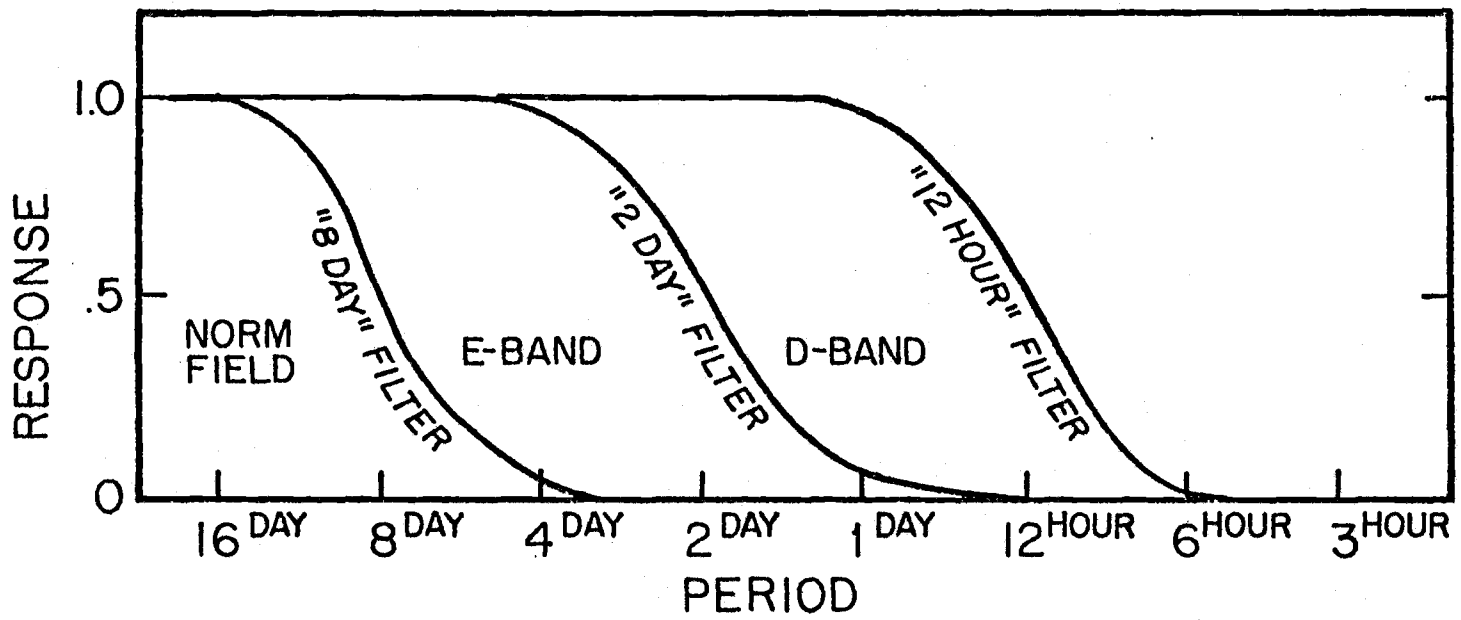

Figure 3.3. Frequency response functions of filters used in analysis of wind and thermodynamic data.

the ITCZ were modulated by easterly waves, as the analysis of Chen and Ogura (1982) suggests, then some of the motions associated with the ITCZ would turn up in the E band. At the same time, the easterly waves and clusters occupied spectral regions that were similar enough to make an objective distinction between them difficult.

In terms of features to be found in each band, then, it is likely that ITCZ motions were partly included in the E band, and it is clear from comparison of results that some of the variation due to easterly waves found its way into the D band. Caution must thus be exercised in the interpretation of the motions and the thermodynamic fields in each of the bands.

Some further discussion of the horizontal interpolation scheme introduced by Gandin (1963) is helpful here. The interpolation process may be viewed as beginning with spline-analyzed time-height series of the observed fields of u, v, temperature, and relative humidity produced from edited upper-air soundings at each of the 15 A/B scale ships. Deviation fields $f'_m(t_n)$ (where m is a ship index and n is a time index) are computed from these time series by subtracting the norm field from them, and the subsequent interpolation is performed on these deviation fields.

In the scheme suggested by Gandin, the observed value of the deviation field (denoted by ^) at observing ship m and time n is written

$$\hat{f}'_m(t_n) = f'_m(t_n) + \delta_m(t_n) \qquad (3.1)$$

where $f'_m(t_n)$ is the "true" value and δ is a random observational error at m. The optimally interpolated value at a space point k is assumed to be a linear combination of the observed values of the quantity at each of the M (=15) ships and is given by

$$\tilde{f}'_k(t_n)/\sqrt{D_{fk}} = \sum_{m=1}^{M} \alpha_{mk}\, \hat{f}'_m(t_n)/\sqrt{D_{fm}}$$

$$= \sum_{m=1}^{M} \alpha_{mk}[f'_m(t_n) + \delta_m(t_n)]/\sqrt{D_{fm}} \qquad (3.2)$$

where $\sqrt{D_{fm}}$ is the root mean square deviation of f at m. Thus, associated with each space point k there is a set of coefficients (α_{mk}), each referring to one of the M ships.

The determination of the set of coefficients (or "weights") is in actuality the crux of the interpolation scheme. Several ways to calculate them might be imagined. Many interpolation schemes require that the weights conform to an assumed analytical function, often of distance between the observation and the grid point. The Gandin scheme, on the other hand, uses statistical information from the actual data to determine α_{mk}.

To determine the α_{mk}, the mean square of the interpolation error ε is minimized. Defining the hypothetical "true" value of f' at space point k as f'_k, ε is given by

$$\varepsilon_k = \overline{(\tilde{f}'_k - f'_k)/\sqrt{D_{fk}}}$$

$$= \sum_{i=1}^{M}\sum_{j=1}^{M} \alpha_{ik}\,\alpha_{jk}\,\mu_{ij} + \sum \alpha_{ik}^2\,\eta_i - 2\sum_{i=1}^{M} \alpha_{ik}\,\mu_{ik} + 1 \qquad (3.3)$$

where we have used (3.2) and expressed the result in terms of the autocorrelation μ_{ij} between f at observing ships i and j and the autocorrelation μ_{ik} between f at observing ship i and space point k. By assuming that the observational errors at the different ships are random with respect to each other and nonsystematic, the dependency on observational error in (3.3) is reduced to the second RHS term, where

$$\alpha_{ik}^2\,\eta_i \equiv (\alpha_{ik}^2/D_{fi})\overline{\delta_i^2}$$

The minimization relation (performed at each grid point k) is

$$\partial E_k / \partial \alpha_{ik} = 0 \qquad \text{for} \qquad i = 1,2,\ldots M \; . \tag{3.4}$$

Performing the partial differentiation in (3.4) gives

$$\sum_{j=1}^{M} \mu_{ij} \, \alpha_{jk} + \eta_i \, \alpha_{ik} = \mu_{ik} \qquad \text{for} \qquad i = 1,2,\ldots M \; . \tag{3.5}$$

With (3.5), the weights α_{ik} can be calculated for each observing ship i and grid point k, and the interpolation procedure is then complete. However, in order to do so, we must be able to estimate (1) μ_{ij}, the correlation between observing ships; (2) μ_{ik}, the correlation between grid point k and ship i; and (3) the observational error δ_i at each ship (in order to compute η_i). The first of these can be determined from observations at pairs of ships. As for the third, in Gandin's scheme, observational error must be known a priori. In the schemes devised by Ooyama/Chu and Esbensen, on the other hand, the effects of observational error are handled somewhat differently in that they are estimated from the statistics of the data itself.

Returning to the second requirement, computation of μ_{ik} is complicated by the fact that we do not know $f_k'(t_n)$ (indeed, its computation is the goal of the interpolation). Thus, an assumption must be made about the correlation given by this term. That is, an estimate must be made of the correlation between fields observed at grid points and the same fields observed at the ships.

A plausible approach to this estimate would be to use the information about correlations provided by the empirical correlation between ships. One way to use this information would be to consider the GATE area isotropic in the sense that correlations between a grid point and any other point in the A/B array depends only on the distance between the points. Then the "true" correlation represented by the RHS of (3.5) could be estimated by plotting

the empirical correlations between each set of observing ships on a graph of correlation vs distance between ships (e.g., Fig. 3.4) and fitting a curve through the scatter of points.

In the GATE area, however, isotropy is a severe restriction. Under this assumption, for instance, it is impossible to include phase and propagation information from easterly waves in the analysis scheme. Since easterly waves strongly dominated the variations of wind and thermodynamic variables during Phase 3 of GATE, incorporation of information about them could conceivably improve the interpolated fields. By extending Gandin's optimum interpolation scheme to include phase and propagation information and to allow variations in the correlation function in two dimensions at each pressure level, Ooyama found that the correlation functions required by the analysis were indeed significantly improved. The analysis of non-propagating disturbances (which were substantially non-isotropic) was also improved.

In Ooyama's scheme, the isotropy assumption is not used. However, the scheme does assume statistical homogeneity across the GATE A/B array. That is, correlation values are allowed to change as a function of direction from the reference point, but at the same time the two-dimensional "true" correlation function (from which the RHS term of (3.5) can be computed) is assumed to be the same at all locations in the array. In practice, the procedure for calculating a continuous field of correlation values consisted of placing each ship in turn at the center of a two-dimensional grid and plotting the correlations between that ship and the other ships at the relative position of the other ships. The point estimates of the spatial correlation function were then contoured on each of the 41 pressure surfaces using cubic splines. Conceptually, the process may be thought of as computing curves like that of Fig. 3.4 in two dimensions.

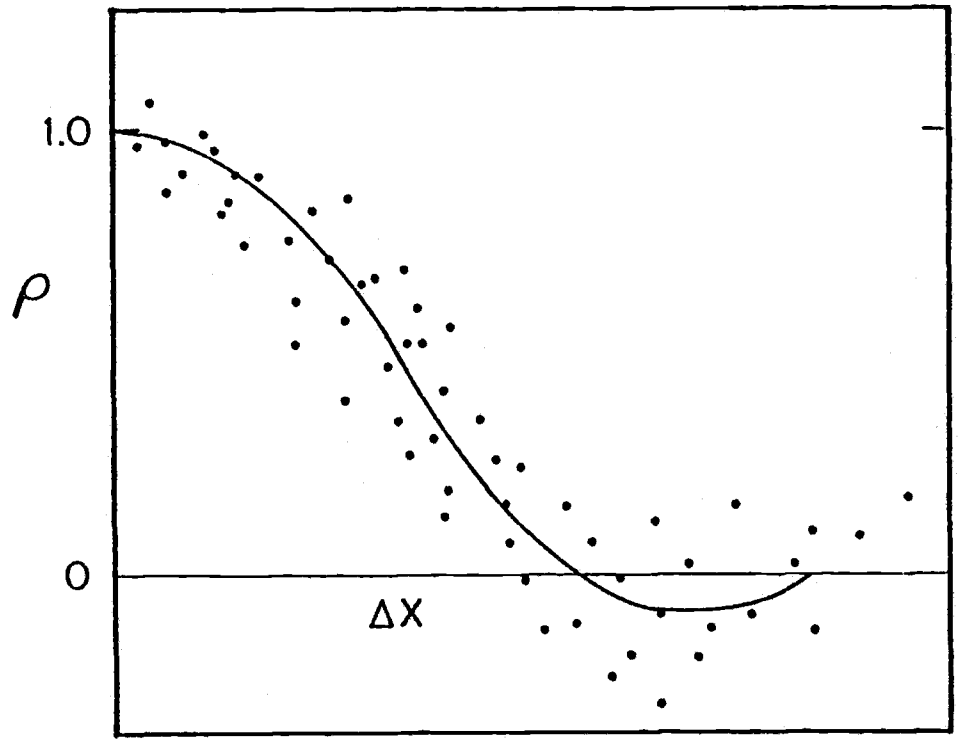

Figure 3.4. Hypothetical scatter plot of observed correlation function of a time series with a time series of the same variable at a distance Δx in any direction from the location of the original time series. The fitted curve is the correlation function that could be used in an optimum interpolation scheme. Isotropy of the field is assumed.

As described above, the optimum interpolation scheme is applied independently to the fields at each observation time. In Ooyama's extension, wave phase and propagation information in the D and E bands was included by transforming the observations into frequency space via Fourier transformation in a manner similar to that proposed by Wallace and Dickinson (1972). Also, because of the vector nature of the wind field, u and v were optimized simultaneously. For these reasons, the interpolation scheme employed by Ooyama is somewhat more complex than the univariate example explained previously. However, many of the principles of the scheme remain similar.

This interpolation scheme is complex and time-consuming. However, the method has several important advantages over simpler analysis schemes.

Perhaps the greatest advantage of this particular scheme is its ability to partially eliminate the aliasing of small-scale data into motions at larger scales. That is, although the radiosonde observations at each ship were affected by small-scale motions (like cumulonimbus clouds, for instance) this influence was partially removed by the analysis. This does not mean that the aggregate affect that an ensemble of cumulus clouds (or other unresolved systems) might have on wind or thermodynamic fields has disappeared; rather, it means that a single observation of u, v, temperature, or relative humidity that was heavily influenced by a large-amplitude deviation due to a cumulonimbus cloud was not spuriously interpreted as a large-amplitude deviation with cluster-scale dimensions.

The interpolation scheme also automatically handled random observational errors, at least in a statistical sense. This ability resulted from the fact that the two-dimensional correlation fields constructed for the interpolation contained information about random error, as (3.1) demonstrates. For this reason,

the constructed correlation fields did not reach 1 at their centers, as might be expected for perfect observations. Equivalently, the correlation curve of Fig. 3.4 would not reach 1 for $\Delta x = 0$, the difference being a measure of the magnitude of the random errors of observation. Systematic errors would still remain, however, in the norm field.

Yet another advantageous feature of optimum interpolation is its ability to automatically compensate for observation density. This is particularly useful in application to the GATE array, which was somewhat irregularly arranged.

It might be noted here that the optimum interpolation of u and v was performed only in the horizontal plane. After the production of the cubic-spline-analyzed time-height sections at the ship locations, no vertical smoothing of the fields was done. Thus, the possibility exists that vertical profiles of the analyzed fields might include abrupt changes or unrealistic gradients. As subsequent figures will demonstrate, the lack of vertical constraints does not appear to have seriously affected the quality of the analysis.

The analysis scheme for the time-height sections did not require that there be data at every ship at every level at every analysis time, but if much more than 12 hours of data were missing, the scheme could give clearly improper values. This turned out to be a problem for only one day, and only in the upper troposphere. For that period, representative data from neighboring ships and other subjective considerations were introduced in order to control the cubic splines in the time-height analysis.

3.2 Satellite-observed cloudtop data

During GATE, a geostationary meteorological satellite (SMS-1) gathered radiation data from the GATE area. Its main function

was to provide observations that could be used to compute longwave (3 μm to 100 μm) and shortwave (.3 μm to 3 μm) radiative divergence profiles with which atmospheric heating (cooling) could be estimated. These computations require knowledge about the vertical and horizontal distribution of cloudiness.

Using satellite-observed longwave and shortwave radiative brightness data and radiosonde temperature and humidity data, CG were able to determine whether or not clouds existed at any given point within the GATE A/B array at any given time in Phase 3. If clouds occurred at a location in the A/B array, the height of the cloudtops could also be estimated by a technique described by CG and summarized in later paragraphs of this section. Each of these "point" estimates of cloudtop were then areally weighted and averaged within each 1/2° by 1/2° grid area for an hour, resulting in grid-area cloudtop distributions which give the percent of area within each 100 mb layer covered by clouds which had their tops within that layer. These cloudtop data were of great value to the work described in this thesis because they could be used to determine the location, time, and extent of the anvil clouds associated with GATE cloud clusters.

Conveniently, the horizontal gridpoints at which CG chose to output their radiation data are the same as those at which the wind and thermodynamic data are stored. The domain of the radiation data is slightly smaller then that of the gridded radiosonde sets, however, extending from 20°W to 27°W and from 5°N to 12°N. The averaging period is one hour centered on the hour and beginning at 0000 GMT, with the set covering all of Phase 3 except for a very few hours when adequate satellite observations were not available. As the curves of cloud top pressure distribution statistics on Fig. 3.5 demonstrate, the radiation data set has 10 vertical grid points, the top nine of which represent layers that are 100 mb in depth. In the case of cloudtop data, the values at each of these nine

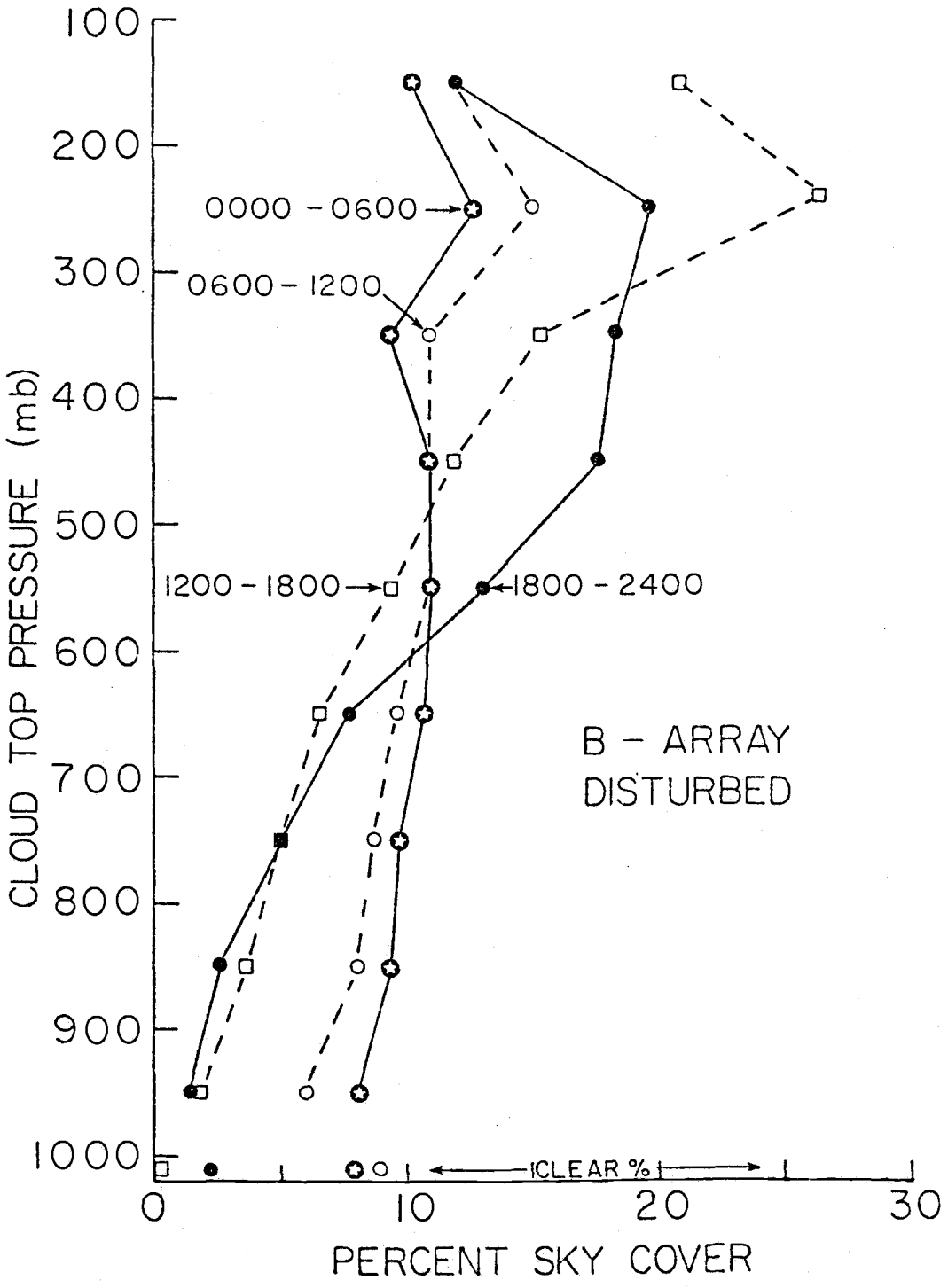

Figure 3.5. GATE B-scale array cloud top pressure distribution statistics and percentage clear area for a five-day disturbed composite over the time periods 0000-0600, 0600-1200, 1200-1800, 1800-2400 local standard time (from Cox and Griffith, 1979). See text for further explanation.

layers (which are nominally centered at mid-century pressures; 950 mb, 850 mb, and so on) represent percentages of the sky covered by cloudtops which fall within that layer. On the curve with solid circles, for instance, approximately 15 percent of the layer between 100 and 200 mb is occupied by clouds whose tops fall somewhere within this layer. In the layer immediately below, the value is 20 percent. Thus, at 300 mb, we can deduce that 35 percent of the sky above 300 mb is covered by cloud. Continuing to add the values at each successively lower layer down to the layer centered at 950 mb gives the total percent of the sky which would appear to be covered to an observer at the surface. The difference, then, between this sum and 100% must be the percent of the sky which is clear (in this case, the value is approximately 2%). These values are stored in the tenth (and bottom) "layer" of data and are represented on the figure as the symbols just beneath the 1000 mb level.

Discussion of the actual data on Fig. 3.5 is included in the description of methodology in the next chapter.

The steps involved in the determination of cloudtop heights were (1) to determine the percentage of each grid area that was cloud-free, (2) to determine the temperature at the tops of the clouds that existed within each grid box, and (3) to associate the temperature at each cloudtop with a pressure.

To accomplish the first step above, the shortwave (or "visible") data was first analyzed. This was done because during the day, at least, the visible data gave a more unequivocal determination of whether or not a cloud existed than did the longwave ("IR") data. It was assumed that in clear regions the satellite would observe the ocean surface, which has a markedly lower albedo than does a cloud at any level and hence is much less bright. In order to obtain a brightness cutoff between clear conditions and cloudy

conditions, the satellite visible data was compared with times and locations reported to be clear from shipboard photography.

Since visible data is available only during daylight hours, CG chose to make the actual determination of "cloud-free" conditions using IR data. Thus, a threshold IR value between clear and cloudy conditions similar to the brightness cutoff in the visible data previously described had to be found. CG established this threshold value by determining what IR value would produce the same percentage of daytime clear area as the visible data.

Step 2 above (the determination of cloudtop heights from IR brightness data) makes use of observed brightness in the so-called "window" region of the longwave radiation spectrum (near 11 μm). Radiation at this wavelength is only weakly absorbed by water vapor or other constituent gases in the atmosphere. Liquid water in clouds, however, does absorb this terrestrial radiation and then re-radiates it to space from cloudtops. Since the atmosphere above the cloudtops (or, in the case of no clouds, above the earth's surface) affects radiation of this wavelength to a fairly small degree and in a relatively predictable manner, this radiation then bears the imprint of the temperature at which it was radiated, that is, the temperature at the cloudtops or at the surface. Conversion from an observed IR brightness count to a temperature was performed by applying the VISSR (Visible Infrared Spin-Scan Radiometer) calibration routine.

The final step was to associate a pressure with each previously-determined cloudtop temperature in the distribution of temperatures obtained in step 2. From these cloudtop pressures, distributions of cloudtop pressures in each averaging area (as in Fig. 3.5, for example) were computed. CG used interpolated values of ship-based radiosonde observations of temperature and pressure to compute temperature vs. pressure relationships for each box and each six-hour time period.

Two significant refinements were added to this procedure. Firstly, a correction was applied to the IR-determined cloudtop temperatures to account for the emission by water vapor due to the relatively large water content of atmospheric columns in the GATE area (that is, the IR "window" channel of the VISSR satellite radiometer was not truly a window). This correction was given in terms of the total precipitable water found in each grid volume (provided again by interpolated radiosonde data). In the boundary layer the correction could be as high as 10°C. The second correction was an adjustment of the computed cloudtop pressures upwards (to lower pressures) to reflect the fact that the infrared radiation that a satellite sees originates from a point some distance below the actual cloudtop. At upper-tropospheric levels this "penetration depth" was of the order of 1000 meters; in lower levels it decreased to less than 100 meters.

Certain assumptions had to be made in the evaluation of the radiation observations. First of all, it was assumed that whenever a cloud existed, the combination of cloud depth and water content would in all cases be sufficient to obtain a cloud emissivity of 1. That is, all incident shortwave radiation is assumed to be absorbed or reflected. In the case of thin cirrus, this might not be true. However, CG show that this assumption does not make a significant difference in their calculations. Secondly, only two types of clouds are allowed: deep clouds that extend from their bases at 950 mb to their computed tops, and layer clouds that have their bases within the same 100 mb layer as their tops. The relative percentage of deep and thin clouds in each grid area is assumed to be the same in all grid boxes and at all times and to vary only with height. The resulting situations do not include other possible multilayer clouds or clouds that have bases above 950 mb. Both of these situations are possible in the complicated decks of clouds in clusters. What effect this exclusion has on

the interpretation of the computed cloudtops associated with clusters is not known. At any rate, it is a necessary assumption, since no information is available about the bases or tops of clouds that might exist below the highest clouds. This thesis is primarily concerned with clouds that have their tops above 300 mb (in the top two layers of the CG data set), where the interpretation should presumably be minimally affected by this assumption.

CHAPTER 4. METHODOLOGY

Two of the major objectives of this thesis are (1) to determine the physical mechanisms that lead to production of vorticity in cloud clusters, and (2) to composite over clusters to reveal the essential features of the winds in the clusters. The first section of this chapter presents the formulation of the vorticity budget used to address the first objective above. To address the second, a procedure was developed which uses satellite cloudiness data to locate GATE clusters in space and time and to classify them into stages of their life cycle. The second section of this chapter describes that procedure.

4.1 Vorticity budget formulation

Neglecting friction, the budget equation in pressure coordinates for the vertical component of relative vorticity (ζ) is

$$\partial\zeta/\partial t + \underset{\sim}{v}\cdot\underset{\sim}{\nabla}\eta + \omega\partial\zeta/\partial p + \delta\eta + \underset{\sim}{k}\cdot\underset{\sim}{\nabla}\omega \times \partial\underset{\sim}{v}/\partial p = 0 \quad . \qquad (4.1)$$

In (4.1), η is absolute vorticity, δ is horizontal divergence (note change in definition from (3.1)), ω is vertical velocity in pressure coordinates (dp/dt), and $\underset{\sim}{v}$ is horizontal velocity. The left-hand-side (LHS) terms in (4.1) represent, respectively, the local change of relative vorticity, the horizontal advection of absolute vorticity, the vertical advection of relative vorticity, the divergence term, and the twisting term. The divergence term describes vorticity production by the squeezing or stretching of vertically-oriented vortex tubes, while the twisting term describes the production of vorticity by the tilting of horizontally-oriented vortex tubes into the vertical by a vertical velocity field that varies horizontally.

Each LHS term is explicitly calculated; the finite-differencing formulations used are given in Appendix B. In this case,

the variables in the LHS terms represent averages made over an area that is determined by parameters in the horizontal interpolation scheme. For the parameters chosen by Ooyama and Esbensen, the averaging area is roughly equivalent to a running mean over the B-scale array (which is about 250 km across) and the averaging period is equivalent to a 6-hour running mean. These horizontal dimensions and time period can be thought of as the short-wavelength, short-period limits of the resolution of the analyis scheme.

In various applications of the vorticity equation, certain terms can be neglected on scaling considerations. For instance, in tropical regions where condensation can be neglected (that is, in regions away from active convection), divergence and vertical velocity are relatively small, as Charney (1963) has shown. Thus, the vorticity budget terms involving vertical velocity and divergence can be neglected, and an approximate "barotropic" balance holds. By this approximation, vorticity can neither be created nor destroyed, nor can it be advected vertically, leaving horizontal advection as the only mechanism by which vorticity can be changed locally. This balance, which is described by Charney (1963), can be given by

$$d\eta/dt = \partial\zeta/\partial t + \underset{\sim}{v}\cdot\underset{\sim}{\nabla}\eta = 0 \quad .$$

Within clusters in the GATE area, however, these assumptions do not necessarily hold. Because of the strong heating produced by condensation, divergence within clusters is typically observed to be as large as vorticity, and vertical velocity is correspondingly large. Therefore, the divergence and vertical advection terms cannot be neglected. Furthermore, since both the vertical shear of the horizontal wind and the horizontal shear of the vertical wind can be large in the GATE area, we also cannot neglect the twisting term. We thus retain all terms in (4.1) in our computations of the vorticity budget. As the results in later

chapters will show, each budget term is important at some stage and location in GATE clusters.

This retention of all terms of the vorticity equation is in contrast to several of the earlier budget studies. Because their analysis is based on only three island observing stations, for instance, Reed and Johnson (1974) neglect the twisting term and must make severe assumptions about horizontal advection. Williams and Gray (1973) and Ruprecht and Gray (1976) in their composite studies of cloud clusters also omit the twisting term. In addition, these last two studies use line integrals around the boundaries of their averaging areas to calculate the large-scale horizontal transport of vorticity, a procedure which requires, as Chu et al. (1981) point out, accurate estimates of vorticity along the lateral boundaries. Holton and Colton (1972) retain only the horizontal advection and divergence terms in their study. The neglect of some of these terms can be partially justified in some of these studies, especially those involving budgets made at large scales. However, for the cluster-scale phenomena studied in this thesis, none of the terms can be systematically neglected on the basis of scaling arguments.

Applying Reynolds-averaging assumptions[1] to (4.1) and using overbars to signify an ensemble average (in this case, over a cluster-scale area and time period), we can express the cluster-scale vorticity budget equation as

$$\partial\bar{\zeta}/\partial t + \bar{\underset{\sim}{v}}\cdot\underset{\sim}{\nabla}\bar{\eta} + \bar{\omega}\partial\bar{\zeta}/\partial p + \bar{\delta}\bar{\eta} + \underset{\sim}{k}\cdot\underset{\sim}{\nabla}\bar{\omega} \times \partial\bar{\underset{\sim}{v}}/\partial p = Z \qquad (4.2a)$$

[1] As Charnock (1957) has pointed out, these assumptions are strictly applicable only if there is no power in the spectral region between $f_c/2$ and $3f_c/2$, where f_c is the cutoff frequency, which in this case is $(12\ \text{hr})^{-1}$. This is not likely to be true in the GATE area, where the frequency cutoff falls very near the frequency of the large cloud clusters that develop here. Thus, (4.2b) is not complete, although it is useful as a conceptual aid.

where

$$Z = -\overline{\underset{\sim}{v}' \cdot \underset{\sim}{\nabla}\eta'} - \overline{\omega' \partial\zeta'/\partial p} - \overline{\delta'\eta'} - \underset{\sim}{k} \cdot \overline{\underset{\sim}{\nabla}\omega' \times \partial \underset{\sim}{v}'/\partial p} \qquad (4.2b)$$

The apparent vorticity source, Z, which is calculated as a residual of the explicitly calculated terms on the LHS of (4.2a), will generally be non-zero because of the correlation terms in (4.2b). Z is ordinarily interpreted as a result of motions at scales unresolved by the wind data (in this case, scales smaller than large clusters are not resolved; we define these motions to be "subcluster-scale" motions). If there are no correlations between the variables that make up the terms on the RHS of (4.2b), then Z will be zero and the explicitly-calculated cluster scale terms will describe all of the vorticity production. If, on the other hand, the correlations are large, then Z will be significant and the vorticity production by subcluster-scale processes can be assumed to be important. Z thus gives an estimate of the magnitude of the aggregate contribution due to all these smaller-scale circulations.

It is also true, of course, that any non-canceling observational errors in the LHS terms will also contribute to Z. Since they involve second-order derivatives of observed fields, the horizontal advection and twisting terms will be especially sensitive to observational errors. Furthermore, in these heavily analyzed fields, errors due to the analysis scheme, which can be systematic as well as random,[2] may also contribute to Z. In the next several paragraphs, an attempt is made to estimate the magnitude of the observational error in the vorticity and the vorticity budget terms..

Qualitatively, the Ooyama wind analysis appears to be quite

---

[2]Unless a specific distinction is made between these two sources of error, they will be referred to collectively as observational error.

accurate in its description of the divergent wind field in the vicinity of large cloud clusters. For instance, Fig. 4.1 shows that cluster-scale rising motion at 316 mb during the 5 September cluster is centered on the anvil clouds, as might be expected. Our confidence in the divergence estimates is thus bolstered by our independent knowledge of the cloud patterns in the region.

However, since we have no clear expectation about the relationship between vorticity and vertical motion even at synoptic scales in the tropics, it is difficult to qualitatively assess the reliability of the rotational part of the wind by comparing the vorticity fields to cloudiness data. At middle latitudes, the production of synoptic-scale vorticity can be closely approximated by the quasi-geostrophic vorticity equation

$$\partial \zeta_g / \partial t = \underset{\sim}{v}_g \cdot \underset{\sim}{\nabla}(\zeta_g + f) - f_0(\underset{\sim}{\nabla} \cdot \underset{\sim}{v})$$

where ζ_g is the geostrophic relative vorticity and $\underset{\sim}{v}_g$ is the geostrophic wind. The second RHS term suggests that in the region of large upper-tropospheric divergence in large convective systems we should also expect to find significant production of anticyclonic vorticity. In the tropics, however, as Charney (1963) pointed out, the production of vorticity by stretching depends on the smaller relative vorticity rather than on planetary vorticity (f_0), which is small at low latitudes. Thus, we have no clear expectation concerning the relationship between vorticity and regions of vertical velocity associated with large clusters on the basis of large-scale dynamical arguments.

It is also difficult to make meaningful quantitative estimates (by calculating, for instance, root-mean-square, or rms, values) of the error of the vorticity budget terms. For one thing, the rms values apply to observed variables like u and v rather than to a gradient variable like vorticity. Other factors that complicate quantitative estimates are the different observing

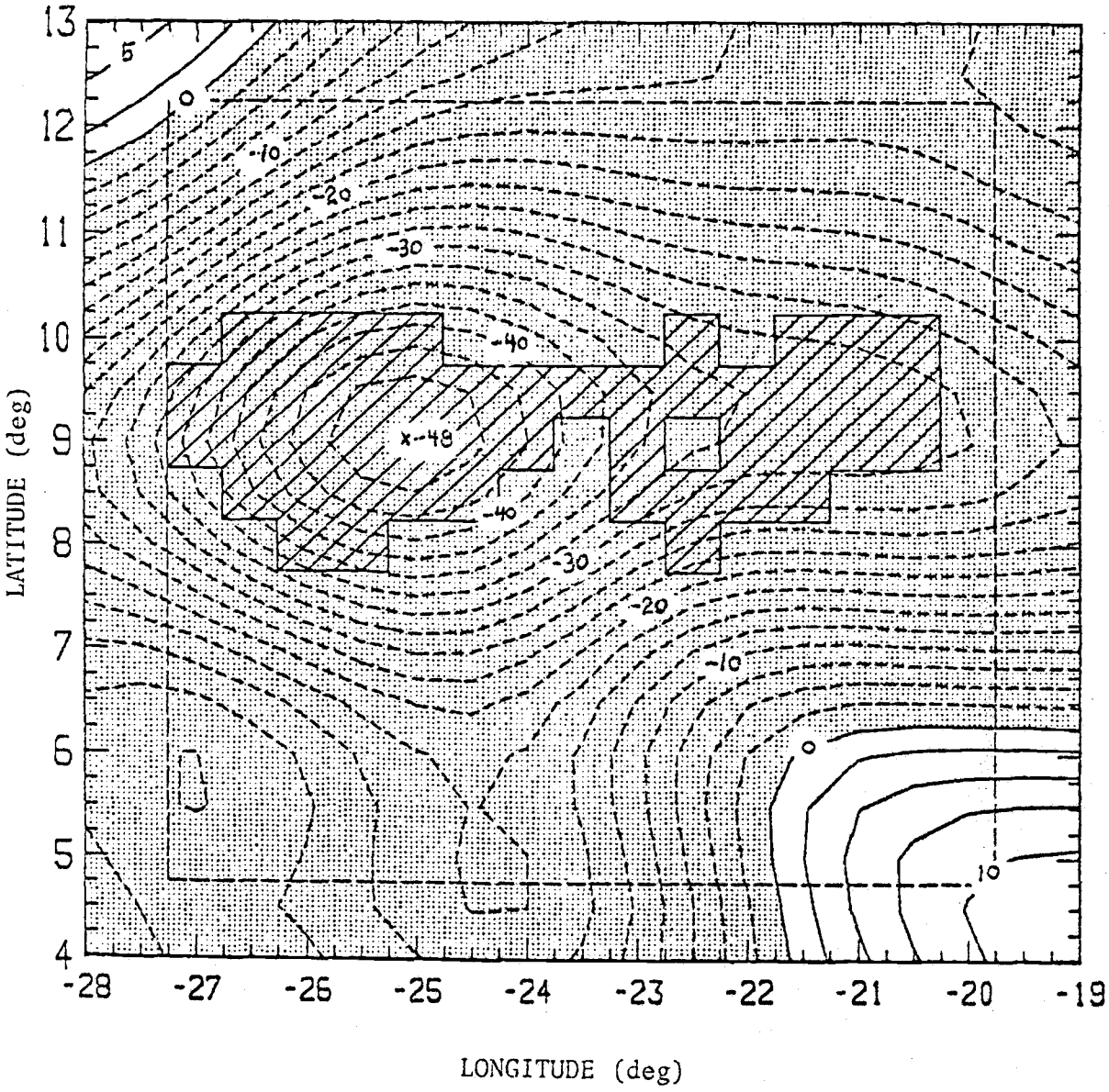

Figure 4.1. Horizontal field of vertical velocity (dp/dt) at 317 mb on 5 September, 1500 GMT. Velocities are negative (upward) in stippled areas. Hatching indicates anvil cloud, and inner (dashed) box indicates extent of cloudiness data. Units are 10^{-4} mbs^{-1}.

systems used to gather the wind and thermodynamic data and the complex editing and analysis procedure applied to the data.

Perhaps the best estimate of the reliability of Z and the other budget terms can be made by appraising their consistency in time and space and their adherence to physically reasonable hypotheses about their origin. Errors in the vorticity budget terms computed from the Ooyama-Chu wind set are examined in this manner in ETC. Since the data and the vorticity budget formulation that they used are exactly the same as those used in this thesis, their results should also apply here. By comparing values of Z during convectively suppressed periods, when small-scale circulations (and presumably Z) should be small, with values computed during convectively active periods, they are able to roughly estimate errors in Z. Fig. 4.2, which has been adapted from their paper, shows the time-height section of Z at the A/B array center upon which they base their conclusions. The solid bars which have been added along the horizontal axis indicate convectively active periods and the open bars indicate convectively suppressed periods. The determination of convectively suppressed days were made by CG; the convectively active periods are a combination of disturbed days chosen by CG and other periods when clusters were occurring near the array center (cf. discussion of Fig. 7.6). On the basis of this figure, ETC estimate observational error to be approximately 5×10^{-11} s^{-2}. This value is one-third as large as the values of Z associated with the residual features that are described in this thesis, which reach values of 15×10^{-11} s^{-2}. It is accordingly asserted that the major features of Z discussed in this thesis are physically meaningful.

4.2 Computation of anvil index and determination of stages of cluster development

To identify the anvil clouds of the largest and most active clusters, an "anvil index" is defined by assuming that the tops of

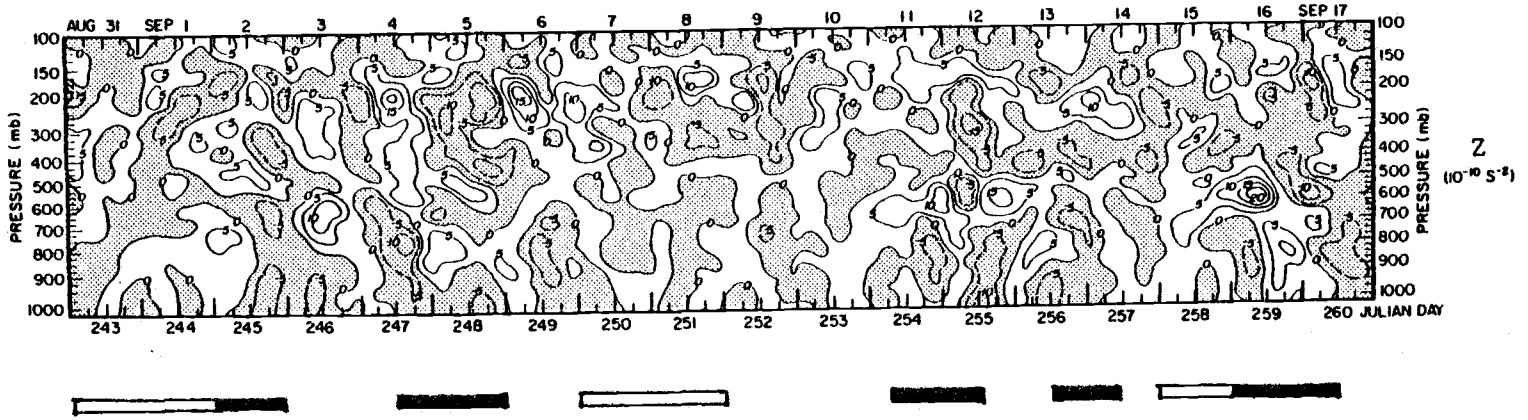

Figure 4.2. Time-height section of vorticity budget residual Z at center of A/B array during Phase 3 of GATE. Open bars beneath the plot indicate periods classified as convectively suppressed; solid bars indicate convectively active periods. Units are 10^{-10} s^{-2}. Plot is from Esbensen et al. (1982); see text for explanation of convective classification. Stippled regions are negative.

large cloud clusters reach the layer between 100 mb and 300 mb. Using the sum of the cloudtop percentages in the top two layers of the CG data set, the anvil index is set to 1 in each 1/2° by 1/2° grid area where 90% or more of the sky above 300 mb is covered by cloud. All other grid points are assigned a value of zero. The hatched regions on the horizontal plots on the figures in this thesis (e.g., Fig. 4.1) identify areas where the index is 1.

The anvil index is used to locate cluster centers in the compositing procedure described in Chapter 6. It is also used as an indicator of a cluster's stage of development. The life cycle of each cluster is broken into three stages: growing, mature, and dissipating. In the growing stage, the anvil first appears (that is, the index becomes 1 at some location in the vicinity of the cluster) and grows rapidly in size. During the mature stage the cluster anvil attains its greatest horizontal extent and remains approximately the same size. In the dissipating stage the anvil begins to break up and eventually disappears (the index at all grid points in the previous anvil region becomes zero).

It is noted that although our definitions of life cycle stages roughly parallel those of LH, exact correspondence should not be expected. The criteria used here are based on satellite data which cannot resolve cloud features smaller than anvils, while the classification criteria of LH are based on radar data which can resolve smaller-scale convective features. There is typically a 2-3 hour lag between the two classification schemes, with the beginning of the life stages determined here trailing those determined in the manner of LH.

Fig. 3.5 shows profiles of cloudtop distribution statistics calculated as described in Chapter 3. The four curves represent averages made over the B-scale ship array (the inner hexagon of ships) in four diurnal time periods during 5 days that CG classify

as "disturbed" (that is, convectively active). Most of the clusters examined in this thesis reached their most intense stages between 1200 GMT and 2400 GMT. As the two curves on Fig. 3.5 corresponding to this period show, the largest percent coverages tend to occur above 300 mb and the average amount of clear sky during these disturbed periods is quite small (less than 5 percent). At individual times and locations within clusters, the coverage by clouds with tops in the top two layers commonly increases to values very near 100%. Adding the coverages in the top two values to form the anvil index thus gives index values of 1 at the location of clusters.

CHAPTER 5. CASE STUDIES OF THE 4 SEPTEMBER SQUALL AND THE 5 SEPTEMBER CLUSTERS

5.1 Synoptic setting and general description

This chapter consists of detailed examinations of the wind and thermodynamic fields associated with the squall cluster (hereafter we shall refer to it as the "squall") that occurred on 4 September and the slow-moving "nonsquall" clusters on 5 September. The squall occurred in connection with an especially vigorous section of the easterly wind maximum near 635 mb which occurred just prior to passage of an easterly wave trough. Streamlines showing the position of the easterly wave at 1200 GMT on 4 September are shown on Fig. 5.1 taken from Krishnamurti et al. (1979). The satellite photograph on Fig. 2.5, taken 6 hours later, also displays this wave. The satellite and radar depictions on Figs. 2.6 and 2.7 show the double clusters on 5 September.

Figs. 5.2 and 5.3 show the anvil index for the two days superimposed on the 945 mb divergence fields. The positions of the surface gust front of the squall (as determined by Houze, 1977) are indicated by the heavy dashed lines on Fig. 5.2. During the early development of the squall there was a pre-existing band of cloudiness along the ITCZ and an associated center of boundary-layer convergence. The squall moved along this convergence line and reached its peak intensity at 1800 GMT, thereafter beginning to dissipate as it moved westward. Simultaneously, the region of maximum convergence shifted northward to (25°W, 9°N), the eventual location of one of the clusters on the following day.

The clusters of 5 September were among the largest of GATE. The eastern cluster appeared slightly earlier than the western cluster (on which we will here concentrate our attention). The western cluster began to intensify around 0600 GMT near the

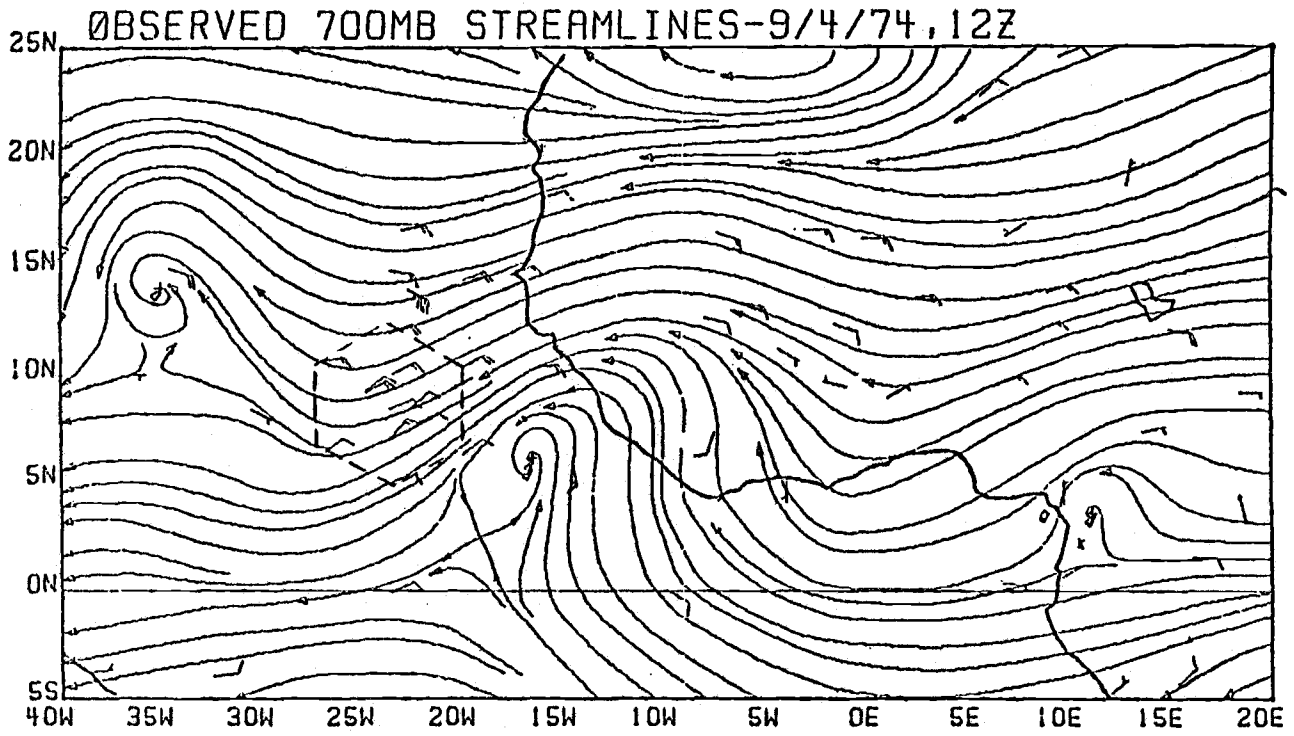

Figure 5.1. Objectively analyzed 700 mb streamlines at 1200 GMT, 4 September, 1974. Dashed hexagon indicates position of GATE A/B ship array. From Krishnamurti et al. (1979).

Figure 5.2. Time sequences of horizontal fields of horizontal divergence (δ) at 227 mb (a-c) and 945 mb (d-f) for the life cycle of the 4 September squall. Heavy dashed lines at 945 mb are positions of the surface gust front. Heavy solid circles indicate locations of profiles discussed in text and displayed in later figures. Units are 10^{-6} s^{-1}. Contour interval is 2.5 x 10^{-6} s^{-1}.

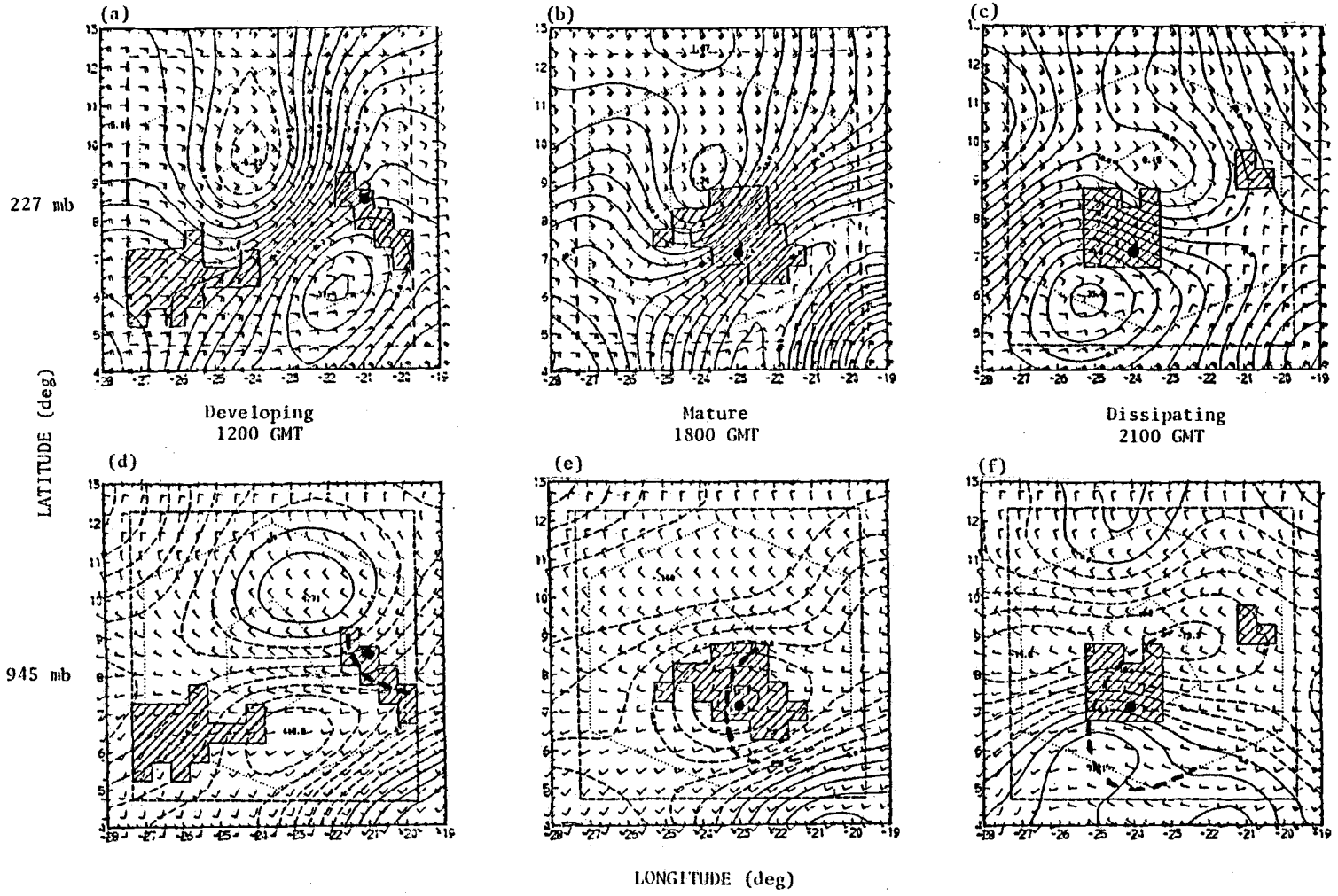

Fig. 5.2 (continued)

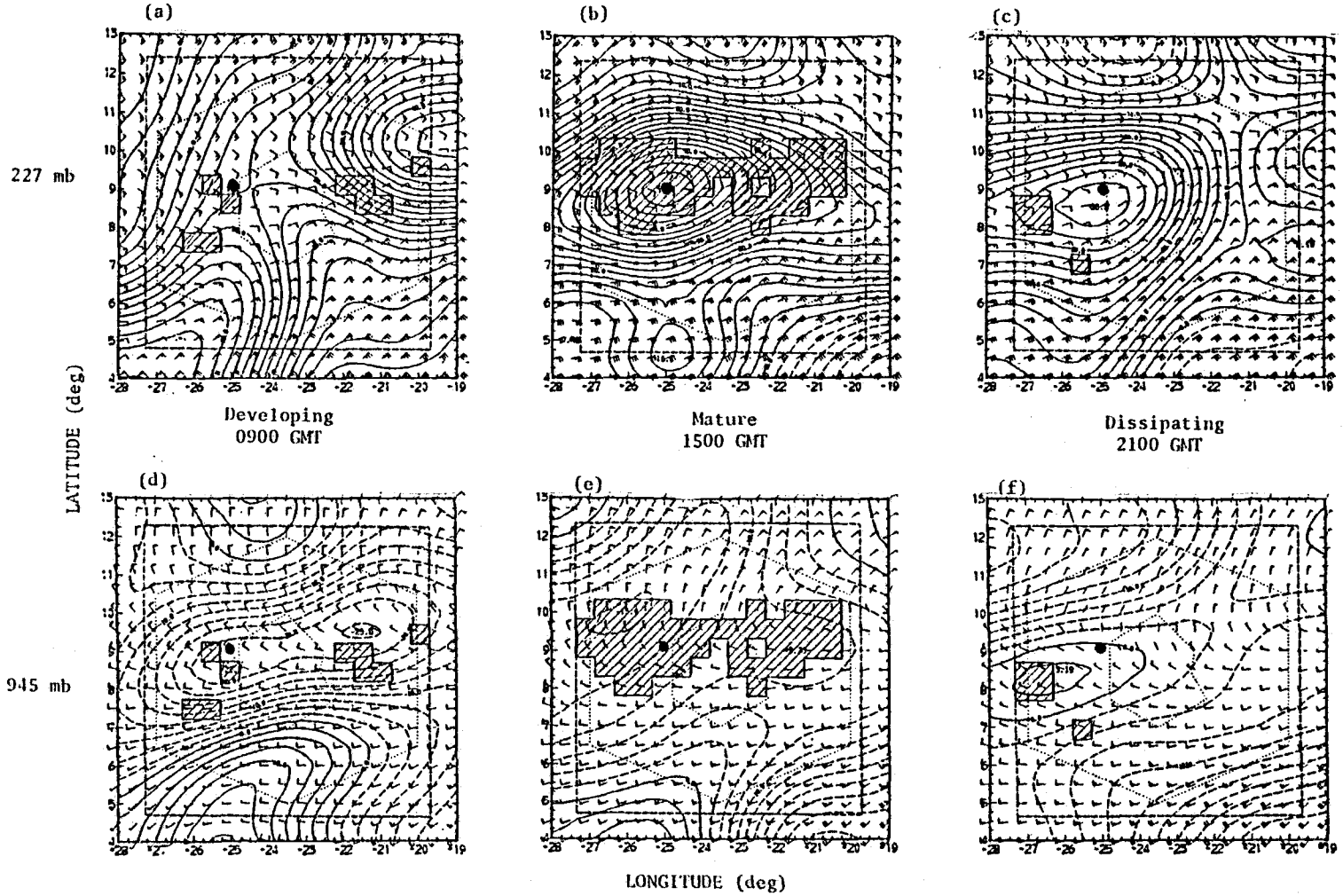

Figure 5.3. Same as Fig. 5.2 except for 5 September cluster.

northern end of the arc formed by the surface gust front of the dissipating squall of the previous day. As Fig. 5.3 shows, strong boundary-layer convergence had become well established in a two-lobed pattern similar to the convective pattern six hours later. Between 1200 GMT and 1500 GMT both clusters reached their mature stage. By 2100 GMT its cloud structure had begun to disintegrate and convection had largely disappeared by the early morning of 6 September. At 1500 GMT, during the mature stage of convection, boundary-layer convergence had already substantially decreased from its maximum value during cluster intensification, and by 2100 GMT there is boundary-layer divergence beneath the remaining cloudiness.

Upper-level divergence (shown on Figs. 5.2 and 5.3) also coincided closely with anvil cloudiness. Unlike boundary-layer convergence, however, 227 mb divergence reached its peak when convection was most intense and then decreased at a much slower rate. Strong divergence at anvil height still existed at 0000 GMT on 5 September and again at 2100 GMT on 5 September well after deep convection had ceased in both systems.

5.2 Momentum, divergence and vertical velocity profiles

Since the cluster on 5 September is essentially stationary, we can illustrate the evolution of its interior structure with vertical profiles made at the same geographic location (25°W, 9°N) for its full life cycle. The squall, however, moved continually westward during its life cycle. Thus, profiles made at different times are also at different locations, each time within the anvil associated with the squall. For the mature and dissipating stages, the center of convection was located within the arc formed by the surface gust front, about 100 km behind the leading edge of the squall. The locations and times of the profiles are given on Table 5.1. The closed circles in Figs. 5.2 and 5.3 also show the locations of the profiles.

Table 5.1. Times, stage of development, and location of profiles made at centers of convective systems on 4 September and 5 September, 1974.

System/Day	Time (GMT)	Stage	Location
Squall, Sept. 4	1200	Growing	21°W, 8.5°N
	1800	Mature	23°W, 7°N
	2400	Dissipating	24°W, 7°N
Cluster, Sept. 5	0600	Growing	25°W, 9°N
	1500	Mature	25°W, 9°N
	2100	Dissipating	25°W, 9°N

As the profiles of u and v show (Fig. 5.4), the squall developed in an environment with greater low-level wind shear than that associated with the cluster. In each case there were two easterly jets, one near 700 mb and another at the tropopause. During the squall there is a northerly maximum in the easterly jet, appropriate to its location in the easterly wave phase category 2 (as defined by Reed and Recker, 1971), the category of maximum northerly velocities.

Profiles of horizontal divergence on Fig. 5.5 are very much the same in both cases. In each, though greater in the cluster, a near-surface convergent layer deepens to 800 mb during the growing stage, in the process progressively destroying the previous divergence at 800 mb. Near 500 mb the divergence values are small in all profiles. A deep layer of large divergence extends from 300 mb to 150 mb becoming particularly large in magnitude in the latter stages of the cluster, when it reaches values of 5×10^{-5} s^{-1}. During the squall the maximum remains about the same. One important difference between the cases is at 350 mb, where a convergence maximum develops in the later stages of both systems but is significantly greater in the squall. Another difference is the deeper layer of mid-level divergence associated with the cluster.

As with the divergence profiles, which they reflect, the essential features of both sets of vertical velocity profiles (Fig. 5.6) are the same. All profiles show a tendency toward a double maximum, a major one at 300 mb and a lesser one at 850 mb. Mid-level upward velocity increases as the systems intensify and then begins to decrease as convection dissipates. The maximum near 850 mb decreased slightly during cluster intensification, while it increased in the squall; however, the difference may be due to sampling each system at a slightly different point in its development. It is evident in both cases that the upper maximum remained large in the dissipating stage well after the lower maximum disappeared. This lag between upper and lower maxima can also

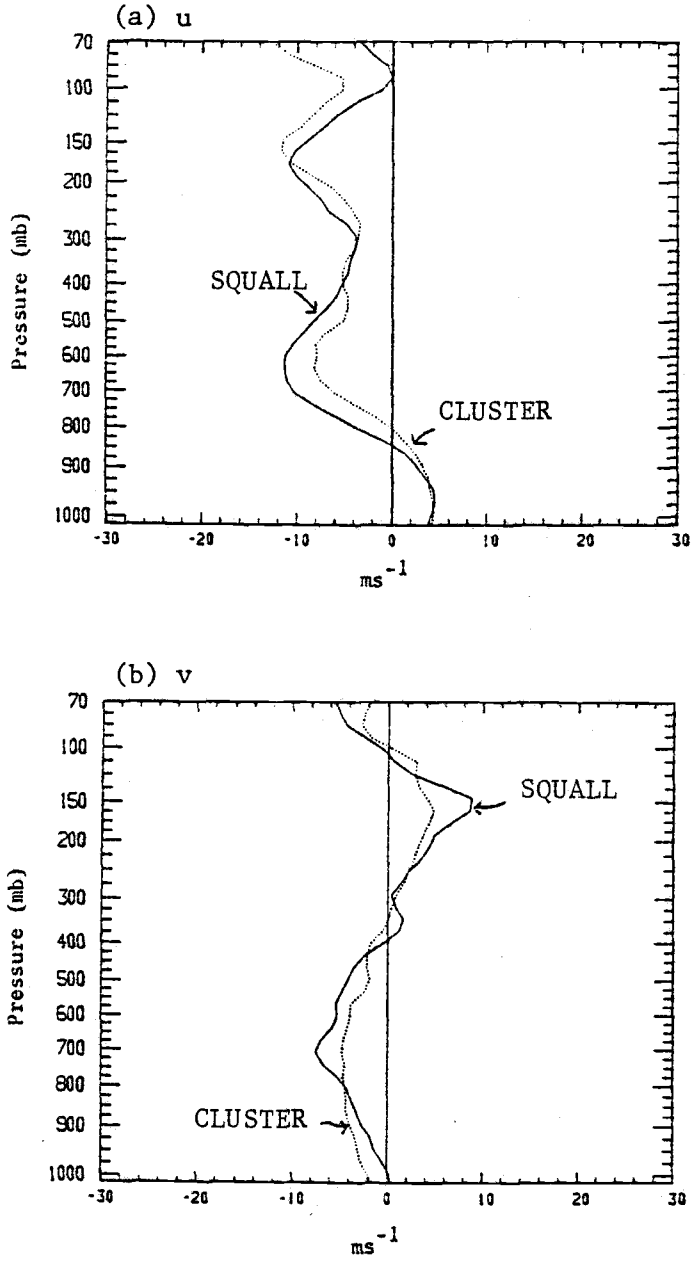

Figure 5.4. Vertical profiles of (a) zonal wind component (u), and (b) meridional wind component (v), at center of anvil during the growing stage of the 4 September squall (solid lines) and the 5 September cluster (dotted lines). See Table 5.1 for locations and times of profiles.

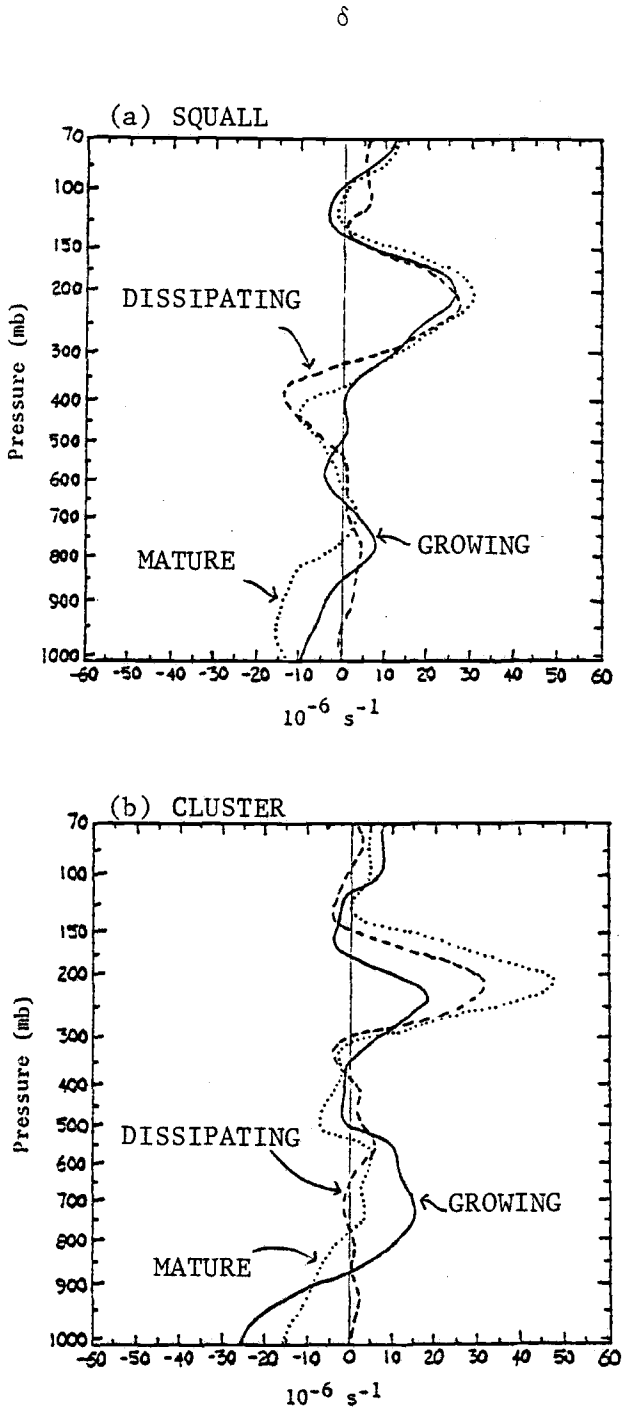

Figure 5.5. Vertical profiles of horizontal divergence (δ) for (a) the 4 September squall, and (b) the 5 September cluster. See Table 5.1 for locations and times of profiles.

ω

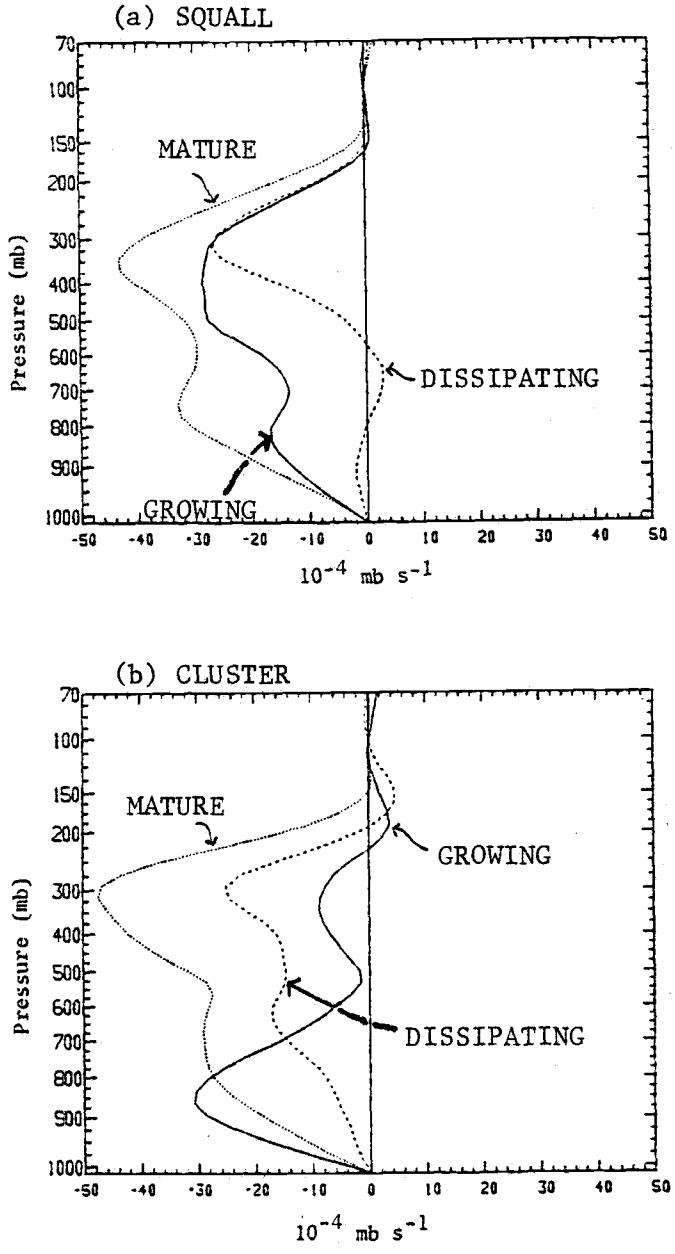

Figure 5.6. As in Fig. 5.5 except for vertical velocity (ω = dp/dt).

be seen in the composite GATE cluster of Frank (1978) and even in easterly wave composites (Thompson et al., 1979).

The base of the upper maximum is near 550 mb, which is also the approximate base of anvil cloud (LH). This fact, together with the persistent nature of the divergence and vertical velocity after deep convection has diminished, suggest an anvil circulation similar to those inferred by Zipser (1977) and LH and modeled by Brown (1979). In the present study, the combination of a convergent layer within the bottom half of the anvil and the strong divergence in the top half produces the upward motion in the anvil.

Beneath the squall anvil at 600 mb in the dissipating stage, ω becomes slightly positive. The existence of mesoscale downdraft in the wake of squalls has been noted by Zipser (1977) and LH. In the cluster downward motion is not observed although weakening of the low-level upward motion can be seen. Kinematically, the reason for this difference is the larger convergence in the lower half of the squall anvil and the slightly larger divergence beneath it. The absence of significant cluster-scale downdraft velocity does not rule out the possibility of downdrafts at smaller (meso-) scales.

5.3 Vorticity budget

Profiles of squall and cluster relative vorticity are shown in Fig. 5.7. As with divergence and vertical velocity, the major features of the two sets of profiles are similar. In each, generally cyclonic vorticity near the surface increases upwards to a maximum of about 4×10^{-5} s^{-1} at the level of the lower-tropospheric easterly jet. Each profile also has an anticyclonic maximum between 300 mb and 170 mb. However, in several other respects the two sets vary. In this section, we will compare and contrast the evolution of some of the squall and cluster vorticity features by computing the terms of the vorticity budget equation (4.2a).

ζ

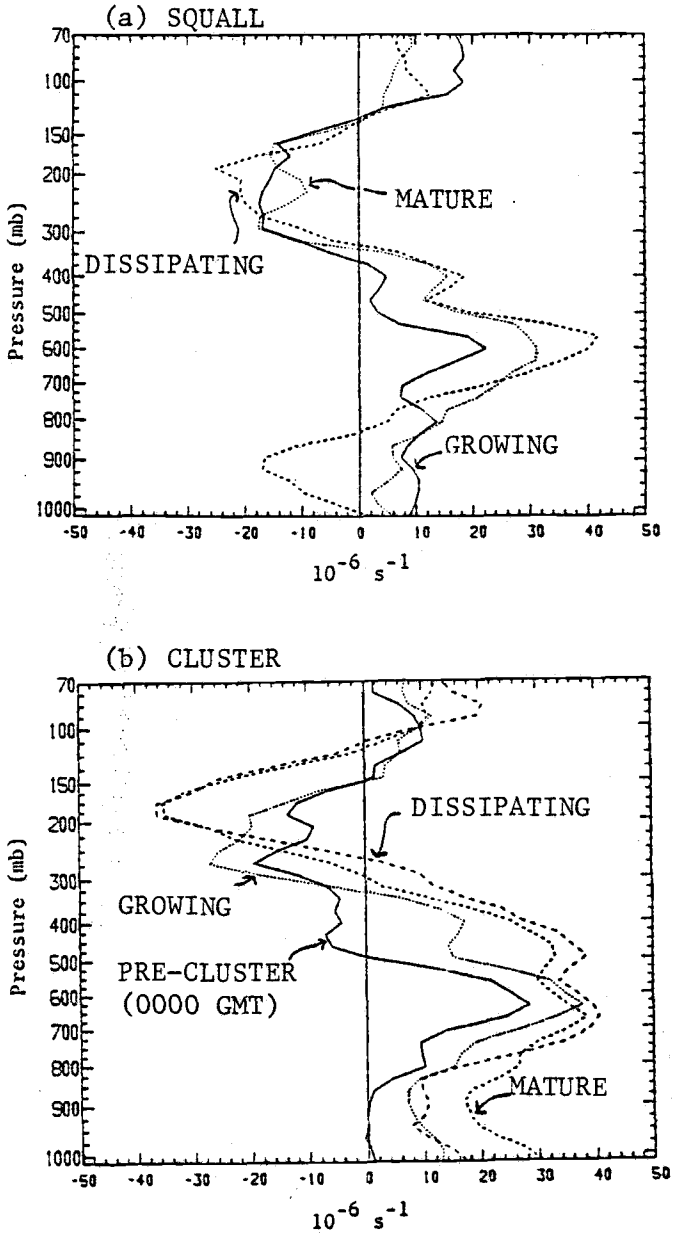

Figure 5.7. As in Fig. 5.5 except for horizontal component of relative vorticity (ζ).

One noticeable difference between cluster and squall vorticity profiles exists in the boundary layer. There, vorticity in the cluster at 950 mb increased from near zero to almost 2 X 10^{-5} s^{-1} during cluster intensification and then decreased to 1 X 10^{-5} s^{-1} by 2100 GMT. Squall boundary-layer vorticity, on the other hand, decreases through the life of the squall and is significantly negative at 900 mb in the dissipating stage. Part of the decrease could be due to the squall moving forward (with respect to the easterly wave) into regions of the wave with greater anticyclonic vorticity. However, it seems clear from Fig. 5.8 that the major part of the increase is due to local negative vorticity production in the regions that the squall traverses rather than to changes in vorticity across the easterly wave. The vorticity budget terms in Fig. 5.9a show that the local vorticity decrease near 900 mb is caused by the residual and opposed by the divergence term. In the cluster case (Fig. 5.9b), the boundary-layer residual is also negative but small, and the increase in cyclonic vorticity is produced by a very large divergence effect and offset by horizontal advection. Other terms are small below 900 mb.

Another difference between the squall and cluster occurs at the jet level of the lower tropospheric easterly maximum. While the vorticity at the level of the easterly jet maximum ($\sim$630 mb) increased only slightly during the cluster life cycle, the vorticity at a similar level in the squall very nearly doubled between developing and dissipating stages. From Fig. 5.8a-b it appears that the maximum in intensification of vorticity around 575 mb is related to the squall convection. The dominant vorticity budget terms in the mature squall (Fig. 5.10a) are the local change term and the residual, which approximately balance. Although of lesser importance, the vertical advection and divergence terms oppose the vorticity increase in a layer just below 600 mb and the horizontal advection (which includes the increase due to the advance of the easterly wave) imports higher vorticity.

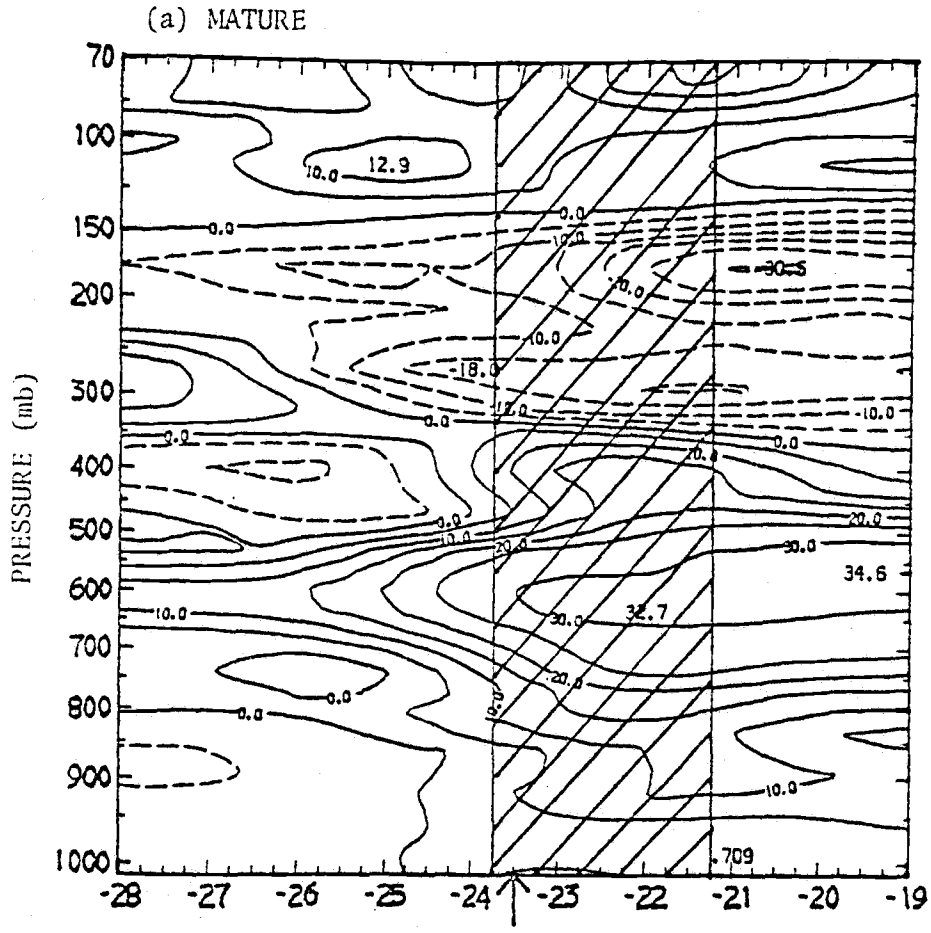

Figure 5.8. Zonal cross-sections of relative vorticity (ζ) for the 4 September squall during (a) the mature stage at 1800 GMT and (b) the dissipating stage at 2400 GMT. Both sections are at 7°N. Hatched longitudes are covered by anvil clouds. The arrow on the horizontal axis indicates position of surface gust front. Units are 10^{-6} s^{-1}.

(b) DISSIPATING

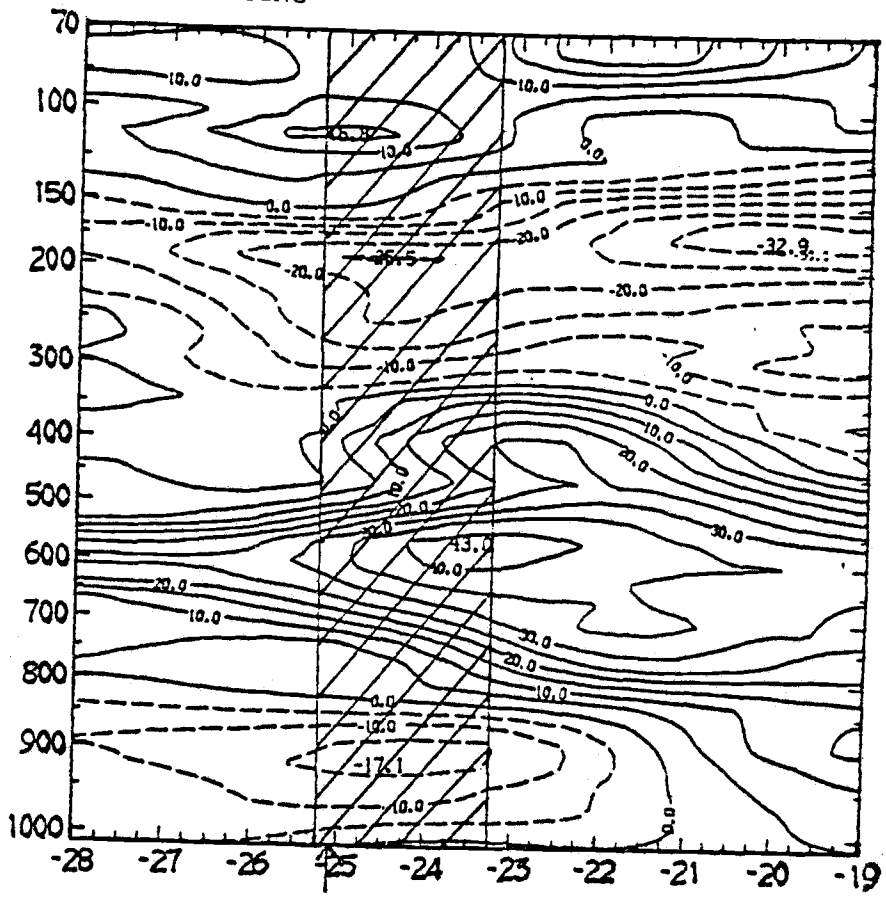

Figure 5.8 (continued)

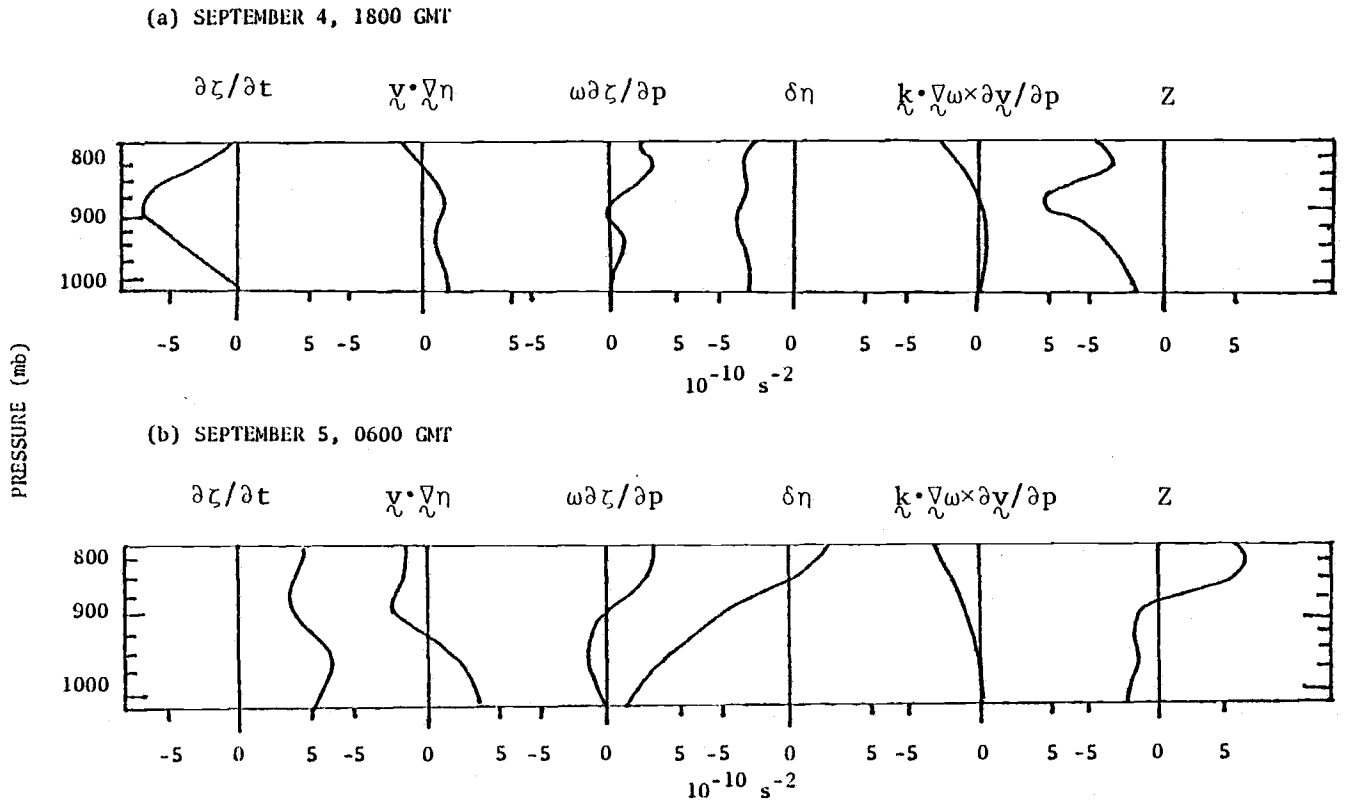

Figure 5.9. Profiles of vorticity budget terms in the boundary layer for (a) the mature stage of the 4 September squall and (b) the growing stage of the 5 September cluster. See Table 5.1 for locations of profiles.

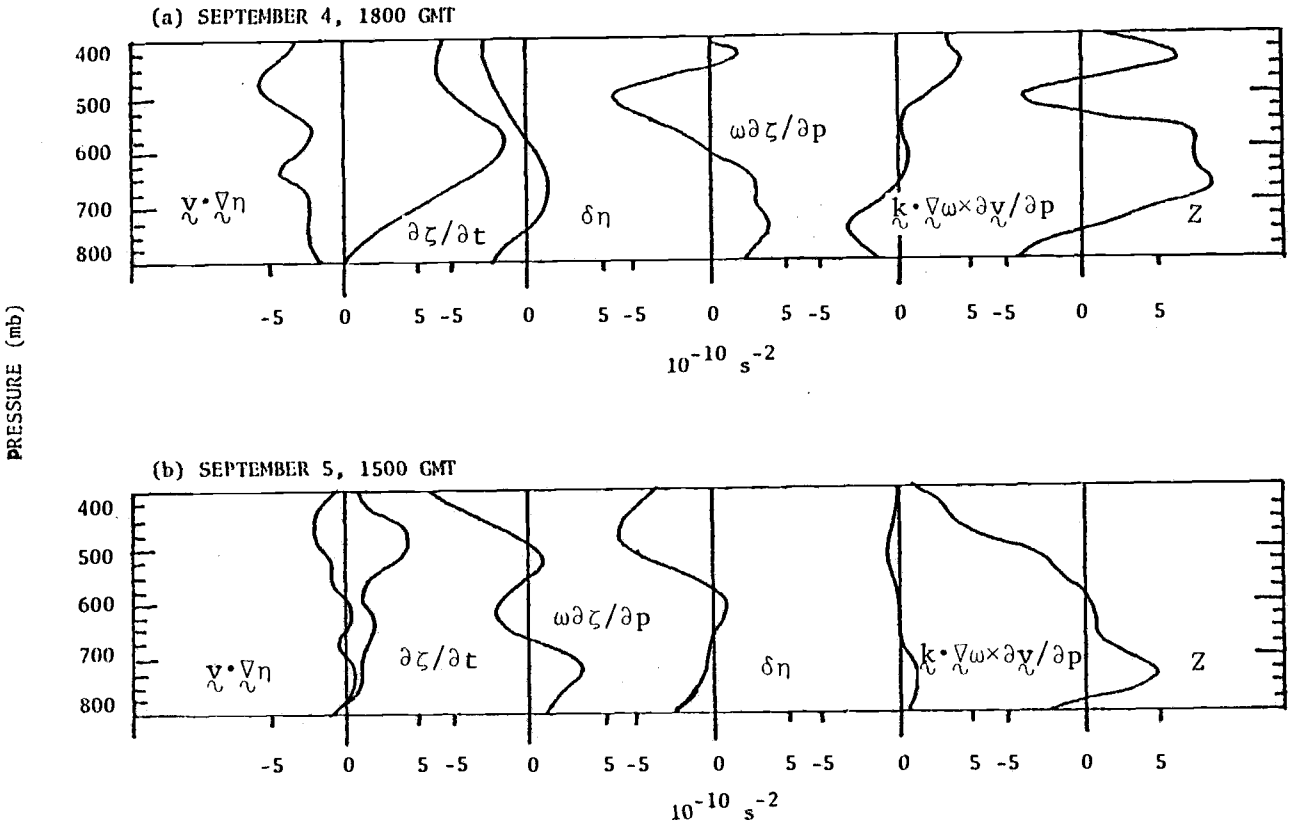

Figure 5.10. As in Fig. 5.9 except at mid-levels for the mature stages of (a) the 4 September squall and (b) the 5 September cluster.

In contrast, the change in vorticity of the low-level jet in the 5 September cluster is about what would be expected from the easterly wave advance. As Fig. 5.10b shows, none of the vorticity budget terms in the mature cluster are significantly large near the level of the easterly wind maximum at 635 mb.

In light of these results, then, and interpreting the residual as being the result of unresolved processes, we may conclude that convective, mesoscale, and/or small cluster-scale circulations do interact with the easterly wave in the 4 September squall, while the interaction between the easterly wave and the cluster on 5 September is small or non-existent. This possibility was also suggested by Houze and Betts (1981).

The anticyclonic maximum near the top of the troposphere in all stages of the squall and cluster is somewhat greater in magnitude and higher at the cluster center than it is at the center of squall anvil. It is misleading to look at the vorticity only at the center of convection, however, because there are large horizontal gradients at this level. The horizontal structure of vorticity near the tropopause in cluster regions will be the subject of Chapter 7.

5.4 Thermodynamic fields

Figs. 5.11 and 5.12 show horizontal sections of humidity and temperature anomalies at four different pressure levels during the 4 September squall. On each of these figures the norm field has been removed, leaving the E and D bands. Thus, features with periods greater than eight days are not included, but easterly wave and cluster-scale features remain.

The most striking feature on the relative humidity plots is at upper levels, where there is a strong relative maximum situated within the squall anvil. That relative humidity should be high at

Figure 5.11. Horizontal contour plots of relative humidity deviations (E + D bands) during the life cycle of the 4 September squall at (a) 227 mb, (b) 317 mb, (c) 463 mb, and (d) 738 mb. Units are percents; contour interval is 5%.

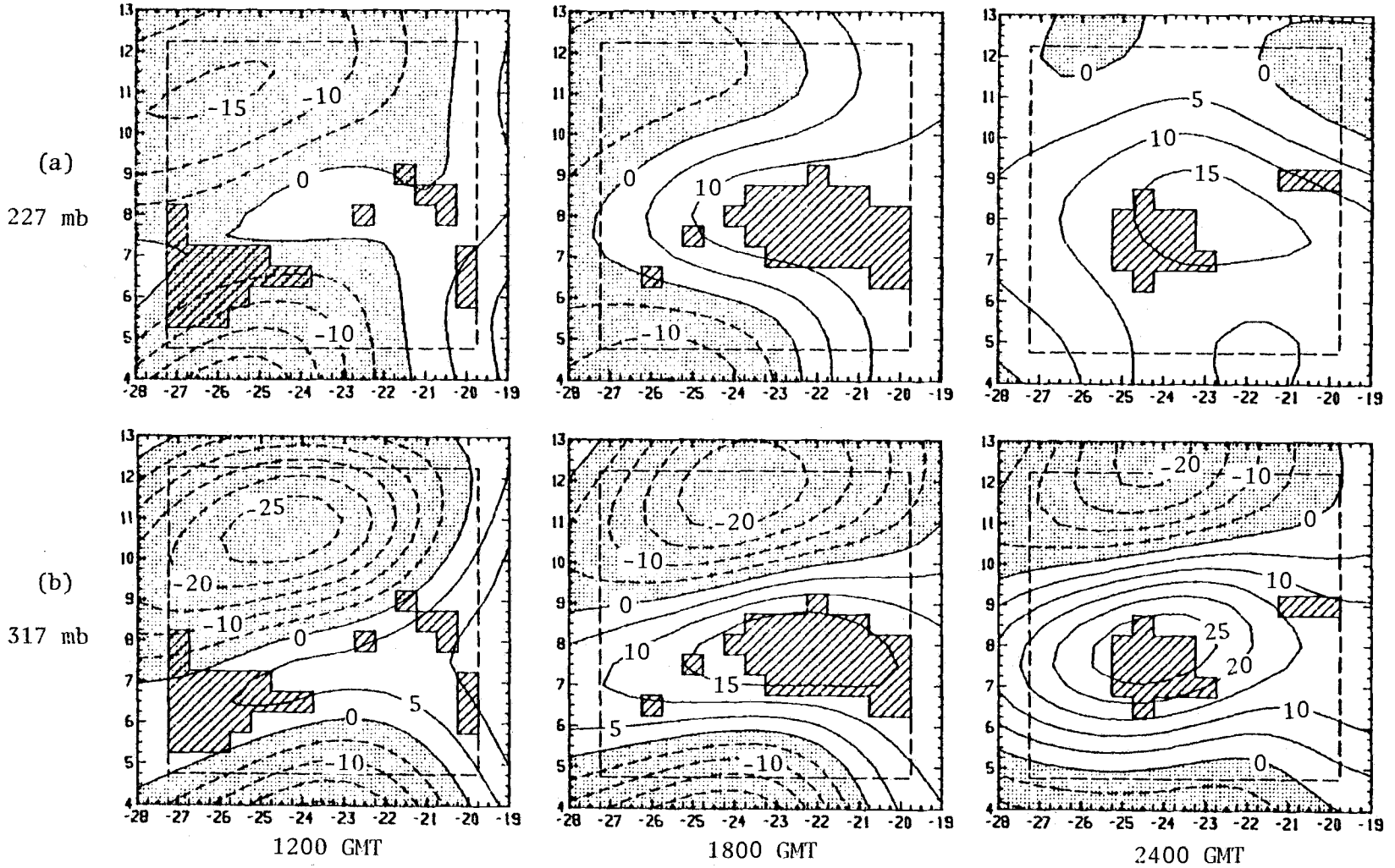

Fig. 5.11 (continued)

(c)

463 mb

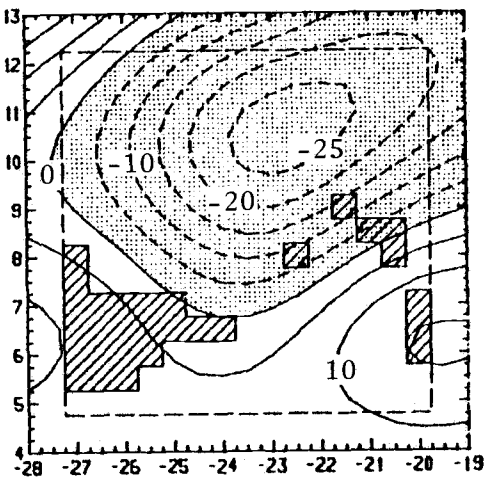

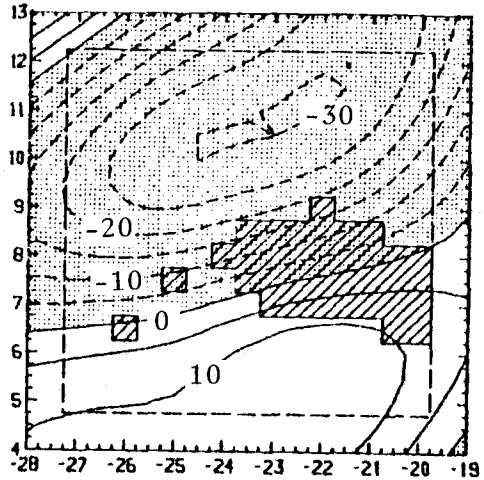

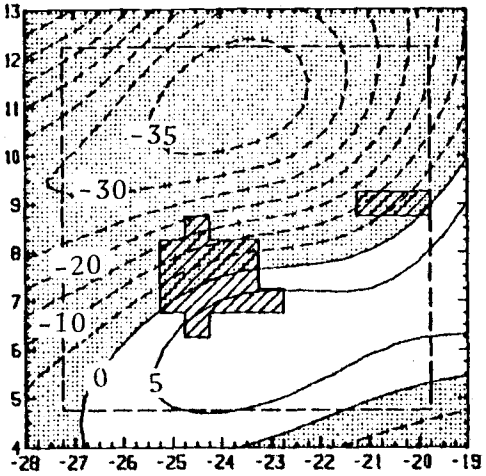

(d)

738 mb

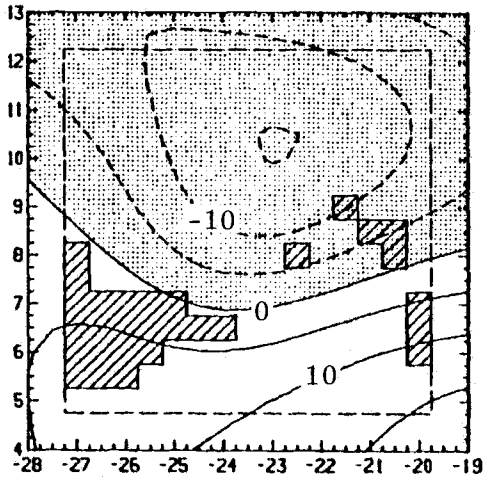

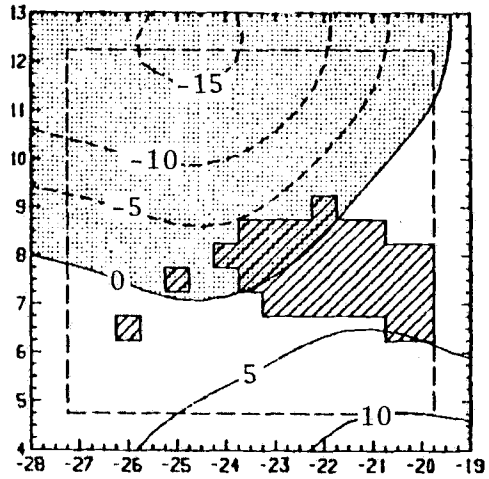

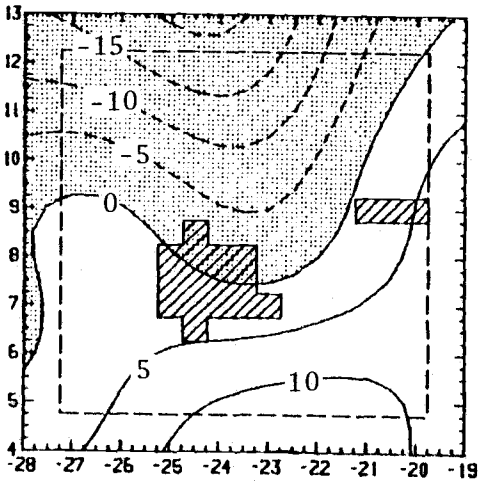

1200 GMT 1800 GMT 2400 GMT

Figure 5.11 (continued)

Figure 5.12. As in Fig. 5.11 except for temperature deviations. Units are 10^{-1} ^{o}C; contour interval is 0.2 ^{o}C.

(a)

227 mb

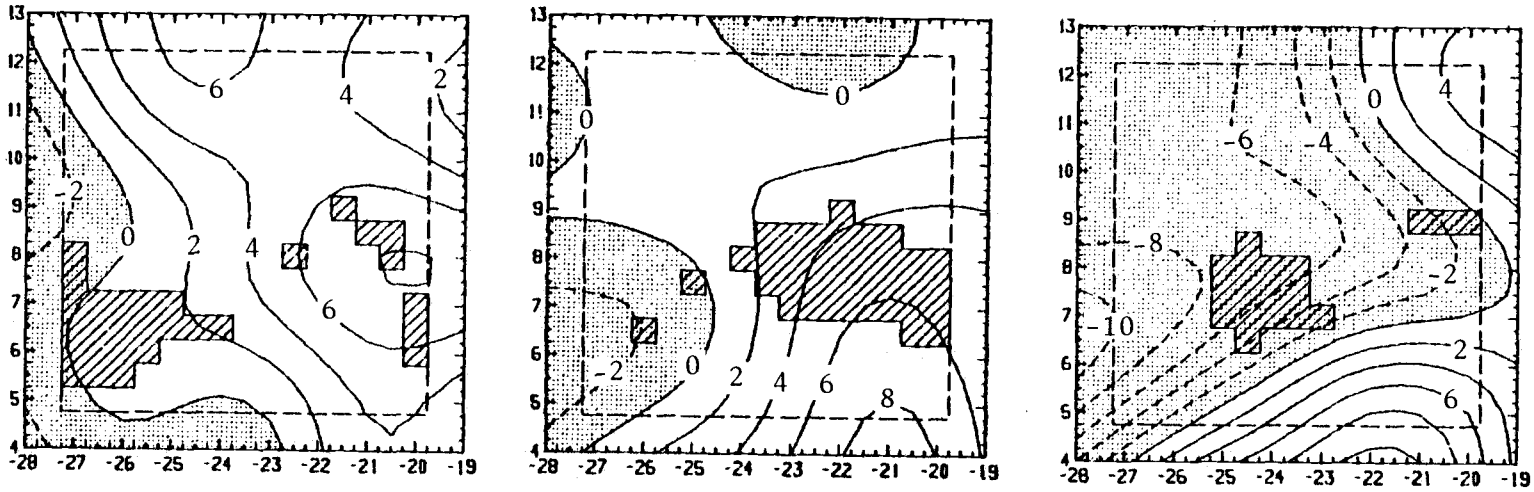

(b)

317 mb

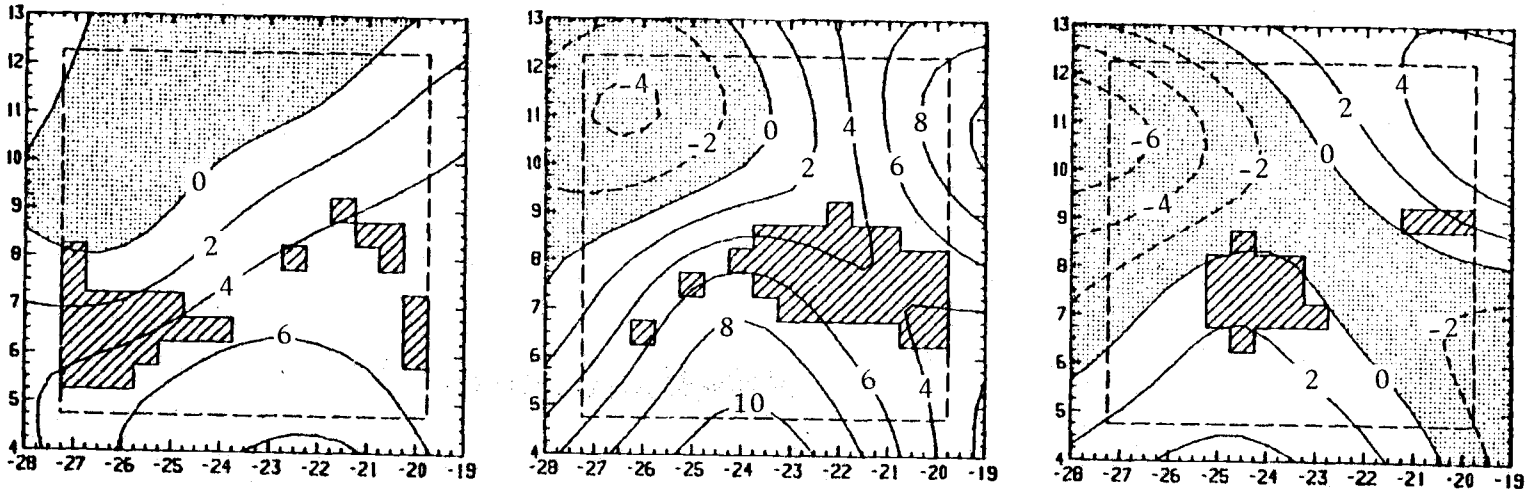

1200 GMT 1800 GMT 2400 GMT

Fig. 5.12 (continued)

(c)

463 mb

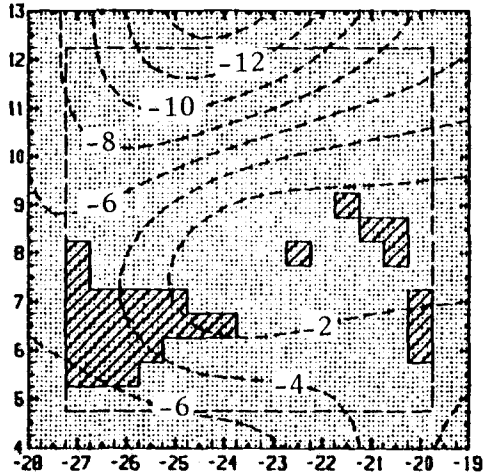

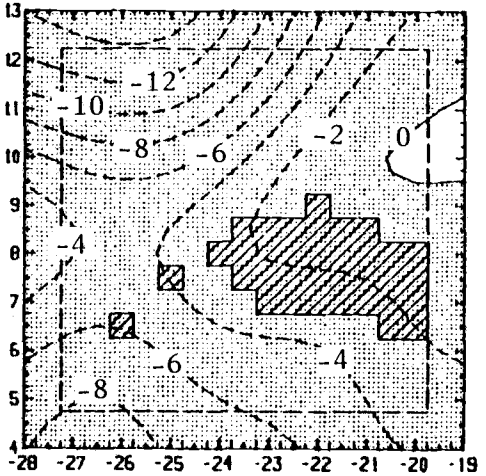

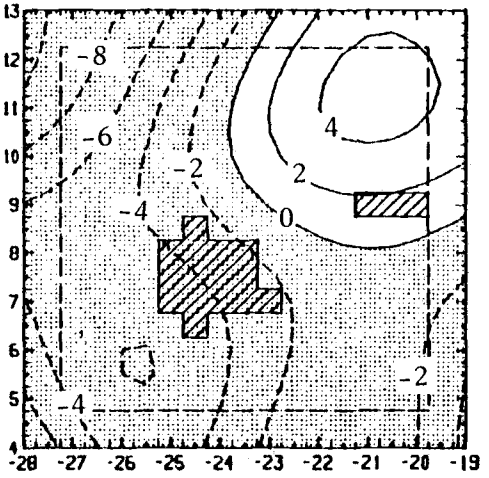

(d)

738 mb

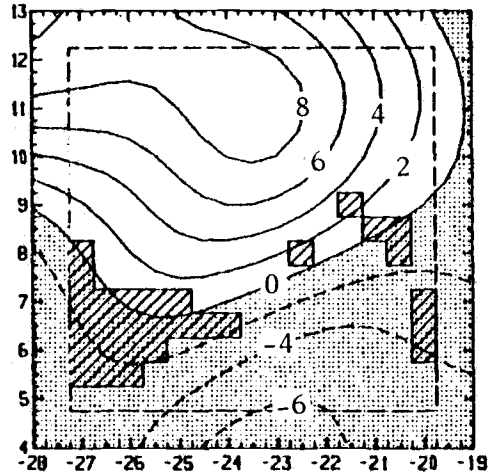

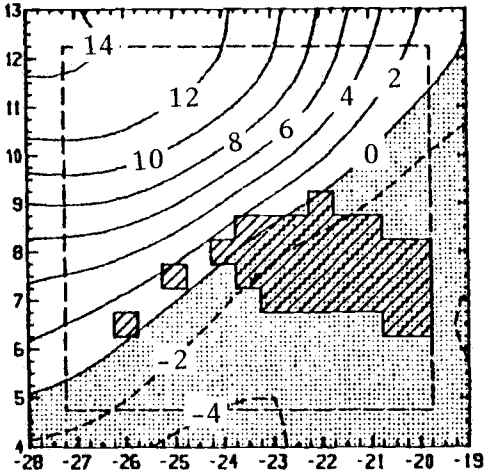

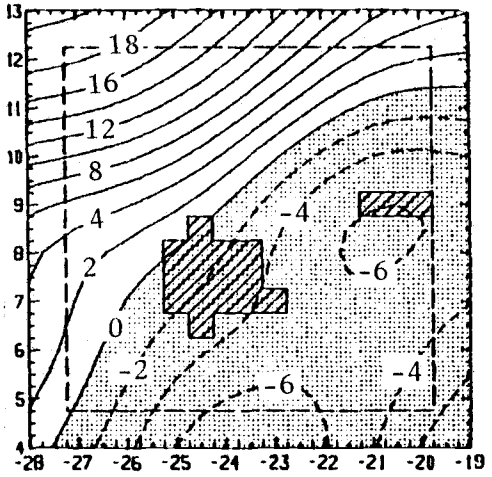

1200 GMT 1800 GMT 2400 GMT

Figure 5.12 (continued)

a location in the vicinity of an anvil cloud is not surprising, of course, but this good relationship between the independently determined anvil location and the maximum of relative humidity gives added confidence to the humidity data.

If the norm field is added to these anomaly fields, RH increases to almost 70% at 316 mb in the mature and dissipating stages. Because of the limits of resolution, the analysis cannot pick out the mesoscale patterns of moist air at humidities near saturation. Thus, the RH values represent an average of air that is saturated along with air that is less moist.

Disregarding the relatively large positive anomalies in temperature near the south and east boundaries of the 227 mb and 317 mb plots on Fig. 5.12, which are unreliable because they are extrapolated rather than interpolated, it appears that the temperature is warmer during the growing and mature stages in the regions immediately surrounding anvil clouds than in other regions of the analysis domain. This finding would accord with the reasonable hypothesis that the effect of penetrating convection (which is active in both the growing and mature stages) is a moistening and warming of the air in the upper levels of the anvil. However, the temperature fields appear to have a larger spatial scale, with a less clear horizontal relationship to the cluster anvils.

An observation that might be made with greater confidence is that there is a significant cooling at the top of the anvil between the mature and dissipating stages (on the order of one degree). Fritsch and Brown (1982) have also noticed cooling near the tops of anvils of numerically modeled convective systems, a cooling that they attribute to adiabatic expansion due to lifting by mesoscale circulations within the anvil. Rising motion within the anvil of the 4 September squall is evident from Fig. 5.6, though it is difficult to determine if the rising air is forcibly

lifted, which would result in local cooling, or is instead rising due to buoyancy generated by heat of condensation, which probably would not. It may also be true, of course, that this cooling is simply part of the diurnal radiative cycle, perhaps enhanced by cloudtop radiative cooling within the top layers of the anvil. Gray and Jacobson (1977) and McBride and Gray (1980a) have suggested that this cluster-related cloudtop cooling is part of a feedback process by which the diurnal radiative cycle modulates the occurrence of convection in the tropics. Since the E-band temperature fields (not shown) do not show cooling at this horizontal scale or of this magnitude, a diurnal or cluster-related cooling is suggested. Both of these possible sources are contained within the same band (the D band); thus it is not possible to conclusively determine solely on the basis of the temperature fields which type of forcing is producing the observed cooling. Examination of time series of temperature at individual observing ships suggests that the magnitude of the diurnal temperature cycle at this level is about 1-2 degrees K, and that early-evening cooling may be enhanced by the presence of organized convection. Some combination of the possible types of forcing may therefore be responsible.

Within the anvils there is a marked apparent moistening between the mature and dissipating stages (Figs. 5.11a and 5.11b). This increase in RH is explained by the decrease in temperature; at this pressure, relative humidity, and temperature, the observed drop in temperature of 1 degree K would lead to an increase in relative humidity of about 6%, which is about that observed.

At 738 mb both the temperature and relative humidity fields exhibit the imprint of an easterly wave, with warming and drying to the northwest and cooling and moistening to the southeast. At 462 mb, an intermediate level between the cluster anvil above and the easterly wave regime below, the temperature field is relatively

featureless. The relative humidity fields here, on the other hand, strongly suggest wave properties. In its phase and its southwest-to-northwest orientation, this apparent wave-like feature resembles the easterly wave at 635 mb. Its wavelength, however, is about half as long as a typical easterly wave. The progression and coherence of this "wave" is readily seen on a succession of plots of RH at this level over the next few days (not shown). In its wavelength, phase, and propagation characteristics, it is remarkably similar to an apparent wave pattern in the vorticity field at 430 mb on these same days (Fig. 5.13). Whether these waves are a vertical extension of the synoptic easterly wave, or whether they are a result of wave motions of a different nature and origin, is a potentially interesting subject for further research.

When the 5 September clusters are examined at the same levels and in the same manner as described in the previous discussion of the 4 September squall, very similar features appear.

A meridional cross section of relative humidity through the center of the western cluster on 5 September is shown on Fig. 5.14. Also denoted on this section are all regions where the windspeed is less than 2 ms^{-1}, the smallest contour on the section of windspeed made at the same location (Fig. 3.2). A comparison of the two fields shows that there is a distinct relationship in the anvil between windspeed and RH, with a "dome" of decelerated winds evident on Fig. 3.2 mirrored by a dome of high relative humidities near the same location on Fig. 5.14. The location of centers of moist air and decelerated winds in a region of strong convection is in accord with the hypothesis that cumulus or mesoscale updrafts are transporting moisture and momentum upward.

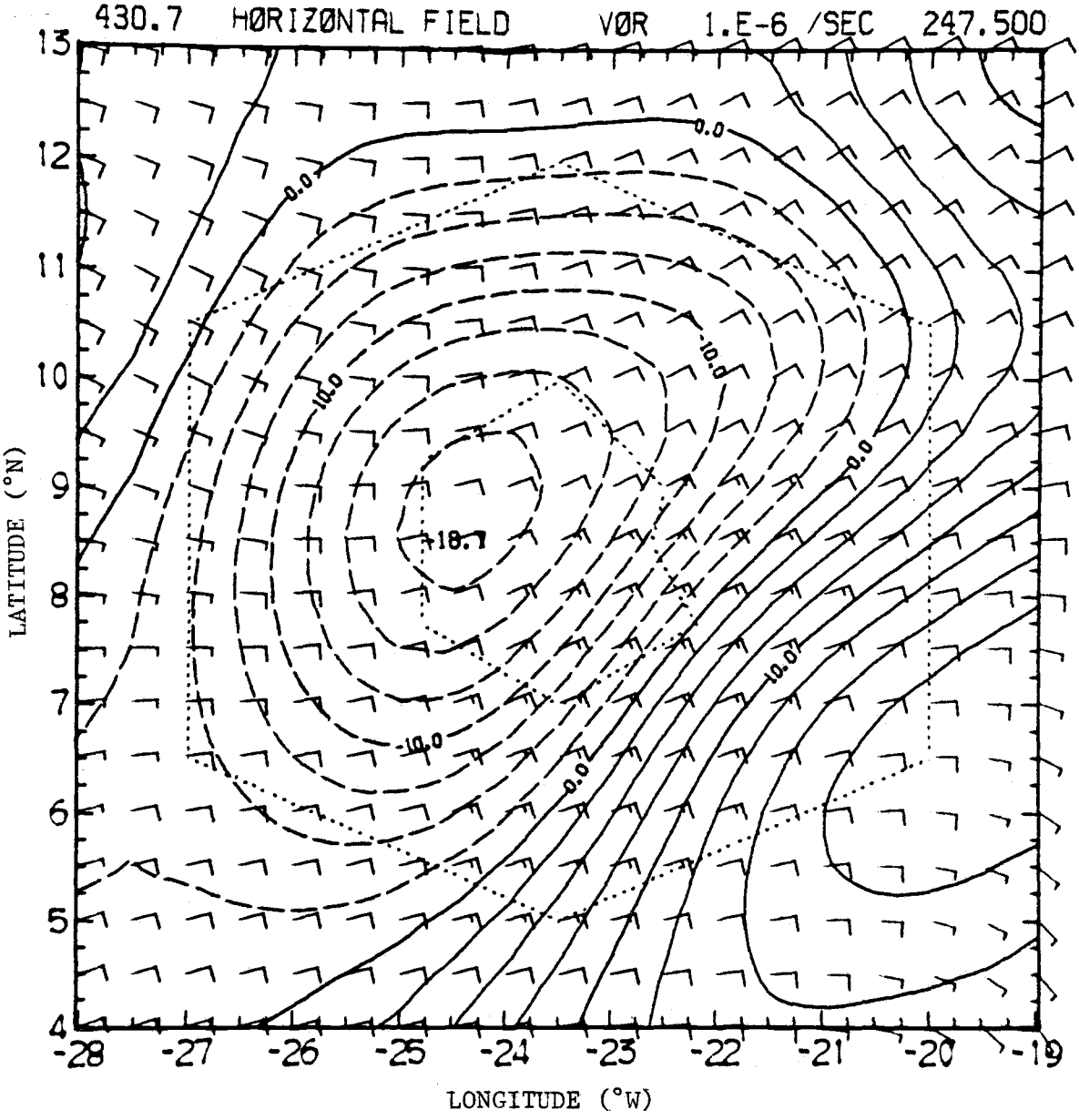

Figure 5.13. Horizontal field of ζ at 431 mb at 1200 GMT on 4 September 1974. Units are 10^{-6} s^{-1}; contour interval is 2.5 x 10^{-6} s^{-1}.

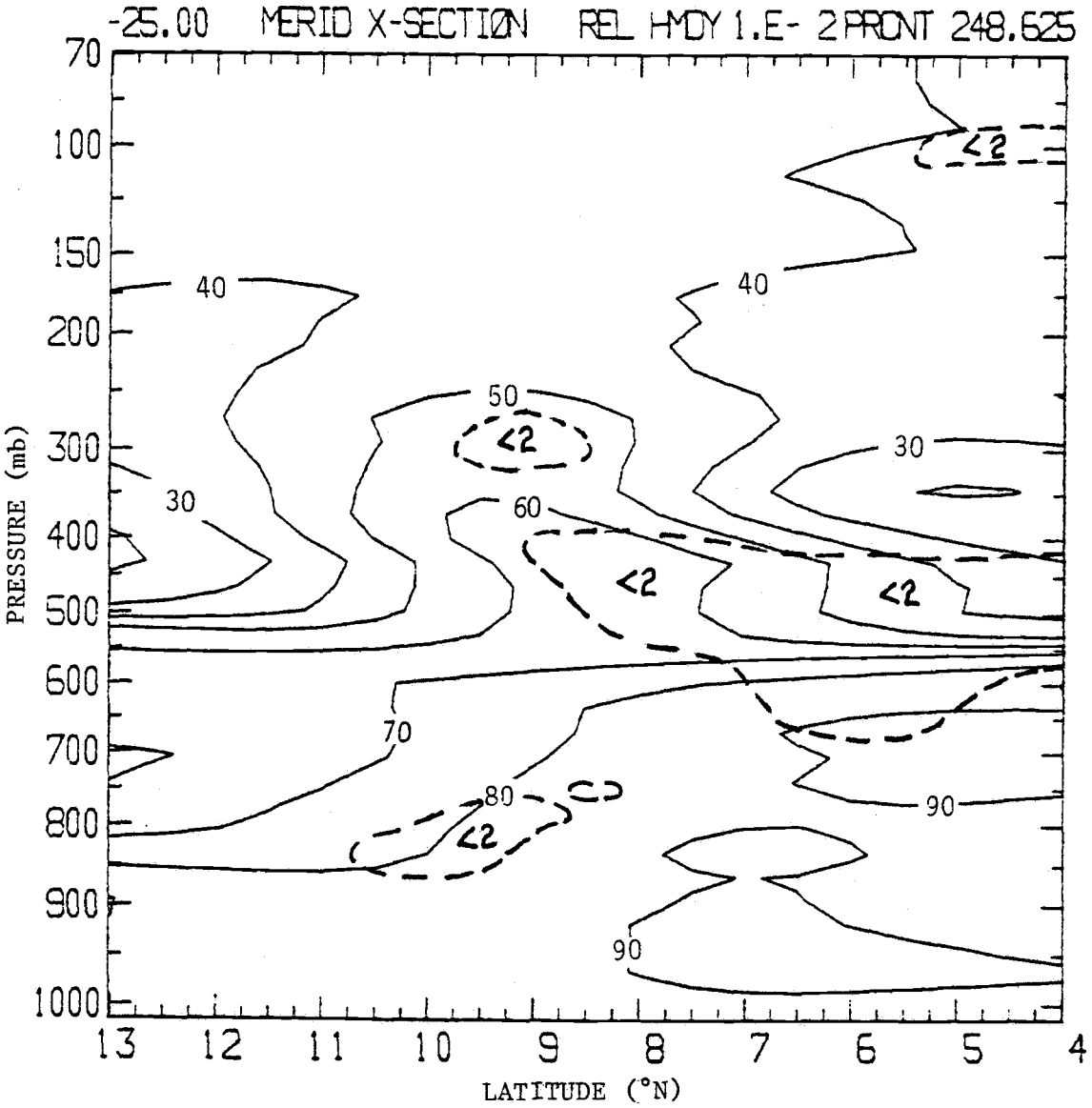

Figure 5.14. Meridional cross-section of relative humidity through the center of the western cluster during its mature stage. Section is made at 25°W at 1500 GMT on 5 September. Units are percents; contour interval is 10%. Dashed contours are the 2 ms^{-1} contour of windspeed at the same time; the enclosed regions thus have windspeeds less than 2 ms^{-1}.

CHAPTER 6. COMPOSITE RESULTS

6.1 Purpose and methodology of composite study

To generalize the results of one case study and to at least partially remove random error, winds from the largest slow-moving cloud clusters observed during Phase 3 of GATE were composited. It will be of particular interest to see if the features that were found in the vorticity and momentum fields of the 5 September cluster appear also in the composites.

In order to composite the three-dimensional fields associated with clusters, a criterion for determining the times and horizontal locations of clusters must be defined. It would be preferable if that criterion were not based on wind data, which will be composited. Because of their large size, the extensive anvils of tropical clusters are a good feature upon which to base a compositing scheme. The 1-hr averages of satellite-derived percent cloudtop computed by Cox and Griffith (1979) have ample resolution in time and space to resolve these anvil clouds. Thus, these data will be used to determine anvil locations and times. Definitions of an "anvil index" and cluster life stages are those given in Chapter 3.

In applying this criterion the inherent time and space resolution of the wind data must be considered. It would be of no use, for instance, to define as "anvil" an isolated 1/2° by 1/2° cloud that lasted one hour when the analysis scheme for the wind data has no hope of resolving features of this size and duration. Therefore only those anvils that persisted in the satellite data for six hours or more and reached an approximate diameter of 200 km are included in the composite.

This chapter deals exclusively with composites of the slow-moving "non-squall" clusters, which are referred to simply as "clusters." The structure of the flow in the vicinity of the

relatively fast-moving "squall" clusters, which occurred in GATE with about the same frequency as the slow-moving clusters, will not be discussed.

On the first and last days of Phase 3 not all ships were on station. Since the missing data at these ship locations resulted in some degradation of the quality of the analyzed winds, these two days were not included in the compositing period, which then extended from 31 August through 17 September. This exclusion eliminated one possible system, a cluster on 30 August.

The five clusters identified for compositing are summarized on Table 6.1 and Fig. 6.1. The easterly wave phase categories used to produce Fig. 6.1 were determined by Thompson et al. (1979) using a procedure first suggested by Reed and Recker (1971). As can be seen from the figure, the clusters' mature stages tend to occur during the mid- to late afternoon. The positive slope of the clusters' "life lines" indicates that these slow-moving clusters develop in earlier easterly wave phase categories than those in which they later dissipate, intensifying within or just before the wave trough and dissipating just behind it. These relationships between cluster development, time of day, and easterly wave phase are in accordance with numerous other studies of GATE convective systems (cf. Houze and Betts, 1981).

The actual compositing procedure consists of placing a 13 point by 13 point rectangular composite grid over each cluster, with the composite grid axes oriented north-south and east-west. The grid intervals are approximately 1/2° latitude by 1/2° longitude. The composite grid center point is placed in each case at the center of the anvil (as determined from plots of the anvil index). Except for cluster 5, which was determined to have just one sampling time clearly in the dissipating stage, two sampling times were selected from each stage of each cluster. The resulting set of values are then averaged within each stage at each grid

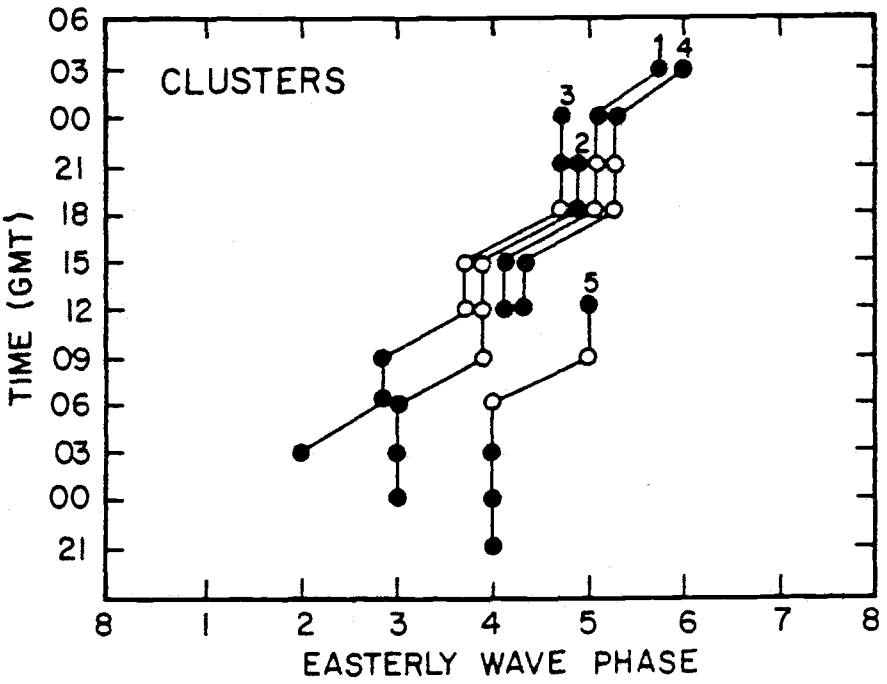

Figure 6.1. Life cycles of GATE Phase 3 cloud clusters included in cluster composite. Open circles identify mature stage of each cluster. The chronology of easterly wave phases are from Thompson et al. (1979). Numbers on cluster life cycle lines correspond to the numbers on Table 6.1.

Table 6.1 Slow-moving clusters included in composite.

Cluster No. (see Fig. 6.1)	Date	Center Location, Mature Stage
1	2 Sept. 1974	25°W, 8°N
2	5 Sept.	21°W, 9.5°N
3	5 Sept.	25°W, 9°N
4	16-17 Sept.	21°W, 9°N
5	17 Sept.	25°W, 10°N

point in the 3-dimensional composite grid volume. Wind fields thus composited include u, v, windspeed, divergence, ω, and ζ. Vorticity budget terms are also composited.

Fig. 6.2 shows contour plots of percent cloudtops computed by adding together the percent of sky covered by clouds that have their tops in either of the top two layers of the CG radiation data set and then compositing these values as described above. It is not surprising, of course, that the cloudtop percents are approximately centered on the cluster composites, since cloudtops were used to locate the cluster centers. The plots do, however, illustrate the typical horizontal extent of anvil clouds and their evolution during a cluster life cycle.

6.2 Composite wind fields

Perhaps the most revealing view of the individual composited fields is provided by meridional sections through the cluster center.

The sections of the zonal component of the wind (u) on Fig. 6.3 illustrate the typical wind structure in the region where the clusters form. Below 800 mb (shallower to the north), u is positive where the low-level West African monsoon flow is evident. Near 635 mb to the north of the cluster is the easterly wind maximum associated with the synoptic easterly waves which have their maximum amplitude at this level. Between the growing and dissipating stages the jet maximum decreases in magnitude (see also the vertical profiles at the cluster center on Fig. 6.4); this decrease reflects the movement of the easterly wave with respect to the nearly-stationary cluster. The apparent reduction in u at, and to the north of, the cluster center in a layer between 200 and 300 mb during the lifetime of the cluster will be discussed in detail in Chapter 7. The upper-tropospheric easterly jet centered south of the cluster intensifies during the cluster development.

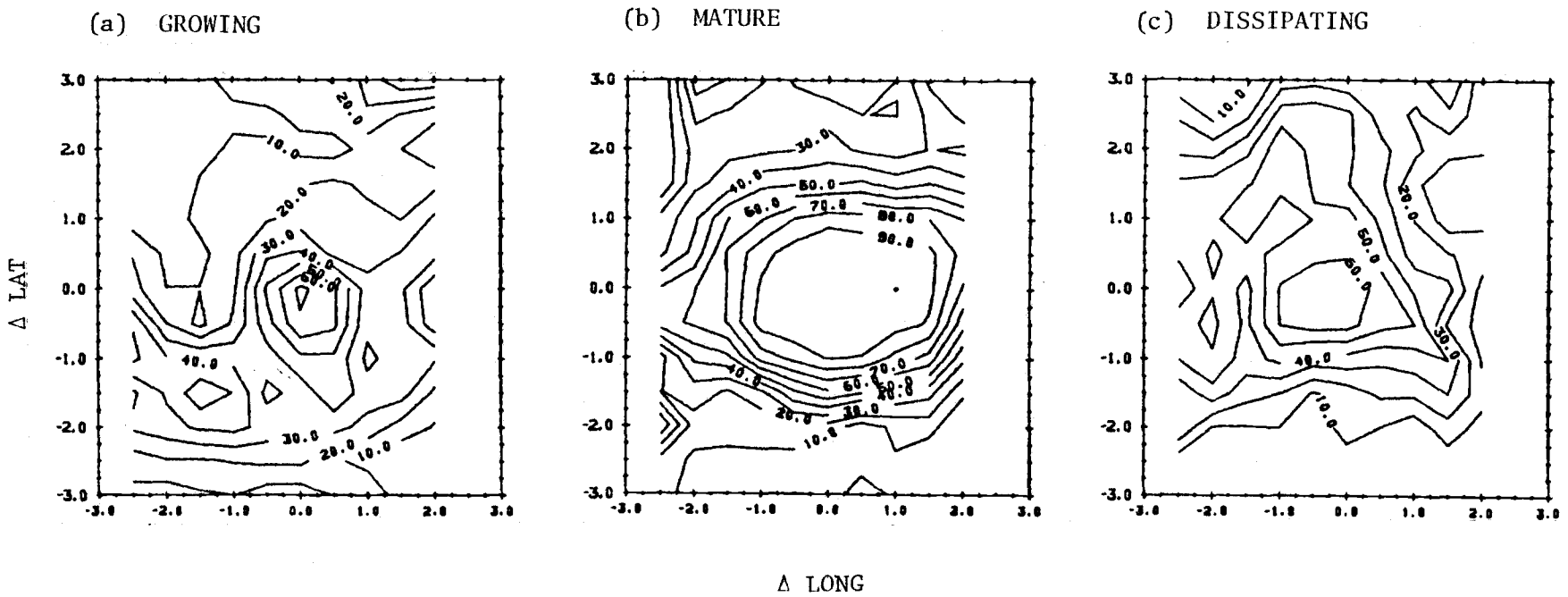

Figure 6.2. Horizontal fields of composited cloud cover above 300 mb during the (a) growing, (b) mature, and (c) dissipating stages of the cluster life cycle. Units are percent; the contour interval is 10%. Axes labels are degrees of latitude and longitude from the cluster center, with north upward and east to the right.

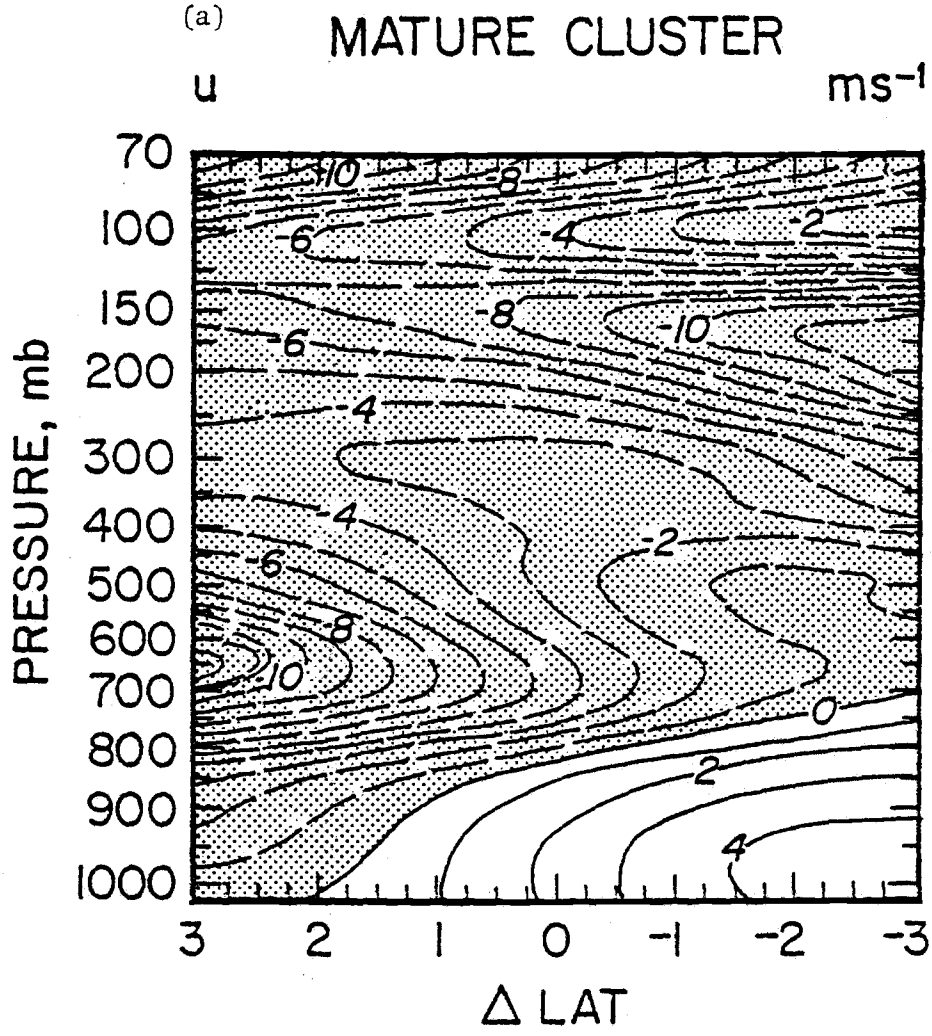

Figure 6.3. Meridional cross-sections of the zonal component of the horizontal wind (u) during the (a) mature, (b) growing, and (c) dissipating stages. Sections are through the center of the cluster. Stippled areas are negative. ΔLAT is the distance in degrees from the center; north is to the left.

(b) GROWING CLUSTER

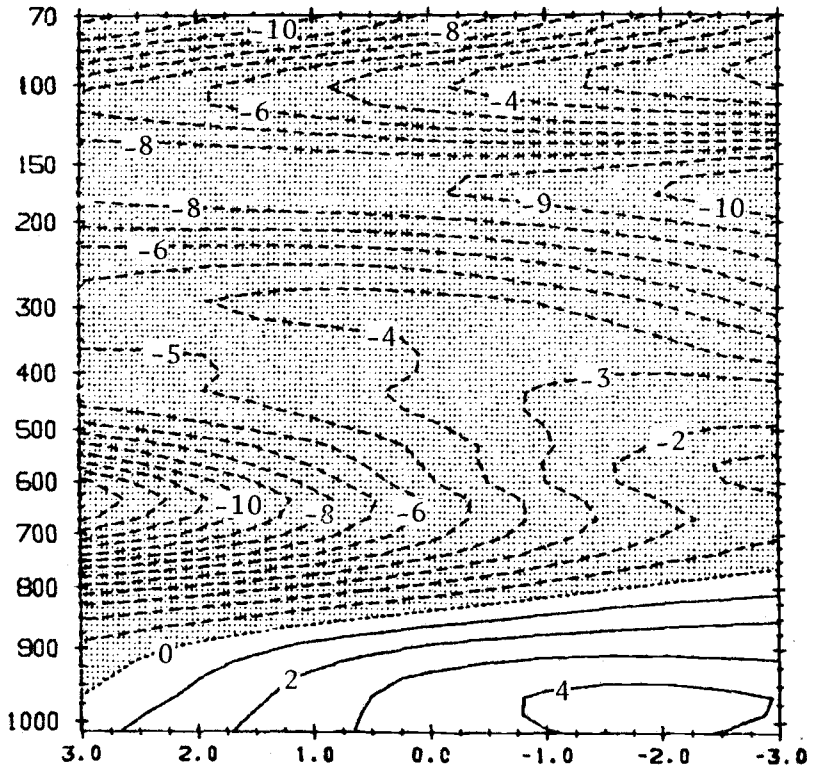

(c) DISSIPATING CLUSTER

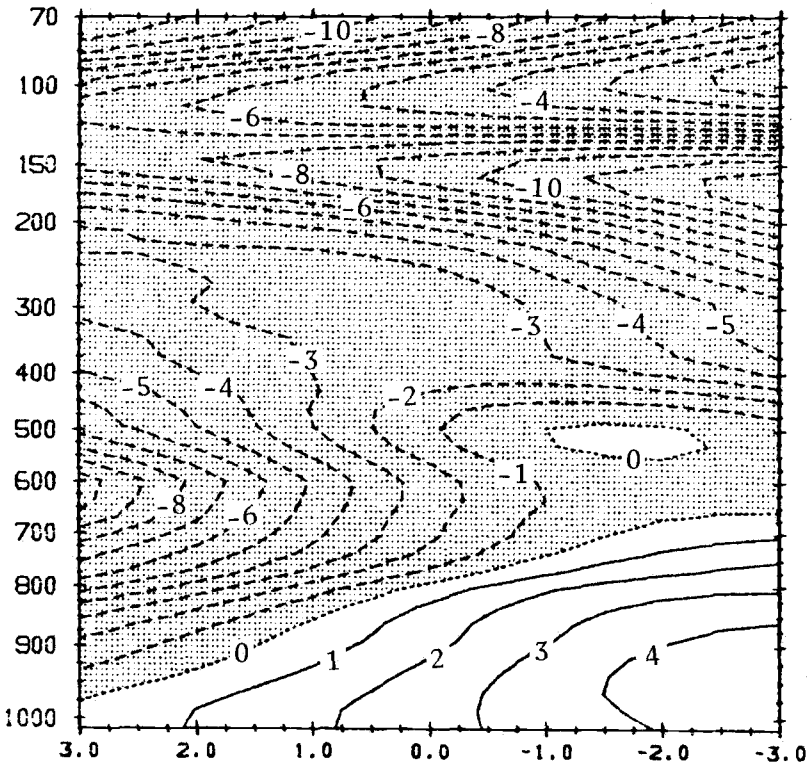

u ms^{-1}

Figure 6.3 (continued)

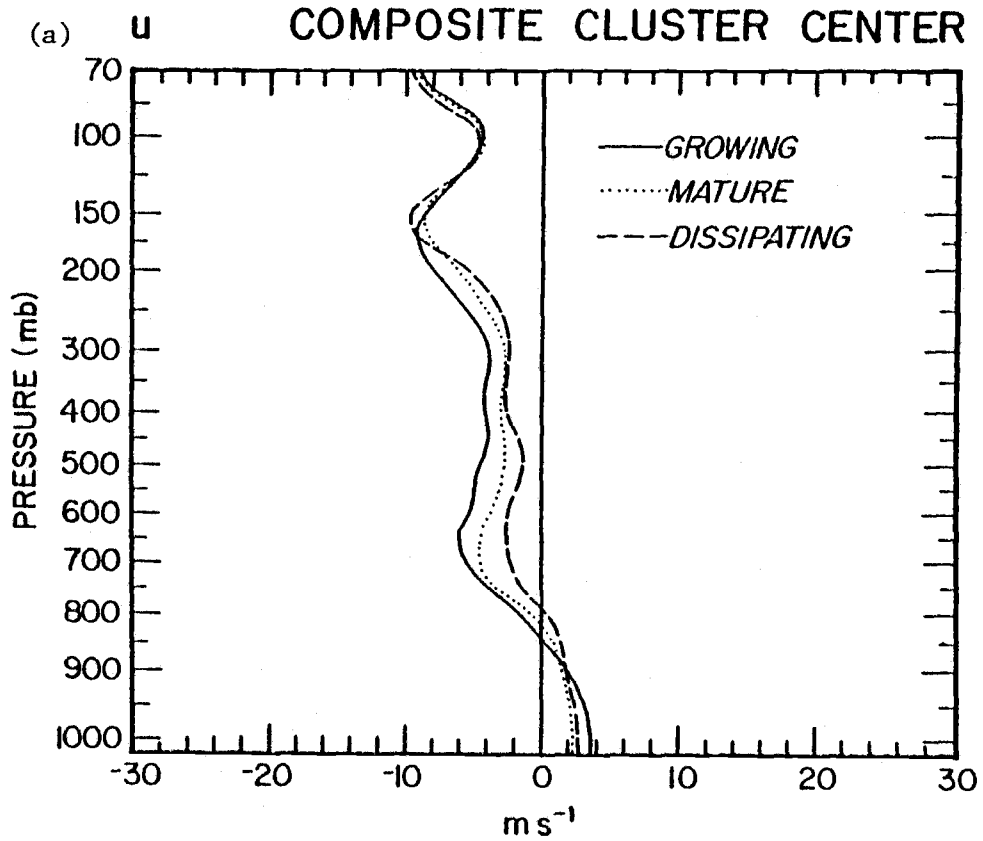

Figure 6.4. Composited vertical profiles of the zonal component of the wind (u) at the cluster center.

The distinguishing feature of the plots of meridional wind (v) on Fig. 6.5 is the layered structure. At the surface there is a layer of strong confluence below 900 mb, with the changeover from northward to southward momentum occurring just south of the cluster center in the growing phase, just north in the mature stage, and almost 2 degrees north in the dissipating stage. This northward migration of the zero contour at the surface is mirrored by a similar migration in the layer of difluence in the upper troposphere. Indeed, the zero contours in both layers appear to be closely related in the sense that they maintain a similar latitudinal location. Between these two levels there is a progressive development of northward momentum south of the cluster center and southward momentum to the north of the center. The weakening of the negative values of v near 625 mb during the cluster lifetime reflects, again, the easterly wave advance. As Fig. 6.6 shows, the meridional velocity at the cluster center is small at all levels but gradually changes from negative to positive below 300 mb during the lifetime of the cluster.

Because the zonal velocity is generally large compared to the meridional velocity at most levels near the cluster, the sections of windspeed (Fig. 6.7) resemble those of u. Two of the most noticeable features in windspeed are the "dome" of reduced windspeed at the cluster center in the upper troposphere and the straightening out of the windspeed vertical profile as the cluster develops (seen more clearly on the vertical profiles on Fig. 6.8). At 225 mb, for instance, windspeed goes from 7 ms^{-1} in the growing stage to 5 ms^{-1} in the mature and dissipating stages. A typical phase 3 mean value is 11 ms^{-1}. Possible sources of this deceleration and its implications for the upper tropospheric circulation are discussed in Chapter 7.

In all of the wind variables thus far shown, the clusters form at that latitudinal location where the vertical wind shear between cloud base and near the top of the troposphere is least. In part,

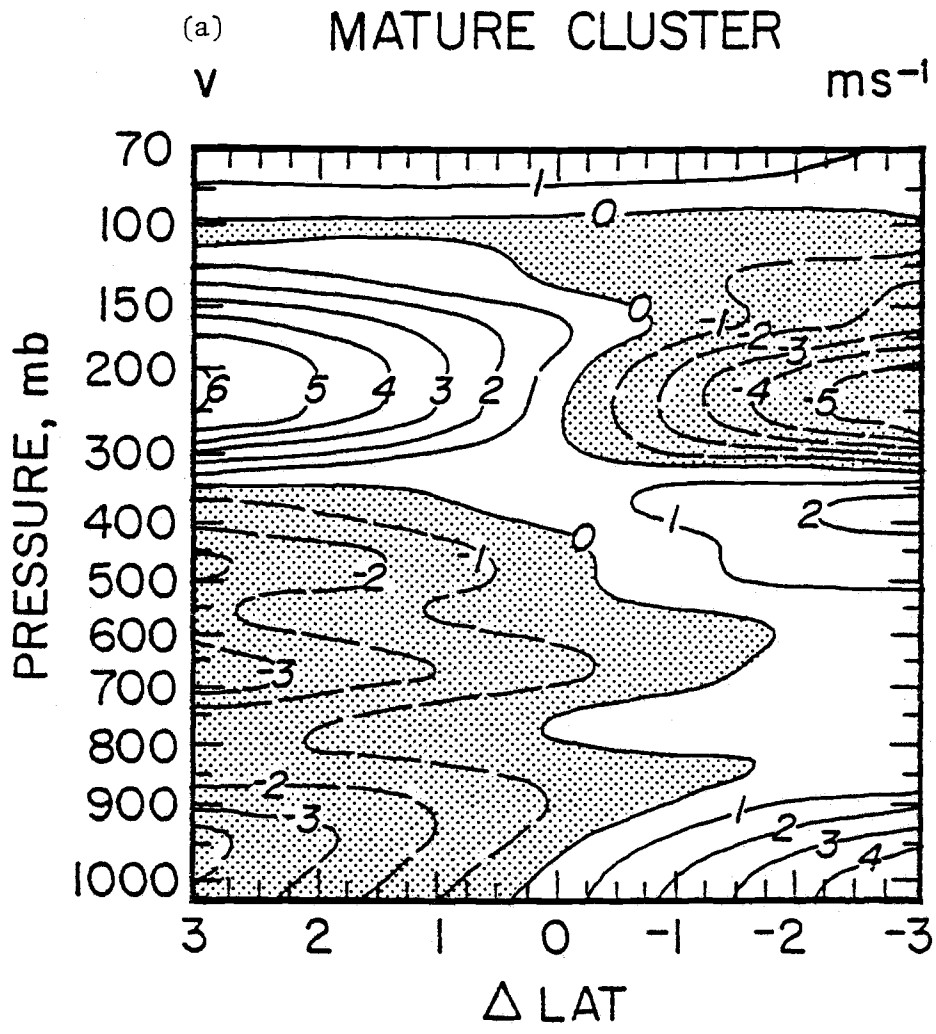

Figure 6.5. As in Fig. 6.3 except for the meridional component of the horizontal wind (v).

(b) GROWING CLUSTER

(c) DISSIPATING CLUSTER

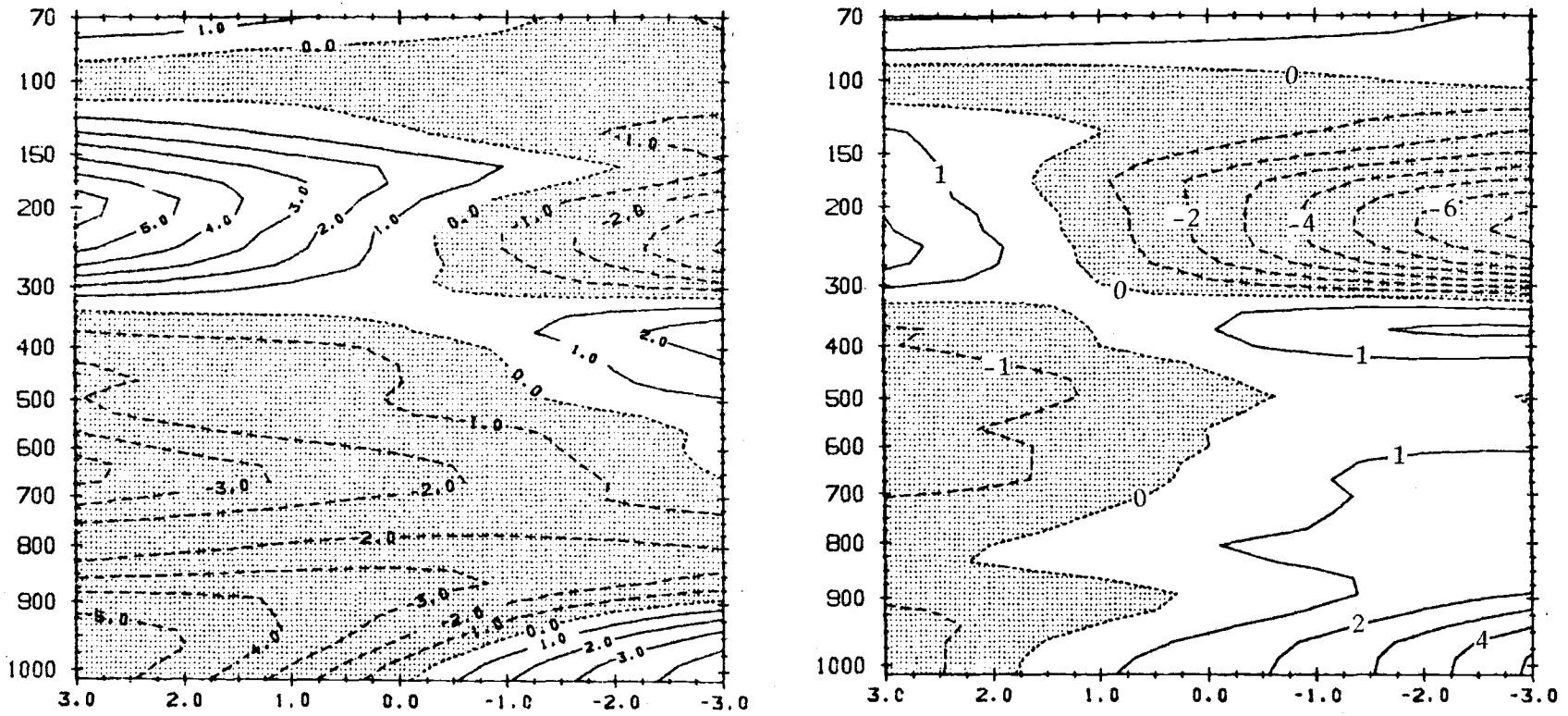

Figure 6.5 (continued)

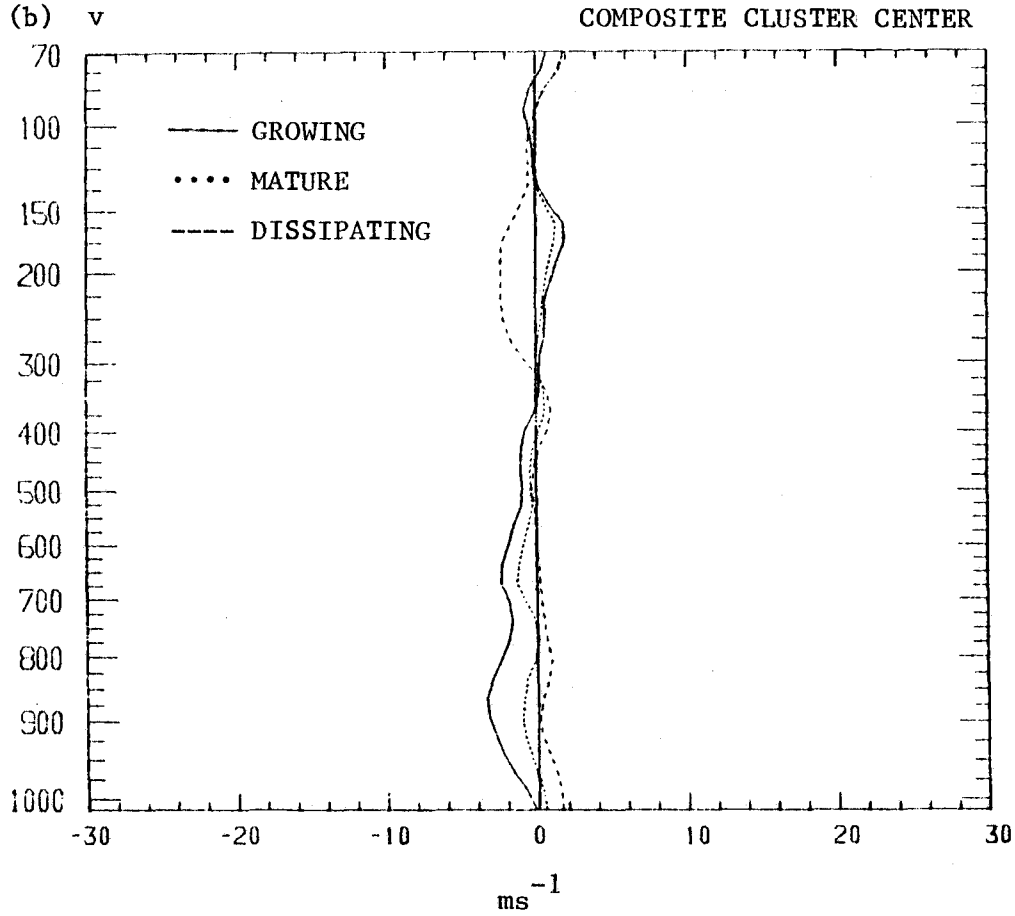

Figure 6.6. Composited vertical profiles of the meridional component of the wind (v) at the cluster center.

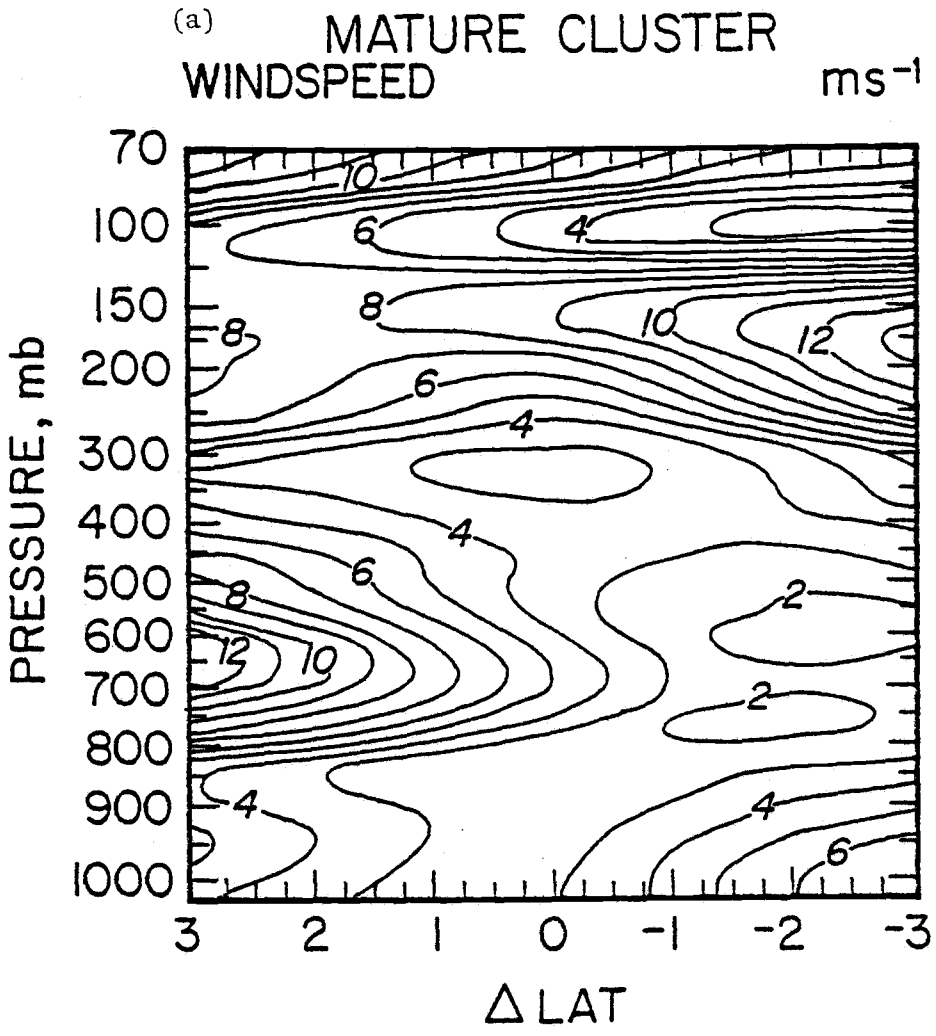

Figure 6.7. As in Fig. 6.3 except for windspeed.

(b) GROWING CLUSTER

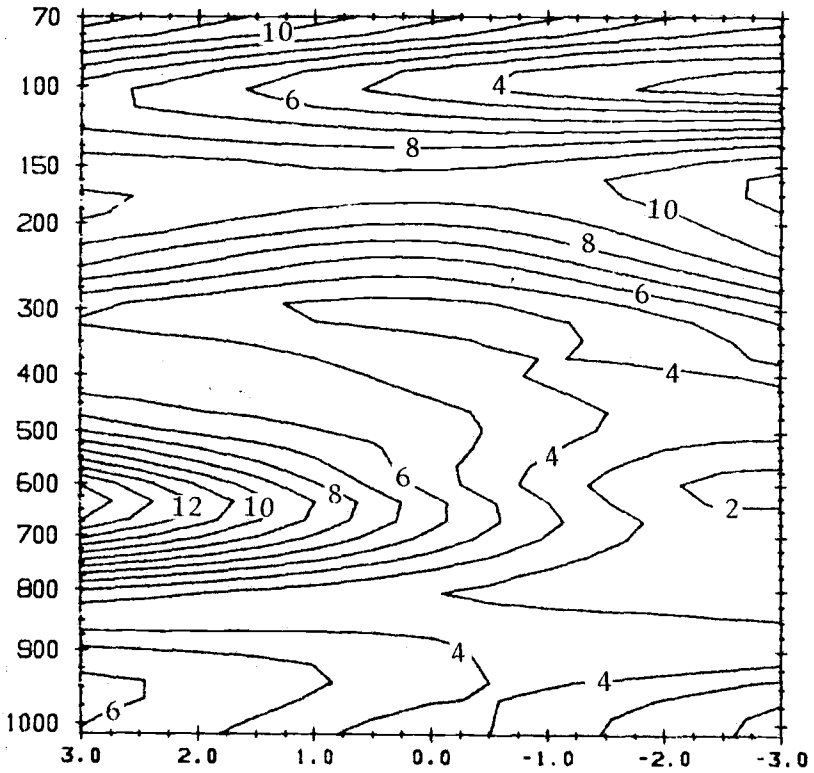

(c) DISSIPATING CLUSTER

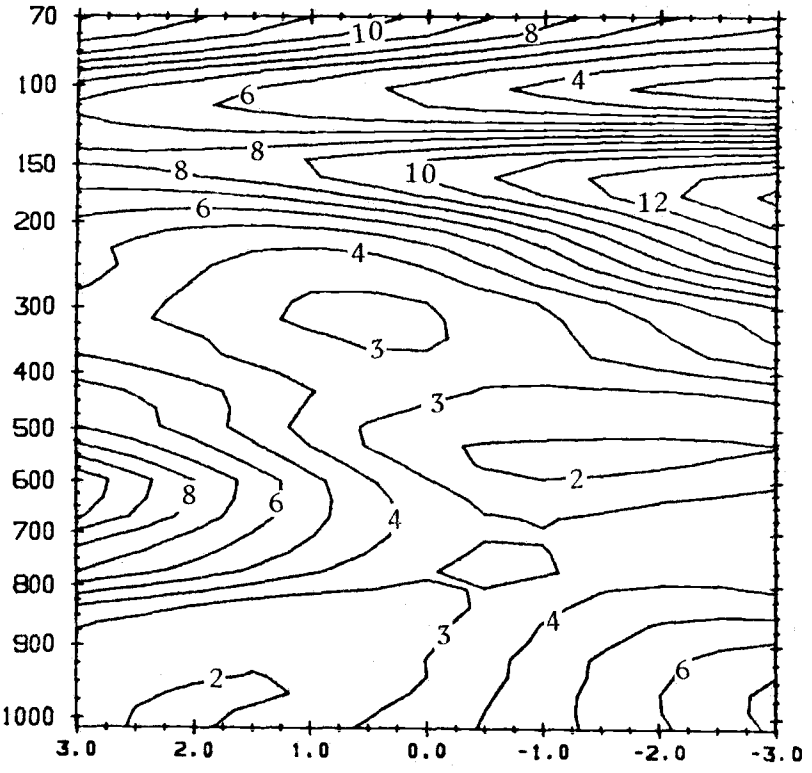

WINDSPEED ms^{-1}

Figure 6.7 (continued)

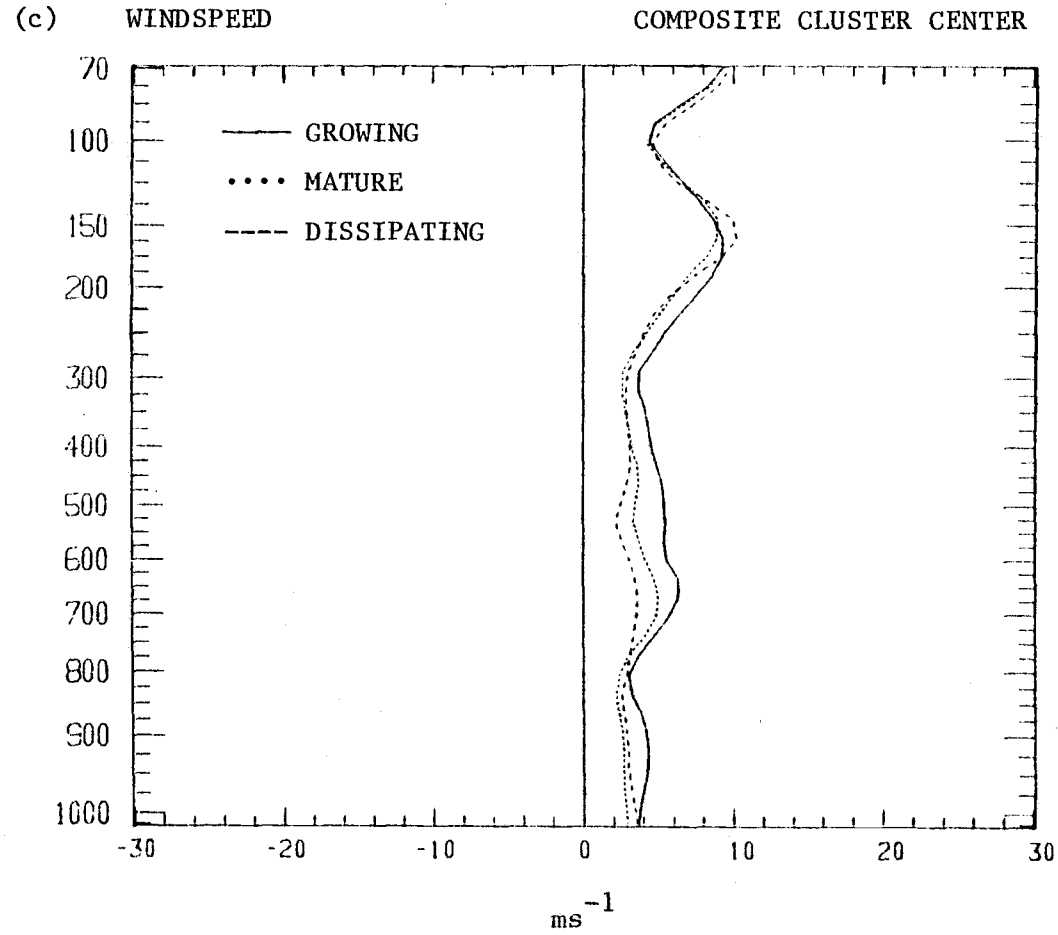

Figure 6.8. Composited vertical profiles of the windspeed at the cluster center.

this may be due to a reduction of shear by the cumulus convection itself (there is substantial deep convection in the growing stage as well as in the mature stage). However, examination of wind sections made well before and after the individual clusters reveals that the reduced shear is a general feature of the environment of the clusters as well as of the clusters themselves. This result is in accordance with the oft-cited preference of some types of convective systems to form in regions of small vertical wind shear. Plausible reasons may be proposed as to why cumulus clouds should grow best in an unsheared environment. For instance, the strong tilt that clouds assume in the presence of shear means that individual buoyant elements ("bubbles") within the cloud that rise more nearly vertically will soon move away from the protective core and become more vulnerable to dilution from the drier air outside of the cloud. In this way, a strongly-sheared environment may result in more turbulent entrainment into the updraft cores of the individual cumulonimbi. As a consequence, these cores may be diluted with less buoyant air and fail to develop to the same degree that they would have in a relatively unsheared environment.

On the other hand, observational and numerical studies of thunderstorms suggest that many long-lasting storms require some tilt (and thus some shear) in order to allow their precipitation to fall out of the updraft core without destroying the updraft with evaporative cooling and particle drag (Browning and Ludlam, 1962). Furthermore, wind shear may be an integral feature of systems that must propagate in order to insure their supply of energetic near-surface air (Klemp and Wilhelmson, 1978). In this regard, it is significant that the relatively fast-moving large squall clusters in GATE tended to form in the more highly-sheared flow in easterly wave phase category 2, while the slowly-moving clusters (which are the subject of the composites of this chapter) tended to form nearer to the trough region, where the shear is less.

In the sections of divergence (Fig. 6.9), layered structure is again evident. The relative extrema in the divergence field are located at or very near the latitude of the cluster center. Lower-tropospheric convergence is strongest at the cluster center during the growing stage (cf. Fig. 6.10) and then diminishes gradually until there is actually a minimum at the cluster center in the dissipating stage. At 200 mb the divergence is strongest during the mature stage when it is twice its value during the growing and dissipating stages. The layer just below the divergence maximum (between 350 and 500 mb) is weakly convergent in the mature and dissipating stages, an interesting result in light of the recent speculation about possible sources for the upward vertical velocity found in the anvils of cloud clusters. The remaining depth of the troposphere, from 900 mb to 500 mb (thus including the level of maximum easterly wave amplitude), has small and inconclusive divergence values.

The kinematically computed vertical velocities (shown in meridional section on Fig. 6.11 and in vertical profile at the cluster center on Fig. 6.12) follow directly from the divergences. In the growing stage the largest values are found near 800 mb above the layer of strong surface convergence. However, by the mature stage the vertical velocity within the anvil near 300 mb is stronger than the other maximum now at 700 mb, a change which is due at least in part to the convergent layer just below the anvil. At both of these times, there is a double maxima in ω.

The vertical velocity structure during the dissipating stage is considerably different. Now there is a local minimum of upward vertical velocity at the center of the cluster at low levels (the anvil maximum is still noticeable). A possible explanation for this region of relatively small velocity is that the cluster-scale vertical velocity averages include in them unresolved regions of mesoscale downdraft, as has been suggested by Zipser (1969, 1977),

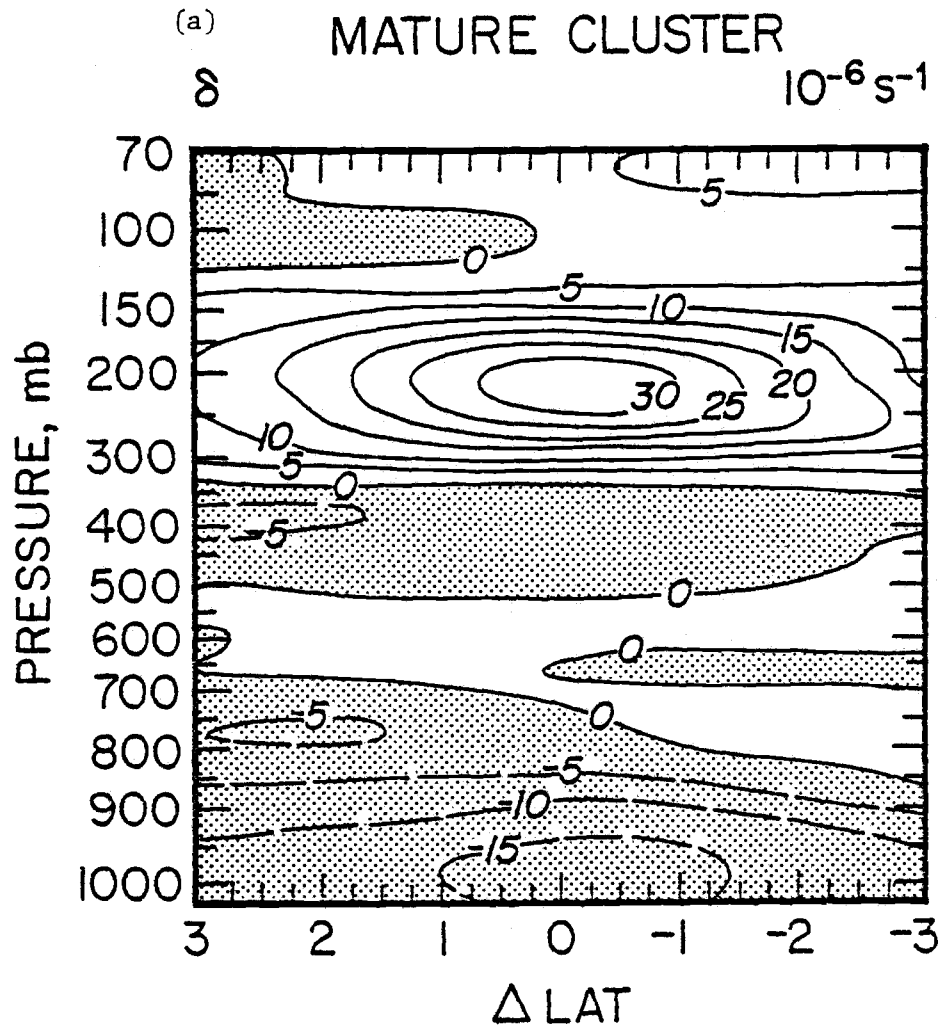

Figure 6.9. As in Fig. 6.3 except for the horizontal divergence (δ).

(b) GROWING CLUSTER

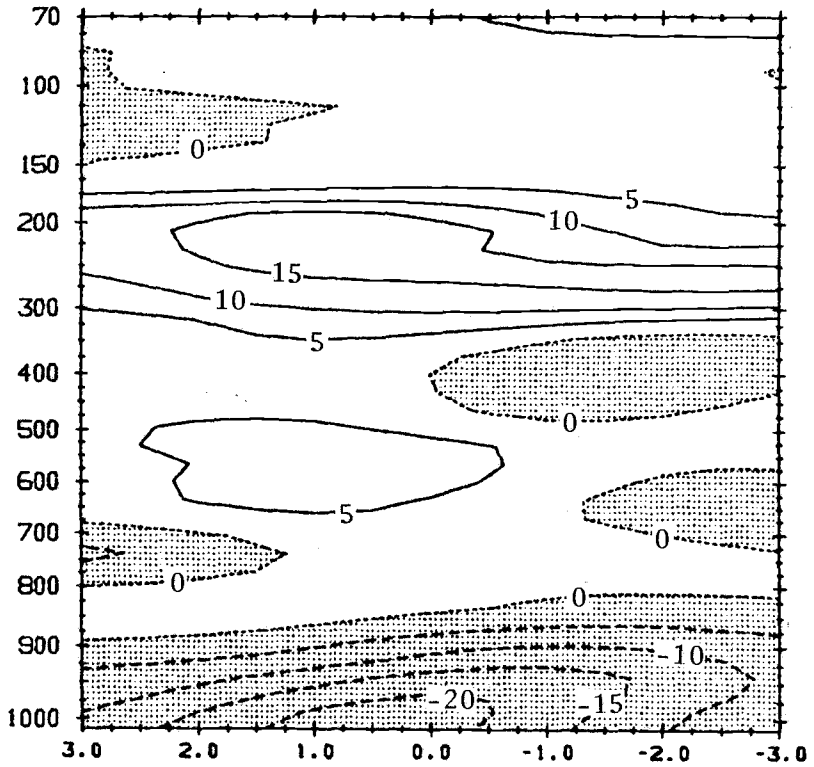

(c) DISSIPATING CLUSTER

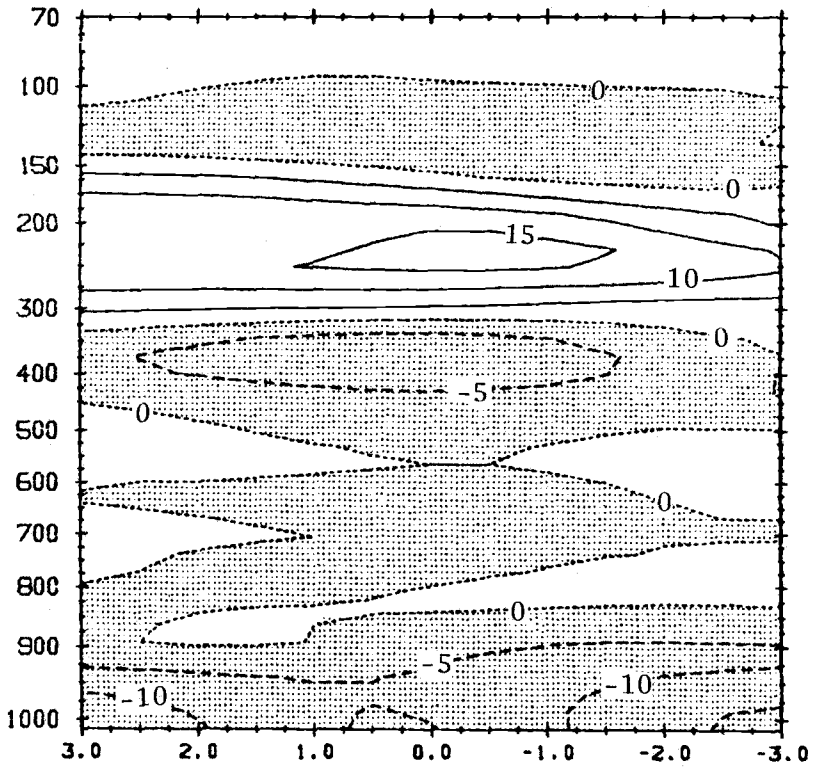

DIVERGENCE 10^{-6} s^{-1}

Figure 6.9 (continued)

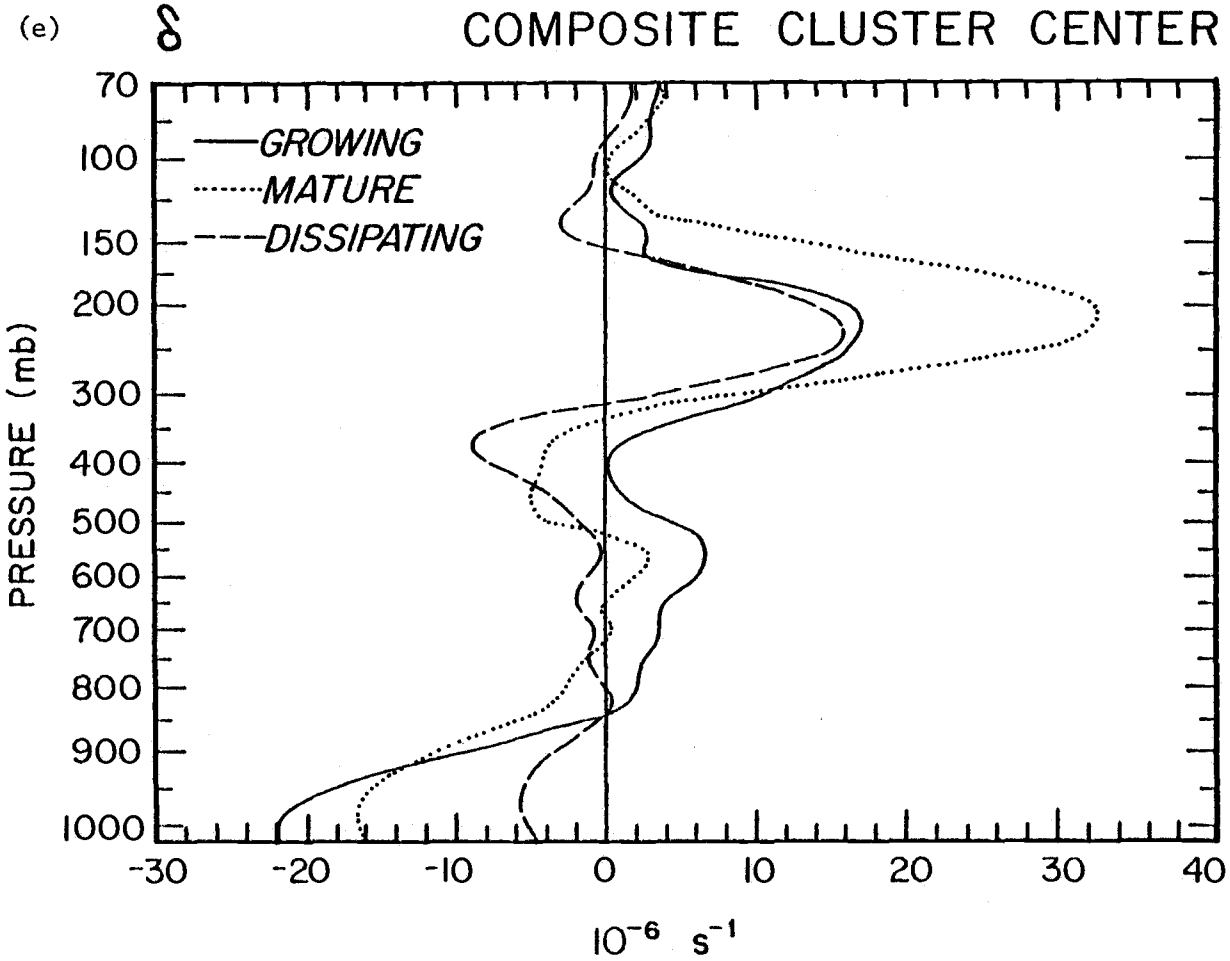

Figure 6.10. Composited vertical profiles of horizontal divergence (δ) at the cluster center.

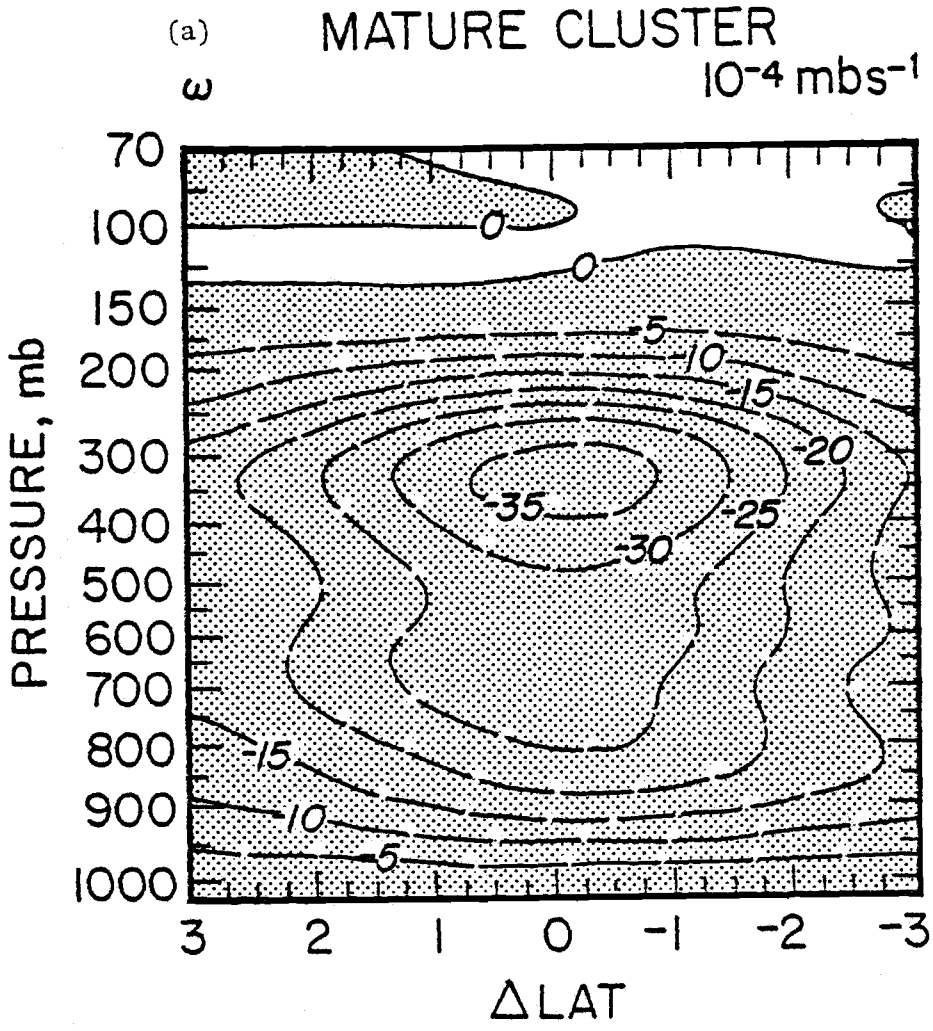

Figure 6.11. As in Fig. 6.3 except for the vertical velocity (ω).

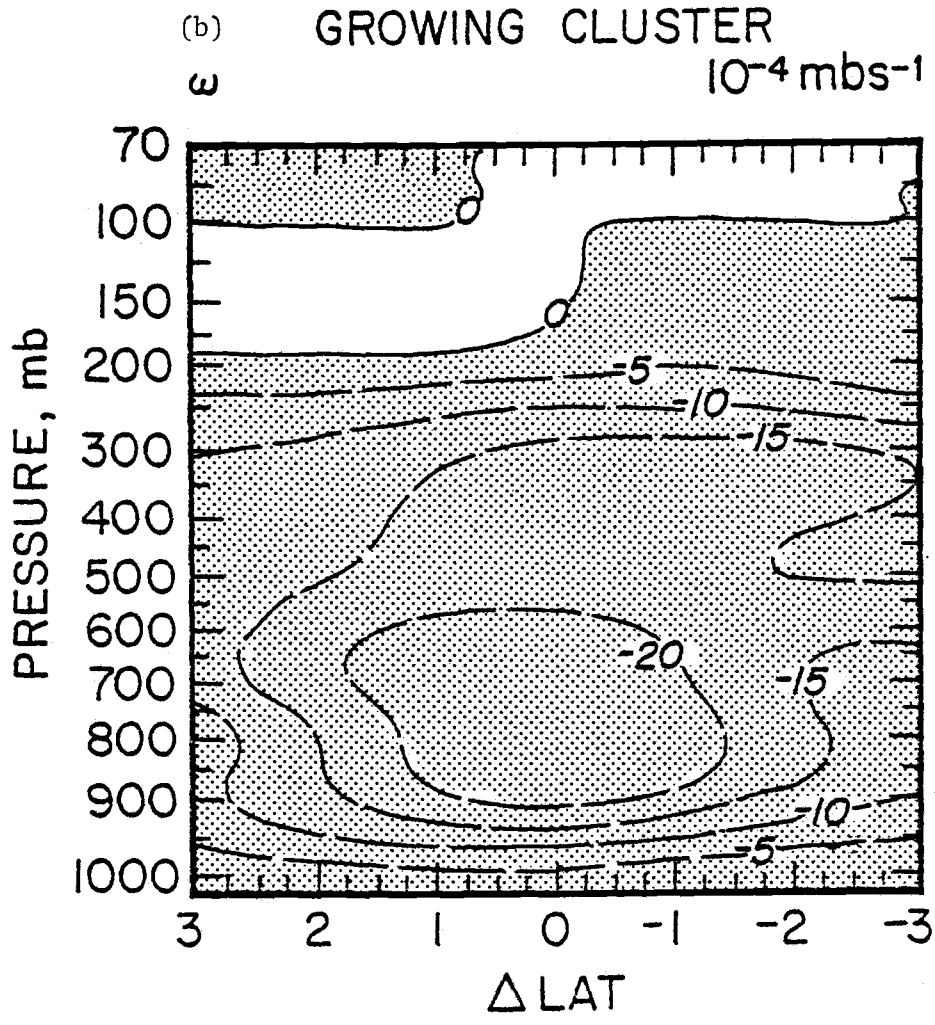

Figure 6.11 (continued)

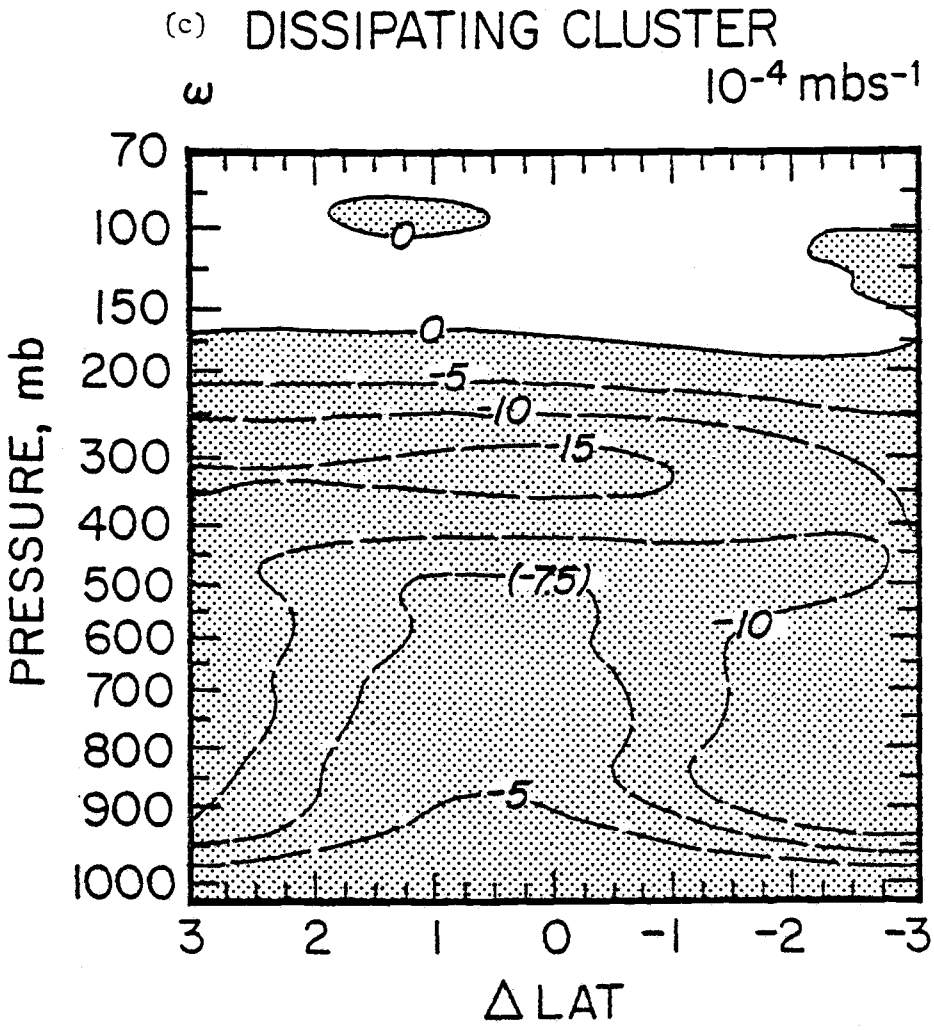

Figure 6.11 (continued)

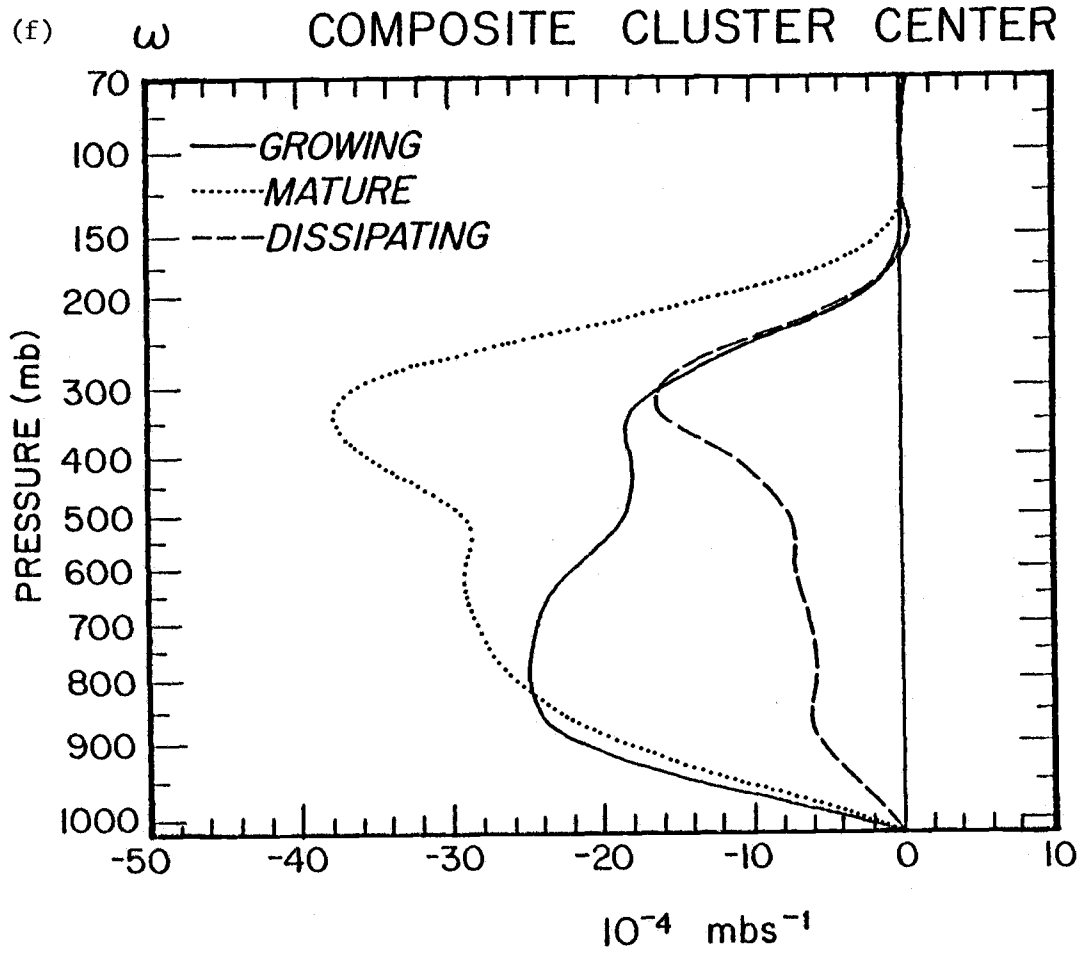

Figure 6.12. Composited vertical profiles of vertical velocity in pressure coordinates (ω) at the cluster center.

LH, Gamache and Houze (1982), and others. If so, then it may be these regions of downdrafts that cause the average velocities to be less strongly upward than the velocities in the region surrounding the cluster or even than the overall average upward velocity in the A/B array during Phase 3.

The meridional sections of relative vorticity on Fig. 6.13 are dominated by two features: The strong positive maximum near 625 mb north of the cluster center and the strong center of negative vorticity south of the cluster center near 225 mb. During all three stages the positive center, which is an easterly wave feature, remains very nearly the same, with a magnitude that is about the same as that found at this level in the trough of composited easterly waves (cf. Thompson et al., 1979). The negative center at 225 mb intensifies during the lifetime of the clusters, reaching a maximum negative value during the mature phase. It is actually part of a vorticity couplet which develops at this level. The next chapter contains a thorough examination of this interesting feature. The couplet formation seems to be in addition to a general decrease in vorticity at this level and up to 125 mb. At the surface, a maximum in cyclonic vorticity develops in the mature stage, a maximum which is also partially discernible in the growing stage (see also Fig. 6.14).

The relatively large values of cyclonic vorticity and convergence near the surface at the center of the cluster suggest the possibility that frictionally-induced inflow might be partly responsible for the development and/or maintenance of the convection in the cluster. In the classic explanation for this "Ekman pumping," frictionally-induced inflow toward the center of the cluster and a resultant upward velocity within and above the friction layer are produced in a cyclonically-rotating vortex. Thus, there should be a close relationship between near-surface convergence and vorticity in regions where this mechanism is operating. On the basis of

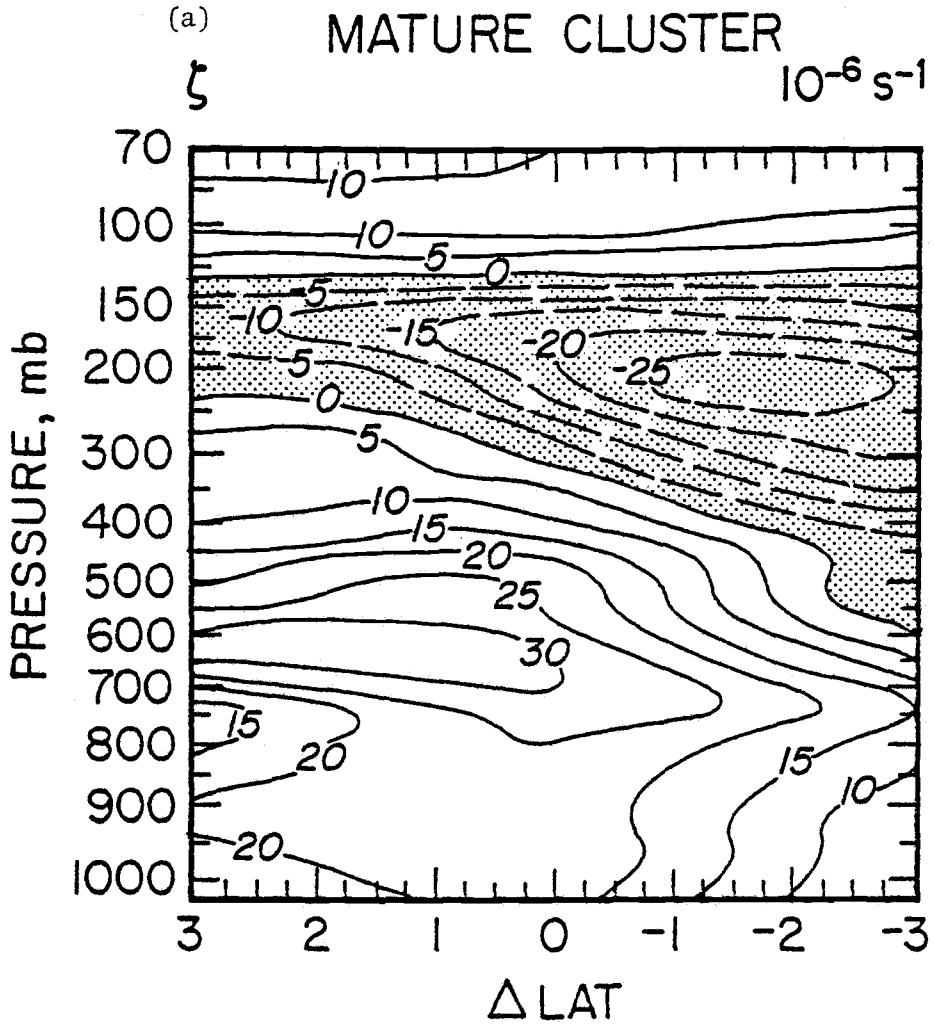

Figure 6.13. As in Fig. 6.3 except for the vertical component of the relative vorticity (ζ).

(b) GROWING CLUSTER

(c) DISSIPATING CLUSTER

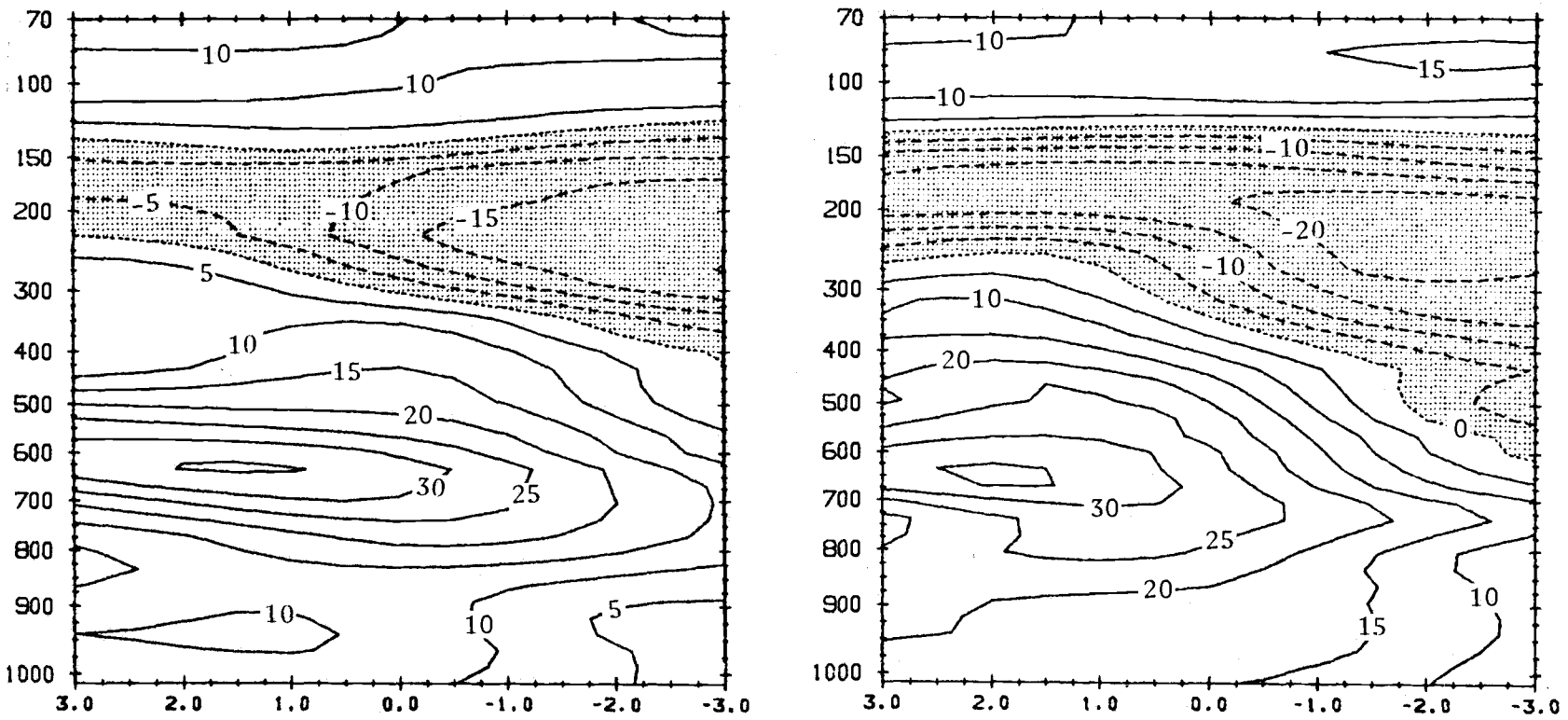

RELATIVE VORTICITY 10^{-6} s^{-1}

Figure 6.13 (continued)

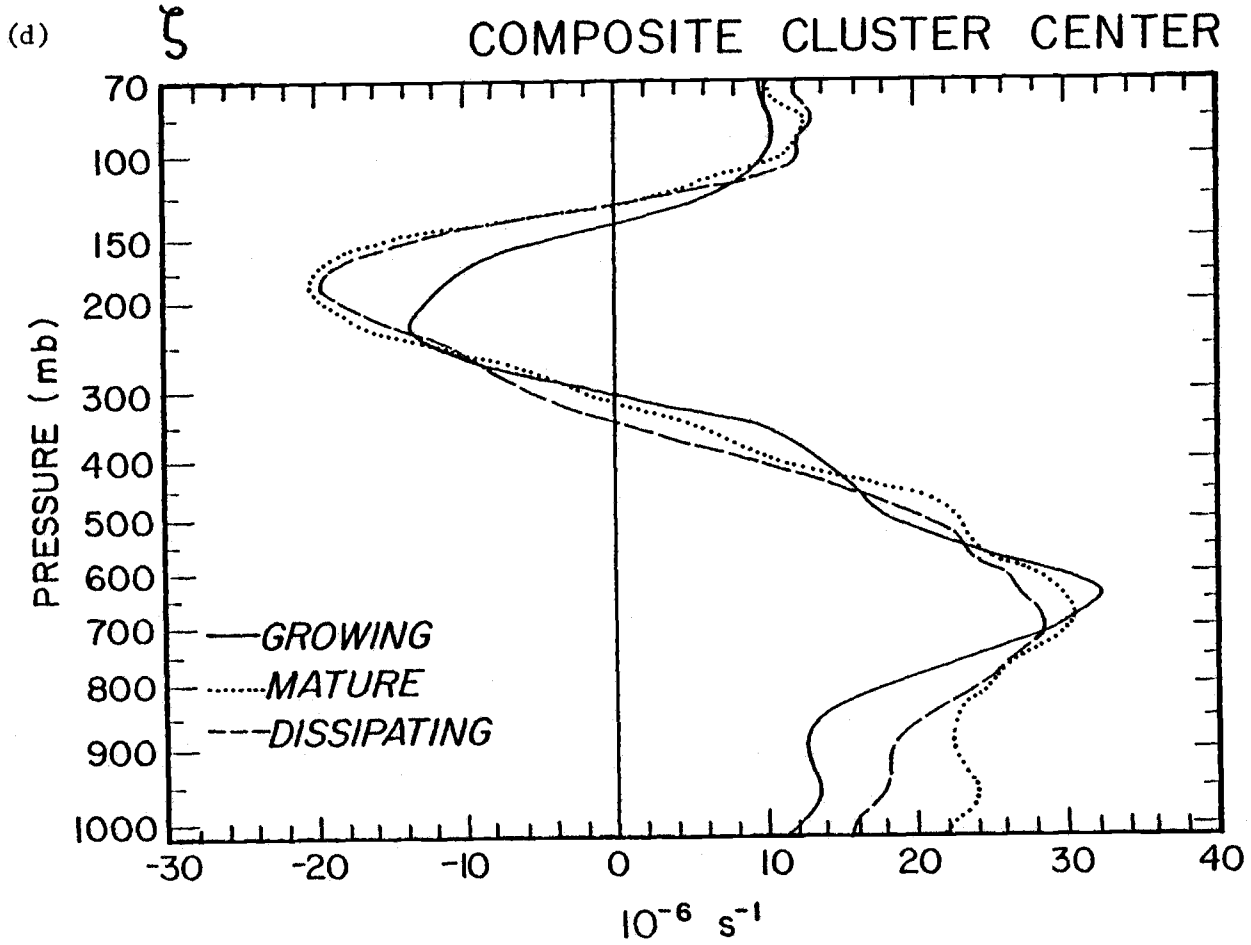

Figure 6.14. Composited vertical profiles of relative vorticity (ζ) at the cluster center.

their analyses of divergence and vorticity fields, which do not show a good correlation between vorticity and convergence near the surface, McBride and Gray (1980b) and Chen and Ogura (1982) conclude that this mechanism cannot be an important source for disturbances in the GATE area. The fact that their analyses are at a somewhat larger scale than those of the analysis presented here could be the reason for the discrepancy between their results and the relatively good correlation evident on Fig. 6.15.

However, the qualitative agreement between the observations on Fig. 6.15 and the classic description of a frictional convergence mechanism for convective development does not guarantee that such a mechanism can quantitatively explain the upward velocities in clusters. With the composited wind observations described in this chapter, it is possible to make a rough estimate of the percentage of the upward motion near the top of the friction layer that can be explained by Ekman pumping. The frictionally-induced vertical velocity (w_D) at this level can be calculated from the relation

$$w_D = \zeta_g (K/2f)^{1/2} \qquad (6.1)$$

from Holton (1972; p. 89). In (6.1), K is the kinematic viscosity, ζ_g is the geostrophic vorticity (that is, the curl of the geostrophic wind), and f is, as before, the coriolis parameter. In the tropics, the wind is more nearly in gradient balance than in geostrophic balance. Considering the surface-layer cluster circulation to be adequately approximated as a cyclonic vortex and assuming that the tangential wind (V_T) is in gradient balance allows the geostrophic tangential wind V_{Tg} (and the geostrophic vorticity ζ_g) to be estimated from observed values of the cluster radius (R) and the tangential wind at this radius. The composited winds in the lowest 100 mb of the mature stage cluster suggest that V_T at a radius of 250 km is $\sim$2 ms^{-1}, which gives an estimate of ζ_g near the cluster

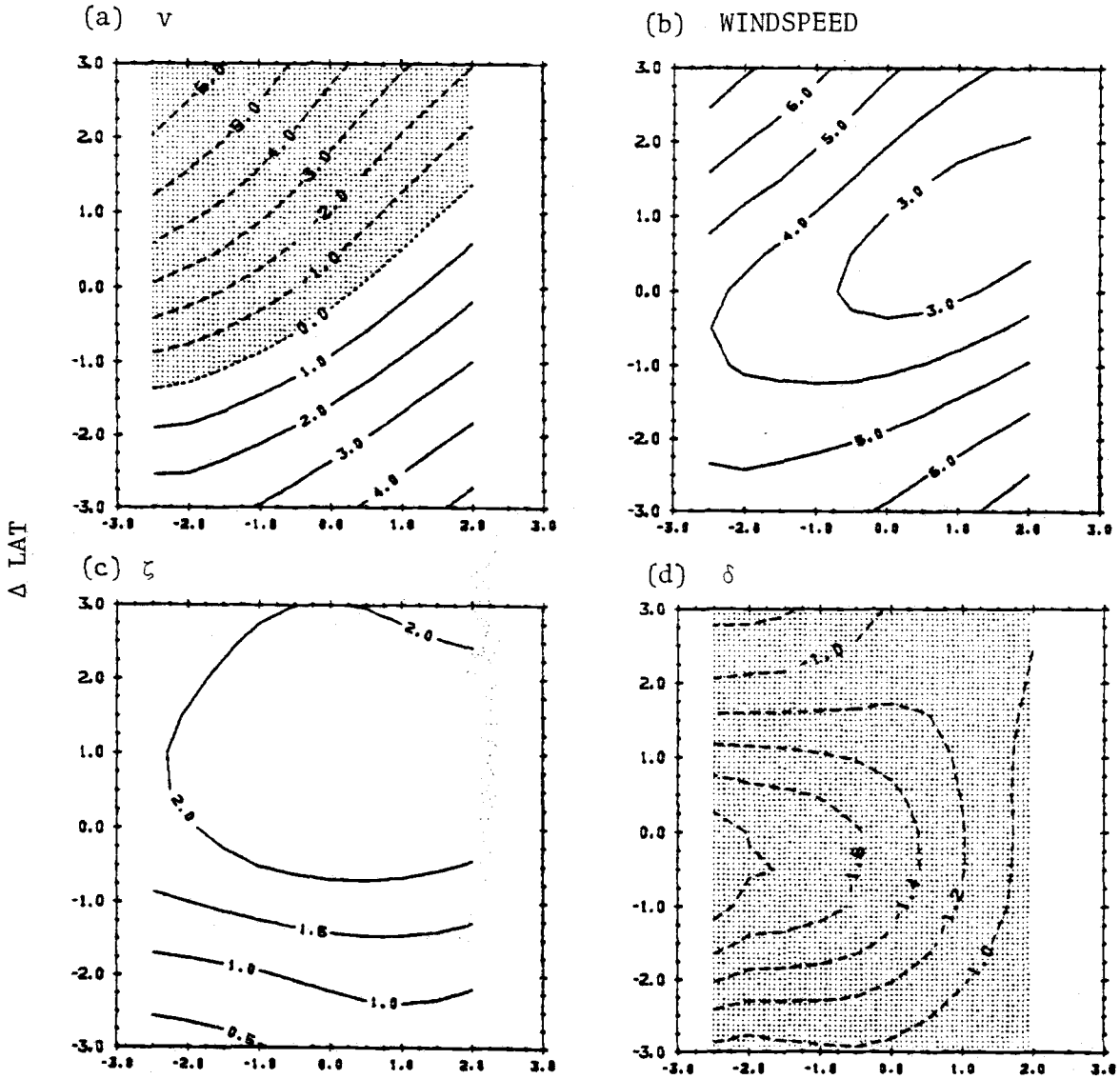

MATURE CLUSTER 945 mb

Figure 6.15. 945 mb fields of: (a) v, in ms^{-1}; (b) windspeed, in ms^{-1}; (c) ζ, in 10^{-5} s^{-1}; and (d) δ, in 10^{-5} s^{-1}. Stippled areas are negative. Axes labels are as in Fig. 6.2.

center of 2×10^{-5} s^{-1}. Substituting this value, a value for K of 5 $(ms)^2$ (suggested by Holton, 1972), and a value for f appropriate for 8.5°N (2×10^{-5} s^{-1}) into (6.1) gives a value for w_D at 900 mb of -7×10^{-4} mbs^{-1}, which is about a third of the observed value (Fig. 6.12). On the basis of this rough estimate, then, it would appear that Ekman pumping is of secondary importance to these clusters.

The meridional sections of kinematic fields just described suggest another intriguing possibility concerning the development of these clusters. As noted previously, surface convergence tends to be situated near the center of the cluster in all stages of the cluster life cycle. The zero-contour of meridional velocity, on the other hand, migrates northward through the center of surface convergence during the cluster lifetime. As a result, during the growing stage the air converging beneath the cluster had its source to the north of the cluster, while in the dissipating stage the source of the surface air is primarily to the south. Returning for a moment to the case study of the 5 September clusters, Table 6.2 shows that the equivalent potential temperature[3] near the top of the atmospheric mixed layer is almost 3 degrees higher to the north of the cluster than it is south of the cluster. Furthermore, in the growing and mature stages of cluster development at 8.5°N (which is near the center of the cluster) the mixed-layer values of θ_e are close to values found to the north, while in the dissipating stage θ_e is more nearly equal to the smaller values found

---

[3]Equivalent potential temperature (θ_e) is the temperature that an air parcel would have if it were lifted adiabatically until its saturation point was reached, then lifted pseudoadiabatically until all of its water vapor was condensed out, and finally returned adiabatically to 1000 mb. It thus gives a measure of the parcel's total thermodynamic energy. It is approximately conserved during typical atmospheric processes (excluding the evaporation of raindrops).

Table 6.2 Equivalent potential temperature (θ_e) in °K during the life cycle of the 5 September cluster. All values are at 945 mb along a meridional section through the cluster center (25°W).

STAGE TIME (GMT)	12°N	8.5°N	5°N
GROWING 0900	343.4	342.1	339.3
MATURE 1500	342.5	341.7	339.2
DISSIP. 2100	345.0	340.9	340.5

to the south. It thus appears that the cluster develops during the time when it is being fed energy-rich air from the north and then dissipates when the source of air changes to the less conducive surface air mass to the south.

The question still remains, of course, as to why the surface convergence at the cluster center develops where and when it does. In his discussion of convective systems in GATE, Marks (1980) speculates that the surface southerly flow during and just previous to the passage of an easterly wave trough enhanced the convergence within the monsoon trough region, leading to cluster development. Along a similar vein, Chen and Ogura (1982) suggest that disturbances in the GATE area developed in response to a superposition of the equatorial confluence air flow and the circulation induced by easterly waves. Neither of these suggestions, however, can explain why the resulting convection should be organized into clusters or other mesoscale systems.

Both of these hypotheses, if correct, require a close relationship between clusters and the monsoon convergence (or ITCZ) region. The monsoon confluence line at the surface within the GATE ship array is typically oriented from southwest to northeast. As the 945 mb plots in Figs. 6.15a and 6.15b show, there is a similar orientation in the cluster composite fields of meridional velocity and windspeed examined in this chapter. In addition, the monsoon confluence line tended to pass through or very close to the centers of the clusters included in the composite set. Thus, these cluster composite results appear to corroborate the finding that cluster-related convection is intimately related to monsoon-related convection. The difficulty that this relationship presents to the diagnosis of cluster fields and the interpretation of the physical processes that effect them has already been discussed in Chapter 2.

6.3 Composite vorticity budget terms

The series of vertical profiles of vorticity budget terms in Figs. 6.16–6.18 describe the development of vorticity at the center of the composite cluster over its life cycle. As Fig. 6.17 shows, the primary balance during the mature stage, when the budget terms are at their largest, is between Z and the divergence term in the layer nearest the surface, and between Z and vertical advection in the layer between 300 mb and 500 mb. At both these levels $\partial\zeta/\partial t$ is relatively small, as are horizontal advection and twisting.

In the boundary layer there is an increase in cyclonic vorticity in the growing stage, little change during cluster maturity, and a decrease in the dissipating stage. Thus there seems to be a production of low-level vorticity associated with the cluster in the lower troposphere. The term apparently producing that vorticity is the divergence term, which is opposed by Z. In the mature stage, the production by divergence is almost completely compensated by Z, leaving a small local change. The decrease in vorticity during cluster dissipation is a result of Z.

Vorticity changes and the budget terms in general tend to be small and inconclusive in terms of structure between 750 mb and 500 mb. The increase in vorticity with time at 450 mb seems to be due to small contributions from several terms, the largest of these being horizontal advection and Z.

Between 300 and 450 mb in the mature and dissipating stages, large values of vertical advection and Z act to very nearly compensate each other, leading to little or no vorticity production. This level is within the cluster anvil, suggesting that there is perhaps an induced anvil-scale circulation that offsets the sub-anvil-scale production. At slightly higher levels, the production by vertical advection, which is still large, is partly compensated

Figure 6.16. Vertical profiles of composited vorticity budget terms at the cluster center during the growing stage. In (a), the solid line is the local change term, the dotted line is horizontal advection, and the dashed line is Z. In (b), the solid line is vertical advection, the dotted line is the divergence term, and the dashed line is twisting.

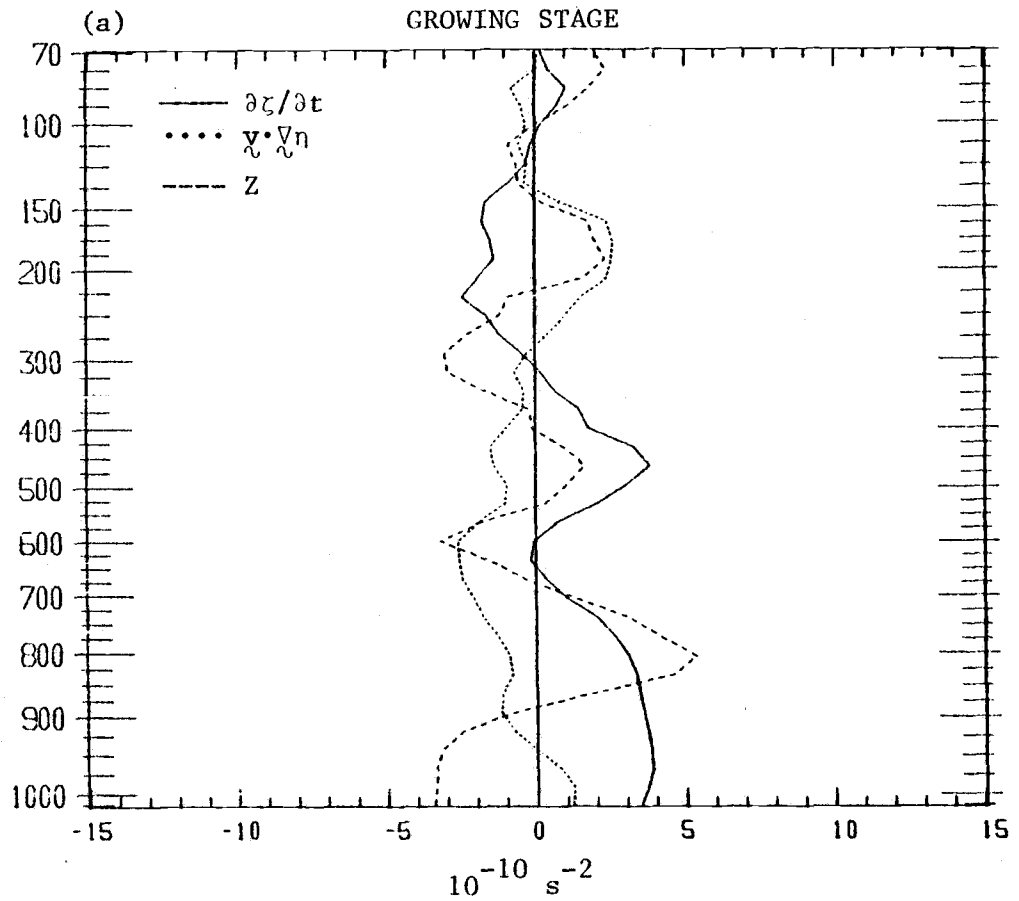

Figure 6.16 (continued)

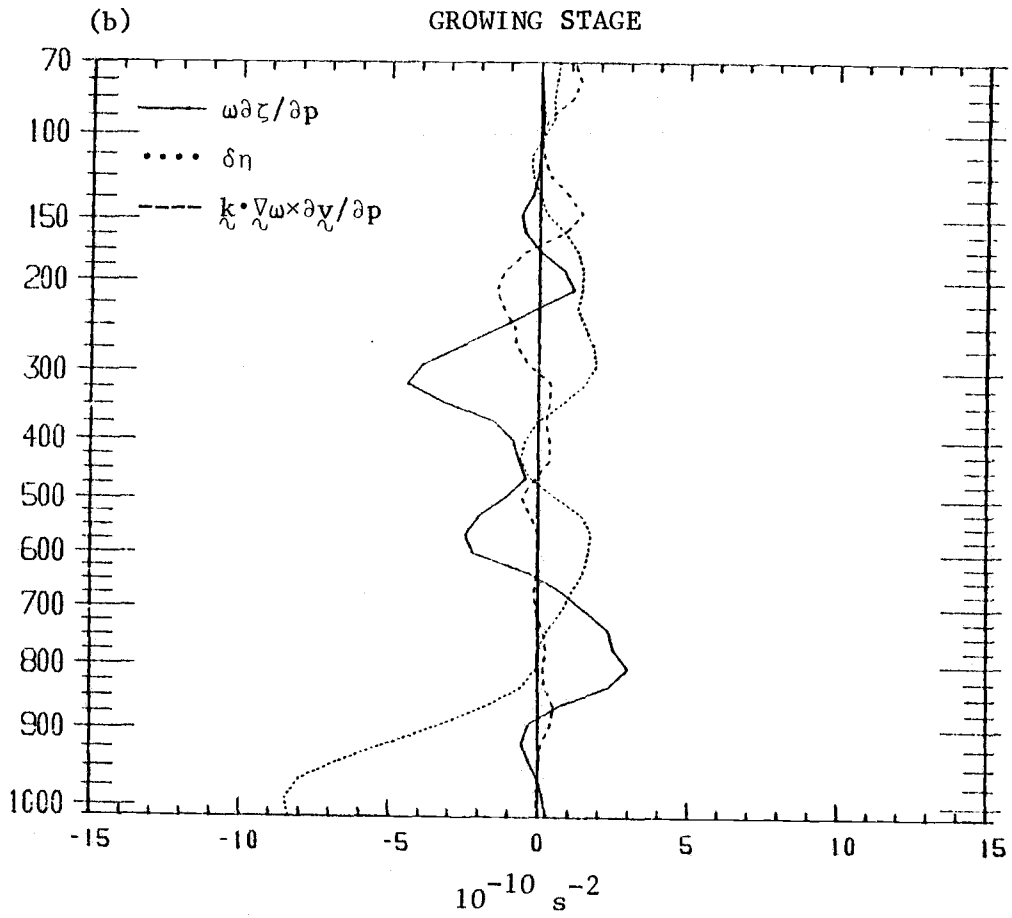

Figure 6.16 (continued)

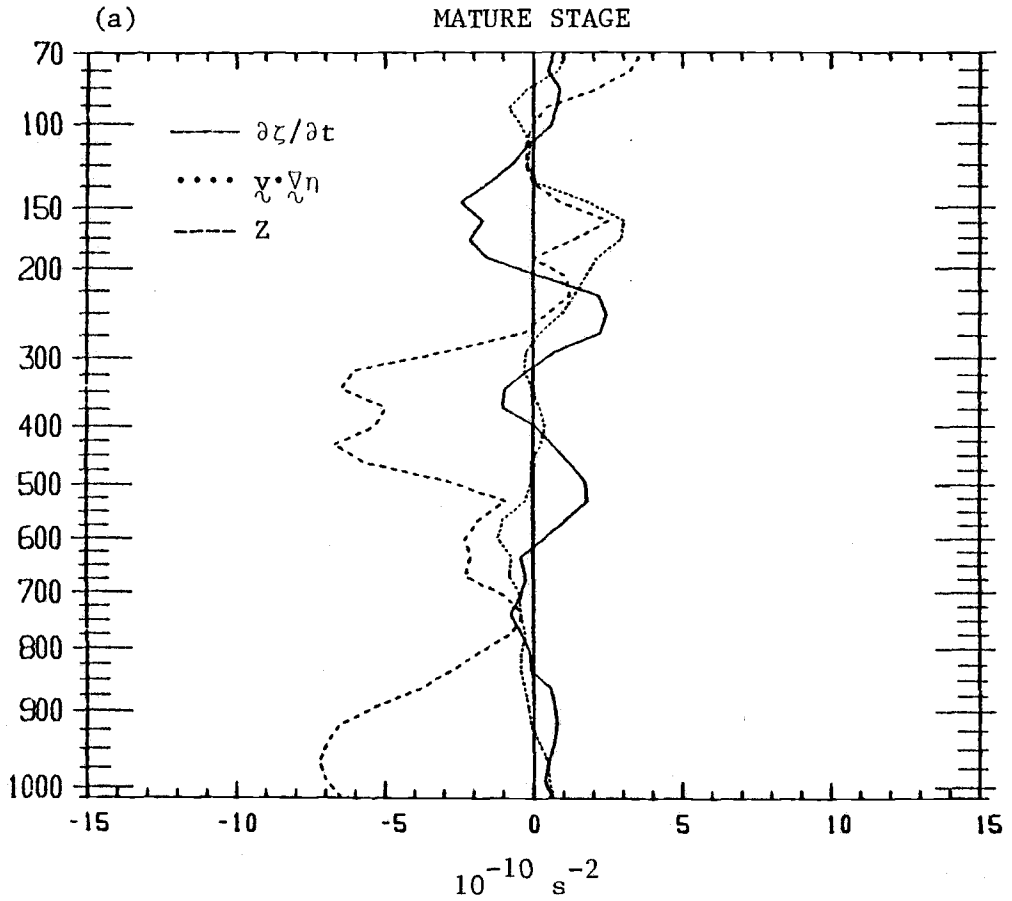

Figure 6.17. As in Fig. 6.16 except for the mature stage.

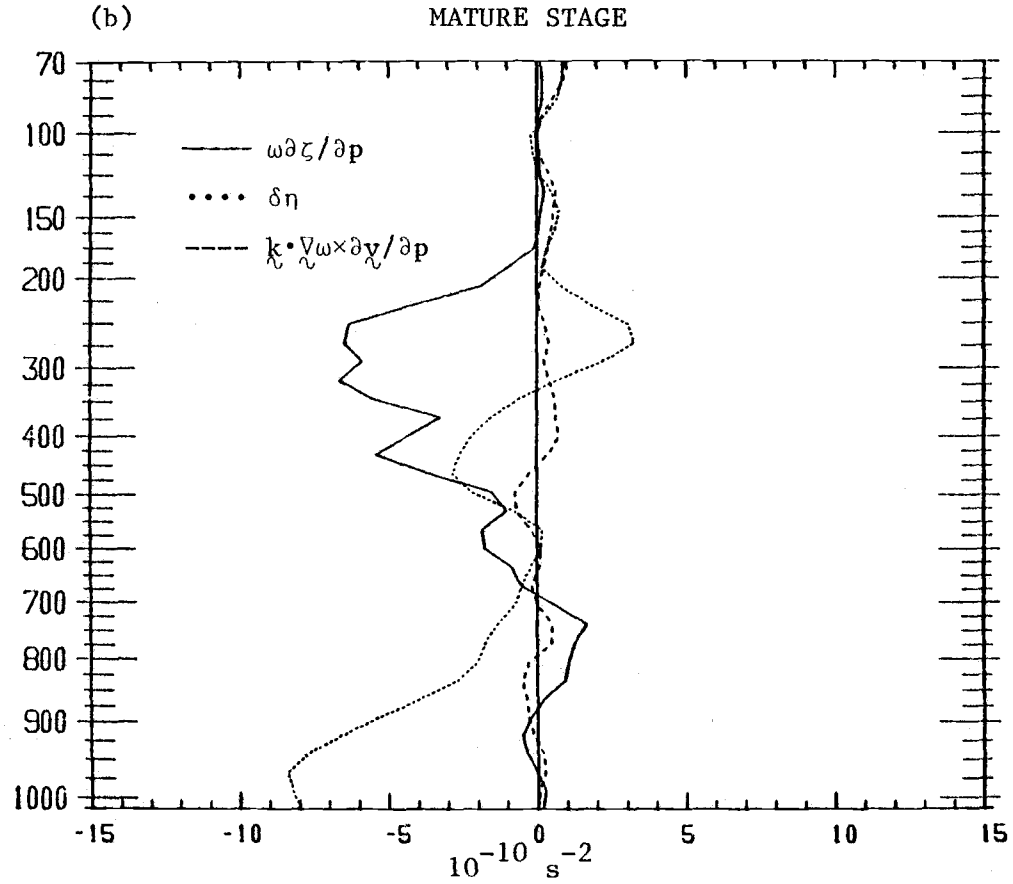

Figure 6.17 (continued)

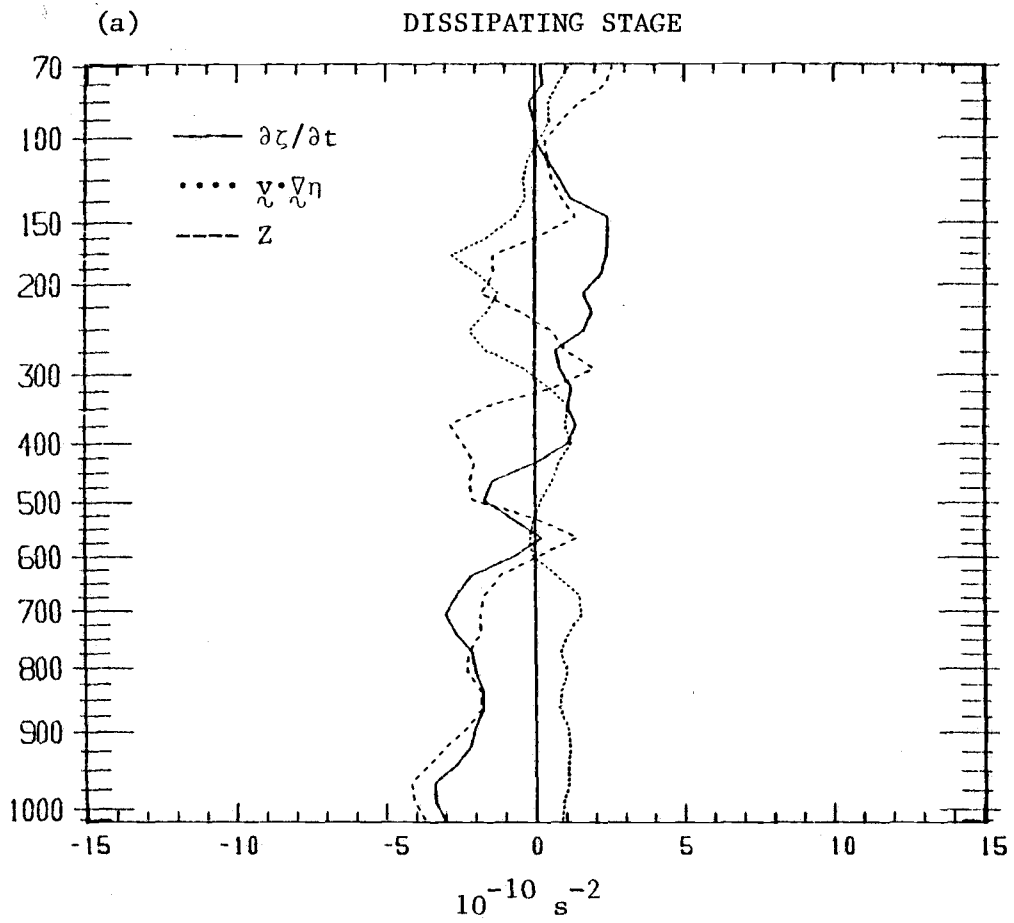

Figure 6.18. As in Fig. 6.16 except for the dissipating stage.

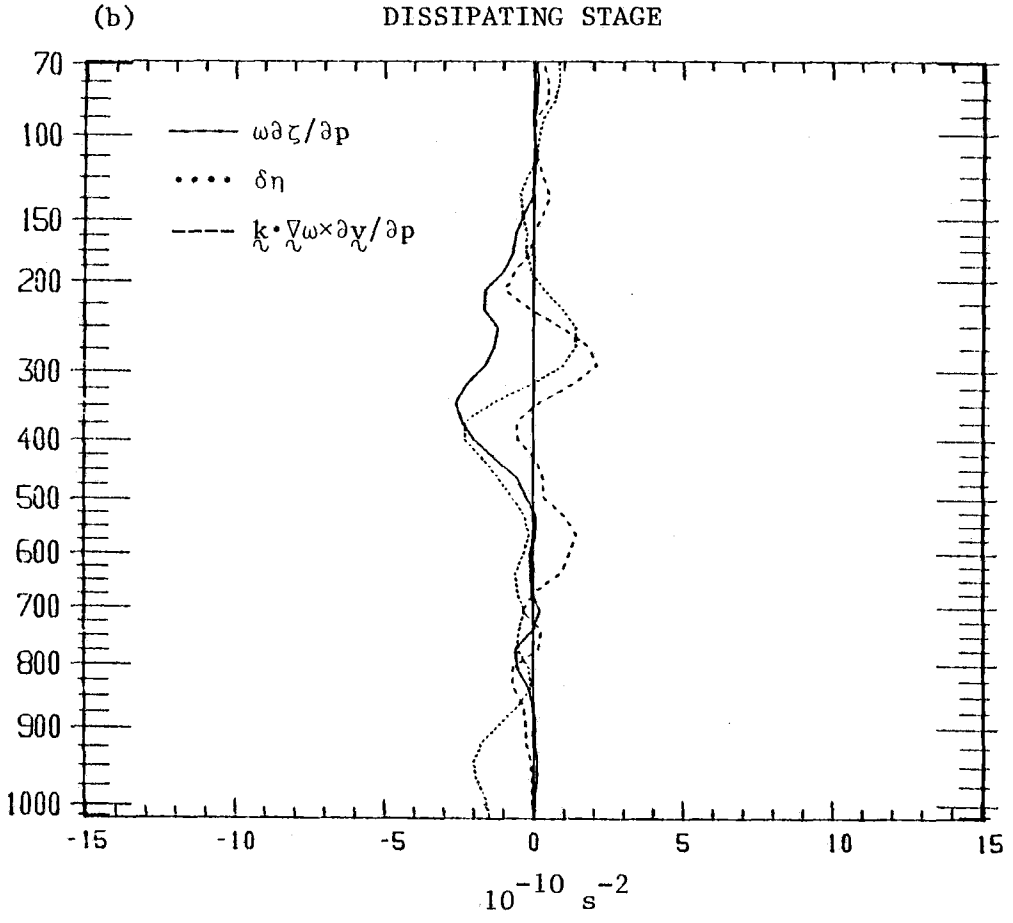

Figure 6.18 (continued)

by the divergence effect, which in this outflow layer is tending to produce anticyclonic motion.

6.4 Comparison with case studies

Several of the findings based on the composite study of this chapter have already been noted in the case studies of Chapter 5. For instance, maxima in the vertical velocity profiles are found at two levels in both the composite results and the case studies. Early in the life cycles of the clusters, a low-level maximum develops near 800 mb. During the mature and dissipating stages another maximum of upward vertical velocity develops within the cluster anvils. These changes in the vertical velocity profiles reflect the large boundary-layer convergence in both the case studies and the composite during the growing and mature stages and the large upper-tropospheric divergence that develops in the mature and dissipating stages.

The strongest features of the vorticity fields in the individual clusters seem also to have been captured by the composites. The overall vertical structure, with large positive values near 700 mb and large negative values near the tropopause, is the same in both. Similar mechanisms (as given by terms of the vorticity budget) contribute to the vorticity changes in the case studies and the composite. In the boundary layer, for instance, vortex stretching by the large-scale convergence is the predominant effect, while within the middle levels of the cluster anvils vertical advection of vorticity is important. Small-scale vorticity production is evidently very important in the case studies, and these effects remain large and coherent in the composite study as well. As given by Z, these small-scale effects are pronounced in the boundary layer, where they act as a sink of positive vorticity, and at mid-anvil levels, where they act to compensate the vertical advection of large-scale vorticity.

In the following chapter, horizontal variations of vorticity in the upper levels of cluster anvils will be investigated. The wind fields and vorticity budget terms at this level in the case studies will also be found to be quite similar to the corresponding composite fields.

CHAPTER 7. UPPER-TROPOSPHERIC CIRCULATIONS

7.1 General description

In the large volume of work to come out of GATE pertaining to cloud clusters, a particular area of interest has been the flow in the large, deep, anvil-like clouds found in the upper-tropospheric portion of clusters. Several investigators have speculated that these anvils have a circulation of their own, a circulation which is affected by but still distinct from the circulations of the individual clouds that rise into the anvils from below (Houze, 1977; Zipser, 1977; Brown, 1979; Gamache and Houze, 1982).

This chapter examines the upper level winds associated with GATE clusters with the purpose of investigating anvil circulations. In particular, a large asymmetric vorticity couplet near 225 mb is found to be a common and striking feature of the clusters observed during Phase 3 of GATE (Fig. 7.1). In order to determine the origin of these couplets a vorticity budget is computed for an individual case (the double cluster on 5 September) in Section 7.2. For further investigation of this feature the winds, vorticity, and vorticity budget terms are composited for several slow-moving clusters (Section 7.3).

7.2 The 5 September clusters

The vorticity couplet which developed in the upper troposphere on 5 September was one of the largest in magnitude observed during GATE and one of the most prominent features in the vorticity field at any level. As Fig. 7.1 shows, the couplet consists of a negative relative vorticity center to the south which is larger in magnitude than the positive center to the north. Both centers occur near an anvil boundary. If absolute vorticity were plotted in place of ζ, the vorticity centers would be approximately equal

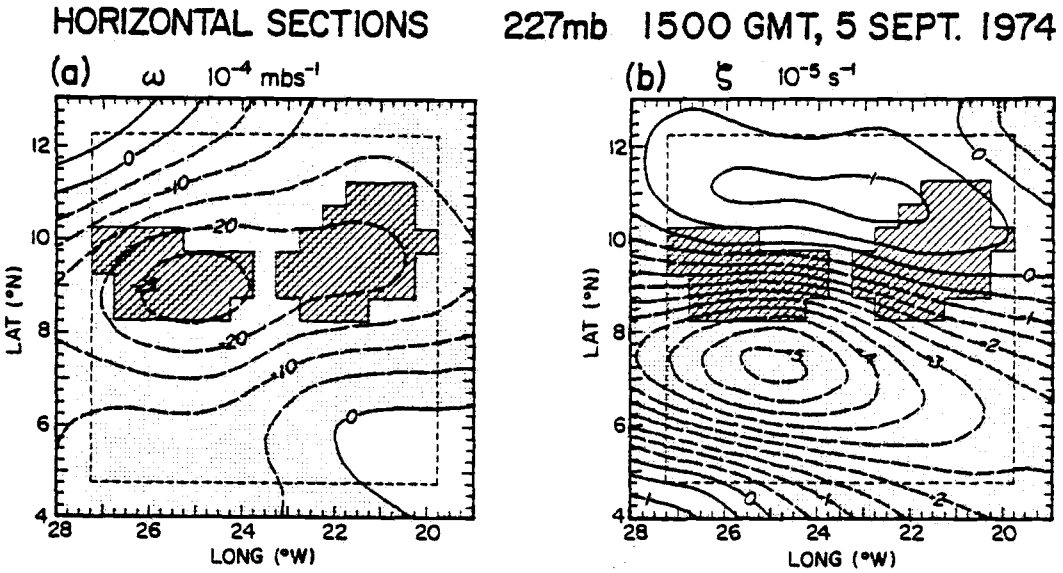

Figure 7.1. Horizontal fields at 227 mb of (a) vertical velocity (ω) and (b) relative vorticity (ζ) over the GATE array for 1500 GMT, 5 September 1974. Stippled areas have negative values. Hatched regions indicate locations of anvil (see text for explanation). Inner dashed box shows extent of cloudtop data.

in magnitude, with the zero contour running through the center of the west anvil. The asymmetry in ζ with respect to the cluster anvils is in marked contrast to the pattern of vertical velocity shown in Fig. 7.1a, where a local minimum in ω is essentially centered on the western anvil.

A sequence of meridional sections through the center of the west cluster is shown in Fig. 7.2. The solid bars on the latitudinal axes indicate regions where the anvil index is 1. Since there was a persistent easterly wind maximum in the upper troposphere near the equator during Phase 3, part of the north-south gradient of ζ on these sections is a "background" feature which results from an increase in $-\partial u/\partial y$ as the wind maximum is approached from the north. However, most of the couplet development occurs concurrently with the cluster development. The greatest change in ζ occurs at the center of negative ζ (7.5°N and 225 mb). Between 0600 GMT and 1500 GMT, when the anvil area reaches its greatest extent, ζ decreases from -3×10^{-5} s^{-1} to -5×10^{-5} s^{-1}. Thereafter, ζ begins to increase again as the anvil progressively breaks up. The vorticity at 270 mb near 8.5°N, on the other hand, changes relatively little during the same period.

The couplet extends in depth from approximately 275 mb to 175 mb. Above this layer there is a general increase in anticyclonic vorticity across the cluster during its lifetime, and below there is a general increase in cyclonic vorticity. Using satellite radiation data, Sikdar and Hentz (1980) approximate the height of the anvil top on this day to be 200 mb, with individual cumulonimbus towers reaching 150 mb. Diagnosing mass flux in cumulus updrafts in the trough of a composite easterly wave, Johnson (1980) finds a relative maximum in detrainment in the layer between 350 mb and 200 mb. Thus, the couplet appears to develop at a level where clouds are, in the mean, detraining.

We can investigate the physical mechanisms that generate this couplet by computing the large-scale terms in the vorticity budget

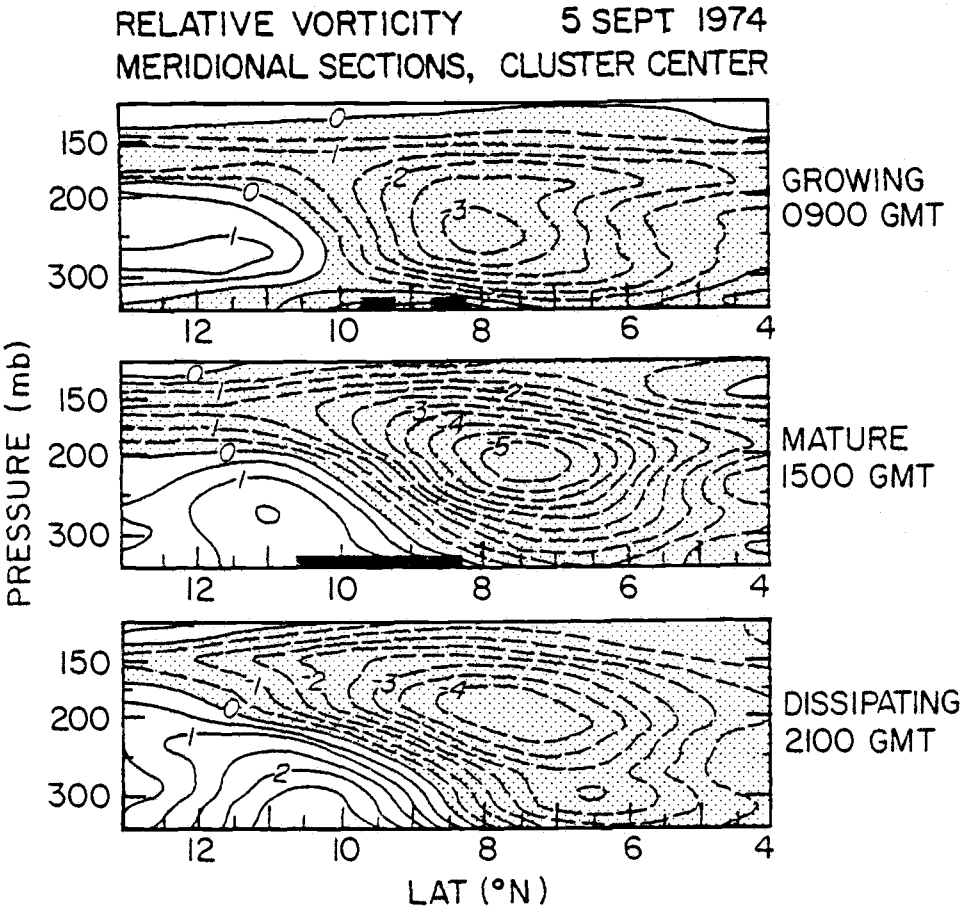

Figure 7.2. Meridional cross-sections of upper-tropospheric relative vorticity during life cycle of the western cluster on 5 September 1974. All sections are made along 25°W. Solid horizontal bars along the latitudinal axes show locations where the anvil index is 1. Units are 10^{-5} s^{-1}.

equation (4.2). In Figs. 7.3-7.5 the budget terms at 227 mb are presented for, respectively, the growing, mature, and dissipating stages of the westernmost cluster (whose anvil appears as the hatched region in the left half of each figure). The local change term in the growing stage shows the development of a vorticity couplet, with a vorticity increase to the north and a decrease to the south of the cluster. Of the remaining terms, the only ones significantly large near the west cluster are Z and horizontal advection, and of these two only Z has the asymmetric pattern of the local change. The terms involving vertical velocity are relatively small during this stage.

By the mature stage all budget terms contribute significantly to the balance. The latitudinal gradient of $\partial\zeta/\partial t$ has lessened near the west cluster, indicating that the vorticity couplet here is near its maximum intensity. In three of the terms, however, the asymmetric pattern of ζ is still clearly reflected. The residual and the twisting term both act to maintain the couplet, while the divergence term acts to destroy it. The asymmetry of the divergence term results from a uniformly divergent field acting on an asymmetric absolute vorticity field. As the plot of horizontal advection shows, the 227 mb flow is advecting the negative center southwestward and the positive center northwestward. The only term that is axially symmetric is vertical advection, which is increasing the vorticity values at this level since ζ decreases with height in the vicinity of the cluster.

At 2100 GMT (Fig. 7.5), in the dissipating stage of the western cluster, the breakdown of the vorticity couplet seen in the local change term appears to be a result of divergence and horizontal advection. The maintenance provided in the mature phase by the twisting term has become small due to a decrease in $|\underset{\sim}{\nabla}\omega|$. The other maintaining term, Z, is also smaller and less clearly organized. The large positive center of horizontal advection located in the lower left part of the plot of $\underset{\sim}{v}\cdot\underset{\sim}{\nabla}\eta$ is reflected

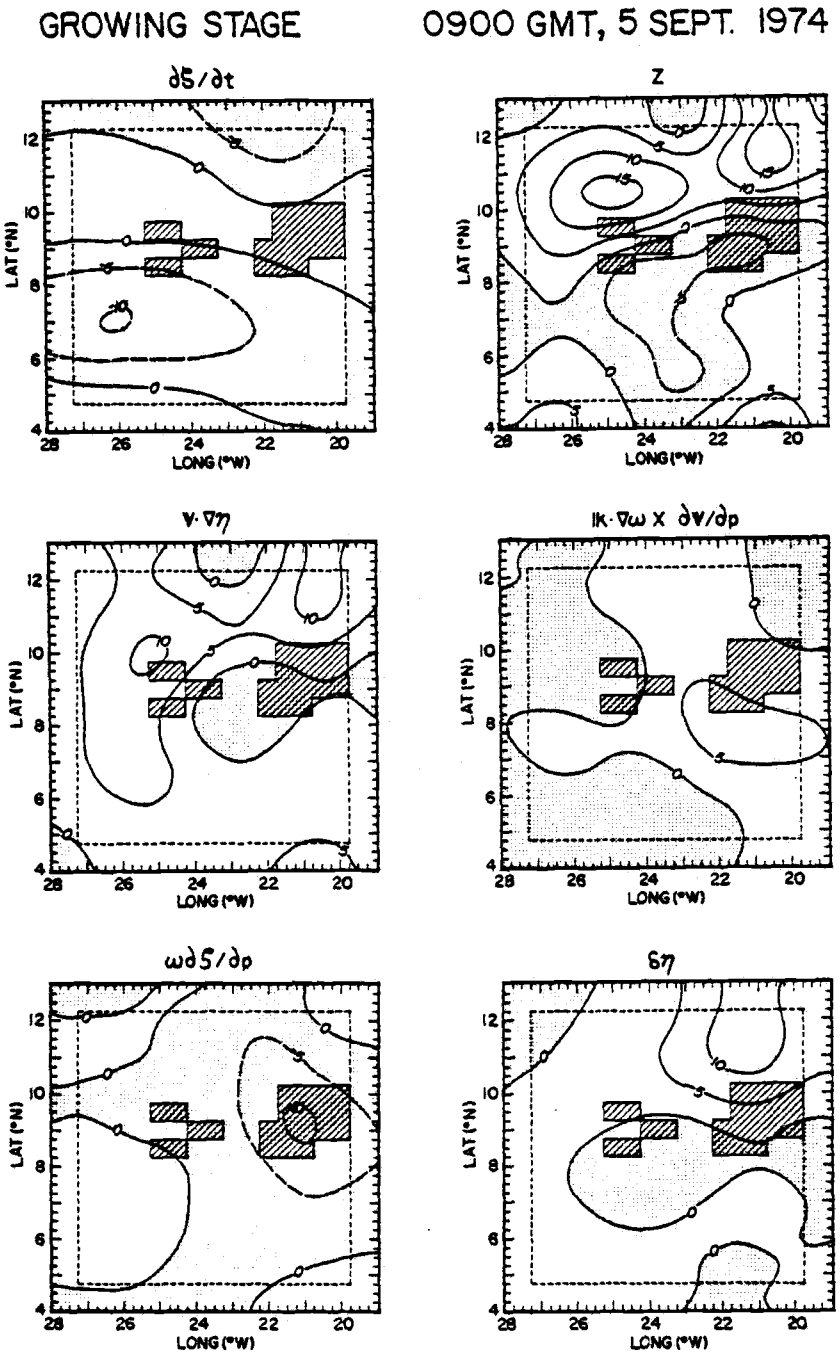

Figure 7.3. As in Fig. 7.1 except for vorticity budget terms at 227 mb at 0900 GMT during the western cluster's growing stage. Units are 10^{-10} s^{-2}.

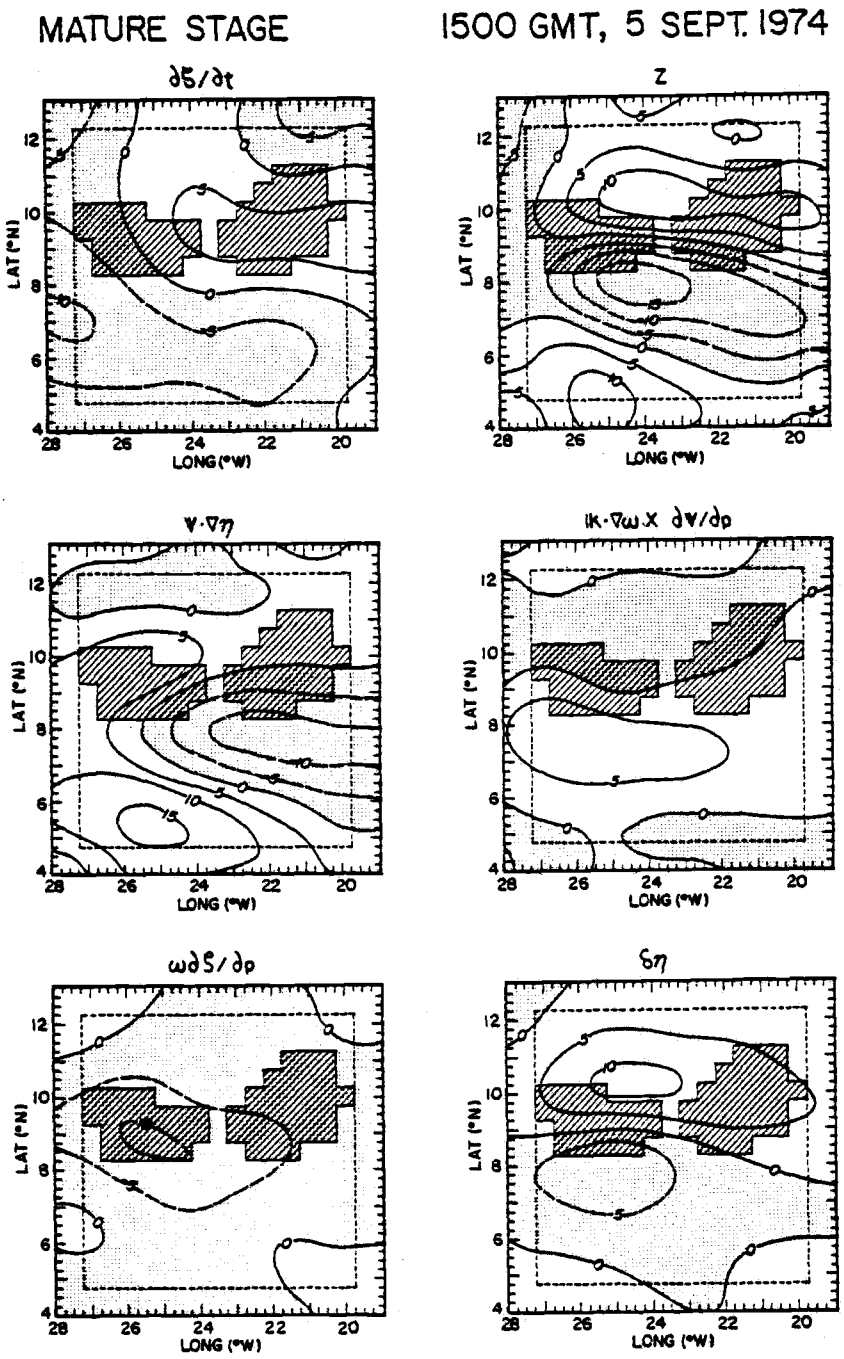

Figure 7.4. As in Fig. 7.1 except for vorticity budget terms at 227 mb at 1500 GMT during the western cluster's mature stage. Units are 10^{-10} s^{-2}.

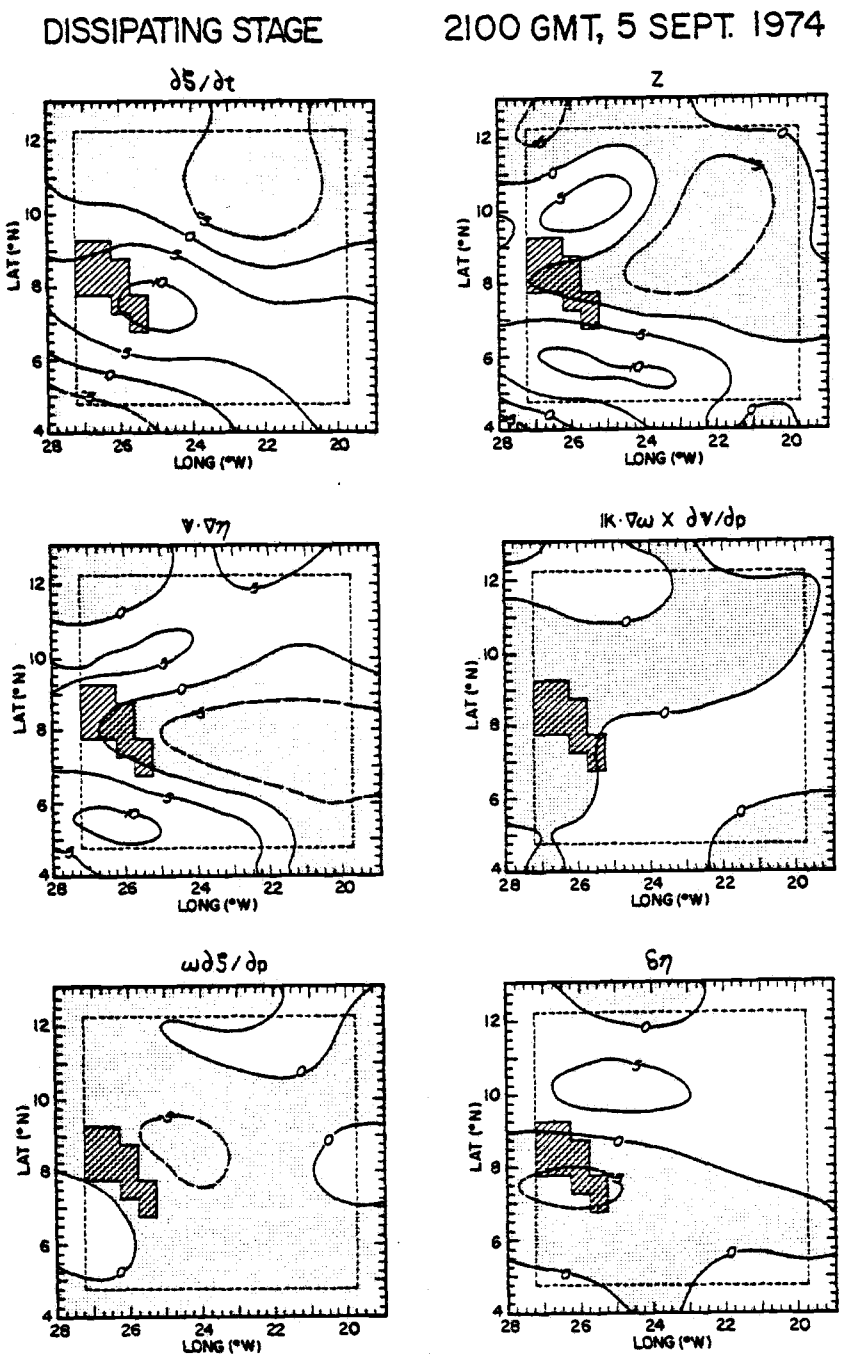

Figure 7.5. As in Fig. 7.1 except for vorticity budget terms at 227 mb at 2100 GMT during the western cluster's dissipating stage. Units are 10^{-10} s^{-2}.

also in Z. Because wind fields in this region (which is southwest of the A/B array) are extrapolated rather than interpolated, the centers of $\underset{\sim}{v}\cdot\underset{\sim}{\nabla}\eta$ and Z may be due in part to observational error.

Some of the same relationships between budget terms are evident in the vicinity of the eastern cluster. Since it developed 3-5 hours earlier than the western cluster, its early mature stage corresponds roughly with the growing stage of the other cluster at 0900 GMT. Similarly, the eastern cluster was in its early dissipating stage at 1500 GMT and had essentially disappeared by 2100 GMT. In this cluster, as in the western cluster, the residual and twisting terms during maturity tend to maintain the couplet against the destructive effects of divergence, although the relationship here is not as clear.

A more detailed view of the development in time of the vorticity centers is afforded by the time series of ζ and the budget terms on Fig. 7.6. The data represented by Fig. 7.6a are located at 227 mb near the center of negative vorticity (25°W, 7.5°N); Fig. 7.6b shows the same terms near the positive center (25°W, 11°N). Stages of development of the cluster are demarked by the vertical dashed lines on the two figures.

Examining first the two time series of ζ, we see again that the couplet intensified and decayed concurrently with the large western cluster. Maximum growth at both centers occurred between 0600 GMT and 1200 GMT, both reached their maximum intensity between 1500 GMT and 1800 GMT, slightly after the maximum extent of anvil cloudiness, and both decayed quickly after 2100 GMT.

Prior to the onset of organized convection at 0300 GMT, the vorticity budget terms involving vertical velocity are small, as is Z, and an approximate barotropic balance exists between local change and horizontal advection. Chu et al. (1981) found a similar balance during undisturbed periods over the western tropical Pacific. In the early stages of the negative center's growth, when

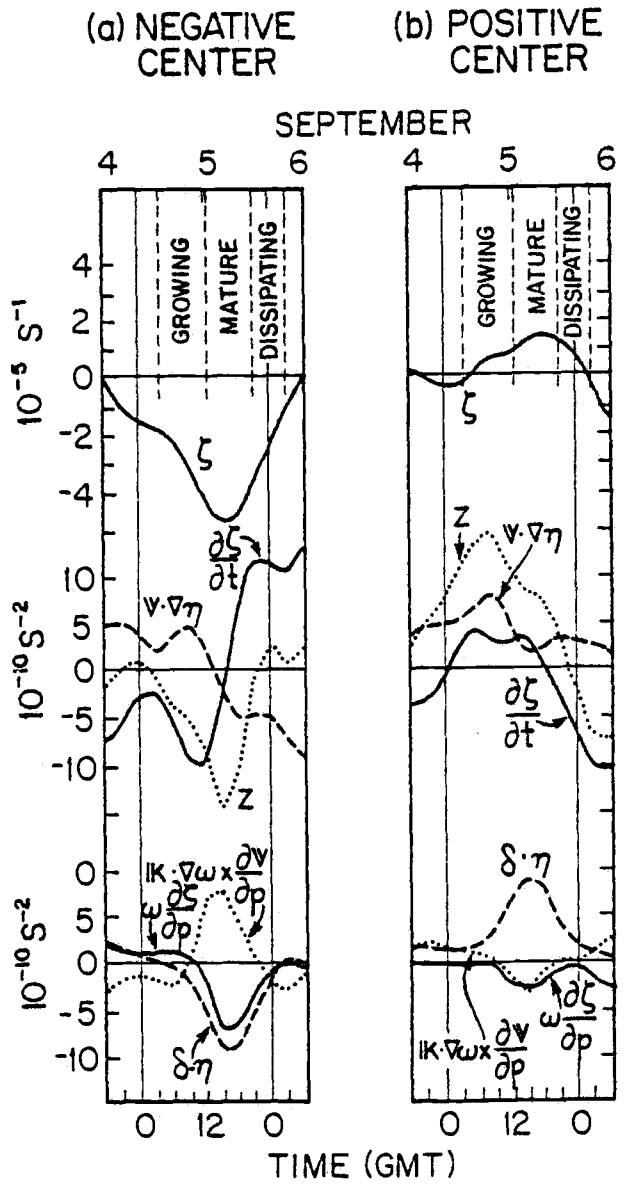

Figure 7.6. Time series of vorticity budget terms at 227 mb at the approximate locations for (a) the negative center (25°W, 7.5°N) and (b) the positive center (25°W, 11°N) of the relative vorticity couplet associated with the clusters on 5 September 1974.

deep convection exists but a large anvil has not yet formed, there is a close balance between $\partial\zeta/\partial t$ and Z. During the period when a large anvil exists the ω terms are also large, decreasing again to small values by early morning on 6 September, at which time the anvil is greatly reduced in size. The maintaining effect of Z and the twisting term during the mature stage is apparent, as is the destructive effect of the other terms. After 0600 GMT on 6 September a nearly barotropic balance again exists.

Some of the same relationships are also observed at the positive center. For instance, the residual acts to produce positive vorticity while the positive center develops and then to maintain the positive vorticity during the mature stage of the cluster. Twisting, though of lesser magnitude here, also acts to maintain the positive center against the large destructive effects of divergence. Vertical advection is a maintaining term at the positive center whereas it acts to destroy the negative vorticity center. The most noticeable difference in the budgets at the two centers is the disappearance of barotropic balance by 0000 GMT on 5 September, before the start of the cluster's growing stage. After the cluster, also, a clearly barotropic balance does not develop. The large values of Z just before and after the cluster are a result of these imbalances between $\partial\zeta/\partial t$ and $\underset{\sim}{v}\cdot\underset{\sim}{\nabla}\eta$.

Interpreting Z as the result of unresolved circulations of individual cumulonimbi or mesoscale circulations, the following is hypothesized: As the cluster intensifies, convection is acting to produce anticyclonic vorticity south of the cluster center and cyclonic vorticity north of the cluster, destroying in the process the barotropic balance of the upper-level flow. Until cluster maturity, this production outstrips the terms that oppose it and the centers intensify. After the mature phase, however, the opposing terms (primarily divergence and, in the negative center, vertical advection) have become large enough to offset the weakening

production by the unresolved processes. The centers then begin to decay and advect away as all sources and sinks gradually decline. During this decay process the cluster convection also dissipates.

At this point the following question may be raised: What is the kinematical reason for the development of the vorticity couplet? The answer is shown by the sequence of plots of 227 mb horizontal winds on Fig. 7.7 and the time-latitude sections of u on Fig. 7.8. The prevailing easterlies at 227 mb are decelerated in the region of the clusters, resulting in large meridional gradients of u to the north and south of the cluster center. At the center of the west cluster, for instance, the windspeed decreases from 6 ms^{-1} at 0900 GMT during the growing stage to 5 ms^{-1} during the mature stage and to 2.5 ms^{-1} in the dissipating stage. This deceleration on 5 September is in addition to a previous deceleration on 4 September, when the ambient winds of 10 ms^{-1} decrease by half or more over the eastern half of the A/B array. Part of this previous decrease may have been due to the advance of an easterly wave, as the decrease in u at 635 mb evidently is (cf. the dashed contours on Fig. 7.8). However, much of the decrease at 227 mb appears to have been related to a large squall-cluster which moved through the array the afternoon and night of 4 September. The relationship between small values of u and anvil cloudiness on both days is clear on Fig. 7.8, where the stippled areas denote anvil index values of 1.

As Fig. 7.7 demonstrates, the deceleration of the wind at 227 mb tends to be centered between the two clusters. While it is possible that a center of decelerated wind moves across both clusters from east to west, it is more likely that the analysis scheme applied to the winds (which has a short-wavelength cutoff of 450 km) cannot completely resolve the relatively small distance between the clusters. The result could be the elongated windspeed minimum centered between the clusters. A tendency toward zonal

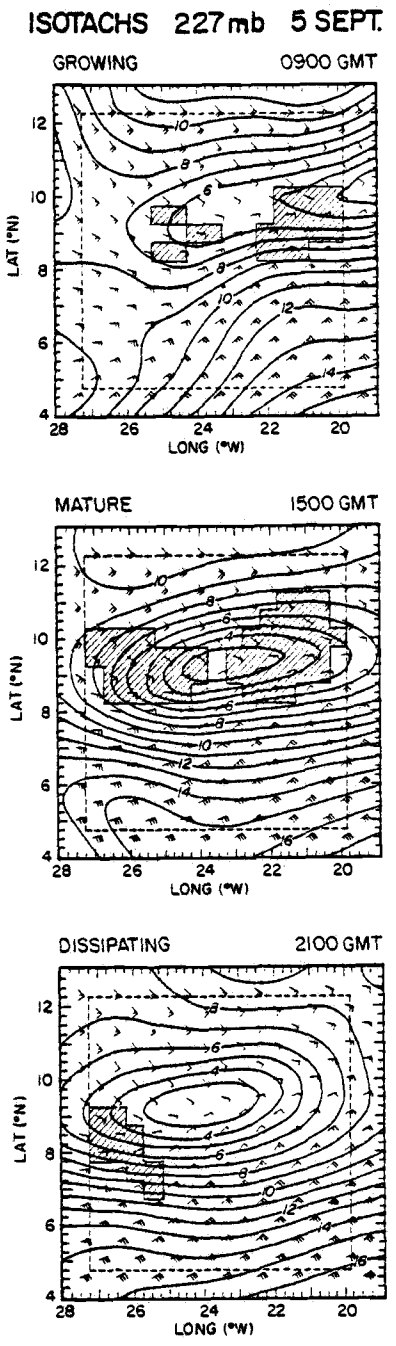

Figure 7.7. As in Fig. 7.1 except for isotachs during the life cycle of the western cluster. Units are ms^{-1}.

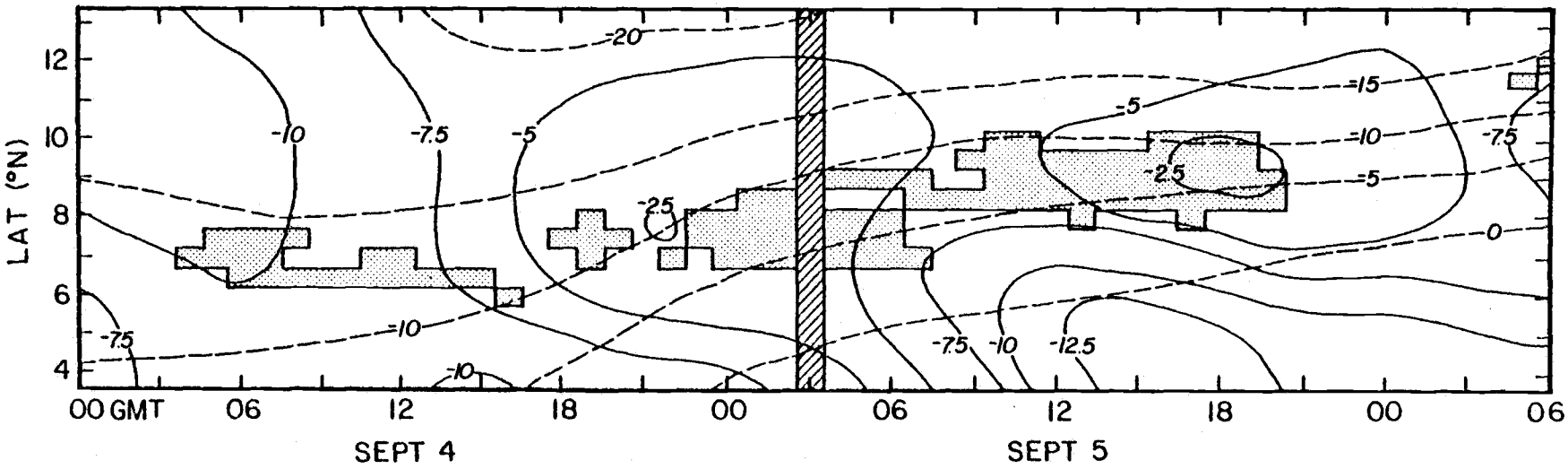

Figure 7.8. Time vs. latitude sections of the zonal component of the wind between 0000 GMT, 4 September, and 0600 GMT, 6 September 1974. Solid contour lines are for the zonal component at 227 mb; dashed contour lines are at 635 mb. Stippled areas indicate anvil index values of 1 (see text for explanation). In the hatched region, no anvil index values were available. Units are ms^{-1}.

elongation can also be seen on some of the other horizontal fields (cf. Figs. 7.3-7.5).

Possible sources of these upper-level wind decelerations will be discussed in the next section.

7.3 Composites of cluster wind fields

7.3.1 Motivation

To generalize the previous results of one case study and to at least partially remove random errors, winds from the largest slow-moving cloud clusters observed during Phase 3 of GATE were composited. It would be particularly interesting to see if the features found in the upper-tropospheric vorticity and momentum fields of the 5 September cluster would appear also in the composites.

Fig. 7.9 strongly suggests that the relationship between weak easterly winds in the upper troposphere and large anvil clouds which was found for the 5 September cluster is a common feature of the flow during Phase 3. On the figure is shown a time series of u at 227 mb at the center of the A/B array during Phase 3. Solid bars along the time axis mark periods when a cluster (as determined below) is occurring near the array center. A qualitative examination reveals a tendency for small negative values of u to occur during or just after clusters. The time series of total windspeed (not shown) is nearly identical, suggesting that the decrease in u is primarily due to a local deceleration and not simply to a turning of the wind.

7.3.2 Results

Fig. 7.10 shows the resulting composite fields of $\dot{\omega}$ and ζ at 227 mb for the mature stage. Regions within the grid area that

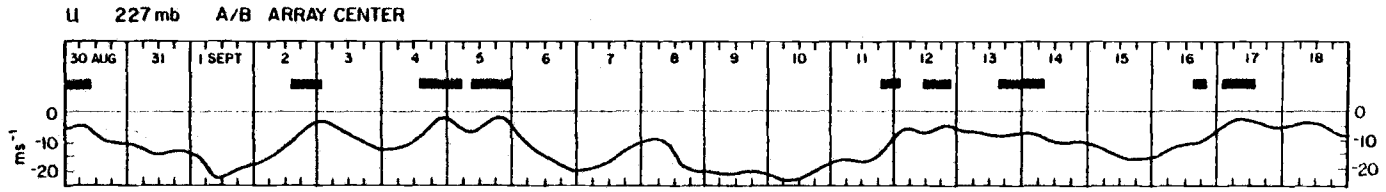

Figure 7.9. Time series of the zonal component of wind at 227 mb at the center of the A/B array during Phase 3 of GATE. Solid bars above the plot of u indicate times when large clusters or squall-clusters were located near the array center. See text for further explanation.

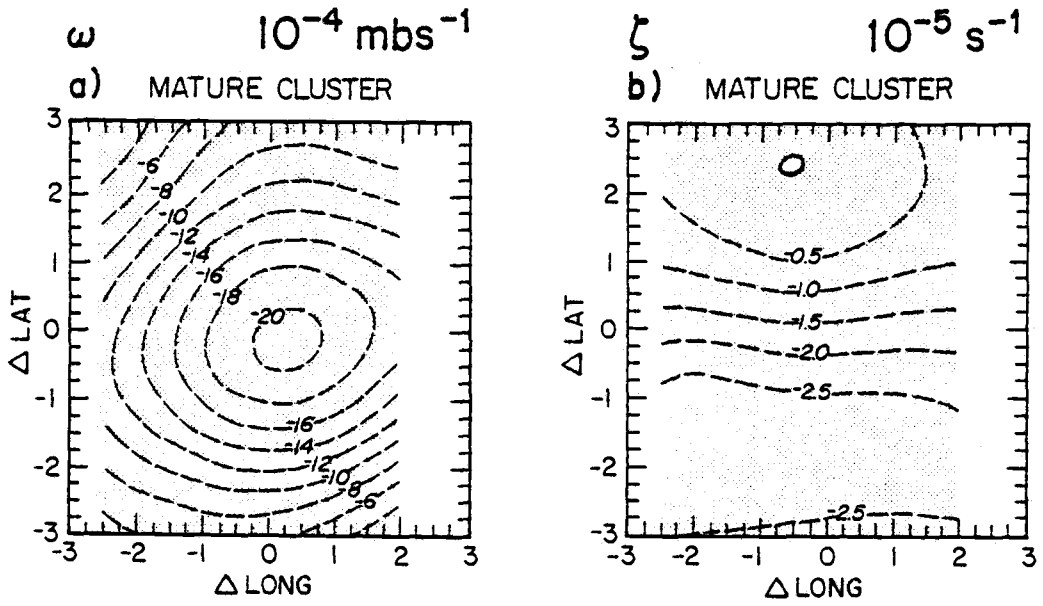

Figure 7.10. Horizontal contour plots of composited fields of(a) vertical velocity and (b) relative vorticity at 227 mb for mature stage of composite cluster. Axes labels are distances in degrees of latitude and longitude from the composite cluster center. Stippled areas have negative values.

are not contoured were not adequately sampled to be consistent with the remaining grid points. Vertical velocity tends to be centered on the composite grid, demonstrating that the compositing procedure does a good job of picking up the expected maximum of upward motion in the cluster anvils. It thus increases our confidence in the reliability of our composite results.

The composite vorticity field has a couplet structure that is very similar to that of 5 September. Wile the longitudinal extent of the positive center is evident, the east and west boundaries of the negative center are not captured by the shortened longitudinal range of the plots (they do begin to appear in the uncontoured regions when data there is included). Part of the elongation may be due to the short distance between the two 5 September clusters, as suggested in the previous section. Part may also be due to the inevitable smearing of features during compositing. However, it is also possible that the large-scale conditions which are favorable for the development of the slow-moving clusters are also, in general, enhancing deep convection along the ITCZ, resulting in a zonal elongation of the vorticity pattern. Frank (1983) presents meridional composites of the GATE ITCZ which show weak easterlies in the trough region at 225 mb with positive ζ to the north and negative ζ to the south.

The individual terms in the vorticity budget equation for the mature stage are shown on Fig. 7.11. Growing- and dissipating-stage residuals are included on Fig. 7.12. We see that the residual term in the growing stage shows the closest resemblance to the vorticity couplet. Its couplet-like latitudinal and longitudinal structure and its magnitude suggest that it is the main source of the observed vorticity production. During the mature stage all terms involving ω are significant and show cluster-scale horizontal dimensions. Twisting and Z act to maintain the vorticity couplet, divergence acts to destroy it, and vertical advection decreases ζ

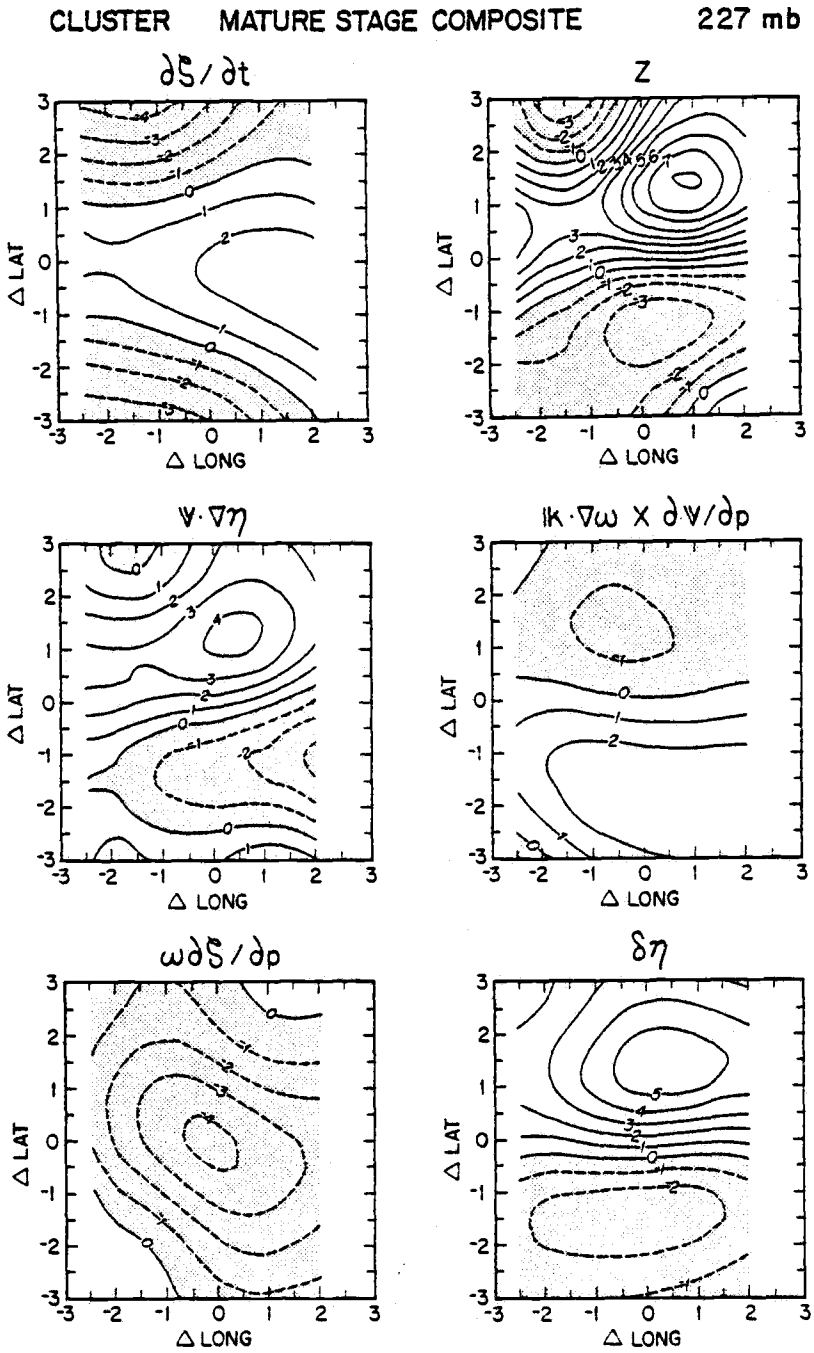

Figure 7.11. As in Fig. 7.10 except for vorticity budget terms for the mature stage. Units are 10^{-10} s^{-2}.

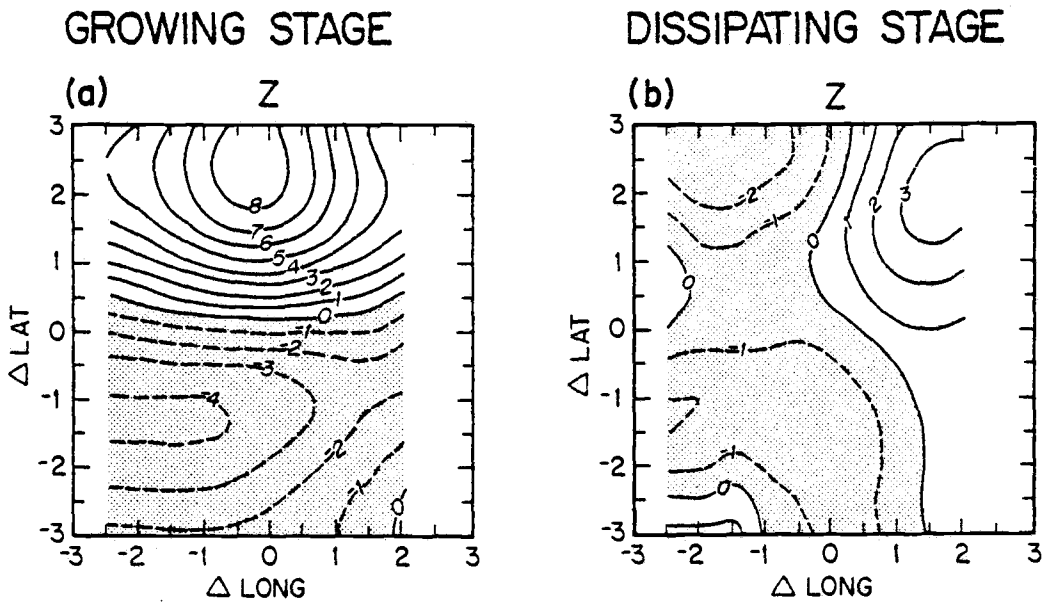

Figure 7.12. As in Fig. 7.10 except for residual fields for (a) the growing stage and (b) the dissipating stage of the composite cluster. Units are 10^{-10} s^{-2}.

in a region centered on the cluster. During the dissipating stage, the primary asymmetric terms producing the local decrease of both vorticity centers are the divergence and horizontal advection terms (not shown). Z is reduced in magnitude from its earlier values and shows a relatively featureless pattern.

These budget fields are similar in most respects to those found for the 5 September cluster.

The composite fields of windspeed on Fig. 7.13 show a region of decelerated winds which includes the cluster but extends beyond it to the east and west. In the growing and mature stages the maximum deceleration is upwind of the cluster center. By the dissipating stage, however, the region of greatest deceleration has moved to a position slightly downwind of the cluster center. Possible physical mechanisms that can explain these features are discussed in Section 7.5. Before doing so it is of interest to introduce another composite, one made within wave phase categories in the trough region of easterly waves.

7.4 Easterly wave composites

ETC calculated easterly wave composites of kinematic fields and vorticity budget terms using the same set of winds employed in this study. Their composites were presented as vertical profiles made in each wave phase category at the center of the A/B ship array. In this section, the horizontal structure of the wave-category composite fields are compared with the horizontal structure of the composite cluster fields described earlier in this chapter.

Some of the features appearing in the composite cluster and the case study appear again in composite fields made in the near-trough categories. For instance, in category 4, when three of the composited clusters were in their mature stage and two were in their growing stage, there is a windspeed minimum near 9°N and an

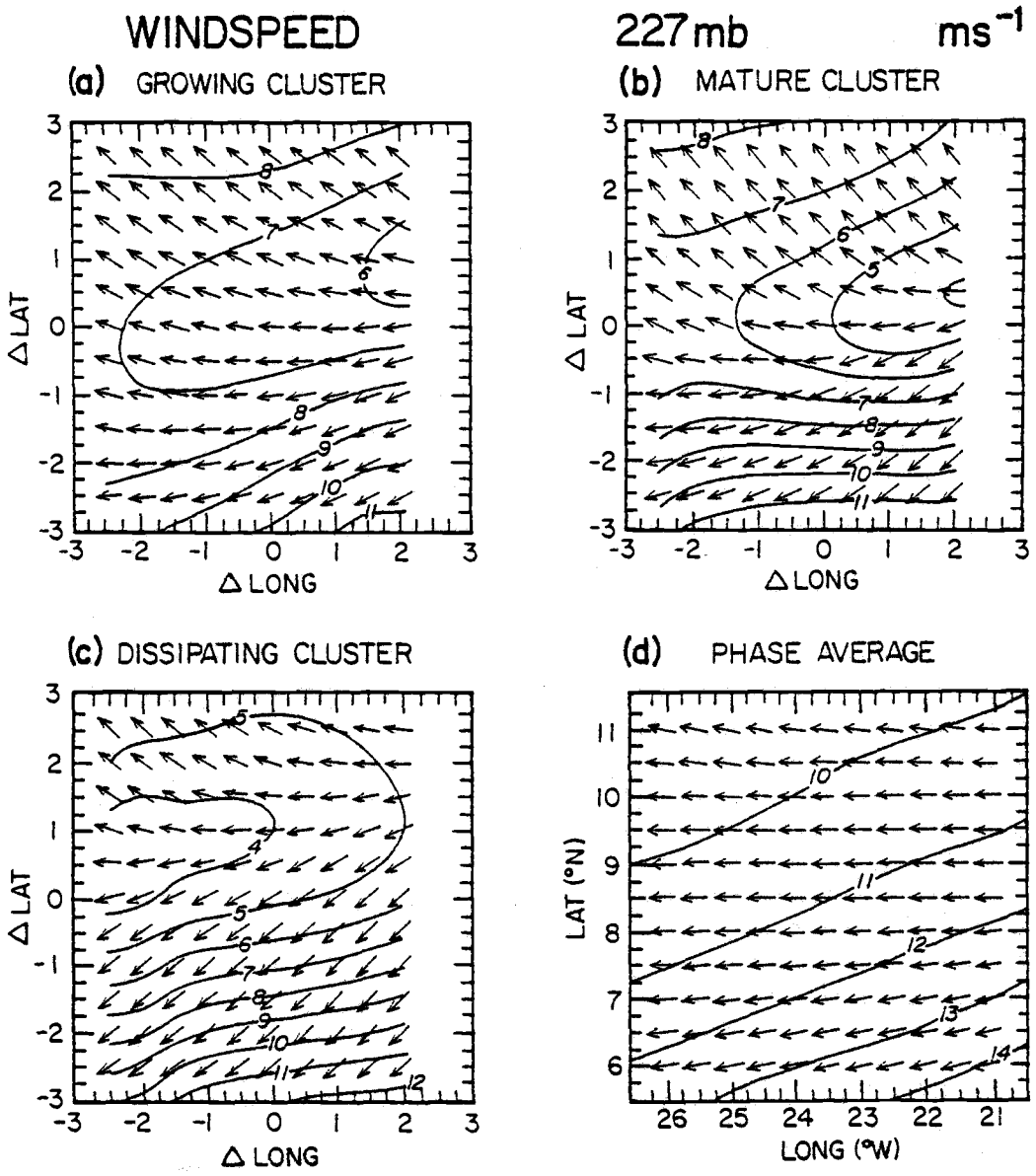

Figure 7.13. As in Fig. 7.10 except for windspeed for the (a) growing, (b) mature, and (c) dissipating stages of the composite cluster. GATE Phase 3 averages at 227 mb are shown in (d). Units are ms^{-1}.

associated vorticity couplet (Fig. 7.14). Similarly, in category 3, when two of the set of composited clusters were in their growing stage, the production of a vorticity couplet is obvious in the local change term and in Z, which is the term that most nearly reflects $\partial\zeta/\partial t$ (Fig. 7.15). The hatched regions on Figs. 7.14 and 7.15 indicate locations where the cloudcover above 300 mb (as described in Section 3) composited within categories is greater than 30%. As these plots show, cloudiness tended to be at a maximum in regions of small u and along the zero contour of $\partial\zeta/\partial t$ and Z.

The horizontal variability of Z evident on Fig. 7.15 is in accordance with other GATE studies of the vorticity budget of easterly waves. Shapiro (1978) found substantial differences between easterly wave composite residuals computed at 7°N and those computed at 11°N. At 7°N in categories 3 and 4, values of Z at 225 mb were negative while at 11°N they were positive.

The similarity between the easterly wave composites in the trough region and the cluster composites demonstrates the difficulty in making a clear separation between "easterly wave circulations" and the cluster-scale circulations associated with slow-moving systems during Phase 3. Most of the easterly wave troughs contained slow-moving clusters and the latitudinal positions of these clusters did not vary greatly (Table 6.1 and Fig. 6.1). Had the clusters been more randomly distributed with respect to latitude, the similarity between the geographically-fixed easterly wave composites (Fig. 7.14 and Fig. 7.15) and the cluster composites would likely have been less. Alternatively, had the easterly wave composites been performed relative to the latitude of maximum wave amplitude, as in Reed *et al.* (1977), the similarity might again have been reduced. As it is, however, the similarity of our composites suggests that near the time of the passage of the easterly wave trough at middle levels, there is no clear separation

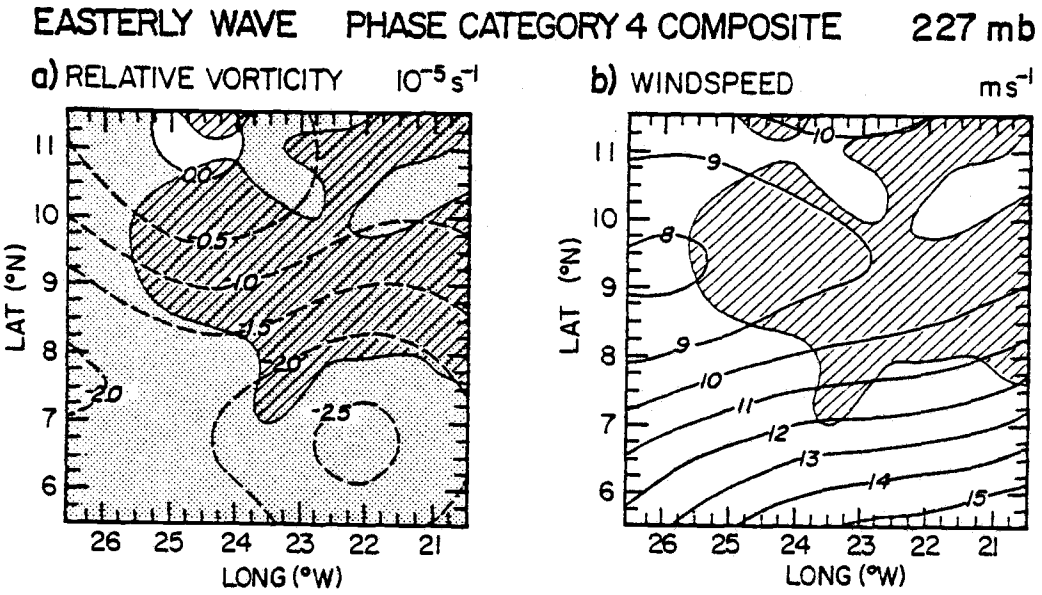

Figure 7.14. Composite fields of (a) relative vorticity and (b) windspeed at 227 mb for easterly wave phase 4 (trough). Stippled regions have negative values. In hatched regions, composited cloud cover at 300 mb is 30% or greater. See text for further explanation.

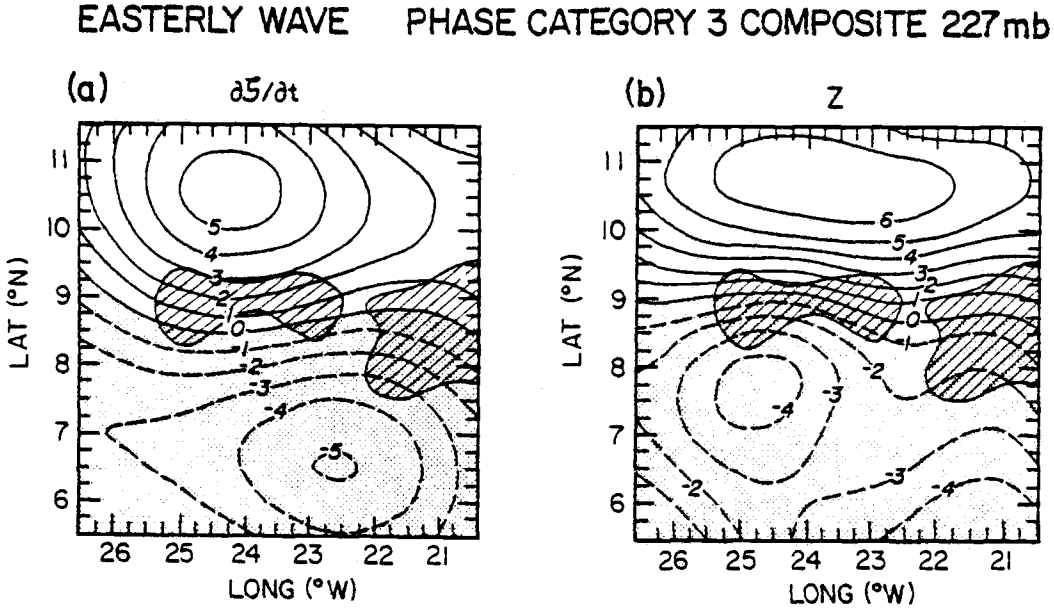

Figure 7.15. As in Fig. 7.14 except for (a) local vorticity change and (b) the vorticity budget residual Z composited in easterly wave phase category 3 (pre-trough). Units are 10^{-10} s^{-2}.

between the upper-tropospheric circulations associated with the anvil clouds of slow-moving cloud clusters and the circulations associated with the easterly wave.

7.5 Physical explanation of budget residuals

Results presented so far have suggested that the upper-tropospheric vorticity couplet that appears in the case study and composites is produced by circulations on the mesoscale or convective scales, both of which cannot be explicitly resolved by the upper air data from the A/B and B arrays. The the extent that the diagnosed residuals describe real processes, the deceleration of the rotational component of the wind from which the couplets result must also be due to unresolved circulations. Although the exact nature of these circulations cannot be deduced from the budget analyses alone, the following discussion includes reasoned speculation about the kinds of physical processes that could be acting to modify the momentum and vorticity fields.

7.5.1 Cumulus processes

Ooyama (1971) presented a simple framework for representing the effects of cumulus convection on the large-scale momentum fields. Within this framework, Schneider and Lindzen (1976) presented a theoretical justification for the assumption that in-cloud momentum is approximately conserved in deep cumulus clouds.

The possibility that the redistribution of momentum by cumulus clouds might be the source of the wind deceleration at 225 mb is shown by the zonal wind profiles at the center of the composite cluster (Fig. 6.4). As indicated earlier in this chapter, empirical evidence suggests that the updraft cores of deep cumuli are typically detraining at 225 mb. Thus, cumuli that entrain air in the lower troposphere and detrain it again without a substantial

change in the in-cloud momentum will tend to decelerate the easterlies near 225 mb. This mechanism would be important only if cumulus clouds process a relatively large amount of air. At easterly wave scales, vertical convergence of the cumulus mass flux (that is, detrainment) at 225 mb has been found to be a significant fraction of the synoptic-scale divergence at this level (cf. Fig. 14 in Johnson, 1980 and Fig. 13 in Thompson et al., 1979). Thus, given the relatively large total divergence at 225 mb in clusters ($\sim 3 \times 10^{-5}$ s^{-1} in our composite), it is reasonable to suppose that the displacement of ambient upper-tropospheric air by air detrained by a cumulus ensemble could have a significant effect on the momentum fields at this level.

A deceleration of u in the upper troposphere during the course of the cluster lifetime is evident on Fig. 6.4. In fact, u decelerates at all levels between 875 mb and the tropopause. The decrease below 300 mb, however, has a character that is different from the decrease that we have been studying at 225 mb. As the horizontal plots of u on Fig. 7.16 show, the change in u at 635 mb (actually in the entire layer between 875 mb and 300 mb) is primarily due to advance of the synoptic-scale easterly wave.

7.5.2 Mesoscale processes

The preceding discussion was based on cumulus-scale processes. It is equally likely that mesoscale circulations could be responsible for the observed momentum and vorticity production. As LH show using radar data, the 5 September clusters consisted of individual mesoscale systems whose upper level clouds merged to form the large anvil deck that shows up in satellite observations. The other clusters included in the set composited in this study undoubtedly also consisted of MPF's. These MPF's frequently take the form of rapidly-propagating squall lines or more slowly moving cloudlines.

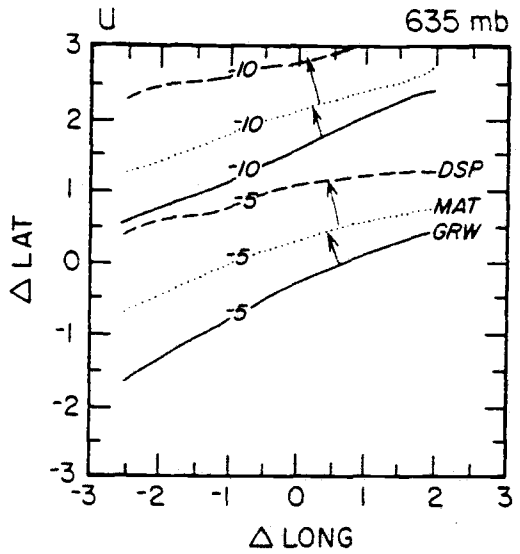

Figure 7.16. Horizontal contours of composited fields of the zonal component of the wind at 635 mb for the growing (solid lines), mature (dotted lines), and dissipating (dashed lines) stages of the composite cluster. Units are ms^{-1}. Axes labels are as in Fig. 7.10.

Evidence from Fig. 6.4 suggests that the transports in these clusters is of a "down-gradient" or diffusive nature. That is, the vertical gradients of velocity tend to decrease with time. Studies of midlatitude squall lines have also found apparent down-gradient transports (Ogura and Liou, 1980). However, other studies have demonstrated a somewhat more complex structure. Observations of Venezuelan squalls (Betts et al., 1976) and GATE cloudlines (Zipser et al., 1981; LeMone, 1983) and results of models of tropical squalls (Moncrief and Miller, 1976) have each shown up-gradient transport of the component of the wind normal to the squall or cloudline. In contrast, the parallel component in the observational studies listed is apparently transported down-gradient. Of the clusters studies here, the cluster on 2 September consisted mainly of east-west oriented cloudlines (cf. radar maps in Arkell and Hudlow, 1977), and radar maps and the diagrams of LH suggest that east-west cloudlines also predominated (though less clearly so) in the 5 September clusters (see Fig. 2.7). Thus, the primarily zonal winds in the cloud layer of these clusters are parallel to the orientation of most of the MPF's they encounter, and a significant downgradient transport of u might reasonably be expected.

The upwind location of the region of greatest deceleration in the growing and mature stages shown on Fig. 7.13 suggests that part of the deceleration of the total horizontal momentum might be due to geopotential gradients. Observational and modeling studies of midlatitude mesoscale convective systems (e.g., Maddox et al., 1981; Fritsch and Brown, 1982) have found relatively higher geopotentials within the systems near the tropopause than at the same pressure levels in the surrounding environment. The upwind decelerations on Fig. 7.13 might then be the combined result of this deceleration of the divergent component of the wind and the deceleration of the rotational component of the wind which gives rise to the vorticity couplet. If relatively higher geopotentials within the anvil than in the surrounding region are postulated and the resulting momentum

change fields (with upstream decelerations and downstream accelerations) were superimposed on a momentum source produced by downgradient transports within the cluster, the resulting momentum field would look much like the mature-stage field in Fig. 7.13.

7.6 Implications

In this chapter I have described a large-amplitude asymmetric vorticity couplet found in the upper level mass divergence associated with most large GATE cloud clusters. This feature appears in a composite of clusters as well as in individual cases. A deceleration of the winds within the cluster anvil is found to be the mechanism producing the couplet.

A vorticity budget analysis shows that the circulations on the scale of the large cloud clusters are unable to account for most of the development and maintenance of the asymmetric vorticity patterns. The budget residuals suggest that small-scale circulations are largely responsible for the development of the couplets. What form these unresolved circulations take, whether it be individual cumulus clouds, mesoscale circulations, or other entities, is an important question that remains to be answered.

The results of this chapter have also shown that the large horizontal variations in the upper-level vorticity fields associated with the slow-moving clusters are also a feature of GATE easterly wave composites near the time of passage of the easterly wave troughs during Phase 3. Stronger than normal anticyclonic vorticity is found in the southern portion of the A/B array, and stronger cyclonic vorticity is found to the north. It is concluded that vorticity budget analyses at the center of the A/B array or at the center of a slow-moving cloud cluster give an incomplete description of the effects of convection in the upper troposphere. As Fig. 7.15 demonstrates, for instance, values of

Z in easterly wave phase category 3 at the A/B array center are near zero and thus give no indication of the large values found to the north and south. Subsequent studies should take full advantage of the exceptional spatial coverage of the GATE upper-air data.

Implications of the results of this chapter for the parameterization of unresolved sources of momentum and vorticity will be discussed in Chapter 8.

CHAPTER 8. PARAMETERIZATION OF UNRESOLVED SOURCES OF MOMENTUM AND VORTICITY

As the results in the preceding chapters have shown, the residual term in the budget equation for vorticity can be as large as any of the explicitly-calculated terms. This finding concurs with a wealth of other investigations that find significant contributions to vorticity and momentum budgets by sources that are not resolved by the observations. The preponderance of these results underscores the importance of including the effects of cumulus clouds and mesoscale cloud systems in numerical models of the circulation of the tropics, whether these models be describing the general circulation, synoptic-scale flow features, or tropical cyclones.

From an observational point of view, it is obviously impossible to mount long-lasting programs to simultaneously observe all these scales over the tropical oceans. Thus, efforts to describe subsynoptic contributions to budgets of thermodynamic or kinematic properties will likely be unable, for the foreseeable future, to proceed from direct measurement of these processes.

Similar restrictions apply to numerical modeling efforts, where computer resources are not sufficient to allow the small space and time increments necessary to resolve cumulus clouds in the large domain of general circulation models. As an alternative, most researchers to date have chosen to include these significant affects by parameterizing them. That is, they have attempted to include unresolvable processes by describing them in terms of variables that can be resolved. In the case of synoptic-scale easterly waves, for instance, subsynoptic-scale momentum and vorticity contributions have typically been parameterized in terms of synoptic-scale momentum and vorticity and M_c, the vertical flux of mass due to cumulus clouds. Although

many simplifying assumptions about the structure of ensembles of cumulus clouds are required in these parameterizations, the parameterized sources have simulated some of the features of the diagnosed residuals fairly well.

At the scales resolved by the data employed in this thesis, it is possible to directly compute some of the quantities that must be inferred from budget residuals in analyses at larger scales. For instance, the large clusters which this thesis describes using direct measurements would have to be parameterized in numerical models that are just able to resolve easterly waves. There are also, of course, circulations that cannot be resolved by either synoptic-scale or cluster-scale analyses. Two of the most significant of the tropical circulations which fall into this category are cumulus clouds and mesoscale systems (such as squall lines and cloud bands).

The discussion in this chapter will be limited to cumulus clouds. It is possible that mesoscale circulations also make important contributions to the apparent momentum and vorticity sources. However, less is known about the effects of these systems and about how to parameterize them. More observational studies of mesoscale circulations of all types are required before our understanding of these systems will be sufficient to adequately parameterize them.

In this chapter I will first describe some of the general features of the models of cloud ensembles that are common to several parameterization schemes. This description will then be used to explain the most widely accepted of the parametric schemes thus far developed to describe cumulus-scale production of vorticity and momentum. It will also help to illuminate the derivations of these schemes given in Appendix C. An apparent inconsistency between the vorticity parameterization and the parallel

parameterization of momentum will then be described and some suggestions made about the origin of the inconsistency. In the process, an alternative parameterization for vorticity will be derived, and its advantages with respect to present schemes discussed. The final section includes a comparison of the diagnosed residuals associated with the large vorticity couplets observed in the upper troposphere of GATE cloud clusters (cf. Chapter 7) with residuals computed with the two alternative parameterizations mentioned previously.

8.1 Preliminary assumptions about cloud ensembles

The conceptual model of an ensemble of cumulus clouds and its environment assumed in this chapter is illustrated in Fig. 8.1 taken from Arakawa and Schubert (1974). Within the rectangular boundary (which corresponds to the large-scale horizontal averaging area) are the cores of cumulus clouds which intersect the area at this level. The portion of the large-scale area that does not consist of clouds is termed the "environment" of the clouds. It is assumed that the large-scale area is large enough to include a representative ensemble of clouds but small enough so that variations due to synoptic easterly waves are not significant.

Only the active portions of the clouds (those regions with strong vertical velocities) are considered as "cloud" regions. Thus, relatively inactive or inert cloud material detrained laterally from the active cumulus cores are not included in the cloudy regions. Relative to their environment, the active cores of clouds occupy a small portion of the large-scale area. Observations suggest the percentage to be on the order of 5%.

It is assumed that the ensemble of individual clouds can be broken into subsets (or "subensembles") of identical cloud types. As a further simplification, each cloud type is assumed to be

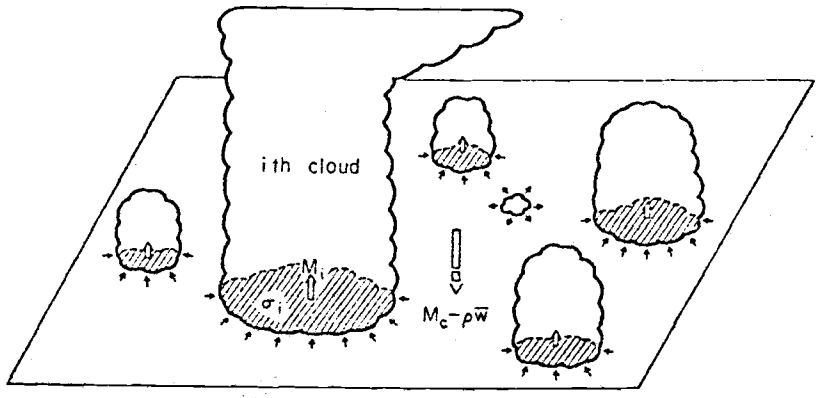

Figure 8.1. Schematic diagram of the conceptual cloud ensemble model assumed in this thesis. The taller clouds are shown penetrating the level given by the rectangular area and entraining environmental air. A cloud which has lost buoyancy is shown detraining cloud air into the environment (from Arakawa and Schubert, 1974).

completely specified by a single parameter (e.g., the entrainment parameter of Arakawa and Schubert, 1974, and Yanai et al., 1973). In this sense, then, the clouds are "one-dimensional." Although such a picture is not explicitly required, a consistent (and conceptually helpful) picture of these clouds portrays them as radially symmetric entraining plumes with a radius that changes relatively little with height and slowly in time. Interactions with their environment can occur at the sides of the clouds as well as at their tops and bottoms. Depending on their entrainment parameters the different cloud types will have tops at different heights. However, all clouds are assumed to have their bases at the lifting condensation level (LCL) of near-surface air. In the GATE area, the LCL was typically near 950 mb, just above the average top of the atmospheric mixed layer.

By virtue of the geometry of Fig. 8.1 and the characteristics of the cloud ensemble and its environment described in the preceding paragraphs, we can define an averaging operator for grid-area averages of a quantity, $(\overline{\ })$, by

$$(\overline{\ }) = (1 - \sigma_c)(\tilde{\ }) + \Sigma\sigma_i(\ )_i \quad . \tag{8.1}$$

In (8.1), σ_i is the percentage of the averaging area (A) occupied by all the clouds in cloud subensemble i, $\sigma_c = \Sigma\sigma_i$ is the percentage of A occupied by all the clouds in A, $(1-\sigma_c)$ is the percentage of A consisting of the cloud environment, $(\tilde{\ })$ is the average value of a quantity in the environment, and $(\ )_i$ is the average value of a quantity within all clouds of subensemble i. The form of (8.1) results from applying the standard area-weighted averaging operator

$$(\overline{\ }) = \frac{1}{A}\iint_A (\ )\, dA \tag{8.1b}$$

to the geometry of Fig. 8.1.

Applying (8.1) to the vertical velocity (in pressure coordinates) within area A gives

$$\bar{\omega} = (1 - \sigma_c)\,\tilde{\omega} + \Sigma\sigma_i\omega_i \tag{8.2}$$

If we define $m_i = -\sigma_i\omega_i$ as the vertical mass flux[4] (positive upwards) through this level within the clouds of subensemble i, and the summation over all subensembles as M_c, the total mass flux due to all clouds, then (8.2) becomes

$$\bar{\omega} = (1 - \sigma_c)\,\tilde{\omega} - M_c \tag{8.3}$$

According to (8.3), the grid-scale mass flux (which is the only quantity in (8.3) that is ordinarily obtained observationally) is the weighted average of two quantities: the vertical mass flux in the environment (which is not ordinarily obtained observationally) and the total mass flux in the clouds of the ensemble enclosed within A (which is determined in various ways based on assumptions about the clouds of the ensemble).

The relationship given by (8.3) is a key one in virtually all parameterizations of the effects of clouds. Hence, a brief discussion of its implications is useful here. If there are no clouds in A, then M_c and σ_c are both equal to zero and the large-scale average vertical velocity is the same as the average in the environment (in this case, of course, A consists of only "environment"). On the other hand, in situations where the large-scale vertical velocity is negligible but where there is significant convective mass flux, there must also be significant environmental mass flux. Usually the net effect of M_c is assumed to be positive; that is, the upward mass flux in cloud updrafts is assumed to be larger than the downward mass flux in cloud downdrafts. According to (8.3), $\tilde{\omega}$ must then also be positive (that is, downward). In

---

[4] M_c and m_i do not have the units of a true "mass flux" ($kgm^{-2}\ s^{-1}$). However, mass flux values can be computed from them by dividing each by the essentially constant acceleration of gravity.

this case, $\tilde{\omega}$ can be interpreted as a compensating mass flux in the environment induced by (and equal to) the upward mass flux in clouds. Under this interpretation, budget equation terms involving $-M_c$ represent the effects of this compensation.

When $\bar{\omega}$ is not zero, the cloud environment is not necessarily subsiding. A situation might be imagined, for instance, in which the upward mass flux in clouds within A is less than the large-scale mass flux ($-\bar{\omega}$), which would then require upward environmental mass flux ($\tilde{\omega}<\phi$). Typically, however, M_c is greater than $-\bar{\omega}$ (Yanai et al., 1973; Johnson, 1980) so that $\tilde{\omega}$ is greater than 0 (subsiding).

8.2 Existing parameterizations for momentum and vorticity

The problem addressed by parametric schemes is demonstrated by the equations for large-scale momentum (8.4) and vorticity (8.5):

$$\begin{aligned}
\partial \bar{\underset{\sim}{v}}/\partial t &= -\nabla\cdot\overline{\underset{\sim}{v}\underset{\sim}{v}} - \partial(\overline{\omega\underset{\sim}{v}})/\partial p - \overline{\nabla\Phi} - \overline{f\underset{\sim}{k}\times\underset{\sim}{v}} \\
&= -\nabla\cdot\bar{\underset{\sim}{v}}\bar{\underset{\sim}{v}} - \partial(\bar{\omega}\bar{\underset{\sim}{v}})/\partial p - \nabla\bar{\Phi} - \bar{f}\underset{\sim}{k}\times\bar{\underset{\sim}{v}} \\
&\quad - \nabla\cdot\overline{\underset{\sim}{v}'\underset{\sim}{v}'} - \partial(\overline{\omega'\underset{\sim}{v}'})/\partial p - \overline{f'\underset{\sim}{k}\times\underset{\sim}{v}'} \\
&\equiv -\nabla\cdot\bar{\underset{\sim}{v}}\bar{\underset{\sim}{v}} - \partial(\bar{\omega}\bar{\underset{\sim}{v}})/\partial p - \nabla\bar{\Phi} - \bar{f}\underset{\sim}{k}\times\bar{\underset{\sim}{v}} + \underset{\sim}{X}
\end{aligned} \tag{8.4}$$

where

$$\underset{\sim}{X} = -\nabla\cdot\overline{\underset{\sim}{v}'\underset{\sim}{v}'} - \partial(\overline{\omega'\underset{\sim}{v}'})/\partial p - \overline{f'\underset{\sim}{k}\times\underset{\sim}{v}'} - \overline{\nabla\Phi'}\ ;$$

and

$$\begin{aligned}
\partial\bar{\zeta}/\partial t &= -\nabla\cdot\overline{\underset{\sim}{v}\eta} - \overline{\omega\,\partial\zeta/\partial p} - \underset{\sim}{k}\cdot\overline{\nabla\omega\times\partial\underset{\sim}{v}/\partial p} \\
&= -\nabla\cdot\bar{\underset{\sim}{v}}\bar{\eta} - \bar{\omega}\,\partial\bar{\zeta}/\partial p - \underset{\sim}{k}\cdot\nabla\bar{\omega}\times\partial\bar{\underset{\sim}{v}}/\partial p \\
&\quad - \nabla\cdot\overline{\underset{\sim}{v}'\eta'} - \overline{\omega'\,\partial\zeta'/\partial p} - \underset{\sim}{k}\cdot\overline{\nabla\omega'\times\partial\underset{\sim}{v}'/\partial p} \\
&= -\nabla\cdot\bar{\underset{\sim}{v}}\bar{\eta} - \bar{\omega}\,\partial\bar{\zeta}/\partial p - \underset{\sim}{k}\cdot\nabla\bar{\omega}\times\partial\bar{\underset{\sim}{v}}/\partial p + Z
\end{aligned} \tag{8.5}$$

where

$$Z = -\underset{\sim}{\nabla}\cdot\overline{\underset{\sim}{v}'\eta'} - \overline{\omega'\partial\zeta'/\partial p} - \underset{\sim}{k}\cdot\overline{\underset{\sim}{\nabla}\omega' \times \partial\underset{\sim}{v}'/\partial p} \ .$$

In diagnostic studies, terms involving large-scale averages of variables (including the local rate of change) are generally available. Thus, the apparent sources of momentum ($\underset{\sim}{X}$) and vorticity (Z) can be computed as a residual. In prognostic studies, on the other hand, it is the local rate of change of momentum and vorticity which must be computed. As a result the production by small-scale processes represented by $\underset{\sim}{X}$ and Z must be modeled. Describing these sources in terms of values of explicitly-calculated large-scale variables is the process of parameterization.

Using a framework suggested by Ooyama (1971) for representing the effects of cumulus convection on the large-scale momentum fields, a simple parameterization for the momentum budget residual $\underset{\sim}{X}$ may be given by

$$\underset{\sim}{X} = \Sigma\delta_i(\underset{\sim}{v}_{\delta i} - \bar{\underset{\sim}{v}}) - M_c\,\partial\bar{\underset{\sim}{v}}/\partial p \qquad (8.6)$$

In (8.6), $\underset{\sim}{v}_{\delta i}$ is the average in-cloud velocity in subensemble i and δ_i is the mass detrained by cloud subensemble i (the relationship between entrainment, detrainment, and cumulus mass flux is described in Appendix C). Shapiro and Stevens (1980) used a similar form of the momentum equation in their study of the momentum budget of a composite easterly wave from GATE. Schneider and Lindzen (1976) presented a theoretical justification for the assumption that in-cloud momentum is approximately conserved in deep cumulus clouds. Under this assumption, $\underset{\sim}{v}_{\delta i}$ may be approximated by the large-scale velocity at cloud base.

Early parameterizations of Z (Reed and Johnson, 1974; Shapiro, 1978) included only the effects of advection of vorticity by compensating mass flux and advection by the updrafts within clouds. Z was thus given by

$$Z = M_c \, \partial (\eta_c - \bar{\eta}) / \partial p \ , \tag{8.7}$$

where η_c is the average in-cloud vorticity of the cloud ensemble. In the study of Reed and Johnson (1974) M_c was determined by solving a set of equations that included observed values of Z and large-scale averages of η. Shapiro (1978) and subsequent studies have generally used thermodynamic budgets to calculate M_c, a procedure that ensures that the calculation is independent of assumptions made about the large-scale vorticity or the vorticity within clouds. Cho et al. (1979) derived a parameterization for Z which included the life-cycle effects of clouds and twisting. Three recent studies (Cho and Cheng, 1980; Shapiro and Stevens, 1980; Yanai et al., 1982) all arrived at the same form:

$$Z_\zeta = \Sigma \delta_i (\eta_{\delta i} - \bar{\eta}) + \bar{\eta} \, \partial M_c / \partial p - M_c \, \partial \bar{\zeta} / \partial p - \underset{\sim}{k} \cdot \underset{\sim}{\nabla} M_c \times \partial \bar{\underset{\sim}{v}} / \partial p \tag{8.8}$$

The subscript ζ has been applied to Z to distinguish this parameterization from others to be derived later. In this parameterization, the direct effects of detrainment and entrainment by clouds have been included for the first time. In the derivation of Cho and Cheng (1980), an attempt was made to also include the horizontal flux of vorticity by cumulus clouds ($\overline{\underset{\sim}{\nabla} \cdot \underset{\sim}{v}' \eta'}$). However, they arrived at the same form (8.8) as the other two studies, which explicitly neglected this effect.

Each of these three studies used slightly different assumptions and techniques to derive (8.8). Another derivation of (8.8), and a parallel derivation of the momentum parameterization (8.6), are given in Appendix C. Although the approach employed in these derivations differs from those of the three studies mentioned above, the underlying assumptions about the physical mechanisms involved are similar.

The physical significance of the terms of Z_ζ can be made more clear by demonstrating how they might contribute to the residuals

obtained in the vorticity budgets described in previous chapters. Between 600 mb and 700 mb in the 4 September squall, for instance, the local decrease in $\bar{\zeta}$ is apparently produced by small-scale processes included in Z (cf. Fig. 5.10a). Referring to the vertical profile of $\bar{\zeta}$ on Fig. 5.7a, we see that $\bar{\zeta}$ is decreasing rapidly with height at this level. Thus, it is possible that the vorticity decrease is produced by advection by the compensating mass flux (as given by $-M_c \partial\bar{\zeta}/\partial p$). This mechanism may also balance the large values of cluster-scale vertical advection near 315 mb in the mature and dissipating stages of the composite cluster of Chapter 6 (cf. Figs. 6.14 and 6.17).

In the boundary layer of the 4 September squall, on the other hand, the large local decrease of $\bar{\zeta}$ near the top of the boundary layer cannot have been a result of this process (cf. Figs. 5.9a and 5.7a). It may be that the environmental stretching represented by the term $\bar{\eta}\partial M_c/\partial p$ is responsible. At this level, which is near cloud base, entrainment by clouds will normally be large ($\partial M_c/\partial p < 0$). In the environment, this entrainment would be felt as an apparent source of horizontal divergence which, acting on the positive relative vorticity here, would tend to decrease $\bar{\zeta}$. Why this effect should predominate in the squall but not in the slow-moving cluster of 5 September is, however, not clear.

Another possible mechanism is illustrated by the schematic representation of the twisting effect of the mass subsidence on Fig. 8.2. Since twisting is asymmetric with respect to the location of maximum M_c, couplet pairs should be expected to form due to this process, as in Fig. 8.2. Convection (and hence $-M_c$) is strongest at or just behind the leading edge of the squall; hence, locally large values of twisting ($-\underset{\sim}{k}\cdot\underset{\sim}{\nabla}M_c \times \partial\underset{\sim}{\bar{v}}/\partial p$) may occur here. If profiles of vorticity budget terms were made in the strongly negative member of the pair (the region indicated by "N" in figure 8.2), a significantly negative source of $\bar{\zeta}$ could result.

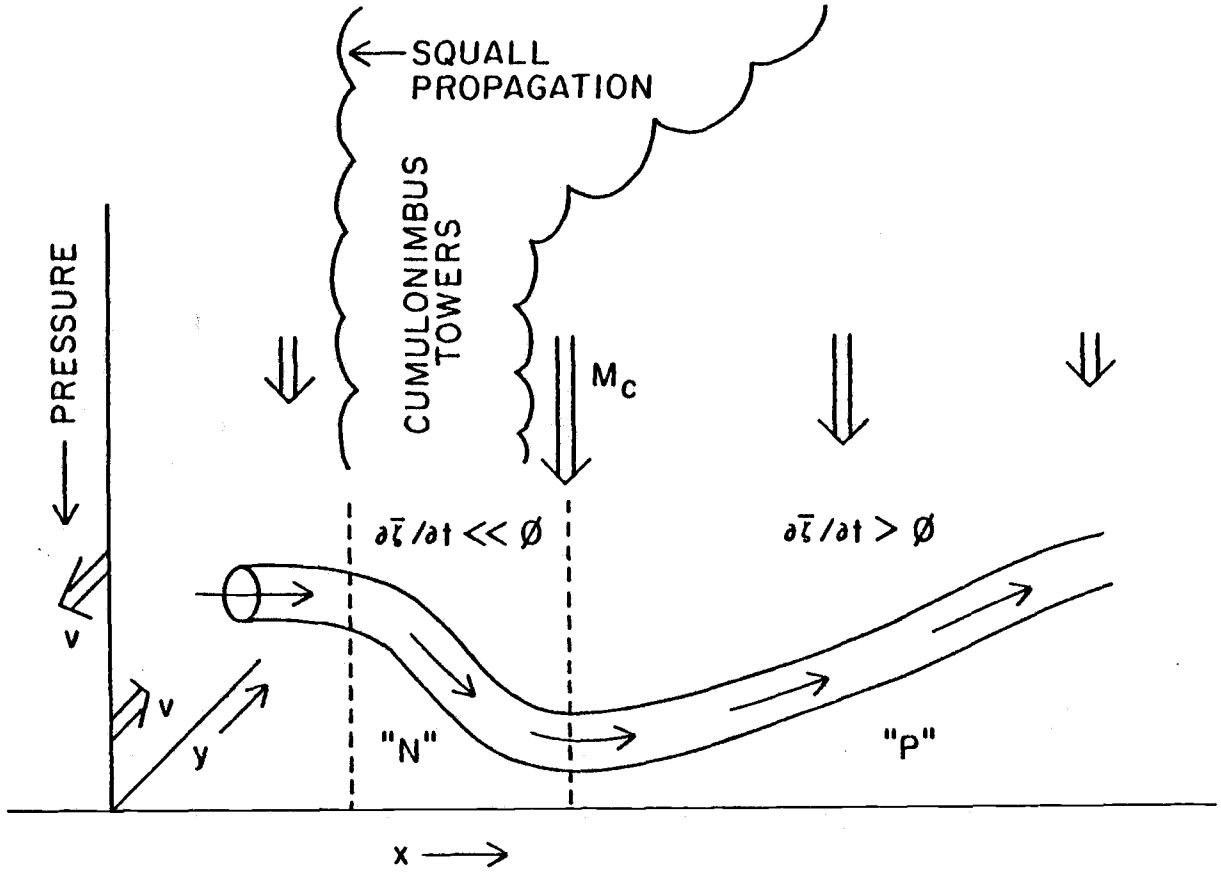

Figure 8.2. Idealized depiction of the production of vorticity by the tilting of horizontal vortex tubes. The portion of the squall cut by the section is oriented approximately north-south and is propagating toward the west (left in the figure). The values of meridional velocity (v) correspond roughly to those observed in the 4 September squall; the M_c field is hypothetical. See the text for further explanation.

In the 4 September squall, however, no clear residual couplet is evident on horizontal plots of Z (not shown). Thus, it is unlikely that this mechanism is predominating, although it may be contributing to, the small-scale destruction of vorticity.

The question of whether or not cloud entrainment/detrainment (as given by the first RHS term of (8.8)) can directly change large-scale vorticity will be addressed in Sections 8.4 and 8.5.

8.3 An alternate parameterization for vorticity

Another parameterization for Z can be derived by noting that the large-scale terms on the LHS of (8.8) can be formed by extracting the vertical component from the curl of the LHS terms of the momentum budget (8.6). Mathematical consistency requires that the same operation performed on the RHS of the momentum equation must be equal to the RHS of the vorticity budget equation. Thus, we can also compute Z as the vertical component of the curl of $\underset{\sim}{X}$, or

$$\begin{aligned} Z_M &= \underset{\sim}{k}\cdot\underset{\sim}{\nabla} \times \{\Sigma\delta_i(\underset{\sim}{v}_{\delta i} - \bar{\underset{\sim}{v}}) - M_c\, \partial\bar{\underset{\sim}{v}}/\partial p\} \\ &= \underset{\sim}{k}\cdot\underset{\sim}{\nabla} \times \Sigma\delta_i(\underset{\sim}{v}_{\delta i} - \bar{\underset{\sim}{v}}) - M_c\partial\bar{\zeta}/\partial p - \underset{\sim}{k}\cdot\underset{\sim}{\nabla}M_c \times \partial\bar{\underset{\sim}{v}}/\partial p \end{aligned} \qquad (8.9)$$

The subscript M, which indicates a basis in the momentum equation, is included to distinguish Z_M from Z_ζ, which is based on the vorticity equation.

To the extent that the assumptions and approximations used in the derivations of Z_M and Z_ζ are appropriate, we might expect that the two resulting parameterizations would be equivalent. However, comparing (8.8) and (8.9), we see that although the indirect terms describing advection and twisting by the compensating mass subsidence are the same in both, the detrainment terms are different. In addition, another term involving the compensating subsidence ($\bar{\eta}\partial M_c/\partial p$, interpreted earlier as the squeezing of the

environment due to cloud entrainment and detrainment) does not appear in Z_M. There is thus an apparent inconsistency between Z_M and Z_ζ, in the sense that Z_M cannot be directly derived from Z_ζ as required by mathematical consistency. Much of the remainder of this section will be an attempt to locate the source of this inconsistency and to determine which of the two parameterizations (Z_M or Z_ζ) best describes the production of vorticity in the clusters observed in GATE.

At first glance, it might appear possible to reduce the discrepancy between Z_M and Z_ζ by moving the curl operator inside the summation on the RHS of (8.9) and then breaking the resulting expression into components. If we also assume (for sake of argument) that $\zeta_{\delta i} = \underset{\sim}{k}\cdot\underset{\sim}{\nabla} \times \underset{\sim}{v}_{\delta i}$, then (8.9) becomes

$$Z_M \stackrel{?}{=} \underset{\sim}{k}\cdot\Sigma\underset{\sim}{\nabla}\delta_i \times (\underset{\sim}{v}_{\delta i} - \bar{\underset{\sim}{v}}) + \Sigma\delta_i(\eta_{\delta i} - \bar{\eta}) - M_c\,\partial\bar{\zeta}/\partial p - \underset{\sim}{k}\cdot\underset{\sim}{\nabla}M_c \times \partial\bar{\underset{\sim}{v}}/\partial p \qquad (8.9b)$$

The second RHS term in (8.9b) is then equal to the term describing detrainment of excess vorticity in (8.8). However, it is not generally true that $\zeta_{\delta i} = \underset{\sim}{k}\cdot\underset{\sim}{\nabla} \times \underset{\sim}{v}_{\delta i}$. To derive (8.6), $\underset{\sim}{v}_{\delta i}$ was defined as an average value of the velocity of all the air detrained by the clouds of subensemble i, which may be scattered throughout the averaging area. Thus $\underset{\sim}{v}_{\delta i}$ is a large-scale average variable and its curl is not equivalent to the vorticity of the detrained air ($\zeta_{\delta i}$). Furthermore, (8.9b) includes a term involving the gradient of detrainment which has no counterpart in (8.9).

8.4 Evaluation of Z_M and Z_ζ

In attempting to resolve the consistency problem posed earlier, it is helpful to examine in more detail the concept of "large-scale average vorticity," $\bar{\zeta}$. As before, we choose an overbar to denote

this large-scale average. By definition, $\bar{\zeta}$ can be represented as

$$\begin{aligned} \bar{\zeta} &\equiv \underset{\sim}{k}\cdot\overline{\underset{\sim}{\nabla} \times \underset{\sim}{v}} \\ &= \underset{\sim}{k}\cdot\underset{\sim}{\nabla} \times \bar{\underset{\sim}{v}} \end{aligned} \tag{8.10}$$

The second line of the equality is actually enforced in Ooyama's data set (and likely also in most other sets of wind data)[5] by calculating $\bar{\zeta}$ by taking the curl of $\bar{\underset{\sim}{v}}$. If the averaging domain does not change with time, we may relate the local time rate of change of $\bar{\zeta}$ to that of $\bar{\underset{\sim}{v}}$ by

$$\partial\bar{\zeta}/\partial t = \underset{\sim}{k}\cdot\underset{\sim}{\nabla} \times \partial\bar{\underset{\sim}{v}}/\partial t \tag{8.11}$$

It is this relation that we implicitly called upon to justify our derivation of Z_M.

A very useful tool in the study of vorticity is Stokes' theorem, which relates the average curl of a vector to a line integral performed along the boundary of the averaging area. This theorem allows us to express the local change of $\bar{\zeta}$ as

$$\begin{aligned} \partial\bar{\zeta}/\partial t &= (1/A)\iint_A \underset{\sim}{k}\cdot(\underset{\sim}{\nabla} \times \partial\underset{\sim}{v}/\partial t)dA \\ &= (1/A)\oint_L (\partial\underset{\sim}{v}/\partial t)\cdot d\underset{\sim}{l} \end{aligned} \tag{8.12}$$

As before, A denotes the area of the large-scale average, and L denotes a closed integration circuit along the boundary of A. It can in fact be shown (see Appendix D) that the definitions given by 8.11 and 8.12 are approximately equivalent. We conclude from

---

[5] A hypothetical alternative would be to observe ζ at each observation platform and then average in some way across all observations of ζ within the averaging area. However, radiosondes measure velocity as their primary wind variable rather than vorticity.

(8.12) that the local rate of change of vorticity in an averaging area A is completely specified by the local rate of change of velocity along the boundary of A, and that the approach used to derive Z_M is theoretically sound, being consistent with Stokes' theorem.

The first of these conclusions has implications concerning some of the assumptions that must be made to derive Z_ζ. Following earlier studies of budgets of thermodynamic quantities, investigators who have derived Z_ζ have represented large-scale averages of vorticity and vorticity budget terms as weighted averages given by the averaging operator (8.1). Under this representation, the average local change of vorticity is given by

$$\partial \bar{\zeta}/\partial t = (1 - \sigma_c)\partial \tilde{\zeta}/\partial t + \Sigma \sigma_i \partial \zeta_i/\partial t \tag{8.13}$$

Representing the local change of environmental vorticity ($\tilde{\zeta}$) and the local change of in-cloud vorticity (ζ_i) for each individual cloud within A as line integrals using Stokes' theorem and substituting into (8.13) gives

$$A\,\partial \bar{\zeta}/\partial t = \oint_E (\partial \underset{\sim}{v}/\partial t)\cdot d\underset{\sim}{l} + \sum_k \oint_C (\partial \underset{\sim}{v}/\partial t)\cdot d\underset{\sim}{l} \tag{8.14}$$

Figure 8.3 illustrates circuits for the line integrals of (8.14). As the grid geometry of Fig. 8.3 suggests, we break the environmental and cloud circuits into components, resulting in

$$\begin{aligned} A\,\partial \bar{\zeta}/\partial t = {} & \{\oint_{E_A} \underset{\sim}{H}\cdot d\underset{\sim}{l} + \sum_n \left(\oint_{E_B} \underset{\sim}{H}\cdot d\underset{\sim}{l} - \oint_{E_C} \underset{\sim}{H}\cdot(-d\underset{\sim}{l})\right) \\ & + \sum_m \oint_{E_I} \underset{\sim}{H}\cdot(-d\underset{\sim}{l})\} + \{\sum_n \oint_C \underset{\sim}{H}\cdot d\underset{\sim}{l} + \sum_m \left(\oint_{C_I} \underset{\sim}{H}\cdot d\underset{\sim}{l} + \oint_{C_B} \underset{\sim}{H}\cdot d\underset{\sim}{l}\right)\}\,, \end{aligned} \tag{8.15}$$

where $\underset{\sim}{H} = \partial \underset{\sim}{v}/\partial t$. Summation over n in (8.15) applies to all interior clouds, and summation over m applies to all clouds that intersect L.

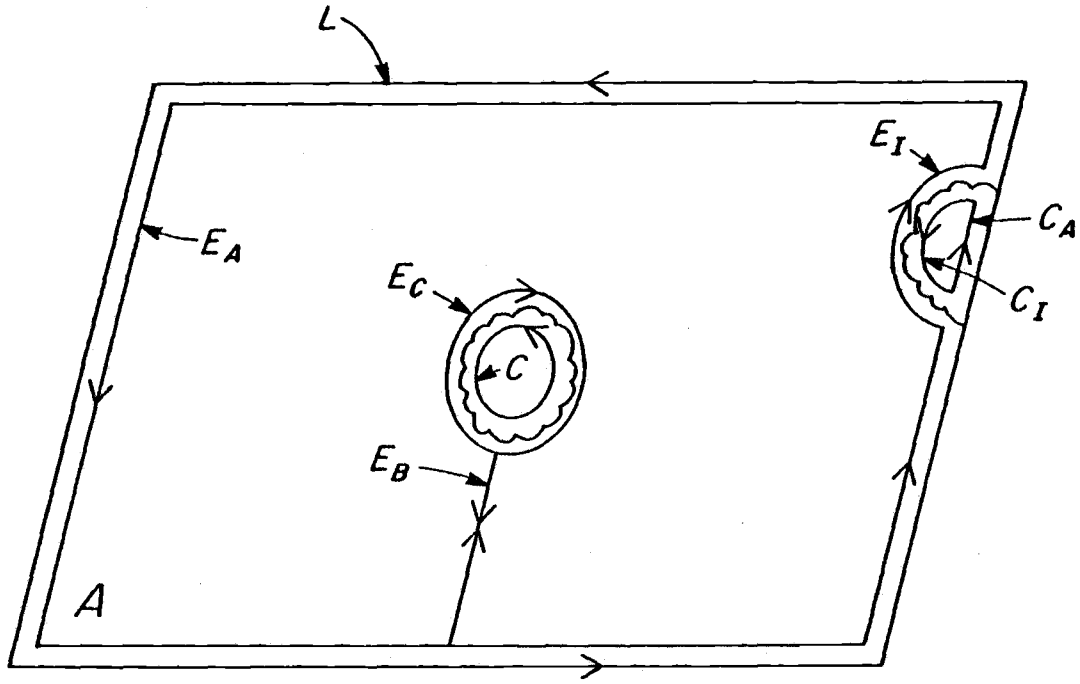

Figure 8.3. Integration circuits around the clouds and the environment within the averaging area A.

The set of line integrals in the first set of brackets describes all circuit components enclosing the environment, while the set of line integrals in the second set of brackets describes cloud-circuit components. In accordance with convention, a negative line increment (-dl) signifies a circuit made in a clockwise direction; all circuits with a positive increment are made in a counterclockwise direction. Since each circuit E_B is traversed twice, once in each direction, their net contribution vanishes. The sets of contributions due to circuits in different directions around each cloud also cancel, and since $L = E_A + C_A$, (8.15) reduces to (8.12). This result is one which we have stated before, and it therefore comes as no surprise. However, the cancellation between the contributions to $\partial\bar{\zeta}/\partial t$ due to interior cloud circuits and those due to internal components of the environmental circuits is a significant finding, because it suggests that it is not appropriate to apply the averaging operator given by (8.1) to vorticity. That is, the conceptual picture implied by (8.1), according to which an "average" of a quantity is computed by sampling the value of the quantity in each cloud and in the environment, is not particularly useful when applied to vorticity, because the sampled cloud contributions must always be canceled by equal but opposite contributions in the environment. By contrast, the contributions that cloud and environmental values of thermodynamic variables (for instance, specific humidity, q) make to the large-scale average will not in general cancel. Thus, to compute a precise large-scale averaged value, it is important to know the values of q in clouds and in the environment. To compute a large-scale average of vorticity, on the other hand, the in-cloud and environmental values of vorticity need not be known.

The nature of the "ambiguity" (if it might be so termed) that arises when (8.1) is applied to vorticity is illustrated by Fig. 8.4. On the figure, the only difference between the situations

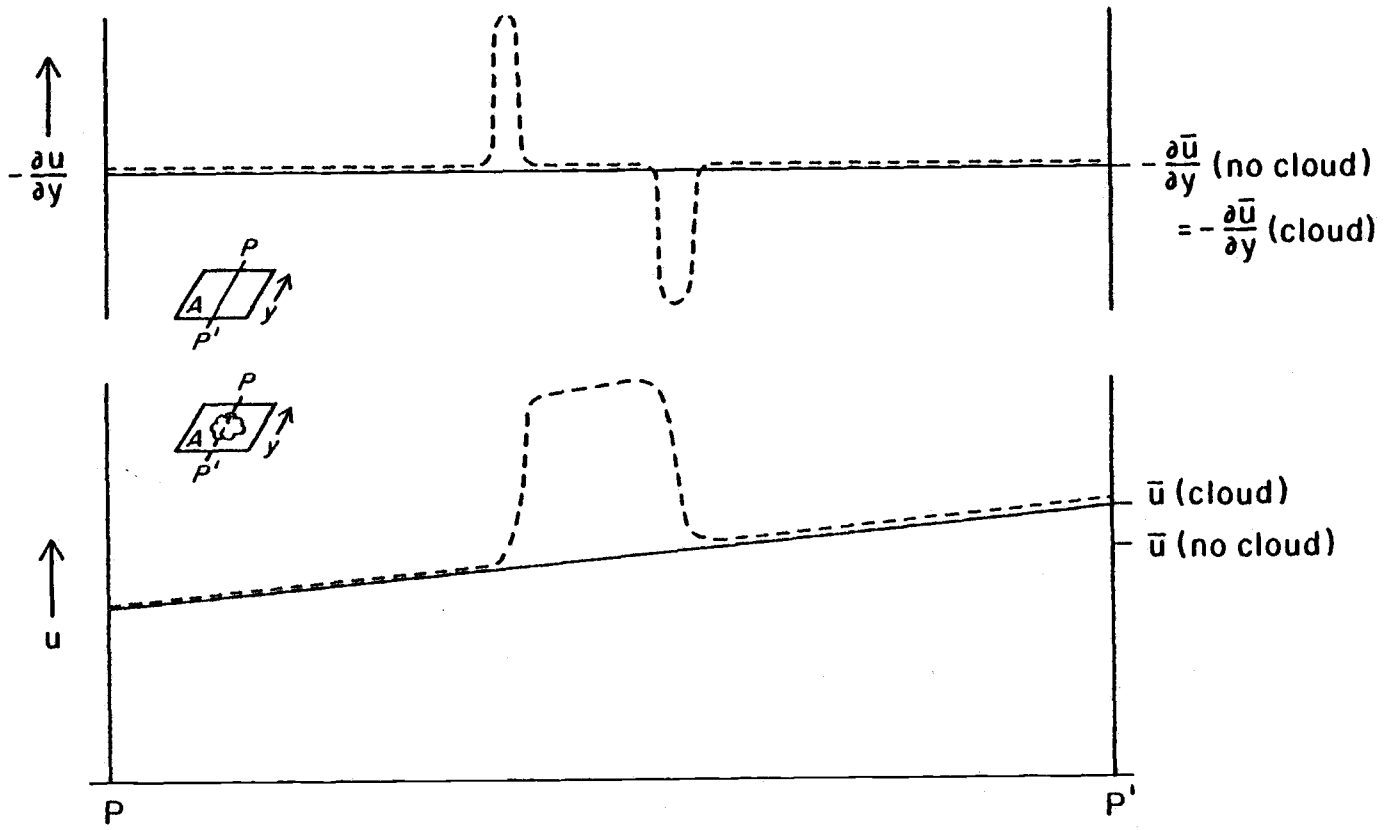

Figure 8.4. Hypothetical meridional variation of zonal velocity and one component of vorticity ($-\partial u/\partial y$) in an averaging area without clouds (solid curves) and with a cloud (dashed curves).

depicted by the solid and dashed lines is the presence of a cloud in the latter case (the horizontal dimensions of the cloud have been greatly exaggerated). Clearly, the presence of the cloud has affected the average value of u in the averaging area, but it has had no effect on vorticity (as given by $-\partial u/\partial y$). The reason for this is that vorticity, as a gradient quantity, is specified completely by the end-point values of u (assuming that u is continuous across A). Thus it is independent of the interior excursions of u. The formalism of (8.1) is well suited to represent the average of scalar quantities in clouds and their environment, particularly when there is not a direct dynamical relationship between the in-cloud and environmental values of the quantity. Examples of such quantities are q (as described before) and static energy. However, when dealing with vector quantities which are kinematically related such as momentum and vorticity, the formalism of (8.1) must be carefully considered in the development of parameterization schemes.

A closely-related issue concerns the consistency of allowing $\tilde{\eta}$ and η_i to be independently determined, as in application they often are. To a degree, this question arises because of the ambiguity involved in determining the location of the cloud boundaries in relation to the vorticity field near the cloud boundary. As the idealized cross-section of u through a cloud in Fig. 8.5 shows, placement of cloud boundaries outside the region of cloud-related momentum perturbations (the short-dashed vertical lines) means that the cloud has the same net vorticity (given, again, as $-\partial u/\partial y$) as the environment. If the boundaries are placed somewhere within the cloud (e.g., the inner long-dashed vertical lines), there can then be a net in-cloud vorticity excess over the average large-scale vorticity, but this excess is compensated by an equal but opposite vorticity excess in the near-environment surrounding the cloud. Neglecting this vorticity excess in the

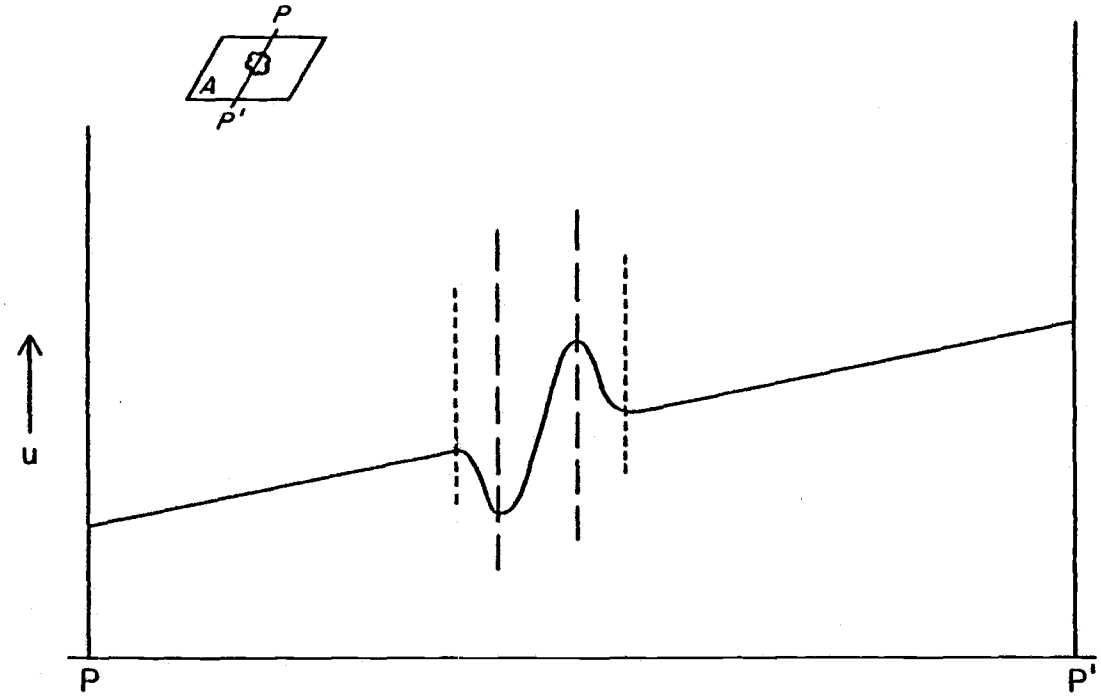

Figure 8.5. Hypothetical meridional variation of zonal velocity in an averaging area containing a cloud with non-zero vorticity. See text for further explanation.

environment (for instance, by assuming that $\tilde{\zeta} \doteq \bar{\zeta}$) but including in-cloud vorticity cannot therefore be justified by scaling arguments. When both are included, they cancel each other. This argument remains valid no matter how intense the in-cloud vorticity is allowed to become.

The schematic diagrams of Fig. 8.6 illustrate another difficulty in the interpretation of (8.8). In Fig. 8.6a, in-cloud vorticity is assumed to be zero, while in-cloud momentum is positive and greater than the environmental momentum. As the solid and dashed curves for times t_0 and t_1 demonstrate, detrainment of momentum by clouds between the two times can produce an increase in the magnitude of the meridional gradient of large-scale momentum ($\bar{u}$). As a result, large-scale cyclonic vorticity has also been produced, a production which is not represented by any of the terms of (8.8). Conversely, in the situation illustrated in Fig. 8.6b in-cloud momentum and environmental momentum are both assumed to be 0, while in-cloud vorticity is finite and positive. The first RHS term of (8.8), which describes the detrainment of excess vorticity, predicts the production of cyclonic vorticity between times t_0 and t_1 in this case, whereas the schematic suggests that no change in $\bar{u}$ (and hence no change in $-\partial\bar{u}/\partial y$ or in $\bar{\zeta}$) will result. In both of these cases, the first RHS term of (8.9) (which represents the detrainment of excess momentum) qualitatively predicts the correct production of $\bar{\zeta}$.

In summary, we re-emphasize our earlier conclusion that clouds can change the large-scale vorticity only insofar as they change the rotational part of the large-scale average momentum. It follows that the detrainment of vorticity from cumulus clouds cannot of itself produce large-scale vorticity unless the detrainment process is taken to include (or consist of) the detrainment of momentum. The operative mechanisms in the production of vorticity by cumulus clouds can then be assumed to include, and be

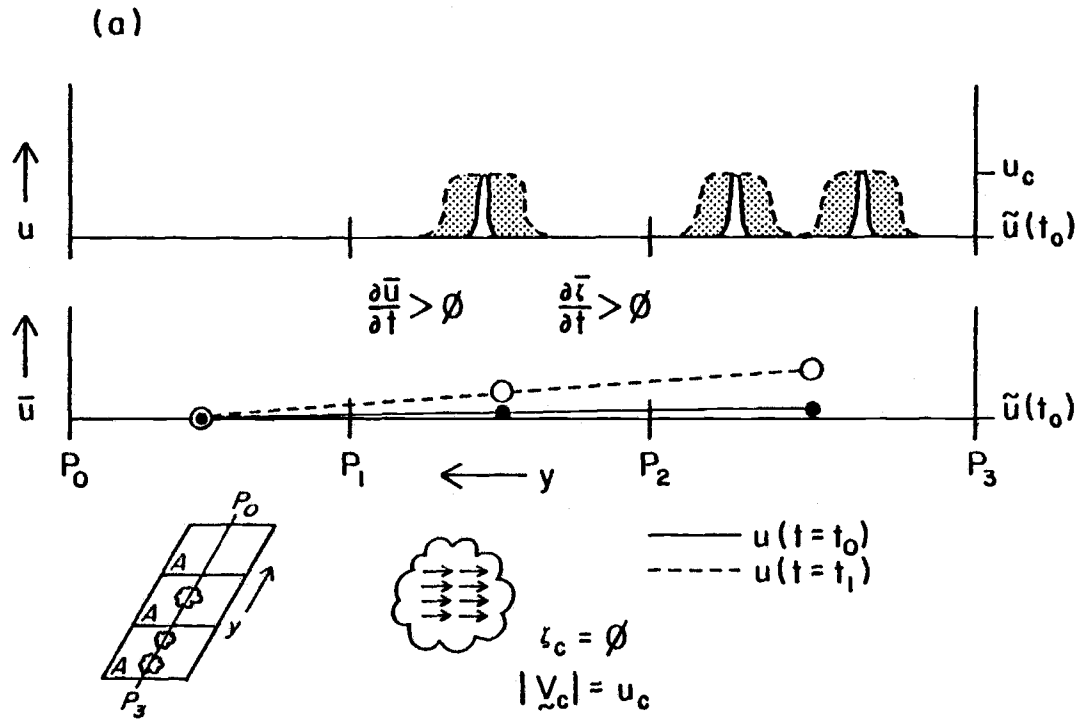

Figure 8.6. Hypothetical meridional variation of zonal velocity (u) and area-averaged zonal velocity ($\bar{u}$) across three averaging areas at successive times t_0 (solid line) and t_1 (dashed line). Net detrainment has occurred between t_0 and t_1. The stippled areas denote the effect of detrainment. In (a), there is a net in-cloud momentum excess (over environmental momentum), but in-cloud vorticity is zero. In (b), in-cloud momentum is zero but in-cloud vorticity is positive.

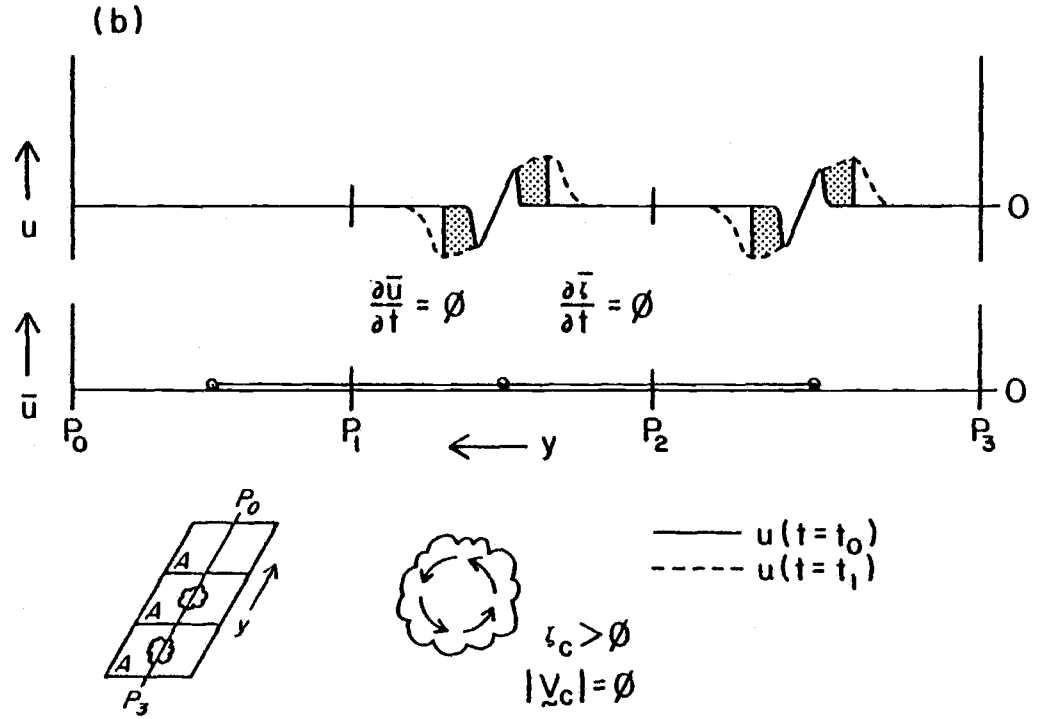

Figure 8.6 (continued)

limited to, (1) a horizontally-varying detrainment of excess momentum, (2) the horizontally-varying vertical advection of momentum by cumulus-induced compensating mass flux, and (3) the twisting of horizontally-oriented large-scale vorticity into the vertical by a horizontally-varying compensating mass flux. These three mechanisms correspond, respectively, to the three terms of Z_M (8.9). Each of these three processes require that there be a horizontal gradient of convective activity.

Without having rigorously specified the source of the inconsistency between Z_M and Z_ζ, we find reason to prefer Z_M because it does not share the interpretational difficulties discussed above. Stated in another way, Z_M more clearly embodies the principles enumerated in the previous paragraph relating to the way in which cumulus clouds can affect large-scale vorticity. Furthermore, as the results of previous chapters have shown, large-scale vorticity can be produced by accelerations or decelerations that vary horizontally, a physical mechanism that is incorporated into Z_M but evidently not into Z_ζ. In the next section we will add further support for this preference by comparing computed values of Z_M and Z_ζ with diagnosed vorticity-budget residuals.

8.5 Comparison of Z_M and Z_ζ with diagnosed residuals in the upper troposphere

The observationally-determined fields of the apparent vorticity source Z_O (the subscript "O" will hereafter denoted "observed") described in previous chapters provide an opportunity to test which of the alternate parameterizations (Z_M or Z_ζ) gives better agreement. In this section, a comparison is made between Z_O and simplified estimates of Z_M and Z_ζ using the composites of upper-tropospheric wind observations described in Chapters 6 and 7. This comparison will show that Z_M more successfully reproduces

the fields of Z_0 associated with the vorticity couplets examined in the previous chapter than does Z_ζ.

In order to compute Z_M and Z_ζ, estimates of M_c, δ_i, $\gamma_{\delta i}$, and $\eta_{\delta i}$ must be made. Several diagnostic models of varying complexity have been developed to compute M_c and δ_i (e.g., Yanai et al., 1973; Arakawa and Schubert, 1974; Johnson, 1976, 1980), each of which proceeds by solving a set of several thermodynamic equations for several unknowns (including M_c, δ_i, and thermodynamic variables). These computations are beyond the scope of this thesis. However, by making various simplifications suggested by the particular characteristics of the analyses in this thesis, and by using applicable results from other GATE diagnostic studies, reasonable estimates of Z_M and Z_ζ can be made quite simply. While these estimates cannot be expected to be definitive in a quantitative sense, they do provide a first-order basis for comparison.

The values of M_c, its vertical gradient, and $D = \Sigma\delta_i$ used in this comparison are based on those calculated by Johnson (1980) for wave category 4 (the trough category) of a composite easterly wave from Phase 3 of GATE. Category 4 was chosen because clusters in GATE normally occurred within the troughs of easterly waves. Since Johnson's analysis was performed on easterly-wave-scale fields, the results are not directly applicable to cluster-scale computations of Z such as those of this thesis. To correct for these scale differences, it is assumed that cumulus mass flux in the upper troposphere can be considered to be proportional to the percent of sky covered by deep clouds (those whose tops reach 300 mb and above). Figure 6.2 shows that sky cover by deep clouds is essentially 100% in clusters, while the analagous coverage in easterly wave troughs is approximately 40% (cf. Fig. 7.14). Johnson's values of M_c and D are accordingly increased by a factor of 100/40. Horizontal gradients of M_c and D are estimated by assuming that both reach a maximum value at the cluster center and

decrease linearly in all directions, approaching a typical background value at 150 km, the approximate radius of large GATE clusters. The background value is taken from Johnson (1980) by averaging across easterly wave categories. The north-to-south variation of the resulting estimates at 250 mb are shown on Fig. 8.7 (variations in any other radial direction would look the same).

Cumulus mass flux and detrainment can be alternatively estimated by simply using the easterly wave values diagnosed by Johnson (1980), or by using the values diagnosed by Nitta (1977) for two particularly intense GATE clusters. By the arguments given in the preceding paragraph, the former is considered to be an underestimate, while the latter is likely an overestimate. A comparison of the resulting values of Z_M are shown on a subsequent figure.

In order to estimate the detrainment terms of Z_M and Z_ζ, we must also estimate the velocity ($\underset{\sim}{v}_{\delta i}$) and the vorticity ($\eta_{\delta i}$) of the detraining air. Using the supposition of Schneider and Lindzen (1976) that momentum is approximately conserved within cumulus updrafts and extending it to include vorticity, $\underset{\sim}{v}_{\delta i}$ and $\eta_{\delta i}$ are assumed to be equal to the large-scale values $\bar{\underset{\sim}{v}}$ and $\bar{\eta}$ at cloud base (taken to be 950 mb). Since $\underset{\sim}{v}_{\delta i}$ and $\eta_{\delta i}$ are now constant with respect to δ_i, they can be given as $\underset{\sim}{v}_c$ and η_c and pulled outside of the summations of cloud subensembles in (8.6) and (8.8). Z_M and Z_ζ can then be given as

$$Z_M = D(\bar{\underset{\sim}{v}}(950) - \bar{\underset{\sim}{v}}) - M_c \partial \bar{\underset{\sim}{v}}/\partial p - \underset{\sim}{k}\cdot\underset{\sim}{\nabla} M_c \times \partial \bar{\underset{\sim}{v}}/\partial p \qquad (8.16)$$

and

$$Z_\zeta = D(\bar{\eta}(950) - \bar{\eta}) + \bar{\eta}\, \partial M_c/\partial p - M_c \partial \bar{\zeta}/\partial p - \underset{\sim}{k}\cdot\underset{\sim}{\nabla} M_c \times \partial \bar{\underset{\sim}{v}}/\partial p \,. \qquad (8.17)$$

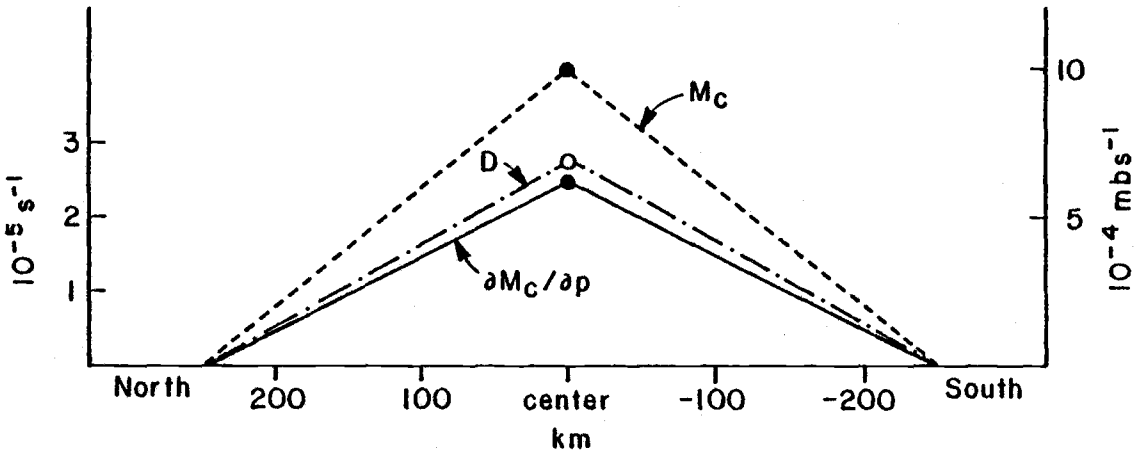

Figure 8.7. Meridional variation of M_c (units on right axis), and total detrainment (D) and vertical convergence of mass flux (units on left axis) through the composite cluster center at 250 mb. See text for source of estimates.

All terms can now be computed from composite cluster fields of $\bar{v}$ and $\bar{\eta}$ and our estimates of cumulus mass flux and detrainment.

Values of Z_M, Z_ζ, and Z_0 at 250 mb are shown on Fig. 8.8 for three locations within the composite cluster: the cluster center, 1-1/2 degrees north (near the location of the positive center of the vorticity couplet), and 1-1/2 degrees south (near the location of the negative center of the vorticity couplet). As the figure demonstrates, Z_M and Z_0 agree well, both quantitatively and qualitatively. While the quantitative agreement is probably somewhat fortuitous, it is clear that the qualitative form of Z_0, with its asymmetric couplet, is reproduced well by Z_M. This conclusion still holds when the other estimates of mass flux and detrainment mentioned previously are used (cf. Fig. 8.9). The axial symmetry of Z_ζ, on the other hand, agrees poorly with Z_0. As the graphs of the components of the parameterizations in Fig. 8.10 demonstrate, the forms of Z_M and Z_ζ, whether symmetric or asymmetric, are essentially determined by the detrainment terms of the two parameterizations. We are thus again lead to the conclusion that the manner in which the direct effects of clouds are included in Z_M is to be preferred to the manner in which they are included in Z_ζ.

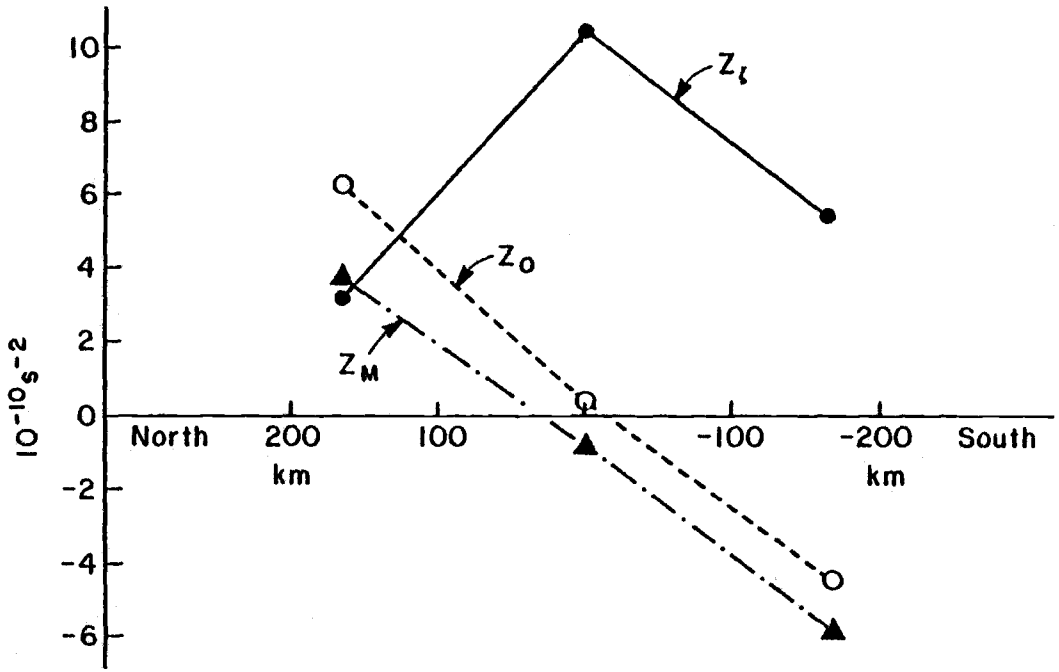

Figure 8.8. As in Fig. 8.7 except for the observed apparent vorticity source (Z_0) and computations of two parameterizations of the apparent source (Z_M and Z_ζ).

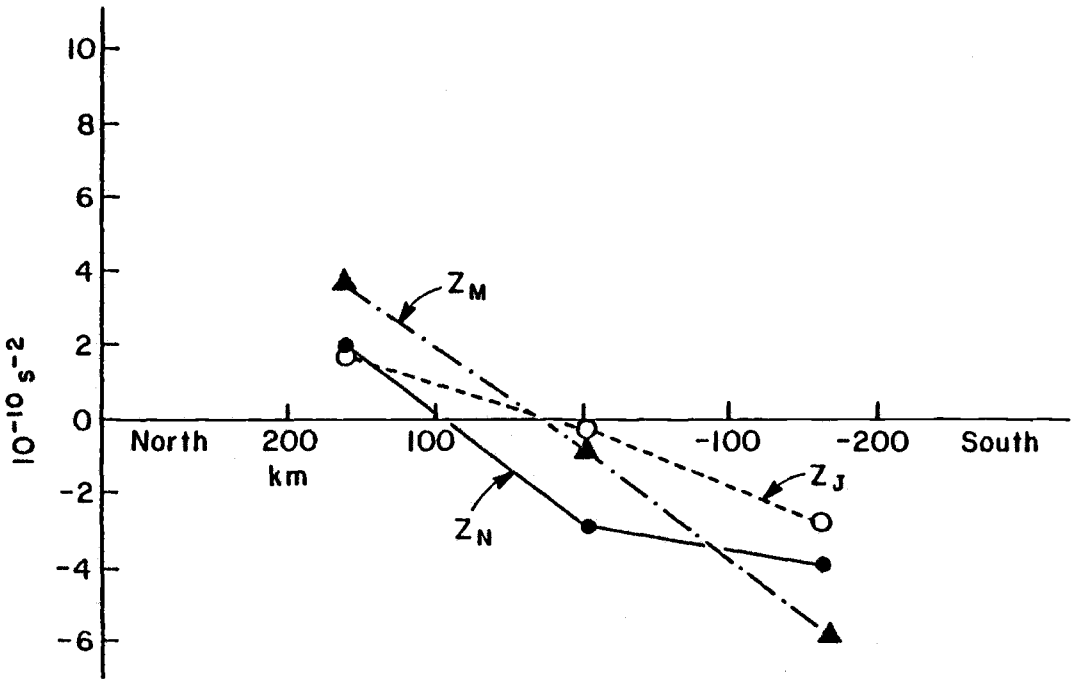

Figure 8.9. As in Fig. 8.7 except for computations of Z_M made using three different estimates of cumulus mass flux. Z_J was computed using easterly-wave-trough values from Johnson (1980), Z_M was computed as described in the text by correcting the cumulus mass flux of Johnson (1980) to make it consistent with cluster-scale phenomena, and Z_N was computed using mass flux values computed by Nitta (1977) for two intense GATE clusters.

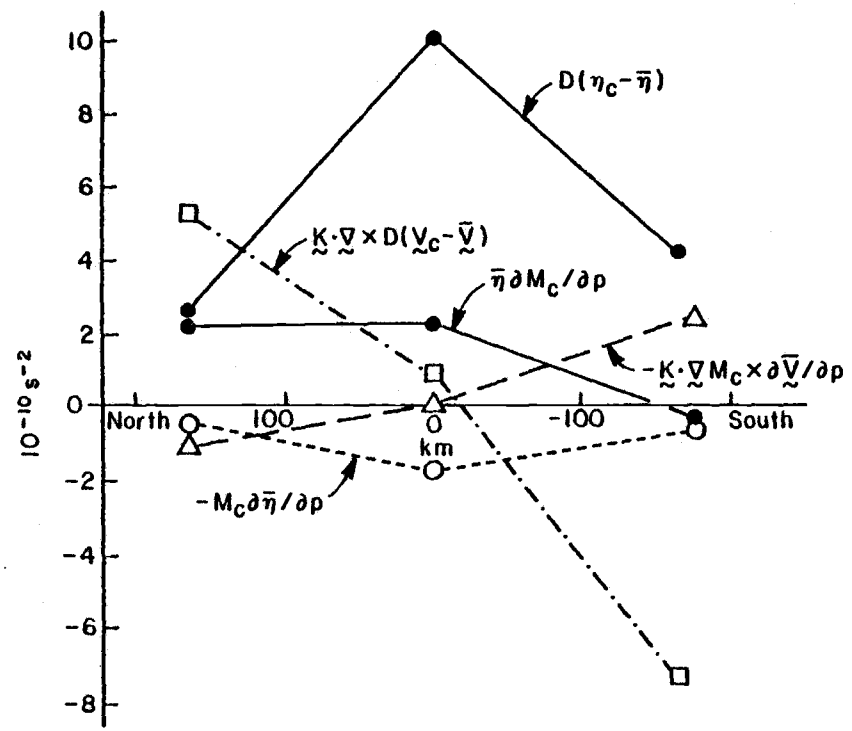

Figure 8.10. As in Fig. 8.7 except for components of Z_M and Z_ζ.

CHAPTER 9. CONCLUSIONS AND SUGGESTIONS FOR FURTHER RESEARCH

In this thesis, the wind and thermodynamic fields associated with two major GATE cloud clusters have been described. Composite fields of the wind components, vorticity, and divergence have also been presented. The primary source of data has been the gridded sets of wind variables prepared from radiosonde observations by Ooyama (AOML-NOAA) and Chu (SSEF, University of Wisconsin, Madison), and the set of thermodynamic data prepared by Esbensen (Oregon State University). The major objectives have been to provide a thorough description of the structure of tropical cloud clusters and to determine the ways in which cluster-scale circulations interact with smaller-scale convective systems (like mesoscale circulations and cumulus clouds).

The most important results of this thesis and their implications are summarized by chapter below.

Because of the exceptional resolution of the Ooyama-Chu and Esbensen data sets (in particular their horizontal resolution), the case studies of the much-studied 4 September and 5 September clusters in Chapter 5 were able to describe cluster-scale features and their evolution in better detail than previously possible. The most interesting features that resulted from these case studies were the localized area of strong boundary layer convergence that preceded the development of the 5 September cluster, a cluster-scale region of downward velocity beneath the anvil of the 4 September squall cluster, and cluster-scale upward velocity within the anvils of both clusters in their mature and dissipating stages. The latter two of these findings add further observational support to the existence of these vertical-velocity features. If they are indeed shown to be of mesoscale or cluster-scale origin (as this thesis and other observational and modeling studies have suggested), it would be clearly indicated that cluster-scale circulations play

an important role in the tropics. The consequent implication to modelers would be that an adequate way must be found to either include them explicitly or parameterize them in synoptic-scale models.

In addition, the time evolution of cluster-scale vorticity and vorticity budget terms in these clusters was described for the first time. Each budget term was found to be significant at some level during some stage of the clusters' development. Apparent production of vorticity by small-scale circulations (as given by the budget residuals) was particularly large in the boundary layer during the growing stage of the 5 September cluster, at the level of maximum easterly wave amplitude in the 4 September squall cluster, and (as examined in detail in Chapter 7) within the anvils of both clusters. While it was not possible to specify the kind of small-scale mechanism that produced cluster-scale vorticity in these clusters (cumulus clouds and mesoscale circulations are among the possibilities), it appears likely that the role of these mechanisms must be understood in order to fully describe the wind fields of these clusters.

The good horizontal resolution is also the most valuable aspect of the cluster composites of slow-moving GATE clusters presented in Chapter 6. No really comparable composites of tropical clusters exist. The composite sections and profiles provide a basis for examining the validity of hypotheses about cluster structure or evolution. For instance, on the basis of the composites it is found that Ekman pumping probably is not the essential formative process in GATE clusters, that clusters form in regions of reduced wind shear, and that the shift of the surface confluence zone from a position south of the cluster center to a position north of the center during the cluster life cycle may have an important influence on the cluster development. The composite profiles of vorticity budget terms at the cluster center demonstrate a more complex balance, and also a more complex budget residual, than that found by Ruprecht and Gray (1976).

Evidence presented in Chapter 7 strongly suggests that cumulus clouds, or mesoscale circulations related to cumulus convection, can produce large-amplitude cluster-scale features. Since the same features appear on easterly wave composites, the importance of the processes that formed them is further substantiated. The large upper-tropospheric vorticity couplets described have only been noted before in GATE data, and their origin is quantitatively investigated for the first time in this thesis. The convective origin of the wind decelerations that produce the vorticity couplets is strongly indicated by the large vorticity budget residuals and by the coincidence of the regions of decelerations with anvil clouds (as determined by anvil index values computed from the radiation data processed by CG).

An important implication of Chapter 7 is that the effects of cumulus clouds on large-scale fields of vorticity probably cannot be interpreted simply as a mixing process. It is suggested that the production of large-scale vorticity by cumulus clouds should be parameterized by considering the effect of the horizontal variations of cumulus momentum effects rather than by consideration of the vorticity budget of the cumulus ensembles. In other words, the effects of cumulus clouds on the large-scale vorticity budget should be parameterized simply as the curl of the parameterized effects on the momentum budget. Discussion of this possibility is presented in Chapter 8, which includes conceptual and theoretical arguments concerning the interpretation and parameterization of vorticity budget residuals.

In the course of this thesis, perhaps as many questions have been raised as have been answered. This was perhaps inevitable, given that the analyses were performed using new data sets that can resolve features that have heretofore been studied mostly by inference from budgets at larger scales. Much further information undoubtedly remains to be discovered in the gridded sets of wind and thermodynamic fields used in this thesis. Hopefully,

many subsequent studies will deal with cluster structure and interaction with other scales of convective systems.

In addition to this general goal, several more specific ideas for further work have been suggested by the results of this thesis. I will list some of them here, in the approximate order of the chapters to which they are most closely related.

There is a need to expand the scope of cluster case studies such as those presented in Chapter 5. As regards the 4 September and 5 September clusters, thermodynamic data may be able to suggest some answers to a few of the questions concerning the anvils on these days. For instance, what is the source of the cluster-scale updrafts within the anvils? Are they due to buoyancy provided by condensation, or are they mechanically forced by the convergence near the base of the anvil? Is there a structural difference between the anvils in the slow-moving clusters and those of the squall-clusters?

It is also important to study other cases of the approximately 10 large clusters (including both the squall and slow-moving types) that occurred during Phase 3 of GATE. Among these, the best cases may be the cluster on 2 September, the squall-cluster on 12 September, and the cluster on 17 September.

Other budgets of kinematic and thermodynamic quantities should also be undertaken. For instance, if geopotential gradients of sufficient quality can be derived, a momentum budget could be computed. The results from these budget computations might help to pinpoint the source of the decelerations near 225 mb that have occupied a significant portion of the effort in this thesis. Are they due to unresolved circulations? Can they be partly produced by pressure gradients on the scale of the clusters?

Budget studies of moisture, heat, and kinetic energy presently being done should also provide valuable information.

A major need (one addressed by the composite study of Chapter 6) is to establish as firm and thorough a description of the fields within clusters as possible. In particular, there have been few detailed studies of the horizontal structure of clusters previous to this thesis. Intelligent compositing can provide a good way to investigate clusters by removing random observational errors and by isolating the common features of the individual clusters.

Thus far, the compositing studies performed here at OSU have concentrated on the kinematic fields of slow-moving clusters. Thermodynamic fields should also be composited. With a complete set of composite fields, including the results of budget studies, any number of hypotheses concerning the development and evolution of clusters could be tested. Such a set of composite fields might also provide guidance and/or initial conditions to mesoscale modeling studies.

Approximately half the large clusters of GATE were squall clusters that moved in various directions at a relatively high rate of speed. Compositing these clusters presents certain problems that do not occur when the slow-moving clusters are composited. For instance, it is possible that the propagation direction of these squalls has some bearing on the orientation of the wind and vorticity fields associated with them. Upper-tropospheric vorticity couplets like those discussed in Chapter 7 did occur in some squalls, but they were generally less distinct, and preliminary attempts to composite squalls by using the procedure of Chapter 6 did not result in a clear couplet structure. Further attempts at compositing should perhaps allow the composite grid to vary its orientation from a strict north-south, east-west grid layout. In this way, inherent directional variations between squalls might perhaps be taken into account. If, on the other hand, some portions of squalls (e.g., the anvils) can be shown to be similar enough to the anvils of slow-moving clusters, the

addition of extra cases to the anvil composites would provide a substantial improvement in sample size.

If it proves to be true, as suggested by Chapter 7, that the upper-tropospheric decelerations associated with GATE clusters are a result of cumulus or mesoscale processes, then there is the strong possibility that these circulations have a significant influence on the wind fields of the tropical atmosphere. It would be very interesting to search for decelerations of this type in other kinds of convective systems (perhaps, for instance, in the "mesoscale convective complexes" or MCC's, identified over the United States).

Evidence presented in Chapter 8 suggests that the alternative parameterization Z_M might be a better representation for the apparent vorticity source than the widely-used Z_ζ. A rigorous mathematical description of the source of the inconsistency between these two parameterizations is needed. Further tests of the comparative validity of these two parameterizations might be accomplished by computing actual values of both and comparing them to vorticity budget residuals like those presented in this thesis.

BIBLIOGRAPHY

Albignat, J. P., and R. J. Reed, 1980: The origin of African wave disturbances during Phase III of GATE. Mon. Wea. Rev., 108, 1827-1839.

Arakawa, A., and W. H. Schubert, 1974: Interaction of a cumulus cloud ensemble with the large-scale environment, Part I. J. Atmos. Sci., 31, 674-701.

Arkell, R., and M. Hudlow, 1977: GATE International Meteorological Radar Atlas. U.S. Department of Commerce, 222 pp. (NTIS PB-277 233/3GI).

Barnes, G. M., and M. Garstang, 1982: Subcloud layer energetics of precipitating convection. Mon. Wea. Rev., 110, 102-117.

Betts, A. K., R. W. Grover, and M. W. Moncrieff, 1976: Structure and motion of tropical squall-lines over Venezuela. Quart. J. Roy. Meteor. Soc., 102, 395-404.

Brown, J. M., 1979: Mesoscale unsaturated downdrafts driven by rainfall evaporation: a numerical study. J. Atmos. Sci., 36, 313-338.

Browning, K. A., and F. H. Ludlam, 1962: Airflow in convective storms. Quart. J. Roy. Meteor. Soc., 88, 117-135.

Burpee, R. W., 1972: The origin and structure of easterly waves in the lower troposphere of North Africa. J. Atmos. Sci., 29, 77-90.

Charney, J. G., 1963: A note on large-scale motions in the tropics. J. Atmos. Sci., 20, 607-609.

_____, and M. E. Stern, 1962: On the stability of internal baroclinic jets in a rotating atmosphere. J. Atmos. Sci., 19, 159-172.

Charnock, H., 1957: Notes on the specification of atmospheric turbulence. Pro. Roy. Statist. Soc., A164, 398-408.

Chen, Y.-L., and Y. Ogura, 1982: Modulation of convective activity by large-scale flow patterns observed in GATE. J. Atmos. Sci., 35, 1260-1279.

Cho, H.-R., and L. Cheng, 1980: Parameterization of horizontal transport of vorticity by cumulus convection. J. Atmos. Sci., 37, 812-826.

_____, _____, and R. M. Bloxam, 1979: The representation of cumulus cloud effects in the large-scale vorticity equation. J. Atmos. Sci., 36, 127-139.

Chu, J.-H., M. Yanai, and C.-H. Sui, 1981: Effects of cumulus convection on the vorticity field in the tropics. Part I: the large-scale budget. J. Meteor. Soc. Japan, 59, 535-546.

Cox, S. K., and K. T. Griffith, 1979: Estimates of radiative divergence during Phase III of the GARP Atlantic Tropical Experiment: Part I. Methodology. J. Atmos. Sci., 36, 576-585.

Esbensen, S. K., E. I. Tollerud, and J.-H. Chu, 1982: Cloud-cluster-scale circulations and the vorticity budget of synoptic-scale waves over the eastern Atlantic intertropical convergence zone. Mon. Wea. Rev., 110, 1677-1692.

Fein, J. S., 1977: Global vorticity budget over the tropics and subtropics at 200 mb during northern hemisphere summer. Pure Appl. Geophys., 115, 1493-1500.

Frank, W. M., 1978: The life cycles of GATE convective systems. J. Atmos. Sci., 35, 1256-1264.

_____, 1983: The structure and energetics of the East Atlantic Intertropical Convergence Zone. J. Atmos. Sci. (accepted for publication).

Fritsch, J. M., and J. M. Brown, 1982: On the generation of convectively driven mesohighs aloft. Mon. Wea. Rev., 110, 1554-1563.

Gamache, J. F., and R. A. Houze, Jr., 1982: Mesoscale air motions associated with a tropical squall line. Mon. Wea. Rev., 110, 118-135.

Gandin, L. S., 1963: Objective Analysis of Meteorological Fields. Gidrometeor. Izdat., Leningrad. (Translated from Russian, Israel Program for Scientific Translations, Jerusalem, 1965, 242 pp.)

Gray, W. M., 1973: Cumulus convection and larger scale circulations. I. Broadscale and mesoscale considerations. Mon. Wea. Rev., 101, 839-855.

_____, and R. W. Jacobson, Jr., 1977: Diurnal variation of deep cumulus convection. Mon. Wea. Rev., 106, 1171-1188.

Hodur, R. M., and J. S. Fein, 1977: A vorticity budget over the Marshall Islands during the spring and summer months. Mon. Wea. Rev., 105, 1521-1526.

Holton, J. R., 1972: An Introduction to Dynamic Meteorology. New York, Academic Press, 319 pp.

_____, and D. E. Colton, 1972: A diagnostic study of the vorticity balance at 200 mb in the tropics during the northern summer. J. Atmos. Sci., 29, 1124-1128.

Houze, R. A., Jr., 1977: Structure and dynamics of a tropical squall-line system. Mon. Wea. Rev., 105, 1540-1567.

_____, and A. K. Betts, 1981: Convection in GATE. Rev. Geophys. Space Phys., 19, 541-576.

Johnson, R. H., 1976: The role of convective-scale precipitation downdrafts in cumulus and synoptic-scale interactions. J. Atmos. Sci., 33, 1890-1910.

_____, 1980: Diagnosis of convective and mesoscale motions during Phase III of GATE. J. Atmos. Sci., 37, 733-753.

Klemp, J. B., and R. B. Wilhelmson, 1978: Simulations of right- and left-moving storms produced through storm splitting. J. Atmos. Sci., 35, 1097-1110.

Krishnamurti, T. N., R. J. Pasch, and P. Ardanuy, 1979: Prediction of African Waves and Specification of Squall Lines. Report No. FSU 79-2, Department of Meteorology, Florida State University, 55 pp.

Leary, C. A., 1979: Behavior of the wind field in the vicinity of a cloud cluster in the Intertropical Convergence Zone. J. Atmos. Sci., 36, 631-639.

_____, and R. A. Houze, Jr., 1979: The structure and evolution of a tropical cloud cluster. J. Atmos. Sci., 36, 437-457.

LeMone, M. A., 1983: Momentum transport by a line of cumulonimbus. J. Atmos. Sci. (accepted for publication).

Maddox, R. A., D. J. Perkey, and J. M. Fritsch, 1981: Evaluation of upper-tropospheric features during the development of a meso-scale convective complex. J. Atmos. Sci., 38, 1664-1674.

Marks, F. D., Jr., 1980: The origin and development of a tropical mesoscale cloud line. Ph.D. Thesis, Dept. of Meteor., M.I.T., 146 pp.

Martin, D. W., and V. E. Suomi, 1972: A satellite study of cloud clusters over the tropical North Atlantic Ocean. Bull. Amer. Meteor. Soc., 53, 135-156.

McBride, J. L., and W. M. Gray, 1980a: Mass divergence in tropical weather systems, Paper I: Diurnal variation. Quart. J. Roy. Meteor. Soc., 106, 501-516.

_____, and _____, 1980b: Mass divergence in tropical weather systems, Paper II: Large-scale controls on convection. Quart. J. Roy. Meteor. Soc., 106, 517-538.

Miller, D. B., and R. G. Feddes, 1971: Global atlas of relative cloud cover 1967-70. U.S. Department of Commerce, 237 pp.

Moncrieff, M. W., and J. M. Miller, 1976: The dynamics and simulation of tropical cumulonimbus and squall lines. Quart. J. Roy. Meteor. Soc., 102, 373-394.

Nitta, Ts., 1975: Observational determination of cloud mass flux distributions. J. Atmos. Sci., 32, 73-91.

_____, 1977: Response of cumulus updraft and downdraft to GATE A/B-scale motion systems. J. Atmos. Sci., 34, 1163-1186.

Norquist, D. C., E. E. Recker, and R. J. Reed, 1977: The energetics of African wave disturbances as observed during Phase III of GATE. Mon. Wea. Rev., 105, 334-342.

Ogura, Y., and H.-R. Cho, 1973: Diagnostic determination of cumulus cloud populations from observed large-scale variables. J. Atmos. Sci., 30, 1276-1286.

_____, Y. L. Chen, J. Russell, and S.-T. Soong, 1979: On the formation of organized convective systems observed over the Eastern Atlantic. Mon. Wea. Rev., 107, 426-441.

_____, and M.-T. Liou, 1980: The structure of a midlatitude squall line: A case study. J. Atmos. Sci., 37, 553-567.

Ooyama, K. V., 1971: A theory on parameterization of cumulus convection. J. Meteor. Soc. Japan, 49, Special Issue, 744-756.

Payne, S. W., and M. M. McGarry, 1977: The relationship of satellite inferred convective activity to easterly waves over West Africa and the adjacent ocean during Phase III of GATE. Mon. Wea. Rev., 105, 413-420.

Reed, R. J., and E. E. Recker, 1971: Structure and properties of synoptic-scale wave disturbances in the equatorial western Pacific. J. Atmos. Sci., 28, 1117-1133.

_____, and R. H. Johnson, 1974: The vorticity budget of synoptic-scale wave disturbances in the tropical western Pacific. J. Atmos. Sci., 31, 1784-1790.

_____, D. C. Norquist, and E. E. Recker, 1977: The structure and properties of African wave disturbances as observed during Phase III of GATE. Mon. Wea. Rev., 105, 317-333.

Riehl, H., and J. S. Malkus, 1958: On the heat balance in the equatorial trough zone. Geophysica, 6, 503-538.

Ruprecht, E., and W. M. Gray, 1976: Analysis of satellite observed tropical cloud clusters. 1. Wind and dynamic fields. Tellus, 28, 391-413.

Schneider, E. K., and R. S. Lindzen, 1976: A discussion of the parameterization of momentum exchange by cumulus convection. J. Geophys. Res., 81, 3158-3160.

Seguin, W., and M. Garstang, 1976: Some evidence of the effects of convection on the structure of the tropical subcloud layer. J. Atmos. Sci., 33, 660-666.

Shapiro, L. J., 1978: The vorticity budget of a composite African tropical wave disturbance. Mon. Wea. Rev., 106, 806-817.

_____, and D. E. Stevens, 1980: Parameterization of convective effects on the momentum and vorticity budgets of synoptic-scale Atlantic tropical waves. Mon. Wea. Rev., 108, 1816-1826.

Sikdar, D. N., and S. J. Hentz, 1980: Kinematic structure of an Atlantic cloud cluster during GATE and its time variation. Tellus, 32, 439-455.

Stevens, D. E., 1979: Vorticity, momentum and divergence budgets of synoptic-scale wave disturbances in the tropical eastern Atlantic. Mon. Wea. Rev., 107, 535-550.

_____, R. S. Lindzen, and L. J. Shapiro, 1977: A new model of tropical waves incorporating momentum mixing by cumulus convection. Dyn. Atmos. Oceans, 1, 365-425.

Thompson, R. M., S. W. Payne, E. E. Recker, and R. J. Reed, 1979: Structure and properties of synoptic-scale wave disturbances in the intertropical convergence zone of the eastern Atlantic. J. Atmos. Sci., 36, 53-72.

Vincent, D. G., 1981: Kinematic analysis of the large-scale mean state during phases I, II and III of GATE. Quart. J. Roy. Meteor. Soc., 107, 899-918.

Wallace, J. M., and R. E. Dickinson, 1972: Empirical orthogonal representation of time series in the frequency domain. Part I: Theoretical considerations. J. Appl. Meteor., 11, 887-892.

Williams, K. T., and W. M. Gray, 1973: Statistical analysis of satellite-observed trade wind cloud clusters in the western North Pacific. Tellus, 25, 313-336.

Yanai, M., S. Esbensen, and J.-H. Chu, 1973: Determination of bulk properties of tropical cloud clusters from large-scale heat and moisture budgets. J. Atmos. Sci., 30, 611-627.

_____, C.-H. Sui, and J.-H. Chu, 1982: Effects of cumulus convection on the vorticity field in the tropics. Part II: Interpretation. J. Meteor. Soc. Japan, 60, Special Issue, 411-424.

Zipser, E. J., 1969: The role of organized unsaturated convective downdrafts in the structure and rapid decay of an equatorial disturbance. J. Appl. Meteor., 8, 799-814.

_____, 1977: Mesoscale and convective-scale downdrafts as distinct components of squall-line structure. Mon. Wea. Rev., 105, 1568-1589.

_____, R. J. Meitin, and M. A. LeMone, 1981: Mesoscale motion field associated with a slowly moving GATE convective band. J. Atmos. Sci., 38, 1725-1750.

APPENDICES

Appendix A. Analysis scheme for radiosonde data

This appendix is taken directly from Esbensen et al. (1982). It describes the analysis scheme that Ooyama devised to interpolate the wind data produced at ship locations to a regular grid. With some alterations in detail but not in overall structure, the description also applies to the thermodynamic analysis performed by Esbensen. The scheme can be broken into four parts.

a. Editing and analysis of radiosonde observations

To make meaningful intership comparisons and to make editing procedures more objective, Ooyama designed a spectrally controlled interpolation technique using cubic B-splines. The technique was applied to produce time-height sections from the series of upper-air wind soundings at each ship, retaining information on disturbances with periods greater than 12 hours and vertical wavelength greater than or equal to 100 mb.

Through this procedure, the wind data are homogenized to the extent that they represent phenomena from the same part of the frequency and wavenumber domain. Such a procedure is essential in view of the variety of upper-air observing systems and the variety of post-processing procedures employed in producing the final Convective Systems Data Center (CSDC) data set.

The time-height sections were then used in an extensive statistical analysis and in a manual inspection of the original sounding data for the purpose of identifying and removing suspicious data. Since CSDC took a very conservative approach to data editing, this part of the research was an essential but time-consuming process.

b. Determination of the norm field

Ooyama's objective analysis scheme is an extension of Gandin's (1963) method for spatially interpolating deviations from a so-called norm field by minimizing the deviations from the norm in a statistical sense. Although Gandin envisioned the analysis being applied to deviations from a climatological norm, the technique also works well for slowly varying functions of time. In either case, the determination of the norm field is a crucial element in the application of optimal statistical interpolation.

Unfortunately, the slowly varying features of the wind field observed during Phase 3 of GATE show considerable spatial variation, especially at low levels where the northeast trades, southeast trades and monsoonal circulations combine to influence the flow. This complicates the analysis of the norm field since the A/B- and B-scale ship arrays are barely adequate to resolve these quasi-stationary features during Phase 3.

Ooyama chose the 8-day low-pass filtered data from the time-height sections to define the norm field. This low-pass data was used both for the statistical analysis and as input to the spectrally controlled B-spline analysis routines to spatially interpolate the norm field onto constant pressure surfaces. Cutoff wavelengths for the horizontal interpolation in the longitudinal and latitudinal directions were necessarily a compromise between resolution and the horizontal and vertical consistency of the analysis as revealed by the mass budget and the vorticity field. The norm field analysis has wavelength cutoffs at 900 and 1800 km in the latitudinal and longitudinal directions, respectively.

c. Detailed examination and modeling of spatial statistics

In preparation for the statistical interpolation of the deviations of the winds from the norm field, a detailed analysis was

performed on the level-by-level sample spatial variance and correlation tensors of the wind observations. The data at each ship were broken down into period bands covering disturbances in the 12 h to 2 day range, and the 2-8 day range. Using the B-spline routines, the continuous correlation functions (e.g., Gandin, 1963) were objectively analyzed from the sample correlation function constructed from wind observations at pairs of ships, under the assumption that the wind field is statistically homogeneous as far as the correlation function is concerned. The spectrally controlled B-spline routine was used for the analysis, and enabled Ooyama to control the amount of detail in the correlation function.

d. Application of statistical interpolation

The correlation functions were then used to statistically interpolate deviations from the norm field to grid points. Ooyama's extension of the method of optimum interpolation incorporates information from the frequency domain of Fourier-transformed time-sequenced data. The advantage of this method is that it can resolve in a statistical sense the phase angle and spatial coherence of propagating disturbances. For example, the regular propagating nature of synoptic-scale easterly waves is recognized by Ooyama's correlation function, and is automatically included in the statistical interpolation. Finally, cubic B-splines with a wavelength cutoff of 450 km were fit to the gridded data to allow the evaluation of the winds and their spatial derivatives at any location over the arrays.

Appendix B. Finite difference formulations

Table B.1 gives the finite difference formulas used to calculate the vorticity budget terms. The local change term is center-differenced using the immediately preceding and succeeding analysis times, giving a $2\Delta t$ time interval of 6 hr. Divergence values are calculated using a centered vertical difference of ζ over a pressure interval of $2\Delta p$ where Δp varies from -23 mb at the surface to -34 mb at 500 mb to -19 mb at 100 mb. The finite difference algorithm for vertical advection was designed so that it would be consistent when presented in flux form. That this is indeed the case can be demonstrated by noting that

$$\partial(\omega\zeta)/\partial p = \omega\partial\zeta/\partial p + \zeta\partial\omega/\partial p$$

in finite difference form is

$$\text{LHS} = (\omega_{k+1}\zeta_{k+1} - \omega_{k-1}\zeta_{k-1})/(\Delta p_k + \Delta p_{k-1})$$

$$\begin{aligned}\text{RHS} &= (\omega_{k-1}\zeta_k - \omega_{k-1}\zeta_{k-1} + \omega_{k+1}\zeta_{k+1} - \omega_{k+1}\zeta_k)/(\Delta p_k + \Delta p_{k-1}) \\ &\quad + (\omega_{k+1}\zeta_k - \omega_{k-1}\zeta_k)/(\Delta p_k + \Delta p_{k-1}) \\ &= (\omega_{k+1}\zeta_{k+1} - \omega_{k-1}\zeta_{k-1})/(\Delta p_k + \Delta p_{k-1}) = \text{LHS} .\end{aligned}$$

The horizontal grid intervals Δx and Δy are the horizontal distances corresponding very closely to 1/2° of latitude and longitude, or approximately 55 km.

Table B.1 Vorticity budget formulas. The subscripts t, x, y and k are integer indices of time and the longitudinal, latitudinal and pressure level coordinates of the grid points respectively. Note that the k index increases upward.

$$\left(\frac{\partial \zeta}{\partial t}\right)_t = (\zeta_{t+1} - \zeta_{t-1})/2\Delta t$$

$$(\underset{\sim}{v} \cdot \underset{\sim}{\nabla}\eta)_{x,y} = [u_{x-1}\,(\zeta_x - \zeta_{x-1}) + u_x\,(\zeta_{x+1} - \zeta_x)]/2\Delta x$$

$$+ [v_{y-1}\,(\zeta_y - \zeta_{y-1}) + v_y\,(\zeta_{y+1} - \zeta_y)]/2\Delta y$$

$$+ [v_{y-1}\,(f_y - f_{y-1}) + v_y\,(f_{y+1} - f_y)]/2\Delta y$$

$$\text{where } u_x = \frac{u_x + u_{x+1}}{2} \text{ and } v_y = \frac{v_y + v_{y+1}}{2}$$

$$\left(\omega \frac{\partial \zeta}{\partial p}\right)_k = [\omega_{k-1}\,(\zeta_k - \zeta_{k-1}) + \omega_{k+1}\,(\zeta_{k+1} - \zeta_k)]/(\Delta p_{k-1} + \Delta p_k)$$

$$\text{where } \Delta p_k = p_{k+1} - p_k$$

$$((\zeta + f)\delta)_k = -(\zeta + f)_k\,(\omega_{k+1} - \omega_{k-1})/(\Delta p_{k-1} + \Delta p_k))$$

$$\underset{\sim}{k} \cdot \left(\underset{\sim}{\nabla}\omega \times \frac{\partial \underset{\sim}{v}}{\partial p}\right)_{x,y} = -[\left(\frac{\partial u}{\partial p}\right)_{y-1}\,(\omega_y - \omega_{y-1}) + \left(\frac{\partial u}{\partial p}\right)_y\,(\omega_{y+1} - \omega_y)]/2\Delta y$$

$$+ [\left(\frac{\partial v}{\partial p}\right)_{x-1}\,(\omega_x - \omega_{x-1}) + \left(\frac{\partial v}{\partial p}\right)_x\,(\omega_{x+1} - \omega_x)]/2\Delta x$$

$$\text{where } \left(\frac{\partial u}{\partial p}\right)_y = \frac{\left(\frac{\partial u}{\partial p}\right)_y + \left(\frac{\partial u}{\partial p}\right)_{y+1}}{2}, \quad \left(\frac{\partial v}{\partial p}\right)_x = \frac{\left(\frac{\partial v}{\partial p}\right)_x + \left(\frac{\partial v}{\partial p}\right)_{x+1}}{2}$$

$$\text{and } \left(\frac{\partial u}{\partial p}\right) = \frac{(u_{k+1} - u_{k-1})}{(\Delta p_{k-1} + \Delta p_k)}, \quad \left(\frac{\partial v}{\partial p}\right) = \frac{(v_{k+1} - v_{k-1})}{(\Delta p_{k+1} + \Delta p_k)}$$

Appendix C. Derivation of $\underset{\sim}{X}$ and Z

Utilizing the approach developed by Arakawa and Schubert (1974) to represent the apparent sources of dry static energy and specific humidity, the environmental equations for momentum and vorticity can be given as

$$\partial\{(1-\sigma_c)\tilde{\underset{\sim}{v}}\}/\partial t = \Sigma\delta_i \underset{\sim}{v}_{\delta i} - E\tilde{\underset{\sim}{v}} - \overline{\underset{\sim}{\nabla}\cdot\underset{\sim}{vv}} - \partial(\tilde{\omega}\tilde{\underset{\sim}{v}})/\partial p - \underset{\sim}{\nabla}\bar{\Phi} - \bar{f}\underset{\sim}{k}\times\tilde{\underset{\sim}{v}} \tag{C.1}$$

and

$$\partial\{(1-\sigma_c)\tilde{\eta}\}/\partial t = \Sigma\delta_i \eta_{\delta i} - E\tilde{\eta} - \overline{\underset{\sim}{\nabla}\cdot\underset{\sim}{v}\eta} - \tilde{\omega}\,\partial\tilde{\eta}/\partial p - \underset{\sim}{k}\cdot\underset{\sim}{\nabla}\tilde{\omega}\times\partial\tilde{\underset{\sim}{v}}/\partial p \quad . \tag{C.2}$$

The averaging conventions are the same as described in Chapter 8 and illustrated in Fig. 8.1. Thus, an overbar tilda represents an environmental average, a plain overbar represents a grid-area average, and a subscript i indicates an average over all clouds of subensemble i. $\sigma_c (= \Sigma\sigma_i)$ is the sum of the area coverage of each subensemble, and is thus the total percentage of the averaging area occupied by clouds. ε_i and δ_i are, respectively, the total entrainment and detrainment due to subensemble i, and $\underset{\sim}{v}_{\delta i}$ and $\eta_{\delta i}$ are the average velocity and vorticity, respectively, of the air detrained by subensemble i. These quantities are related to the cumulus mass flux by the mass conservation equation

$$D - E = \partial M_c/\partial p - \partial\delta_c/\partial t \tag{C.3}$$

where $E = \Sigma\varepsilon_i$, $D = \Sigma\delta_i$, and $M_c = \Sigma m_i \equiv -\Sigma\delta_i\omega_i$. The first three RHS terms of (C.1) and (C.2) arise from the representation of the environmental averages of the horizontal transport of $\underset{\sim}{v}$ and η;

$$-\widetilde{\underset{\sim}{\nabla}\cdot\underset{\sim}{vv}} = \Sigma\delta_i \underset{\sim}{v}_{\delta i} - E\tilde{\underset{\sim}{v}} - \overline{\underset{\sim}{\nabla}\cdot\underset{\sim}{vv}} \tag{C.4}$$

$$-\widetilde{\underset{\sim}{\nabla}\cdot\underset{\sim}{v}\eta} = \Sigma\delta_i \eta_{\delta i} - E\tilde{\eta} - \overline{\underset{\sim}{\nabla}\cdot\underset{\sim}{v}\eta} \quad . \tag{C.5}$$

In (C.1) and (C.2), homogeneity of the environment has been assumed. For simplicity, it is also assumed in (C.1) that the environmental geopotential gradient can be approximated by the large-scale gradient, and that the average environmental coriolis parameter (f) can be approximated by its large-scale value.

Applying (C.3) and substituting for $\tilde{\omega}$ using

$$\tilde{\omega} = \bar{\omega} + M_c \tag{C.6}$$

allows (C.1) and (C.2) to be given as

$$\begin{aligned}(1-\sigma_c)\partial\tilde{\underset{\sim}{v}}/\partial t = \Sigma\delta_i(\underset{\sim}{v}_{\delta i} - \tilde{\underset{\sim}{v}}) - \overline{\underset{\sim}{\nabla}\cdot\underset{\sim}{v}\underset{\sim}{v}} \\ - \partial(\bar{\omega}\tilde{\underset{\sim}{v}})/\partial p - \underset{\sim}{\nabla}\bar{\Phi} - \bar{f}\underset{\sim}{k}\times\tilde{\underset{\sim}{v}} - M_c\partial\tilde{\underset{\sim}{v}}/\partial p\end{aligned} \tag{C.7}$$

and

$$\begin{aligned}(1-\sigma_c)\partial\tilde{\eta}/\partial t = \Sigma\delta_i(\eta_{\delta i} - \tilde{\eta}) + \tilde{\eta}\,\partial M_c/\partial p - \overline{\underset{\sim}{\nabla}\cdot\underset{\sim}{v}\eta} - \bar{\omega}\,\partial\tilde{\eta}/\partial p \\ - \underset{\sim}{k}\cdot\underset{\sim}{\nabla}\bar{\omega}\times\partial\tilde{\underset{\sim}{v}}/\partial p - M_c\partial\bar{\eta}/\partial p - \underset{\sim}{k}\cdot\underset{\sim}{\nabla}M_c\times\partial\tilde{\underset{\sim}{v}}/\partial p\end{aligned} \tag{C.8}$$

If the total area covered by clouds is considered to be a small fraction of the total averaging area, then $(1 - \sigma_c) \simeq 1$. If in addition it is assumed that the in-cloud values of momentum and vorticity are of the same order as the environmental momentum and vorticity, then it can be shown that

$$\tilde{\underset{\sim}{v}} \simeq \bar{\underset{\sim}{v}} \tag{C.9}$$

and

$$\tilde{\eta} \simeq \bar{\eta} \quad . \tag{C.10}$$

It is also assumed that the horizontal transports of $\underset{\sim}{v}$ and η across the averaging-area boundaries due to cumulus clouds are small with respect to the large-scale transports, so that

$$\overline{\underset{\sim}{\nabla}\cdot\underset{\sim}{v}\underset{\sim}{v}} \simeq \underset{\sim}{\nabla}\cdot\bar{\underset{\sim}{v}}\bar{\underset{\sim}{v}} \tag{C.11}$$

and

$$\overline{\underset{\sim}{\nabla}\cdot\underset{\sim}{v}\eta} \simeq \underset{\sim}{\nabla}\cdot\bar{\underset{\sim}{v}}\bar{\eta} \quad . \tag{C.12}$$

Using these approximations in (C.7) and (C.8) and bringing all large-scale terms to the left-hand side gives

$$\begin{aligned} &\partial \underset{\sim}{\bar{v}}/\partial t + \underset{\sim}{\nabla}\cdot\underset{\sim}{\underset{\sim}{\bar{v}\bar{v}}} + \partial(\bar{\omega}\underset{\sim}{\bar{v}})/\partial p + \underset{\sim}{\nabla}\bar{\Phi} + \bar{f}\underset{\sim}{k} \times \underset{\sim}{\bar{v}} \\ &\qquad = \Sigma\delta_i(\underset{\sim}{v}_{\delta i} - \underset{\sim}{\bar{v}}) - M_c\partial\underset{\sim}{\bar{v}}/\partial p \\ &\qquad \equiv \underset{\sim}{X} \end{aligned} \tag{C.13}$$

and

$$\begin{aligned} &\partial\bar{\zeta}/\partial t + \underset{\sim}{\nabla}\cdot\underset{\sim}{\bar{v}}\bar{\eta} + \bar{\omega}\ \partial\ \bar{\zeta}/\partial p + \underset{\sim}{k}\cdot\underset{\sim}{\nabla}\bar{\omega} \times \partial\underset{\sim}{\bar{v}}/\partial p \\ &\qquad = \Sigma\delta_i(\eta_{\delta i} - \bar{\eta}) + \bar{\eta}\ \partial M_c/\partial p - M_c\partial\bar{\eta}/\partial p \\ &\qquad - \underset{\sim}{k}\cdot\underset{\sim}{\nabla}M_c \times \partial\underset{\sim}{\bar{v}}/\partial p \\ &\qquad \equiv Z_\zeta \ . \end{aligned} \tag{C.14}$$

Appendix D. Application of Stokes' theorem to areally-averaged momentum

Areally-averaged vorticity can be given using Stokes' theorem as

$$A\bar{\zeta}^{A} = \oint \underset{\sim}{v} \cdot d\underset{\sim}{l} \quad . \tag{D.1}$$

The grid-area geometry and the breakdown of the integration circuit into four "legs" are shown on Fig. D.1. $\overline{(\ )}^{A}$ denotes an average over the area A. From (D.1) we have, assuming that the area and the path of integration do not change with time,

$$(\delta x \delta y)\, \partial \bar{\zeta}^{A}/\partial t = \partial \left(\oint \underset{\sim}{v} \cdot d\underset{\sim}{l}\right)/\partial t = \oint \partial \underset{\sim}{v}/\partial t \cdot d\underset{\sim}{l} \quad . \tag{D.2}$$

Thus, if vorticity is given by (D.1), then it follows that to determine the rate of change of $\bar{\zeta}$ we need only know the rate of change of velocity at each point along the boundary of A. If we assume (for convenience) that the boundary legs N and S are oriented north-south and the legs W and E are oriented east-west, then along the separate legs we need to determine only one component of velocity. We then break (D.2) into sections:

$$\begin{aligned}(\delta x \delta y)\partial \bar{\zeta}^{A}/\partial t = {} & \int_{N} (\partial v/\partial t)dy + \int_{W} (\partial u/\partial t)dx \\ & + \int_{S} (\partial v/\partial t)dy + \int_{E} (\partial u/\partial t)dx \quad .\end{aligned} \tag{D.3}$$

We define an averaging operator along a leg L of length δr as

$$\overline{(\ )}^{L} \equiv (1/\delta r) \int_{k} (\ )dr \quad . \tag{D.4}$$

$\overline{(\ )}^{L}$ may then be thought of as an average value of ( ) in a strip of unit width and length δr. From (D.4) it follows that

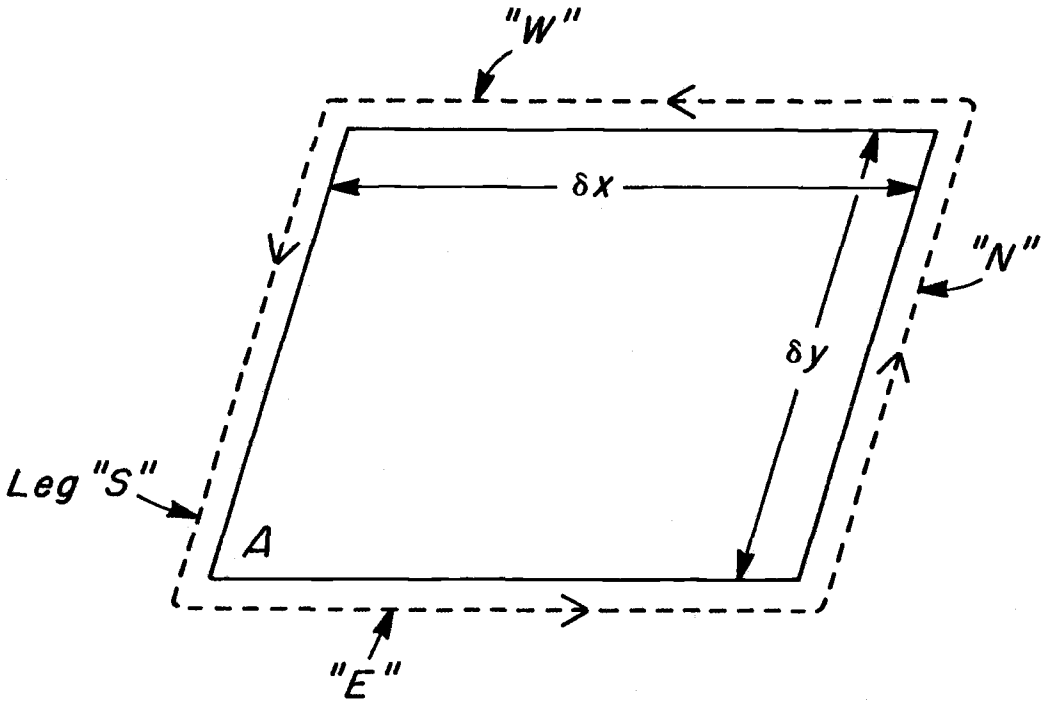

Figure D.1. Grid geometry used in derivation.

$$\int_N (\partial v/\partial t)dy = \overline{(\partial v/\partial t)}^N(\delta y)$$

$$\int_W (\partial u/\partial t)dx = \overline{(\partial u/\partial t)}^W(-\delta x)$$

$$\int_S (\partial v/\partial t)dy = \overline{(\partial v/\partial t)}^S(-\delta y) \qquad (D.5)$$

$$\int_E (\partial u/\partial t)dx = \overline{(\partial u/\partial t)}^E(\delta x) \quad .$$

The negative increments for legs W and S indicate that the line integral is made in a negative direction on these legs.

Combining the N and S legs and the E and W legs of (D.5) gives

$$\int_{N,S} (\partial v/\partial t)dy = \{\overline{(\partial v/\partial t)}^N - \overline{(\partial v/\partial t)}^S\}\delta y$$

$$\int_{W,E} (\partial u/\partial t)dx = \{\overline{(\partial u/\partial t)}^E - \overline{(\partial u/\partial t)}^W\}\delta x \quad , \qquad (D.6)$$

or, in shorthand,

$$\int_{N,S} (\partial v/\partial t)dy = \delta\overline{(\partial v/\partial t)}^{N-S}\delta y$$

$$\int_{W,E} (\partial u/\partial t)dx = \delta\overline{(\partial u/\partial t)}^{E-W}\delta x \quad . \qquad (D.7)$$

Multiplying and dividing by length increments gives

$$\int_{N,S} (\partial v/\partial t)dy = \delta\overline{(\partial v/\partial t)}^{N-S}(1/\delta x)\delta x\delta y$$

$$\int_{W,E} (\partial u/\partial t)dx = \delta\overline{(\partial u/\partial t)}^{E-W}(1/\delta y)\delta x\delta y \qquad (D.8)$$

If we assume that $\overline{\partial(\ )/\partial r}^r = \delta(\ )/\delta r$ for r = x and r = y, (D.8) can be written as

$$\int_{N,S} (\partial v/\partial t)dy = \overline{\{\frac{\partial \overline{(\partial v/\partial t)}^{N-S}}{\partial x}\}}^{E-W}$$

$$\int_{W,E} (\partial u/\partial t)dx = -\overline{\{\frac{\partial \overline{(\partial u/\partial t)}^{E-W}}{\partial y}\}}^{N-S} \quad . \tag{D.9}$$

The negative sign on the RHS of the second of these equations results because the increment $\delta\overline{(\partial u/\partial t)}^{E-W}$ is made from north to south while by convention δ_y is made from south to north.

We assume that

$$\overline{(\overline{(\ )}^{N-S})}^{E-W} = \overline{(\overline{(\ )}^{E-W})}^{N-S} = \overline{(\ )}^{E-W,N-S} = \overline{(\ )}^{A} \quad . \tag{D.10}$$

The last equality in (D.10) follows from the parallel definition of an area-averaging operator such that

$$\overline{(\ )}^{A} \equiv \iint_{A} (\ )dxdy \tag{D.11}$$

Applying (D.10) and (D.11) to (D.9), and then substituting the results into (D.3), gives

$$(\delta x\delta y)(\partial \bar{\zeta}^{A}/\partial t) = (\delta x\delta y)\{\overline{\partial(\partial v/\partial t)/\partial x}^{A} - \overline{\partial(\partial u/\partial t)/\partial y}^{A}\} \tag{D.12}$$

We next assume that the partial derivatives with respect to x and y can be removed from within the averaging operator, yielding

$$(\delta x\delta y)\ (\partial\bar{\zeta}^{A}/\partial t) = (\delta x\delta y)\ \{\overline{\partial(\partial v/\partial t)}^{A}/\partial x - \partial\overline{(\partial u/\partial t)}^{A}/\partial y\} \quad . \tag{D.13}$$

This last assumption is equivalent to assuming that partials with respect to x and y can be moved outside the integrals on the RHS of (D.11).

Since we have previously assumed that the boundary of the averaging area remains constant, (D.13) is equivalent to

$$\partial \bar{\zeta}^A / \partial t = \underset{\sim}{k} \cdot \underset{\sim}{\nabla} \times \partial \underset{\sim}{\bar{v}}^A / \partial t \qquad \text{(D.14)}$$

by the same reasoning as given in the preceding paragraph.

We have thus shown that the rate of change of the large-scale vorticity can be given either by (D.2) or by (D.14), and that the two definitions follow from each other (within the assumptions that we have used).